Chemistry related to the [Fe]-Hydrogenases

Cédric Tard

To cite this version:

Cédric Tard. Chemistry related to the [Fe]-Hydrogenases. Other. University of East Anglia, Norwich, 2005. English. NNT : . tel-00011568

HAL Id: tel-00011568
https://theses.hal.science/tel-00011568

Submitted on 8 Feb 2006

CHEMISTRY RELATED

TO THE

[Fe]-HYDROGENASES

A thesis submitted to the University of East Anglia

for the degree of Doctor of Philosophy

Submitted July 2005

Cédric Tard

Department of Biological Chemistry

John Innes Centre

Norwich

Abstract

The work in this thesis is focused on the synthesis, reactivity and electrochemistry of chemical models of the active site structures found in [Fe]-hydrogenase, an enzyme that catalyses the reversible reduction of protons to dihydrogen. This enzyme possesses an unusual active site, the "H-cluster", which is comprised of an {Fe_4S_4}-cubane linked by a cysteinyl bridge to a di-iron organometallic subsite which is ligated by dithiolate, CO and CN groups.

Chapter I gives a general overview of the biology and chemistry of iron-sulfur proteins and chemical models of their prosthetic groups, with emphasis on the [Fe]-hydrogenase.

Chapter II describes the synthesis, structures and spectroscopic features of 6 new {2Fe3S}-subsite model complexes with a range of functional groups together with X-ray crystallographic structures for all of these.

Chapter III reports and discusses the electrochemical properties of the new {2Fe3S}-complexes. Studies on electrocatalytic hydrogen evolution by these systems are also described.

Chapter IV reports the first synthesis of a free-standing "H-cluster" model complex in which an {Fe_4S_4}-cubane cluster is coupled to an {2Fe3S}-subsite as in [Fe]-hydrogenase. Spectroscopic, electrochemical and DFT calculations provide an insight into the electronic properties of the synthetic assembly and this is placed in the context of the natural system.

Chapter V describes some early results on the incorporation of synthetic di-iron subsites into electropolymers to provide solid-state electrocatalysts together with the prospects for future work in the area.

Acknowledgements

First I would like to thank my supervisor, Pr. Chris Pickett, for his enthusiastic and friendly supervision during the past three years, and I am greatly indebted to him for the work we have carried out and the successes we have achieved.

I also wish to thank my second supervisor, Dr. Gary Sawers, for supporting me during this PhD and for proofreading my thesis, as well as my two advisors, Dr. Dave Evans and Pr. Ray Dixon.

I would also like to acknowledge Dr. Stephen Best for giving me the opportunity to work in his laboratory at the School of Chemistry of the University of Melbourne (May-June 2005). Thank you to the Best group in the Tower, Claire, Karolina, Mark and Michael, and especially to the "Collingwood supporter" Stacey Borg who carried out the spectroelectrochemical experiments with me.

My sincere acknowledgment to the people at the John Innes Centre who assisted me during this PhD: Dr. Xiaoming Liu and Dr. Saad Ibrahim for their lab skills in electrochemistry and organometallic synthesis and for their friendship; Dr. David Hughes and Siân Davies (X-ray crystallography); Dr. Lionel Hill (mass spectrometry); Dr. Dave Evans and Elaine Barclay (Mössbauer spectroscopy); Dr. Shirley Fairhurst (NMR fluctionality experiments). I also would like to thank people who carried out some experiments on my model complexes: Dr. Peter Hitchcock (X-ray crystallography, University of Sussex); Pr. Luca De Gioia and Dr. Maurizio Bruschi (DFT calculations, University of Milano); Pr. Lai-Sheng Wang and Dr. Xin Yang (MS-PES, Pacific Northwest National Laboratory, WA); Dr. Robert Szilagyi (S-K edge ligand spectroscopy, University of Montana).

I wish also to thank colleagues and friends met in Norwich: Nolwenn, Roger, Amy, Kylie, Elaine, Carla, Monica, Violaine, Jane, the "Tuesday morning football crew" and Matthieu who established the main basis of this exciting project during his PhD.

To my family and friends in France, I would like to thank them for their patience and encouragements during my short visits.

And finally, I wish to thank Caroline for her support, patience and love.

The French complain about everything, and always.

Napoléon Bonaparte

Contents

Abstract 2

Acknowledgements 3

I. Introduction 11

I.1. Inorganic chemistry of biological systems 11

I.2. Roles of iron in metalloproteins 11

- **I.2.a. Dioxygen uptake, transport, and storage** 12
- **I.2.b. Dioxygen activation** 12
- **I.2.c. Electron transfer** 12

I.3. Iron-sulfur proteins 13

- **I.3.a Iron-sulfur cluster biosynthesis** 13
- **I.3.b Classes of Fe-S clusters** 14
- I.3.b.α Rubredoxins (Rb) 14
- I.3.c.β $\{Fe_2S_2\}$-centres (2-Iron ferredoxin) 16
- I.3.d.γ $\{Fe_3S_4\}$-centres (3-Iron ferredoxin) 17
- I.3.e.δ $\{Fe_4S_4\}$-centres (4-Iron ferredoxin) 17

I.4. Complex iron-sulfur proteins 19

- **I.4.a. Nitrogenase** 19
- **I.4.b. Other iron-sulfur enzymes** 20

I.5. Hydrogenases 20

- **I.5.a. Iron-Sulfur Cluster-Free Hydrogenase** 21
- **I.5.b. [Ni-Fe]-Hydrogenase** 23
- **I.5.c. [Fe]-Hydrogenase** 24

I.5.c.α Physiological Role 24

I.5.c.β The catalytic subunit 25

I.5.c.γ Spectroscopic features and oxidation states of the "H-cluster" 26

I.5.c.δ Catalytic mechanism 29

I.5.c.ε Biosynthesis of the H-cluster and origin of the CO and CN ligands 30

I.6. Synthetic models of the active sites of iron-sulfur proteins 32

I.6.a Analogues of rubredoxin and ferredoxin sites 32

I.6.b Site-differentiated clusters 33

I.6.c Synthetic analogues of iron-sulfur complexes 34

I.7. Synthetic models of the di-iron subsite of [Fe]-hydrogenase 36

I.7.a. Early {2Fe2S}-complexes 36

I.7.b. {2Fe2S}-frameworks 37

I.7.c. {2Fe3S}-framework 38

I.7.d. Hydride complexes 39

I.7.e. Hydrogen evolution and model complexes 40

II. {2Fe3S}-Systems: synthesis, structures and spectroscopic properties 42

II.1 Tripodal ligand CH$_3$C(CH$_2$SH)$_3$ 42

II.2 Synthesis of {2Fe3S}-pyridine derivatives 44

II.2.a Ligand synthesis 44

II.2.b Complex synthesis 45

II.3 Synthesis of {2Fe3S}-nitrobenzene and aniline Derivatives 47
  II.3.a Ligand synthesis 47
  II.3.b Complex synthesis 48
II.4 Other functionalisation: Synthesis of pyrrole and ethanol derivatives 50
  II.4.a Ligand synthesis 51
  II.4.b Complex synthesis 51
II.5 Synthesis of a mixed-valence tetra-iron complex 53
II.6 Structural comparisons of different {2Fe3S}-complexes 54
II.7 Infra-red spectra of carbonyl compounds: back bonding 56
  II.7.a General aspects 56
  II.7.b {2Fe3S}-carbonyl complexes 58
II.8 Studies of dynamic / equilibrium properties of the thioether ligand 60
  II.8.a NMR coalescence 60
  II.8.b Lability of the thioether ligand under CO 66
II.9 On the bonding and reactivity of the thioether ligand 69
  II.9.a Free energy correlations between inversion and substitution reactions 69
  II.9.b Back-bonding to the thioether ligand: possible influence on metal-metal bond strength 73
II.10 General conclusions 76
II.10 Experimental 77

III Electrochemistry and proton reduction by {2Fe3S}-complexes 92

III.1 Electrochemical behaviour of the {2Fe3S}-complexes 92
  III.1.a General Features 92
  III.1.b Relationship between redox potentials and structure 96
III.2 Electrocatalytic reduction of protons 96

III.2.a General aspects of electrocatalysis 96
III.2.b {2Fe3S}-pyridine derivatives 10 and 11 98
III.2.c {2Fe3S}-aniline derivative 15 101
III.3 {2Fe3S}-nitrobenzene derivative 14 103
III.3.a Electrochemical studies 103
III.3.b Spectroelectrochemical studies 107
III.4 Electrocatalysis of hydrogen evolution by the mixed-valence tetra-iron complex 114
III.5 Surface deposition of a catalytic material 119

IV. Synthesis of the "H-cluster" Framework 121

IV.1 {Fe$_4$S$_4$}-cluster and the trithiol ligand 121
IV.2 [Fe$_2$(CO)$_6$(CH$_3$C(CH$_2$S)$_2$CH$_2$SCOCH$_3$)]: an activated di-iron subsite 122
IV.3 Multiple subsites around the {Fe$_4$S$_4$}-core 124
IV.4 The "H-cluster" model (HCM) 129
IV.4.a Synthesis of the "Holm ligand" 130
IV.4.b Synthesis and properties of the "Holm cluster" 132
IV.4.c "H-cluster" model (HCM) 135
IV.4.c.α FTIR spectroscopy 136
IV.4.c.β Mössbauer spectroscopy 137
IV.4.c.γ DFT calculation 139
IV.4.c.δ Electrochemistry 140
IV.4.c.ε Electrocatalysis of proton reduction 145
IV.4.c.ζ FTIR-Spectroelectrochemistry 146
IV.4.c.η Summary of redox reactions of **HCM** 153
IV.5 Relevance to the natural system 153
IV.X Experimental 155

V. Toward new assemblies related to the “H-cluster” 164

V.1 {2Fe3S}-subsites and electropolymers 164
V.1.a Fuel cells 164
V.1.b Kinetics of electrode processes 166
V.1.c The poly(pyrrole) framework 169
V.1.d {2Fe3S}-pyrrole polymerisation 170
V.1.e Post-polymerisation 172
V.1.e.α {2Fe3S}-pentacarbonyl polymers 172
V.1.e.β Proton reduction by modified poly(pyrrole) 174
V.1.e.γ Cyanation of di-iron subsite complexes 175
V.2 Replacing iron by cobalt: a route toward stable Co(I)-Co(II) and / or Co(II)-Co(II) “H-cluster” analogues? 178
V.2.a Cobalt-carbonyl complexes 178
V.2.b Cobalt-carbonyl clusters 180
V.2.c Reaction of $[Co_2(CO)_8]$ and $CH_3C(CH_2SH)_2CH_2SCH_3$ 180
V.X Experimental 187

VI. Summary and future work 189

VII. Materials and methods 192

VII.1 General 192
VII.2 Mössbauer spectroscopy 192
VII.3 Electrochemistry 195
VII.4 IR-Spectroelectrochemistry 197
VII.5 Gas-phase photoelectron spectroscopy 198
VII.6 DFT calculations 200

VIII. Appendix 202

VIII.1 X-ray structure data of $[Fe_2(CO)_5\{CH_3C(CH_2S)CH_2SCH_2\text{-2-Py}\}]$ (10) 202

VIII.2 X-ray structure data of $[Fe_2(CO)_5\{CH_3C(CH_2S)CH_2SCH_2CH_2\text{-2-Py}\}]$ (11) 204

VIII.5 X-ray structure data of $[Fe_2(CO)_5\{CH_3C(CH_2S)CH_2SC_6H_4\text{-}p\text{-}NO_2\}]$ (14) 207

VIII.5 X-ray structure data of $[Fe_2(CO)_5\{CH_3C(CH_2S)CH_2SC_6H_4\text{-}p\text{-}NH_2\}]$ (15) 210

VIII.5 X-ray structure data of $[Fe_2(CO)_5\{CH_3C(CH_2S)CH_2SCH_2CH_2OH\}]$ (20) 212

VIII.6 X-ray structure data of $[Fe_2(CO)_4\{CH_3C(CH_2S)_3\}]_2$ (22) 215

VIII.7 X-ray structure data of $[Fe_2(CO)_6\{CH_3C(CH_2S)_2CH_2SCOCH_3\}]$ (27) 217

VIII.8 X-ray structure data of $[Co_4(CO)_4(\mu_3\text{-}S)\{CH_3C(CH_2S)_2CH_2SCH_3\}_2]$ (43) 220

IX. References 225

List of publications 240

Conferences 240

- Chapter I -

Introduction

I.1. Inorganic chemistry of biological systems

Metals are key components of living systems. Most of the reactions that provide energy to these systems are fundamentally inorganic (*e.g.* photosynthesis or respiration). It has been estimated that minimally one-third of all proteins and enzymes require metal ions as cofactor for biological function.[1] These “biological” metals include magnesium, calcium, members of the first transition series (except scandium, titanium and chromium), and molybdenum, tungsten, cadmium and mercury. They are usually covalently bound to the polypeptide backbone by endogenous ligands provided by amino acid side chains.

One of these metals essential for living organisms is iron. It is omnipresent on earth (*ca.* 5% in the Earth’s crust), and due to its availability has been widely used by living organisms in which it is responsible for vital biological mechanisms.

I.2. Roles of iron in metalloproteins

Nature has learned to use the specific properties of metal ions to perform a wide variety of functions associated with life processes. Metalloproteins are able to bind substrates, and these processes are accompanied by redox changes, even when the overall reaction does not involve a net oxidation-state change. Major functions of iron metalloproteins involve dioxygen and its metabolic products, and electron transfer.

Iron metalloproteins can be separated into three classes: heme proteins, non-heme proteins and iron-sulfur proteins. The term *heme*, is derived from the Greek root meaning “blood”, corresponding to the porphyrin macrocycle. This tetrapyrrole molecule can be anchored covalently to the protein by substituents on the pyrrole rings, or by amino acids coordinating the two axial positions above and below the macrocycle. It is the most common prosthetic group for iron in the human body.[2]

I.2.a. Dioxygen uptake, transport, and storage

These processes do not require the enzymatic function of the proteins but instead involve the reversible binding of the dioxygen molecule. Three known systems are able to transport and store O_2, and all involve metalloproteins (two with iron and one with copper). Only hemoglobin (Hb) possesses a heme prosthetic group. Hemerythrin (Hr) has two octahedrally-coordinated irons joined by a μ-oxo and two bridging carboxylate groups. The O_2 molecule is stored in tissues (as muscle) by myoglobin (Mb) and myohemerythrin (myo Hr), which have metal core structures analogous to those of the transport proteins.

I.2.b. Dioxygen activation

Iron-porphyrin proteins are involved in a variety of catalytic biochemical processes. Depending on the number of oxygen atoms inserted into C–H or C–C bonds, these enzymes are called dioxygenases (*e.g.* catechol dioxygenase) or monooxygenases (*e.g.* cytochrome P-450 and methane monooxygenase).

I.2.c. Electron transfer

Hemoproteins can be used by organisms to transfer electrons in both the respiratory chain and in photosynthesis. This class of proteins is called cytochrome, and can be divided into different groups depending on their structures and physical properties. The heme can be anchored to the protein (cytochromes *b* and *c*) unlike hemoglobin, and ligands to the heme iron can be histidine, methionine, cysteine or lysine. Depending on the nature of these ligands and their coordination environment, redox potentials of the Fe^{III}/Fe^{II} couple can be modulated (*e.g.* cytochrome *c* +260 mV and cytochrome b_5 +20 mV *vs.* SHE). Cytochromes may also contain several heme groups (*e.g.* cytochrome *c* or nitrite reductase).

I.3. Iron-sulfur proteins

Approximately 1% of the iron content of mammals is present in the form of iron-sulfur proteins. The majority of iron-sulfur centres in proteins is involved in electron transfer, but some have catalytic, structural and sensory roles.[3] These proteins are thought to have played an important role in early evolution due to their facile formation, thermal robustness and their distribution in nearly all organisms.

Unlike other electron-transfer proteins like cytochromes and flavoproteins which have complex organic molecules in their active sites, iron-sulfur proteins have only iron and inorganic sulfur, both of which were abundant in the primitive Earth.[4]

I.3.a Iron-sulfur cluster biosynthesis

Biological iron-sulfur clusters were identified about 40 years ago and over 100 different proteins that contain these assemblies have been described. Their role in major biological processes such as nitrogen fixation, photosynthesis and respiration has led to the study of the formation of these systems.

The biosynthesis of such assemblies has not been unravelled, but recent efforts have led to significant advances in our understanding of the physiological pathways responsible for intracellular metal trafficking.[5] In proteins, iron-sulfur clusters can be spontaneously generated from the required components and under the proper conditions (in vitro with apoproteins). However, this can not be achieved in vivo due to the absence of free metal in the cell. To avoid the toxic effect of free metal in the cell, especially the generation of free radicals via Fenton reactions, some proteins called metallochaperones are able to deliver metals to the target apoprotein.

Three different systems have been identified for bacterial iron-sulfur cluster biosynthesis: ISC (iron-sulfur cluster), NIF (nitrogen fixation, only involved in cluster maturation of nitrogenase) and SUF (minor iron-sulfur biosynthetic pathway).[6]

ISC homologues have been identified in most sequenced genomes, from bacteria to plants and humans, and thus represent a fundamental iron-sulfur cluster biosynthesis pathway. Of the ISC proteins, IscU and IscS appear to be the most important.[5] IscU assembles the iron-sulfur cluster that is subsequently transferred to the target protein, whereas IscS provides the sulfur to IscU protein for the cluster biosynthesis.

I.3.b Classes of Fe-S clusters

Iron-sulfur centres can be distinguished into four sites: rubredoxin (Rb) [Fe(S-Cys)$_4$], and three different sites for the ferredoxin (Fd) proteins (rhombic [Fe$_2$S$_2$(S-Cys)$_4$], cuboidal [Fe$_3$S$_4$(S-Cys)$_3$] and cubane [Fe$_4$S$_4$(S-Cys)$_4$]).[3] The oxidation states of irons in these clusters are Fe^{II} and/or Fe^{III} in approximately tetrahedral FeS$_4$ coordination unit.

I.3.b.α Rubredoxins (Rb)

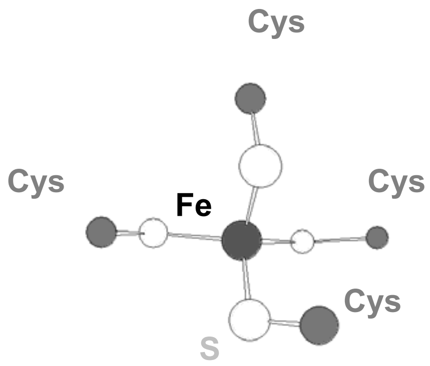

These small proteins contain just one iron centre surrounded by four cysteines from the amino acid chain and have a redox function. Crystallographic data have not shown major changes in Fe-S distances between the reduced and the oxidised proteins (*ca.* 2.3 Å), but a distortion is observed in the tetrahedral geometry around the iron.

In its reduced state (ferrous Fe^{II}), spectroscopic studies (EPR and Mössbauer) have shown clearly that the iron was in a high-spin state in a tetrahedral environment (Scheme **I-1**).

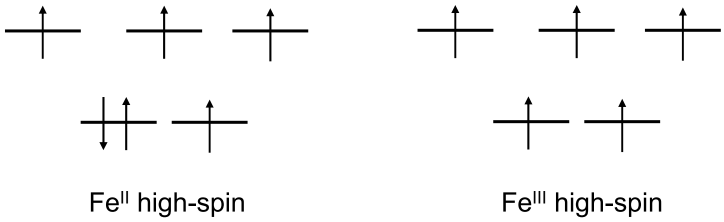

Scheme I-1. High-spin electronic distribution for Fe(II) and Fe(III).

The reduced form of the protein is colourless, but when it is in its oxidised state, an intense red colour is observed resulting from a ligand-to-metal charge-transfer transition (LMCT) from the σ and π orbitals of thiolate ligands (electron-rich) to the oxidised ferric Fe^{III} (electron-poor). This observation highlights the strong electronic interaction between iron and sulfur which will induce specific spectroscopic and redox properties in all the different Fe-S centres.

The reduction potentials for rubredoxins are generally between -50 and +50 mV (*vs.* SHE).

I.3.c.β $\{Fe_2S_2\}$-centres (2-Iron ferredoxin)

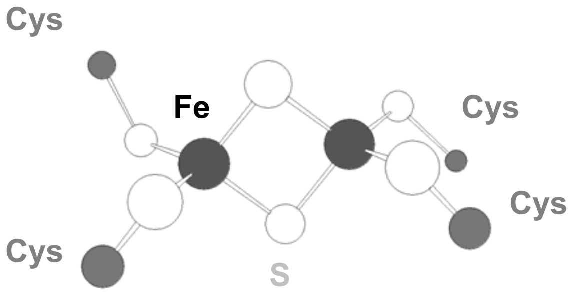

This type of protein has the peculiarity of possessing in the metal centre two inorganic sulfurs (S^{2-}) bridging two irons. The $\{Fe_2S_2\}$-centres are anchored to the protein by the coordination of four cysteines from the backbone of the protein. The doubly bridged $\{Fe_2S_2\}$ unit has an Fe-Fe distance of 2.7 Å.

The two biologically relevant oxidation states are the oxidised form Fd_{ox} $\{Fe_2S_2\}^{2+}$ (Fe^{III}/Fe^{III}) and the mixed-valence form Fd_{red} $\{Fe_2S_2\}^{+}$ (Fe^{II}/Fe^{III}). The one-electron transfer reaction by the protein involves the reduction of Fd_{ox} to Fd_{red}. This can be studied by EPR techniques as the metal centre in the oxidised form is diamagnetic (S = 0, EPR silent) and becomes paramagnetic after one-electron reduction (S = ½).

Reduction potentials for $\{Fe_2S_2\}$-centres are generally between -450 and -150 mV (*vs.* SHE). Some unusual redox potentials have been observed in so-called “Rieske centres”, showing uncommon spectroscopic properties and relatively high redox potentials (-100 to +400 mV). These properties are assigned to the asymmetrical coordination involving two histidines instead of two cysteines $\{(Cys)_2Fe(\mu\text{-}S)_2Fe(His)_2\}$.

I.3.d.γ {Fe_3S_4}-centres (3-Iron ferredoxin)

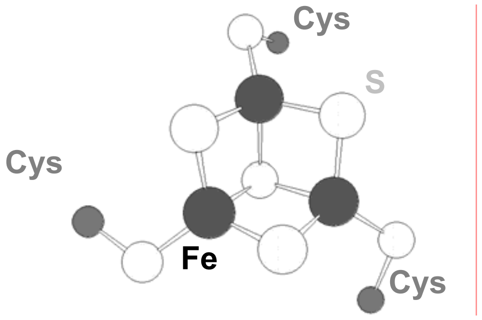

This cuboidal structure (i.e. a cube with one vacancy) has been found in several Fe-S proteins as well as in the inactive form of the enzyme aconitase (aconitase hydratase/isomerase). It is also present as a cofactor in the [Ni-Fe] hydrogenase to transfer electrons after the dihydrogen oxidation.

The reduction potentials of the couple $[Fe_3S_4]^+/[Fe_3S_4]^0$ are variable, ranging from -425 mV in *Azobacter vinelandii* ferredoxin I to -70 mV in *Desulfovibrio gigas* [Ni-Fe]-hydrogenase (*vs.* SHE), and exhibits substantial pH dependence.

I.3.e.δ {Fe_4S_4}-centres (4-Iron ferredoxin)

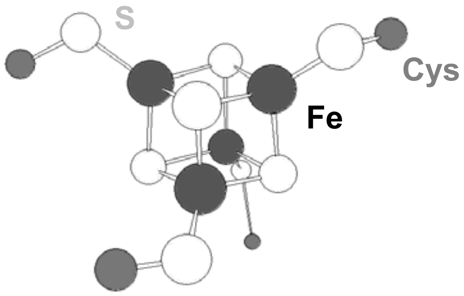

The most common iron-sulfur centre in biology is of the {Fe_4S_4}-type. The crystal structure determined for several proteins is described as a distorted cube with alternating Fe and S at the corners and means Fe-Fe and S-S distances of 2.75 and

3.55 Å respectively. Four cysteines from the polypeptide chain anchor the cubane to the protein.

These types of Fe-S centre exhibit three possible oxidation states, $[Fe_4S_4]^{3+}$, $[Fe_4S_4]^{2+}$ and $[Fe_4S_4]^{+}$, but they have not been observed in any protein unless its tertiary structure is significantly disturbed. The ferredoxin proteins can therefore be divided into two subclasses: Fd using the $[Fe_4S_4]^{2+}/[Fe_4S_4]^{+}$ redox couple (-700 to -300 mV *vs.* SHE) and Fd proteins that can sustain a higher oxidation state using $[Fe_4S_4]^{3+}/[Fe_4S_4]^{2+}$ redox couple (+100 to +400 mV *vs.* SHE) and called HiPIP (high-potential iron protein) (Scheme **I-2**). These potentials are also pH-, ionic strength- and temperature-dependent.

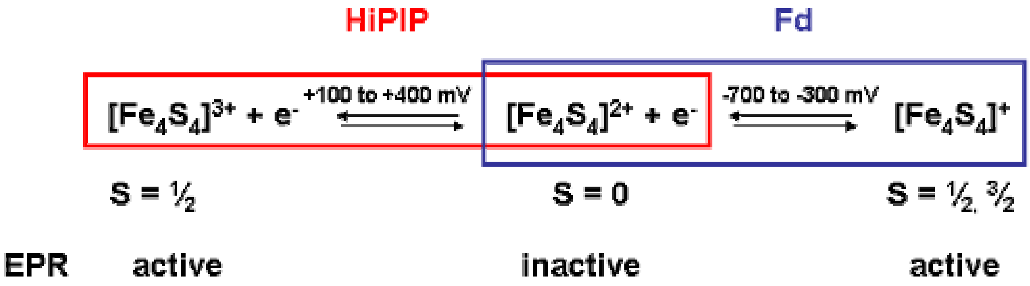

Scheme I-2. Redox potentials for HiPIP and ferredoxin proteins.

Such differences in redox potentials between Fe-S clusters in Fd and HiPIP are not due to their structures, as they appear to be nearly identical, but to the cluster environment. Crystallographic data indicate that in Fd, the Fe-S centre is very close to the protein surface compared to the more buried Fe-S centre in HiPIP. This indicates that the accessibility of the cluster to aqueous solvent and potential hydrogen bonding interaction is easier for Fd, whereas the environment is more rigid for HiPIP.

I.4. Complex iron-sulfur proteins

I.4.a. Nitrogenase

This molybdenum-iron protein can catalyse the transformation of dinitrogen into ammonia (Equation **I-1**) and plays a fundamental role in the biological nitrogen cycle.[7]

$$N_2 + 8H^+ + 16MgATP + 8e^- \longrightarrow 2NH_3 + H_2 + 16MgADP + 16P_i \quad \textbf{(I-1)}$$

The complex enzyme consists of the iron-protein with an $[Fe_4S_4(S{\bullet}Cys)_4]$ cluster and a molybdenum-iron protein. The cofactor of the MoFe protein consists of two cuboidal fragments, one containing four iron atoms and the other one molybdenum atom and three iron atoms (Scheme **I-3**). This cofactor is dissociable from the protein.

The $\{Fe_4S_4\}$-cluster of the iron protein is the ultimate electron donor to the MoFe protein for the catalytic reduction of N_2. The dinitrogen binding site is not known.

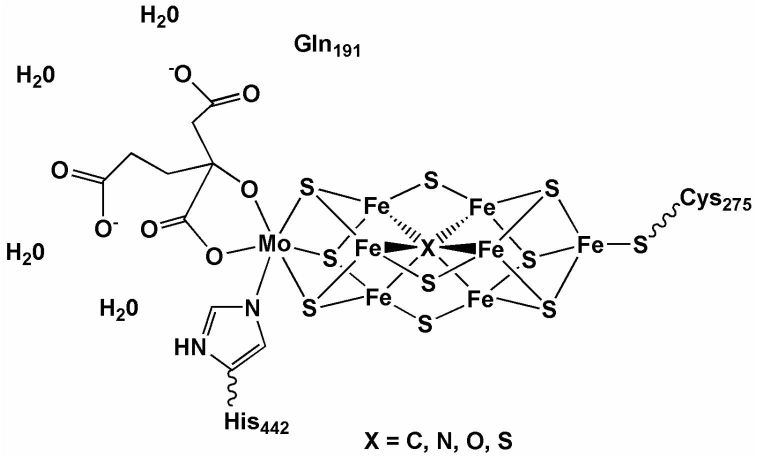

Scheme I-3. FeMoco of nitrogenase with an unknown ligand **X** located in its centre. The immediate protein environment surrounding the homocitrate is also shown.

It is important to note that in the absence of dinitrogen, this enzyme can evolve H_2.

I.4.b. Other iron-sulfur enzymes

The active site of sulfite reductase which catalyses the reaction $SO_3^{2-} + 7H^+ + 6e^- \leftrightarrow HS^- + 3H_2O$, the “A-cluster” of acetylcoenzyme A synthase (ACS), which catalyses the reaction CH_3-Cobalt(III)alamin + CO + HSCoA ↔ $CH_3COSCoA$ + Cobalt(I)alamin and the “C-cluster” of carbon monoxide dehydrogenase (CODH), which catalyses the reaction $CO_2 + 2H^+ + 2e^- \leftrightarrow CO + H_2O$, are examples of Fe-S cluster bridged assemblies, which generally consist of two fragments that are coupled by one or more covalent bridges (Scheme **I-4**).

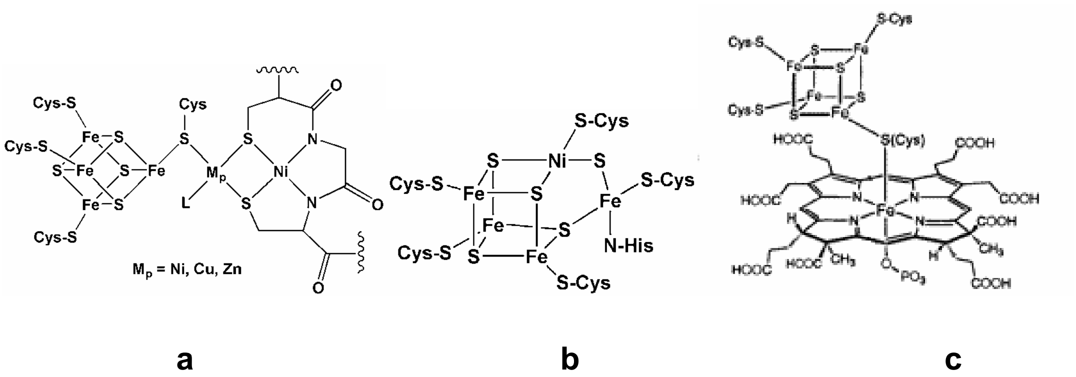

Scheme I-4. Schematic representation of **a)** the “A-cluster” of ACS from *Moorella thermoacetica*. M_p has been identified as Ni, Cu, or Zn; L is an unknown ligand; **b)** the “C-cluster” of reduced CODH from *C. hydrogenoformans*; **c)** the *E. coli* sulfite reductase hemoprotein active site in the phosphate-bound form.

I.5. Hydrogenases

Hydrogenases catalyse the reversible oxidation of dihydrogen and play a central role in microbial energy metabolism (Equation **I-2**).

$$2H^+ + 2e^- \leftrightarrow H_2 \qquad \textbf{(I-2)}$$

This enzyme has been named after Stephenson and Stickland demonstrated that bacteria can evolve H_2 during growth and can use H_2, but not N_2, to reduce artificial and physiological substrates.[8]

Most of these enzymes are found in archaea and bacteria. Three classes of hydrogenase are known: [Ni-Fe]-hydrogenases; [Fe]-hydrogenases; and iron-sulfur cluster-free hydrogenases. The vast majority of known hydrogenases belong to the first two classes and over 100 of these enzymes have been characterised genetically and/or biochemically.[9] Although most hydrogenases can catalyse proton reduction in either direction in vitro, they usually catalyse either hydrogen uptake or evolution in vivo (Table **I-1**).

	[Ni-Fe]-hydrogenase	**[Fe]-hydrogenase**
H_2 production	700	6 000 - 9 000
H_2 consumption	700	28 000

Table I-1. Catalytic activities (measured as molecule of dihydrogen per second per hydrogenase molecule at 30°C) of purified [Ni-Fe]- and [Fe]-hydrogenases.[10]

I.5.a. Iron-Sulfur Cluster-Free Hydrogenase

This enzyme is present in many methanogenic archaea that grow using H_2 and CO_2.[11] H_2-forming methylenetetrahydromethanopterin dehydrogenase (Hmd) catalyses the reversible reduction of methylenyltetrahydromethanopterin (methylenyl-H_4MPT^+) with H_2 to methylenetetrahydromethanopterin (methylene-H_4MPT).[12] A hydride is stereospecifically transferred from H_2 into the *pro-R* site of methylene-H_4MPT (Scheme **I-5**). Hmd does not catalyse H_2/H^+ exchange in the absence of methylenyl-H_4MPT^+.

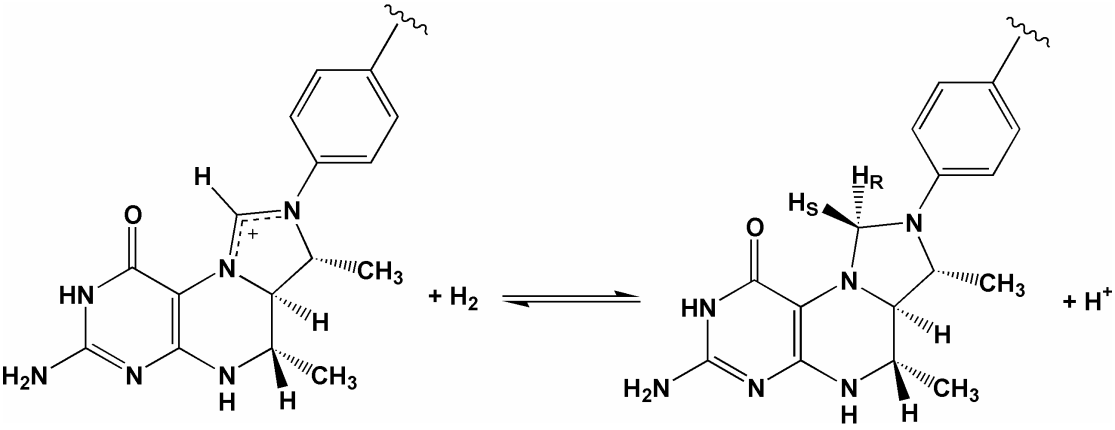

Scheme I-5. Reaction catalysed by Hmd.

Since its discovery more than 10 years ago, this enzyme was thought not to contain any metal.[13] A mechanism for dihydrogen activation has been proposed in analogy with the chemistry of alkanes in superacidic solution.[14,15] Recently, however, a functional iron has been discovered in the enzyme, as well as a cofactor able to bind this iron.[16] The inactivated cofactor has been extracted and characterised by NMR and MS (Scheme **I-6**).[17]

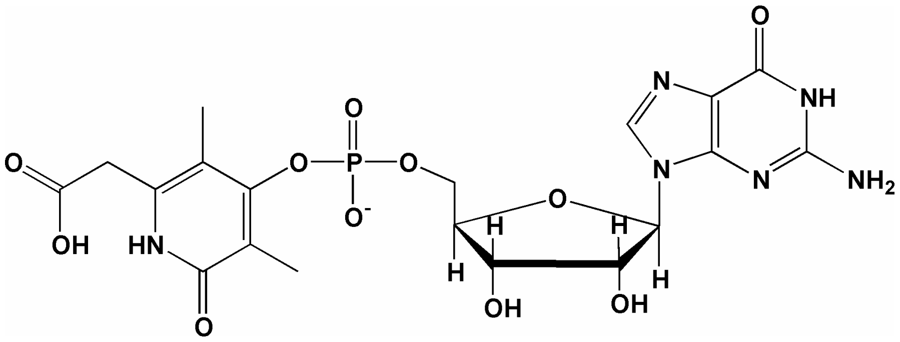

Scheme I-6. Structure proposed for the inactive cofactor of Hmd.

No crystal structure is available yet, but iron is thought to be coordinated at the pyridone derivative. Infrared spectroscopy also showed the presence of two carbonyl ligands coordinated to the iron,[18] but no cyanide ligand has been found, and the activity of the enzyme is inhibited in the presence of CN. The oxidation state of this iron is most probably Fe(II) low-spin as suggested by Mössbauer spectroscopy.

Elucidation of the structure of the enzyme at high resolution will probably be required to shed light on the nature of the iron coordination.

I.5.b. [Ni-Fe]-Hydrogenase

[Ni-Fe]-hydrogenases are mainly involved in the oxidation of dihydrogen to protons and electrons. These hydrogenases are usually heterodimers with a large (60 kDa) and a small (30 kDa) subunit. The X-ray structures of [Ni-Fe]-hydrogenases have revealed a bimetallic nickel-iron centre at the active site, located in the large subunit and buried inside the protein.[19] Up to three Fe-S clusters are contained within the small subunit, which transfer electrons from the active site to the physiological electron acceptor. Hydrophobic channels have been identified by crystallographic analysis of xenon binding and these channels permit the diffusion of H_2 within the interior of the enzyme.[20]

The active site contains the π-acceptor ligands carbonyl and cyanide (Figure **I-1**). The presence of these biologically unusual ligands can stabilise the low-oxidation state of the iron (+2, diamagnetic). Two cysteines from the backbone of the enzyme bridge the two metals. In the oxidised inactive form, an additional bridging ligand is present and is believed to be an oxo or hydroxo, which is a hydride in the active form.

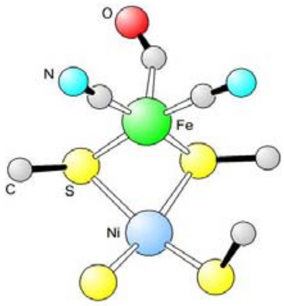

Figure I-1. Active site of [Ni-Fe]-hydrogenase.

The nickel atom exhibits different oxidation states (+1, +2 and +3), and is coordinated by a further two cysteines. One of the terminal cysteines can be replaced by selenocysteine, as found in an enzyme from *Desulfomicrobium baculatum*.

The mechanism of hydrogen uptake has not been entirely resolved, and the binding site for H_2 remains to be determined.[21]

I.5.c. [Fe]-Hydrogenase

I.5.c.α Physiological Role

The absence of nickel in hydrogenase enzymes has been demonstrated in the periplasmic [Fe]-hydrogenase from *Desulfovibrio vulgaris* in 1984 [22] and this class of hydrogenase generally has a role in dihydrogen evolution.

The location of hydrogenases in the bacterial cell reflects the enzyme's function.[23] The periplasmic *Desulfovibrio desulfuricans* [Fe]-hydrogenase (DdH) is involved in dihydrogen uptake. Protons resulting from dihydrogen oxidation by *Desulfovibrio* species [Fe]-hydrogenases create a gradient across the membrane that is thought to be coupled to ATP synthesis in the cytoplasm. *Clostridium pasteurianum* [Fe]-hydrogenase I (Cp1) is a cytoplasmic enzyme that accepts electrons from ferredoxin and generates dihydrogen with protons as electron acceptors. This reaction permits the regeneration of oxidised ferredoxin.

Molecular masses of hydrogenases can vary from 45 to 130 kDa. Unlike [Ni-Fe]-hydrogenases, [Fe]-hydrogenases are mainly monomeric (in the cytoplasm), but dimeric, trimeric and tetrameric enzymes are also known (in the periplasm).

I.5.c.β The catalytic subunit

In the 1980's, EPR spectroscopy showed the presence of a 6Fe cluster (the "H-cluster") in addition to the two $\{Fe_4S_4\}$-clusters (the "F-clusters") generally found in [Fe]-hydrogenases.[24] The unusual active-site unravelled by X-ray crystallographic studies conjointly by two groups in Grenoble (France) and Logan (Utah, USA) in 1998 resolved the structure of this unusual "H-cluster" (crystal structures from DdH[25] and Cp1[26]). The active side is buried deeply within the protein and a continuous hydrophobic channel has been observed between the surface and the "H-cluster" and is conserved in the two [Fe]-hydrogenases studied to date. As these enzymes are involved in different reactions (dihydrogen uptake for DdH and dihydrogen evolution for Cp1), it suggests that the same pathway is used by dihydrogen to access or exit the active site.

The "H-cluster" is composed of an $\{Fe_4S_4\}$-cluster linked by a cysteinyl residue to a {2Fe2S}-subsite (Figure **I-2**). The $\{Fe_4S_4\}$-cluster is anchored to the protein by three cysteines. The binuclear metal centre is bridged by a dithiolate ligand, possibly 1,3-propanedithiolate, di(thiomethyl)amine or di(thiomethyl)oxo. The amino bridge is favoured by the possibility of hydrogen-bonding with amino acids from the protein and also proton transfer to the active site, but no clear X-ray data has so far allowed discrimination between CH_2, NH or O.

Biologically unusual carbonyl and cyanide ligands coordinate the two irons, and a bridging carbonyl has also been observed for Cp1. FTIR studies of the *D. vulgaris* [Fe]-hydrogenase suggested that a bridging CO is present in the oxidised state but absent when the enzyme is reduced.[27] X-ray structures appear to show that the DdH active site is more reduced than the Cp1 active site.

A weak ligand (H_2O) binds the distal iron atom in Cp1, and its absence in DdH suggests that this vacant site might be involved in catalysis, possibly acting as a binding site for an hydride or a dihydrogen molecule. When CO is added to the enzyme at high concentration under turnover conditions, it results in a complete and irreversible inhibition, and the structure of Cp1 showed the terminal binding of CO on the distal iron.[28] This confirms the potential role of this site as being essential for dihydrogen evolution/uptake.

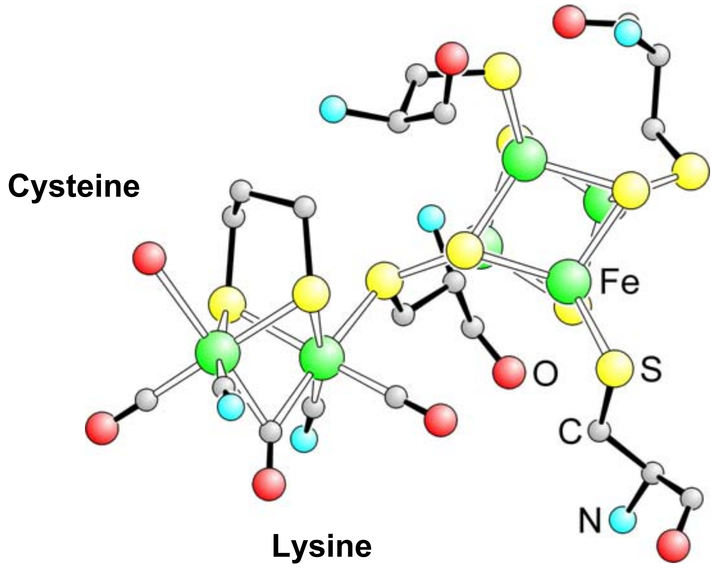

Figure I-2. Composite structure of the H-cluster constructed from the crystal structures of Fe-only hydrogenase isolated from DdH[25] (PDB code 1HFE) and Cp1[26] (PDB code 1FEH) and FTIR data [29] from *D. vulgaris*. The apical group on the sub-site ligand may possibly be CH_2, NH or O.

Crystallographic data also gives information in terms of the potential proton donor or acceptor: a lysine (K358 in Cp1 and K237 in DdH) at ~4 Å from the distal iron forms a hydrogen bond with one of the two cyanides, and a cysteine (C299 in Cp1 and C178 in DdH) at ~5 Å from the distal iron forms a hydrogen bond with the terminally bound water molecule.[23]

I.5.c.γ Spectroscopic features and oxidation states of the “H-cluster”

Spectroscopic studies indicate that the “H-cluster” of proteins from different organisms is essentially the same. The fully oxidised, inactive $H_{ox\text{-}inactive}$ and the reduced H_{red} “H-cluster” are EPR silent, while the partially oxidised, $H_{ox\text{-}active}$ “H-cluster” is paramagnetic.[24] EPR and Mössbauer spectroscopy studies have shown a covalent link between the $\{Fe_4S_4\}$-cluster and the {2Fe2S}-subsite of the “H-cluster”.[30] Isomer shifts directly reflect the s-electron density at the ^{57}Fe nucleus, which is influenced by variation of the valence shell s density and by shielding effects of p and d electron distribution. Equations **I-3** and **I-4** show the linear relationship between isomer shift (δ) and oxidation state (os) at 4.2 and 77 K for iron-sulfur clusters.

$$\delta = 1.51 - 0.41 \times \text{os (4.2 K)} \quad \textbf{(I-3)}$$

$$\delta = 1.43 - 0.40 \times \text{os (77 K)} \quad \textbf{(I-4)}$$

Comparison with isomer shifts of model complexes has shown that the $\{Fe_4S_4\}$-cluster of the “H-cluster” is in the +2 state in both oxidised ($\delta_{ave} = 0.44 \pm 0.02$ mm.s^{-1}) and reduced forms ($\delta_{ave} = 0.44 \pm 0.02$ mm.s^{-1}) of the “H-cluster” (Scheme **I-7**).

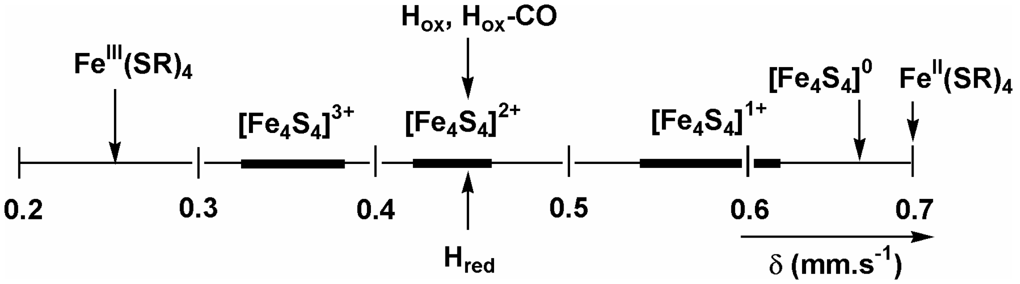

Scheme I-7. Isomer shifts δ for $\{Fe_4S_4\}$-cluster (adapted from reference [31]).

These studies also showed that Mössbauer data are consistent with two low-spin ferrous sites in the {2Fe2S}-subsite for H_{red}, with one ferrous and one ferric iron in the $H_{ox\text{-}active}$ state. The problem for oxidation state attribution to the {2Fe2S}-subsite is that the presence of the strong CO and CN ligands makes the assignment difficult by using the isomer shift parameter. The irons are in the low-spin state, but the binding of CO reduces the ferrous δ value to be practically indistinguishable from the ferric value.[32] From EPR data, the proximal iron in $H_{ox\text{-}active}$ is certainly Fe(II) because of the weak magnetic coupling of the paramagnetic {Fe_4S_4}-cluster to the {2Fe2S}-subsite.[24,30] EPR signal for the $H_{ox\text{-}active}$-CO (CO inhibited form of the active oxidised state) is reminiscent of a low-spin ferrous for the distal iron (g = 2.26, 2.12, 1.89) which has been confirmed by Mössbauer spectroscopy.[30] However, it should be noted that FTIR ^{13}CO labelling studies of DdH support an Fe(I) oxidation state for the distal iron in the $H_{ox\text{-}active}$-CO state (Figure **I-3**).[29]

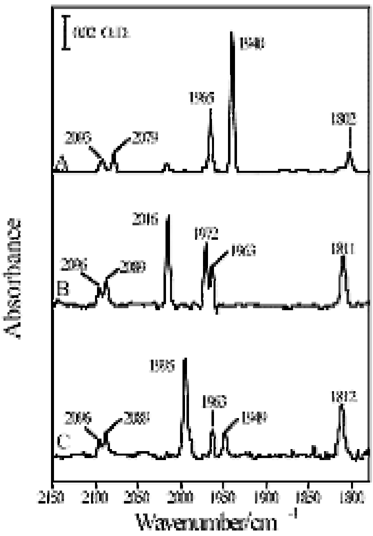

Figure I-3. FTIR spectra of DdH: (A) $H_{ox\text{-}active}$; (B) $H_{ox\text{-}active}$-CO; (C) $H_{ox\text{-}active}$-^{13}CO (taken from reference [29]).

If the distal iron would have a higher oxidation state than the proximal iron, the π-electron density donation on its CO and CN ligands would be weaker, and therefore the frequencies of the bands would be higher. Attributing different frequencies to the CO and CN ligands confirmed that the distal iron should have a lower oxidation state than the proximal iron. Therefore the $H_{ox\text{-}active}$ state should be Fe(I)-Fe(II). These observations have also been confirmed with Cp1.[33]

Density Functional Theory (DFT) studies confirmed that the fully oxidized, inactive state of the cluster $H_{ox\text{-}inactive}$ is more likely to be Fe(II)-Fe(II) and the partially reduced, active state $H_{ox\text{-}active}$ to be Fe(I)-Fe(II).[34,35] Calculations show that the formation of Fe(II)Fe-(III) and Fe(III)-Fe(III) species is not compatible with FTIR data. Replacement of the propanedithiolate ligand by di(thiomethyl)amine led to the same conclusions.[36] Analysis also revealed that the distal iron is more electrophilic than the proximal iron in the mixed valence form μ-CO Fe(II)Fe(I) whereas the opposite is observed for CO-terminal isomers.[35] Therefore, H_2 is thought to bind the proximal iron in CO-terminal isomers.

I.5.c.δ Catalytic mechanism

In terms of hydrogen evolution, [Fe]-hydrogenases are much more active than [Ni-Fe]-hydrogenases, but most of the physicochemical studies have involved [Ni-Fe]-hydrogenases.

A catalytic mechanism can be proposed from FTIR studies and DTF analysis (Scheme **I-8**), but most of the key steps remain speculative.[21] The binding site for dihydrogen, the presence or not of a bridging hydride, the location of the proton donor site or the electron transfer mechanism from the $\{Fe_4S_4\}$-cluster to the $\{2Fe2S\}$-subsite are the main questions which still have to be resolved.

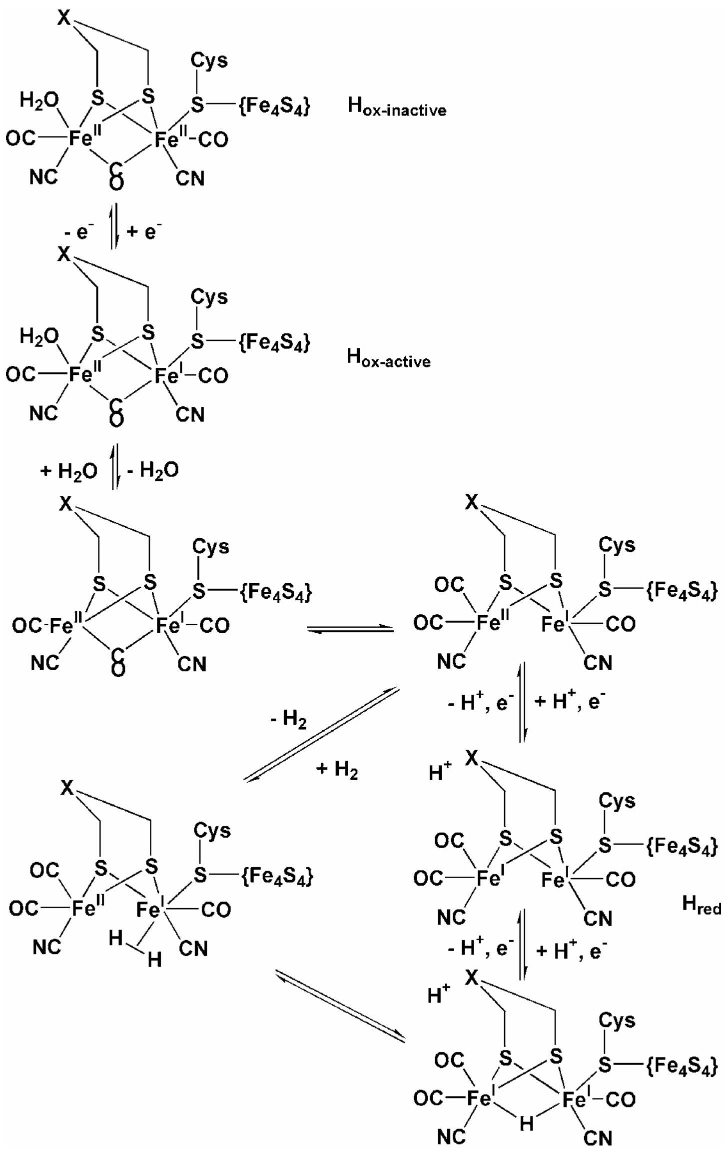

Scheme I-8. Proposed mechanism for H_2 uptake / evolution of [Fe]-hydrogenases (adapted from ref [21]).

I.5.c.ε Biosynthesis of the H-cluster and origin of the CO and CN ligands

It is likely, but not demonstrated, that accessory Fe-S centres in hydrogenases are assembled in a similar way as for general iron-sulfur proteins (see **1.3.a**). Most of the genomic studies have been carried out on [Ni-Fe]-hydrogenases, and although [Ni-Fe] and [Fe]-hydrogenases are genetically unrelated we have seen previously that similarities between the two enzymes exist (CO and CN ligands, binuclear metal centre and H_2 uptake/evolution). Considering the complexity of function and of localisation of these enzymes, many genes are necessary for their biosynthesis. The first report on the nature of the accessory genes *hydEF* and *hydG* required for the maturation of an active [Fe]-hydrogenase was described in a study of photoproduction of H_2 in *Chlamydomonas reinhardtii*.[37] These genes are essential for the formation of an active [Fe]-hydrogenase and are strictly conserved among sequenced organisms containing [Fe]-hydrogenase enzymes.

An interesting question concerns the incorporation of CO and CN in the active sites of [Ni-Fe] and [Fe]-hydrogenases. These two ligands, toxic in their free states, are unprecedented in biology. Seminal work by Böck and co-workers has shown that the synthesis of the cyanide ligands requires the activity of two hydrogenase maturation proteins HypF and HypE for the synthesis and metal centre incorporation in [Ni-Fe]-hydrogenases.[38] HypF protein accepts carbamoyl phosphate and transfers it to a cysteine of HypE to form an enzyme-thiocarbamate. After dehydration of the S-carbamoyl, the enzyme-thiocyanate transfers the cyano group to the iron of the protein (Scheme **I-8**).

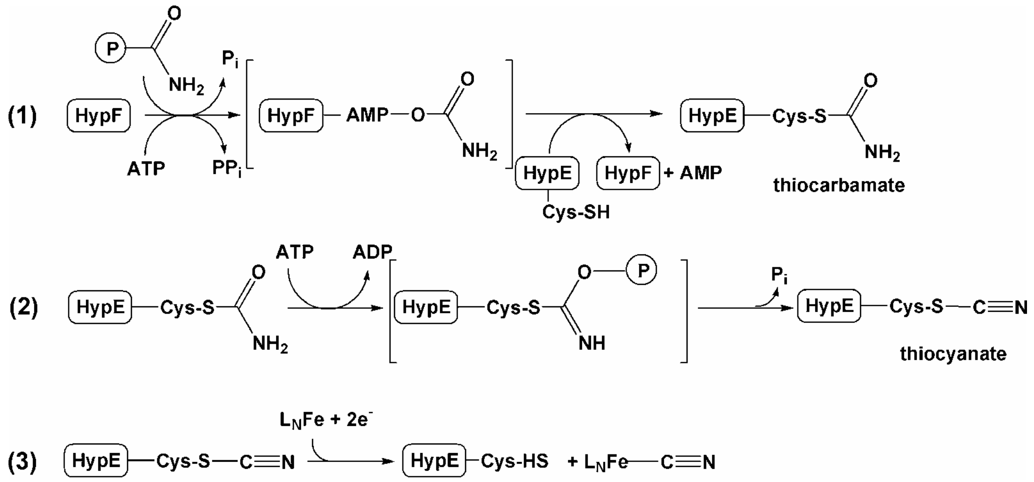

Scheme I-8. Biosynthesis of the cyanide ligand. (1) Formation of the enzyme-thiocarbamate. (2) Dehydration followed by dephosphorylation. (3) Transfer to the iron (adapted from ref [38]).

The feasibility of this process has been compared with chemical models, and it has been shown that the parallel between biochemistry and organometallic chemistry can help us better understand this complex biochemical processes.

No evidence so far has been proposed for the origin of CO, and the suggestion for the deamination of the carbamoyl group to generate a carbonyl ligand had been rejected by evidence which suggests that the biosynthesis of CO follows a different route to that of CN.[39] In the same study, it is proposed that acetate or one of its metabolites might be a precursor of CO, but clear evidence for this proposal is still needed.

I.6. Synthetic models of the active sites of iron-sulfur proteins

I.6.a Analogues of rubredoxin and ferredoxin sites

The synthesis of iron-sulfur active sites was initiated in the early 1970's following X-ray structural determination of iron-sulfur proteins.[31] These complexes, available in highly pure and crystalline form, were the beginning of what is now bioinorganic chemistry. The first analogue was a model of $\{Fe_4S_4\}$-centres, a cubane-type structure $[Fe_4S_4(SCH_2Ph)_4]^{2-}$.[40] The complex was simply prepared from ferric chloride, sodium methoxide, sodium hydrosulfide and the appropriate alkyl mercaptan. The $\{Fe_4S_4\}$-core is a distorted cube, with iron and sulfur atoms at alternate vertices and is closely related to active site structures of HiPIP and ferredoxin proteins.

From the first rubredoxin analogues $[Fe(SR)_4]^{2-}$ in 1975 [41] to cuboidal $[Fe_3S_4(SR)_3]^{3-}$ in 1995,[42] the chemistry of iron-sulfur complexes has been extensively studied and led to a better comprehension of these type of assemblies and their electronic properties.[31]

Nearly all spectroscopic and magnetic techniques have been applied to these synthetic analogues, as well as protein-bound iron-sulfur centres. Mössbauer spectroscopy can be a very powerful tool in terms of determination of the oxidation state (see part **I.5.c.γ**) and elucidation of magnetic coupling and electronic ground states.

I.6.b Site-differentiated clusters

All Fe atoms in {Fe_4S_4}-centres in proteins are not equivalent and can be involved directly in catalysis by the enzyme (*e.g.* aconitase) or they can bind other metal cofactors (see sections **I.4** and **I.5**). Therefore, the synthesis of a polydentate ligand that could differentiate irons in a 3:1 ratio has been investigated. Up to now, five trithiol ligands have been synthesised (Scheme **I-9**), and are able to coordinate {Fe_4S_4}- or {Fe_3S_4}-clusters.[43-45]

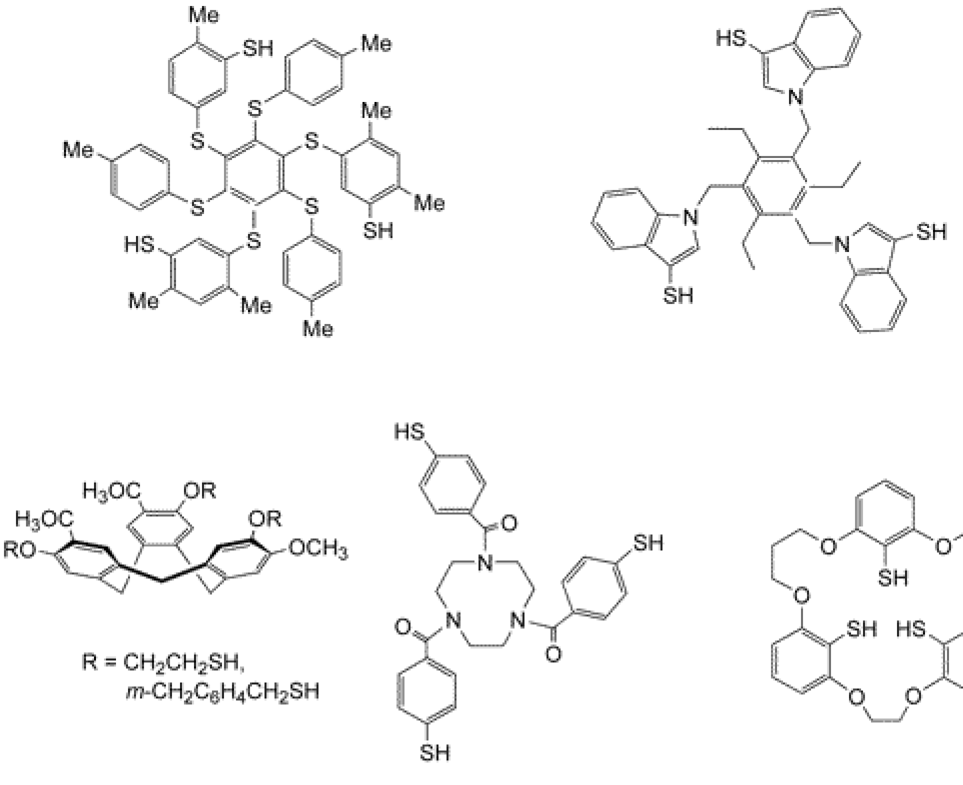

Scheme I-9. Trithiols whose deprotonated forms stabilize 3:1 site-differentiated {Fe_4S_4}-clusters. The trianions bind clusters in a trigonally symmetric arrangement except the crown ethers trithiol, which have mirror symmetry (taken from ref [31]).

The chemistry of LS_3 clusters is highly developed and has been applied to the synthesis of a variety of complexes (Scheme **I-10**).[31]

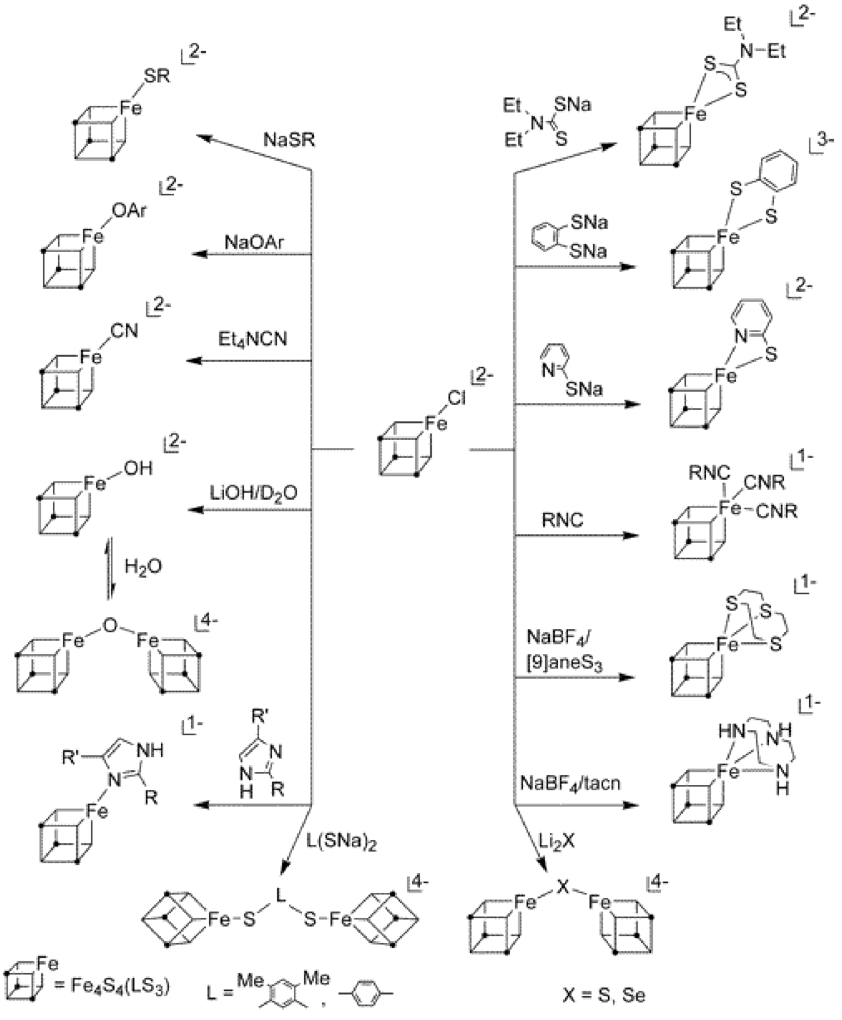

Scheme I-10. Selected site-specific reactions of $[Fe_4S_4(LS_3)Cl]^{2-}$ that afford synthesis of a variety of product clusters, including single cubanes with four-, five-, and six-coordinate unique sites and bridged double cubanes (taken from reference [31]).

I.6.c Synthetic analogues of iron-sulfur complexes

As we have seen in section **I.5**, the complexity of iron-sulfur active sites can be very challenging in terms of organometallic synthesis. Seven bridged metal-sulfur assemblies (sulfite reductase, the "C-cluster" of CODH, the "A-cluster" of acetylcoenzyme A synthase, nitrogenase P and FeMo-co clusters and [Ni-Fe]- and [Fe]-hydrogenases) are receiving a great deal of attention since structural studies have revealed their active sites in the past decade.

Combining subsites of these active sites to iron-sulfur clusters has remained very problematic. Attempts to link a heme group to a [Fe_4S_4]-cluster by a thiolate bridge, to mimic the active site of sulfite reductase, has not led to desired products, and the closest analogues have a sulfide rather than a cysteinate bridge (Scheme **I-11**).[46,47]

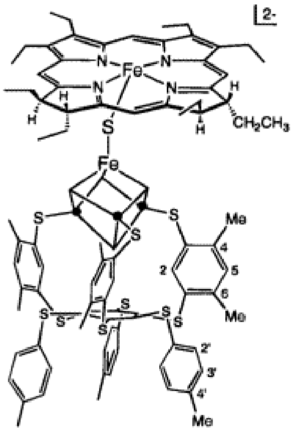

Scheme I-11. The bridged assembly [$Fe_4S_4(LS_3)$-S-Fe(OEiBC)]$^{2-}$.

Insertion of nickel complexes to build analogues of the A-cluster, the C-cluster or the [Ni-Fe]-hydrogenase active site is also studied, but they remain far from functional and structurally relevant model complexes.[48,49]

Synthesis of analogues of the clusters of nitrogenase is an imposing challenge that has not yet been achieved, even after more than twenty years of intense research.[50] Synthetic systems based on {$MoFe_3S_4$}-cubane-type clusters are able to reduce hydrazine to ammonia; however, no reasonable analogue has been characterised so far that mimics the reduction of dinitrogen to ammonia. The recent discovery of an interstitial atom (which could be carbon, nitrogen or oxygen) in the FeMo-cofactor with the high-resolution crystal structure (1.16 Å) [51] raised the question of whether organometallic chemistry is able to provide clues about this ligand. Most recent advances have led to the proposal of inserting nitride complexes, which is the most probable ligand due to the reaction catalysed by the enzyme.[52]

I.7. Synthetic models of the di-iron subsite of [Fe]-hydrogenase

I.7.a. Early {2Fe2S}-complexes

In 1929, Reihlen *et al.* described the synthesis of $Fe_2(CO)_6(SEt)_2$ (Scheme **I-12**),[53] and the striking resemblance with the {2Fe2S}-subsite paved the way for the synthesis of analogues to the “H-cluster”.

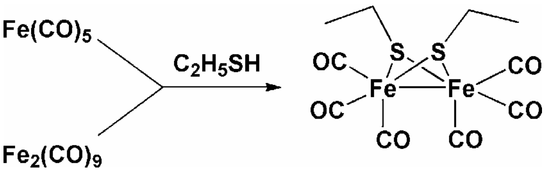

Scheme I-12. Synthesis of $Fe_2(CO)_6(SEt)_2$.[53]

Using this type of compound as a basis, a large number of iron-hexacarbonyl complexes have been synthesised. The volatile $Fe_2(CO)_6S_2$ complex from the “smelly” reaction between $Fe(CO)_5$, KOH and polysulfide has been studied in great detail since 1958.[54] The Fe-Fe bond length of 2.55 Å is very close to the 2.6 Å distance observed in the {2Fe2S}-subsite of the “H-cluster”.[25,26] The complex is butterfly-shaped (distorted Fe_2S_2 tetrahedron) with a bent metal-metal bond (Scheme **I-13**).[55]

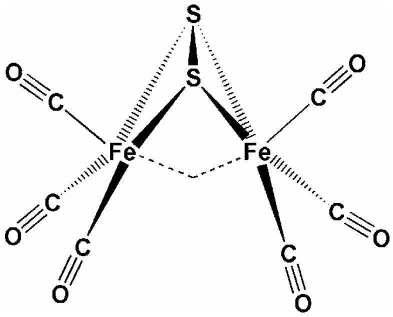

Scheme I-13. Schematic representation of the $Fe_2(CO)_6S_2$ complex. The dashed line represents the bent metal-metal bond.

The sulfur atoms may also be joined by organic linkers and the carbonyl ligands can be replaced by phosphines and phosphites.[56]

I.7.b. {2Fe2S}-frameworks

Determination of the X-ray crystal structure of [Fe]-hydrogenase encouraged the organometallic community to reconsider the chemistry of these $[Fe_2(\mu\text{-}SR)_2(CO)_6]$ systems. The synthesis of the propanedithiolate (pdt) bridged diironhexacarbonyl [57] was the first step through the synthesis of the first models of the {2Fe2S}-subsite. Soon after the publication of the structure of the "H-cluster", three independent groups published the structure of the dianion $[Fe_2(pdt)(CO)_4(CN)_2]^{2-}$ (Figure **I-4**).[58-60]

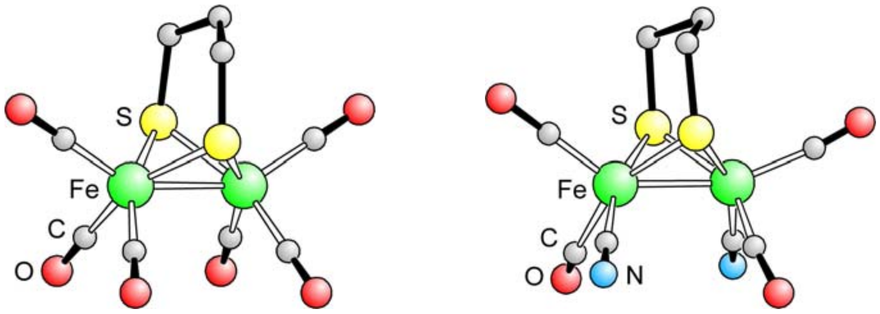

Figure I-4. Crystal structures of analogues of the {2Fe2S}-subsite. $[Fe_2(pdt)(CO)_6]$ (left); $[Fe_2(pdt)(CO)_4(CN)_2]^{2-}$ (right).

Propanedithiolate is one possibility for the bridging dithiolate ligand between the two metals of the subsite, so the amino [61] and oxo [62] derivatives were also synthesised (Scheme **I-14**).

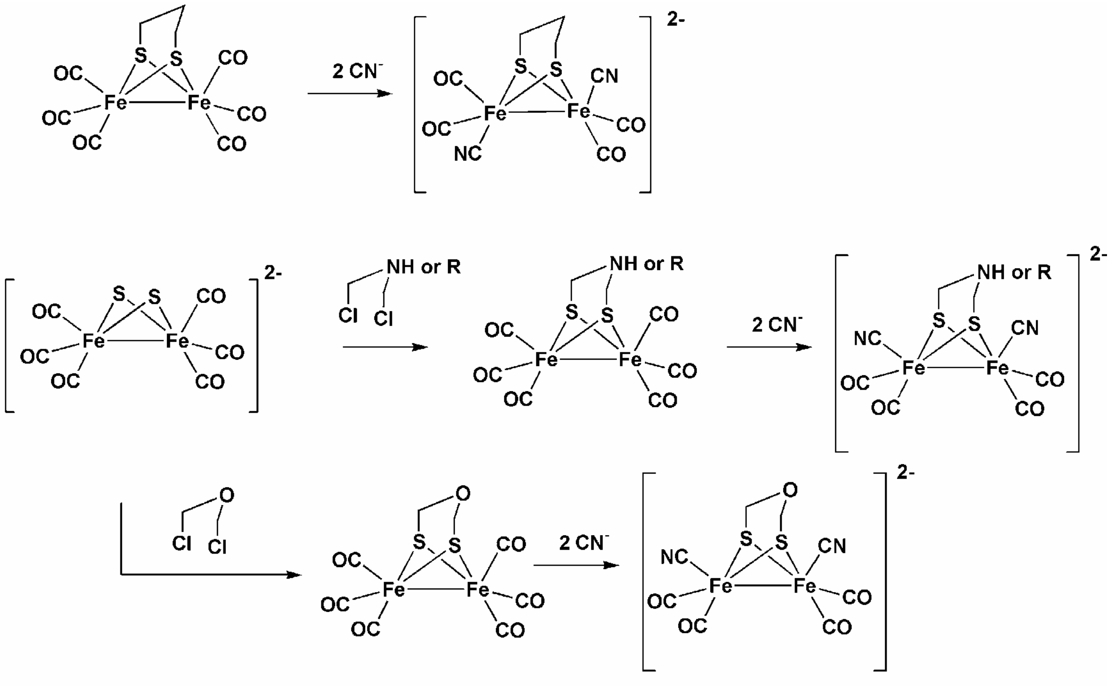

Scheme I-14. Synthesis of {2Fe2S}-subsite analogues.[58-62]

The butterfly arrangement of the dithiolate ligand in these complexes is very similar to that in the "H-cluster", and therefore the subsite is modelled in the CO inhibited form H_{ox}-CO.

Because of the presence of a bridging cysteine between the {Fe_4S_4}-cluster and the {2Fe2S}-subsite of the "H-cluster", these model complexes do not involve the third coordinating sulfur.

I.7.c. {2Fe3S}-framework

The synthesis of the {2Fe3S}-core with carbonyl and cyanide ligands has been achieved by the synthesis of propanedithiolate ligands with a thioether group able to introduce extra-functionality on the proximal iron.[63,64] This framework is structurally very close to the subsite of [Fe]-hydrogenase (Scheme **I-15**).

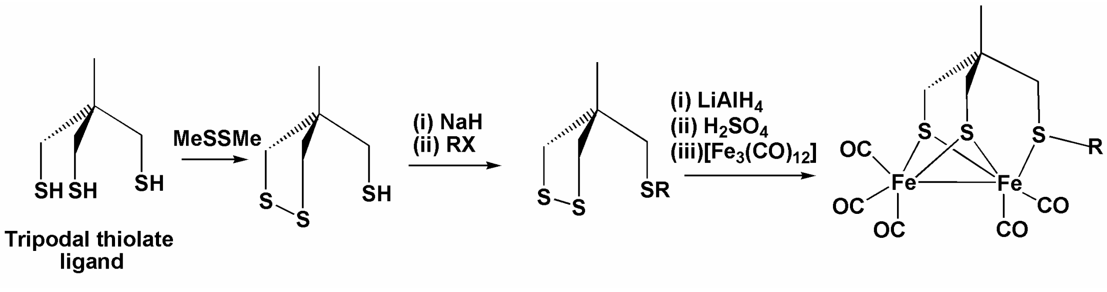

Scheme I-15. Synthesis of {2Fe3S}-complexes (R = Me or CH_2Ph).

The cyanation of the pentacarbonyl complex gives a stable monocyanide on the distal iron, and under further cyanation a moderately stable intermediate can be isolated. It possesses a bridging carbonyl ligand and one CN on each iron, which are key structural elements of the CO inhibited form of the "H-cluster".[65]

A transient {Fe(I)Fe(II)}-bridging carbonyl species can also be generated electrochemically and was characterised by FTIR and stopped-flow methods. It exhibits a very similar spectrum to what has been observed with H_{ox}-CO.[29] This supports the low oxidation state of the irons in the subsite.

I.7.d. Hydride complexes

No spectroscopic data has established the presence of a hydride species during the catalytic mechanism of hydrogen evolution / uptake of hydrogenases, but the formation of HD during the turnover under D_2 [24] suggests the possibility that formation of a metal-hydride can occur. This proposal is also supported by DTF studies.[35,66]

Attempts to obtain a hydride complex with a {2Fe2S}-core have resulted in the characterisation of bridging hydride species [67,68] with CO and phosphine ligands. A complex with both bridging and terminal hydride has also been synthesised with ruthenium atoms instead of iron by the photolytic activation of $Ru_2(CO)_4(PCy_3)_2(pdt)$ under a dihydrogen atmosphere.[69] It has also been shown in that study that dihydrogen can be generated after reaction with HCl.

I.7.e. Hydrogen evolution and model complexes

Alternative energy to fossil fuels and a decrease in the release of greenhouse gases are major goals to face at the beginning of this century. Molecular hydrogen would be an ideal fuel, because when burned or oxidised in a fuel cell it emits no pollution, and gram for gram it releases more energy than any other fuel.[70]

One of the numerous problems associated with the "hydrogen economy" concerns dihydrogen production and uptake. Four main techniques are currently used for hydrogen production: hydrocarbon reforming; ammonia cracking; pyrolysis (decomposition of hydrocarbons into dihydrogen and carbon in water-free and air-free environment); and aqueous reforming.[71] Unfortunately, all these methods utilise unsustainable hydrocarbon feedstocks and release greenhouse gases. Dihydrogen uptake in fuel cells is currently electrocatalysed best by platinum-based metals. This has been recognised to be economically unviable in the long term due to limited availability of this metal and strategic problems with supply have also been noted by the US Department of Energy.[72]

The major challenge of modelling the active site of [Fe]-hydrogenase is to find a complex able to catalyse reversibly proton reduction. The first attempt with $Fe_2(CO)_4(CN)_2(pdt)$ reacting with two equivalents of acid led to an insoluble polymeric material, but with the co-generation of H_2.[60] Electrochemistry is the favoured technique to monitor the ability of different complexes to reduce protons catalytically (see Chapter **III**), and nearly all of the {2Fe2S}-systems have shown this ability, with more or less efficiency compared to the enzyme.[68,73-76]

Modifications of ligands (CO, CN, phosphines), bridging dithiolate ligands (CH_2, NH or O) or oxidation states of the di-iron centre have not provided a means of generating powerful catalysts. Clearly, however, it has been demonstrated that this type of iron-sulfur assembly is able to catalyse proton reduction.

- Chapter II -

{2Fe3S}-Systems: Synthesis, Structures and Spectroscopic Properties

The development of new {2Fe3S}-cores is relevant for a better understanding of "H-cluster" chemistry and for the development of new materials as potential electrocatalysts for hydrogen fuel / producer cells. As we have seen previously, not much is known about the mechanism of dihydrogen evolution / uptake by the enzyme, and organometallic chemistry of model complexes is a way toward the elucidation of the machinery's secrets.

Previous systems synthesised in this laboratory have involved alkyl (-CH_3) and aryl (-CH_2Ph) derivatives on the thioether group of the ligand.[63] We will describe in this chapter the synthesis of new ligands with additional functionality and the di-iron complexes formed from them.

II.1 Tripodal ligand $CH_3C(CH_2SH)_3$

This ligand was first described by Bosnich and coworkers in the early eighties,[77] and its reactivity towards different transition metals has been reported. An iridium-carbonyl complex $[Ir_3(CO)_6(CH_3C(CH_2S)_3)]$ has been characterised by Poilblanc and coworkers where the trithiolato-ligand coordinates a triangle of non-bonded iridium atoms.[78] Analoguous rhodium compounds have been synthesised, as well as complexes in which CO is replaced by tertiary phosphine.[78] Some studies also reported the synthesis of mercury complexes $[CH_3C(CH_2S)_3(HgCH_3)_3]$.[79] The mononuclear complex $[(CH_3C(CH_2PPh_2)_3)Rh(CH_3C(CH_2S)_3)]$ has also been described.[80] Synthetic modifications of this ligand could also lead to organic self-assembled monolayers on gold electrodes.[81]

The ligand is synthesised from 1,1,1-tris(hydroxymethyl)ethane **1** which is activated by tosylation (**2**) to incorporate a thiocyanate group (**3**). The reduction by $LiAlH_4$ of **3** leads to the desired trithiol ligand **4** (Scheme **II-1**). This starting material can be prepared on a multi-gram scale.

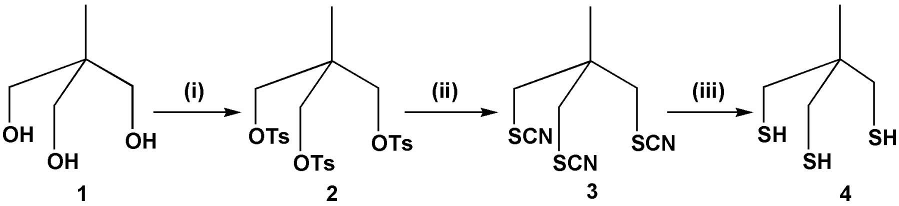

Scheme II-1. Synthesis of the tripodal ligand $CH_3C(CH_2SH)_3$. (i) TsCl, pyridine, RT, 91%; (ii) KSCN, DMF, 135°C, 79%; (iii) $LiAlH_4$, diethyl ether, 40°C, 82%.

With this ligand, we have the backbone of all our {2Fe3S}-complexes. To introduce extra-functionality on one of the thioether, it is necessary to protect two of the three thiols present.[64] This can be achieved by the oxidative coupling of two thiols in the presence of dimethyl disulfide to give a cyclic disulfide **5** (Scheme **II-2**). The third thiol is now left free for further conversion on one of the thioether to introduce extra-functionality.

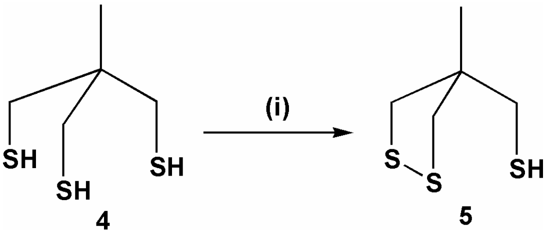

Scheme II-2. Synthesis of the protected tripodal ligand **5**. (i) $(CH_3S)_2$, ^tBuOK, methanol, RT, 91%.

The deprotection of the disulfide is usually carried out under relatively strong reductive conditions ($LiAlH_4$) as outlined below and described in the experimental section.

II.2 Synthesis of {2Fe3S}-pyridine derivatives

It was thought that the introduction of a pyridine group onto the backbone of the ligand could introduce advantages in terms of structure and catalysis. First of all, the possibility of coordinating the nitrogen of the pyridine to the di-iron centre was attractive as a potential means to stabilise the higher oxidation state of the di-iron centre.

It was also reasoned that in the presence of a proton ($pKa_{298} = 5.25$ in water) an appended basic pyridine group might provide a means of delivering protons to the active site and/or assist in heterolytic H-H bond formation or cleavage.

Synthesis of two ligands with an alkyl chain length comprising one or two carbons between the sulfur and the pyridine was therefore undertaken.

II.2.a Ligand synthesis

The disulfide-protected ligand **5** was reacted with activated pyridine derivatives $PyCH_2Br$ and $PyCH_2CH_2OTs$ under basic conditions to give the dithiol ligands **7** and **9** after reduction of the disulfides **6** and **8** (Scheme **II-3**).

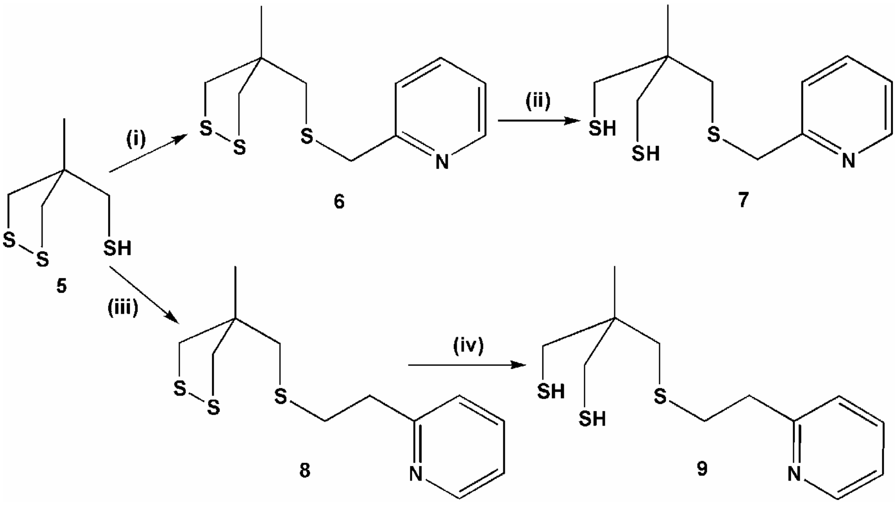

Scheme II-3. Synthesis of the pyridine ligands. (i) $PyCH_2Br$, NaH, THF, RT, 36%; (ii) $LiAlH_4$, diethyl ether, RT, 84%; (iii) $PyCH_2CH_2OTs$, NaH, THF, RT, 71%; (iv) $LiAlH_4$, diethyl ether, RT, 86%.

II.2.b Complex synthesis

The two pyridine functionalised ligands **7** and **9** were reacted with the triirondocedacarbonyl complex $[Fe_3(CO)_{12}]$ in toluene to give after purification by column chromatography, red-brown {2Fe3S}-complexes **10** and **11** with the thioether coordinated on the proximal iron with the pyridine group pendant (Scheme **II-4**).

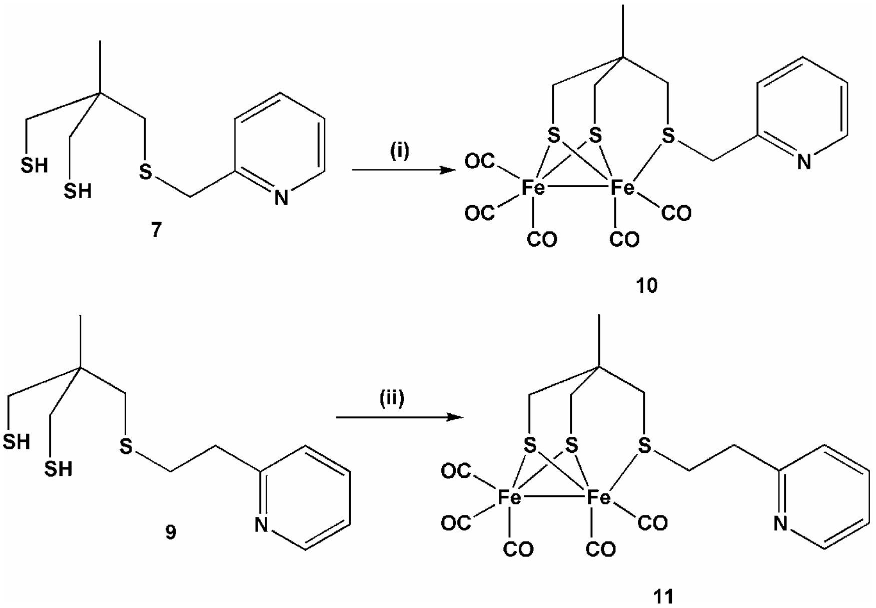

Scheme II-4. Synthesis of the pyridine complexes **10** and **11**. (i) $[Fe_3(CO)_{12}]$, toluene, 80°C, 24%; (ii) $[Fe_3(CO)_{12}]$, toluene, 80°C, 34%.

This was confirmed by X-ray crystallographic studies of both pyridine derivatives (Figure **II-1** and **II-2**).

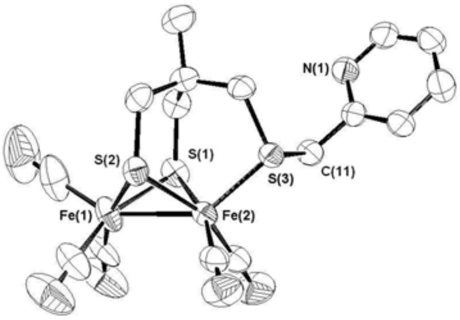

Figure II-1. ORTEP view of [$Fe_2(CO)_5\{CH_3C(CH_2S)_2CH_2SCH_2Py\}$] (**10**) depicted with 50% thermal ellipsoids. All hydrogen atoms have been omitted for clarity. Selected bond distances (Å) and angles (deg): Fe(1)-Fe(2) = 2.5152(8), Fe(1)-S(1) = 2.2677(11), Fe(1)-S(2) = 2.2472(13), Fe(2)-S(1) = 2.2533(13), Fe(2)-S(2) = 2.2514(11), Fe(2)-S(3) = 2.2354(10), S(3)-C(11) = 1.824(4); Fe(1)-S(1)-Fe(2) = 67.61(3), Fe(1)-S(2)-Fe(2) = 67.99(4).

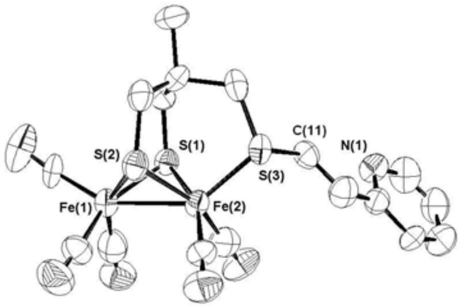

Figure II-2. ORTEP view of [$Fe_2(CO)_5\{CH_3C(CH_2S)_2CH_2SCH_2CH_2Py\}$] (**11**) depicted with 50% thermal ellipsoids. All hydrogen atoms have been omitted for clarity. Selected bond distances (Å) and angles (deg): Fe(1)-Fe(2) = 2.495(2), Fe(1)-S(1) = 2.253(3), Fe(1)-S(2) = 2.264(3), Fe(2)-S(1) = 2.240(3), Fe(2)-S(2) = 2.257(3), Fe(2)-S(3) = 2.241(3), S(3)-C(11) = 1.816(10); Fe(1)-S(1)-Fe(2) = 67.49(9), Fe(1)-S(2)-Fe(2) = 66.98(9).

Even under the forceful conditions of the synthesis (toluene at 80°C) the pyridine did not displace CO. Simple modelling suggested that there are no particular geometric constraints to form five or six member rings involving the pyridine ligated to the iron atom. That such complexes are not formed is either due to thermodynamic, electronic or kinetic reasons. For example, it might be argued that the iron atom would become too electron-rich if the pyridine coordinated, but it is known that the anion CN^- can be added at this centre.[65] However, this ligand has back-bonding capabilities whereas pyridine is generally considered as a σ-donor ligand.

The electrochemical properties of these complexes are described in detail in **Chapter III**.

II.3 Synthesis of {2Fe3S}-nitrobenzene and aniline derivatives

In order to probe the transmission of electronic effects from a group through the thioether ligation to the metal centre(s) the synthesis of aniline and nitrobenzene derivatives was undertaken. A para nitro-substituent has one of the most powerful electron-withdrawing effects on the aromatic ring (Hammet $\sigma_{para} = 0.81$; $\sigma^+_{para} = 0.79$)[82] whilst a para amino-substituent operates at the other extreme, it has a powerful electron-donating group (Hammet $\sigma_{para} = -0.57$; $\sigma^+_{para} = -1.3$)[82]. In addition, the *para*-aniline group can be protonated and the *para*-nitro moiety is reducible. Thereby providing additional means to switch the nature of the substituent and perturb its electronic influence on the di-iron system (see section **II.8** and **Chapter III**).

II.3.a Ligand synthesis

The reaction of the protected thiol **5** with *p*-bromonitrobenzene in basic conditions leads to the 4-((4-nitrophenylthio)methyl)-4-methyl-1,2-dithiolane **12** (Scheme II-5). To obtain a dithiol ligand from the disulfide is problematic. Reduction of the -S-S- bond specifically could not be achieved because the aromatic nitro group is readily reducible.

However, it has been shown by Dr. X. Liu in our laboratory that generally {2Fe3S}-systems can be synthesised from the disulfide thioether precursors directly without going through the reduction step. The disadvantage of this method is that yields are generally poor. However this route provided the means of synthesising the nitrobenzene derivative.

To obtain the aniline ligand, the reduction of the previous disulfide-nitrophenyl ligand should provide a "one-pot" reaction to reduce the disulfide into thiols and the nitro group into an amine. $LiAlH_4$ cannot be used in this case because it would also reduce the nitro group into amine, and then the amine into an azo group.[82] By using $NaBH_4$ (source of dihydrogen) and Pd/C (hydrogenation catalyst), this problem can be avoided and gives selectively, and with high yield, the dithiol-aniline ligand **13** (Scheme **II-5**).[83]

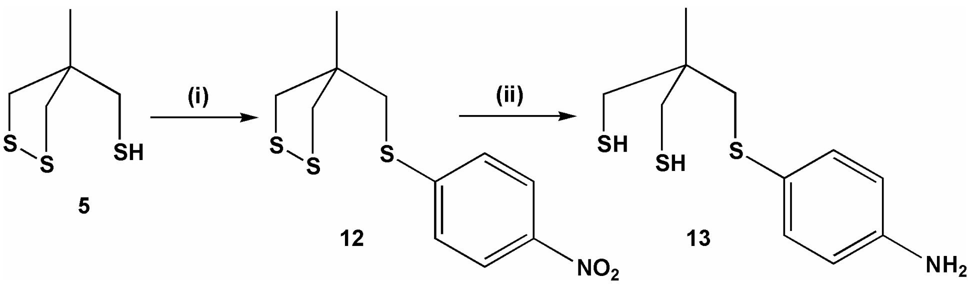

Scheme II-5. Synthesis of the nitrobenzene and aniline ligands **12** and **13**. (i) *p*-$BrC_6H_4NO_2$, NaH, THF, RT, 50%; (ii) Pd/C, $NaBH_4$ (hydrolyses to release dihydrogen), NaOH 2 M, 90°C, 95%.

II.3.b Complex synthesis

By reacting the two ligands prepared with $[Fe_3(CO)_{12}]$ in toluene, the two pentacarbonyl complexes **14** and **15** can be obtained after column chromatography purification (Scheme **II-6**).

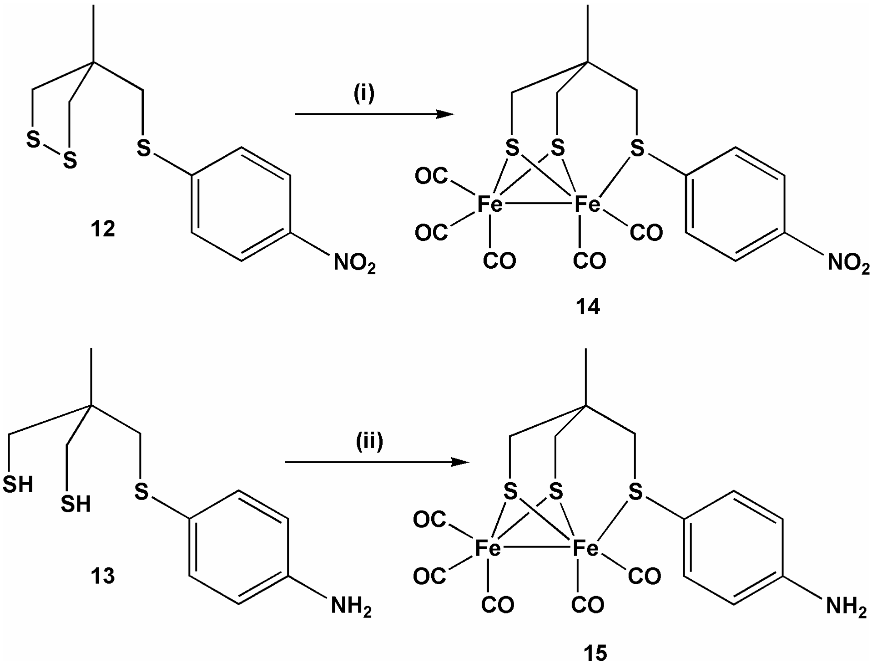

Scheme II-6. Synthesis of nitrobenzene **14** and aniline **15** complexes. (i) [$Fe_3(CO)_{12}$], toluene, 90°C, 32%; (ii) [$Fe_3(CO)_{12}$], toluene, 90°C, 55%.

Crystals of these two complexes **14** and **15** have been grown, and X-ray studies have shown the same type of ligation for the thioether as observed for the pyridine derivatives (Figure **II-3** and **II-4**).

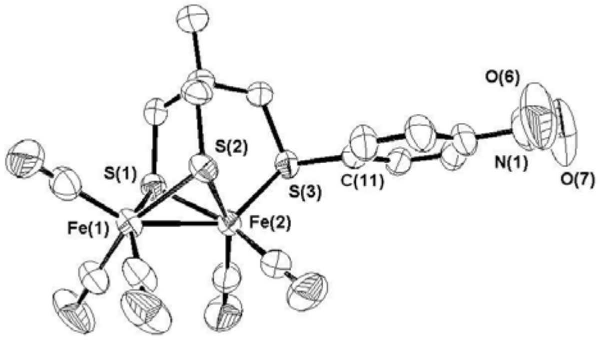

Figure II-3. ORTEP view of [$Fe_2(CO)_5\{CH_3C(CH_2S)_2CH_2SC_6H_5\text{-}p\text{-}NO_2\}$] (**14**) depicted with 50% thermal ellipsoids. All hydrogen atoms have been omitted for clarity. Selected bond distances (Å) and angles (deg): Fe(1)-Fe(2) = 2.501(1), Fe(1)-S(1) = 2.2614(15), Fe(1)-S(2) = 2.2623(15), Fe(2)-S(1) = 2.2508(15), Fe(2)-S(2) = 2.2693(15), Fe(2)-S(3) = 2.2454(15), S(3)-C(11) = 1.793(5); Fe(1)-S(1)-Fe(2) = 67.33(4), Fe(1)-S(2)-Fe(2) = 67.00(5).

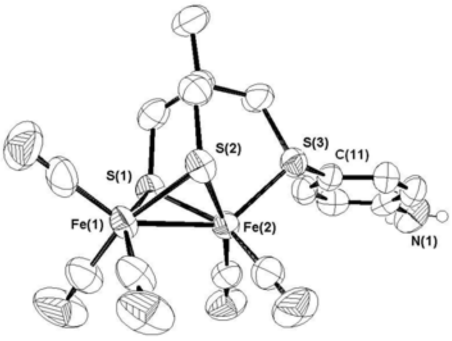

Figure II-4. ORTEP view of [$Fe_2(CO)_5\{CH_3C(CH_2S)_2CH_2SC_6H_5$-*p*-$NH_2\}$] (**15**) depicted with 50% thermal ellipsoids. All hydrogen atoms have been omitted for clarity. Selected bond distances (Å) and angles (deg): Fe(1)-Fe(2) = 2.5165(8), Fe(1)-S(1) = 2.2574(9), Fe(1)-S(2) = 2.2580(10), Fe(2)-S(1) = 2.2555(9), Fe(2)-S(2) = 2.2501(10), Fe(2)-S(3) = 2.2452(8), S(3)-C(11) = 1.775(3); Fe(1)-S(1)-Fe(2) = 67.78(3), Fe(1)-S(2)-Fe(2) = 67.86(2).

Electrochemical features of these complexes will be described in detail in **Chapter III**.

II.4 Other functionalisation: Synthesis of pyrrole and ethanol derivatives

The synthesis of pyrrole derivatives might possibly provide a means of electrosynthesising polymeric solid state materials on electrodes and thence a means of exploring their electrocatalytic properties. The synthesis of one such complex is described. It was found that direct electropolymerisation failed (see **Chapter V**). Therefore a complex with an alcohol function was prepared in order to introduce di-iron sites by reaction with an active ester functionalised poly(pyrrole) (see **Chapter V**).

II.4.a Ligand synthesis

Following the previous procedures, ligands **17** and **19** were prepared from the protected disulfide **16** and **18**, by reaction with the appropriate organohalides, and subsequently reduced to give the desired dithiol ligands (Scheme **II-7**).

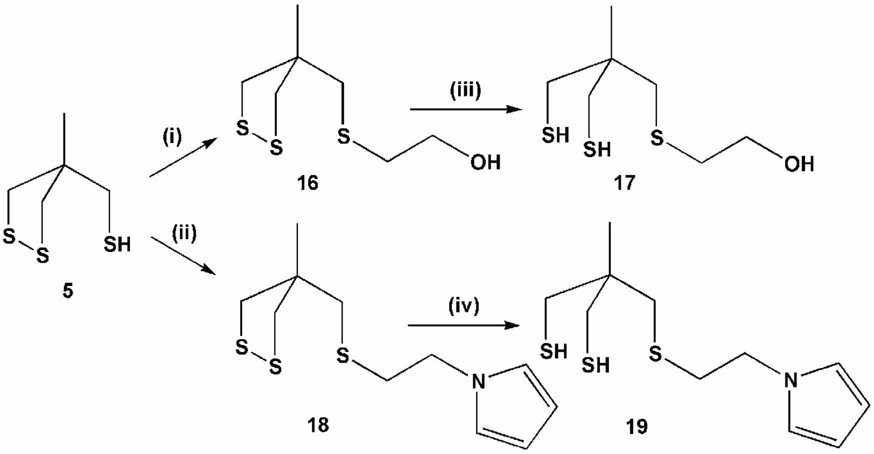

Scheme II-7. Synthesis of ethanol and pyrrole ligands **16** and **18**. (i) ICH_2CH_2OH, NaH, THF, RT, 84%; (ii) $PyrroleCH_2CH_2Cl$; NaH, acetonitrile, 60°C, 74%; (iii) $LiAlH_4$, THF, 40°C, 63%; (iv) $LiAlH_4$, diethyl ether, RT, 72%.

II.4.b Complex synthesis

Reaction of the new ligands **16** and **18** with one equivalent of $[Fe_3(CO)_{12}]$ in toluene gave the 2-{2Fe3S}-ethan-1-ol **20** and N-pyrrole **21** complexes (Scheme **II-8**). The thioether coordinates the di-iron pentacarbonyl unit and X-ray crystal structure shows similarities with previous systems synthesised (Figure **II-5**).

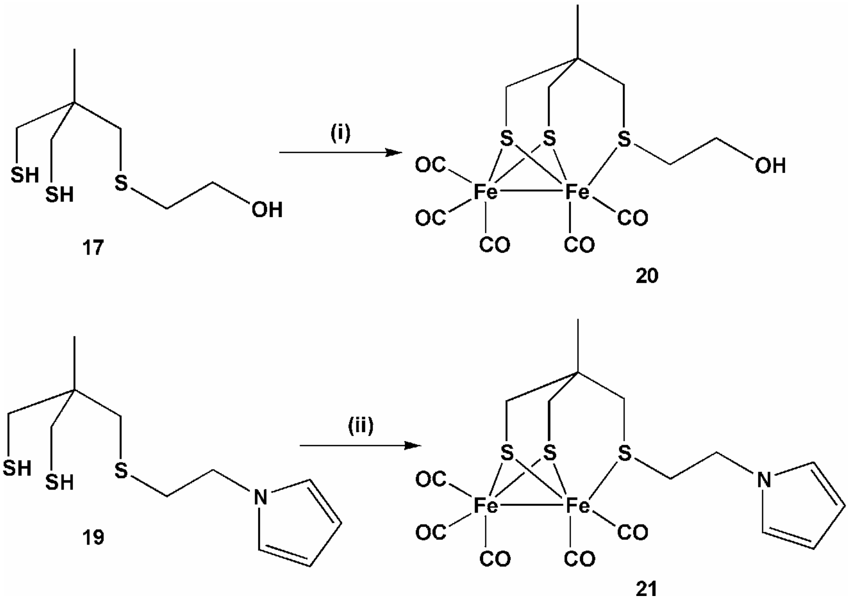

Scheme II-8. Synthesis of ethanol and pyrrole complexes **20** and **21**. [$Fe_3(CO)_{12}$], toluene, 90°C, 50%; (ii) [$Fe_3(CO)_{12}$], toluene, 90°C, 59%.

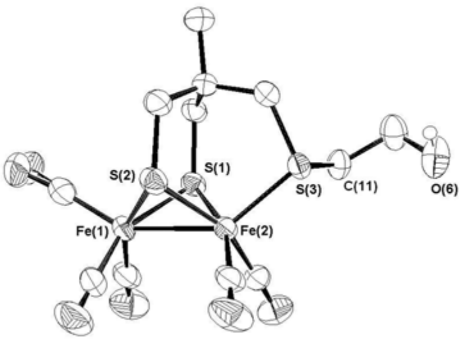

Figure II-5. ORTEP view of [$Fe_2(CO)_5\{CH_3C(CH_2S)_2CH_2SCH_2CH_2OH\}$] (**20**) depicted with 50% thermal ellipsoids. All hydrogen atoms have been omitted for clarity. Selected bond distances (Å) and angles (deg): Fe(1)-Fe(2) = 2.5006(10), Fe(1)-S(1) = 2.2660(9), Fe(1)-S(2) = 2.2569(11), Fe(2)-S(1) = 2.2588(11), Fe(2)-S(2) = 2.2496(11), Fe(2)-S(3) = 2.2551(9), S(3)-C(11) = 1.826(3); Fe(1)-S(1)-Fe(2) = 67.10(3), Fe(1)-S(2)-Fe(2) = 67.41(4).

Electrochemistry and electropolymerisation of these complexes will be described in detail in **Chapter V**.

II.5 Synthesis of a mixed-valence tetra-iron complex

Previous attempts to react the trithiol ligand **4** directly with $[Fe_3(CO)_{12}]$ gave intractable black material.[63] Nevertheless, a soluble fraction can be isolated and purified by column chromatography to give an unprecedented infrared spectrum (2046, 1988 and 1947 cm^{-1}) compared to the well known FTIR of {2Fe3S}-penta and hexacarbonyl complexes. Deep-red crystalline needles can be obtained and the structure of **22** solved by X-ray crystallography showed a dimer of two {2Fe3S}-cores fused together (Figure **II-6**).

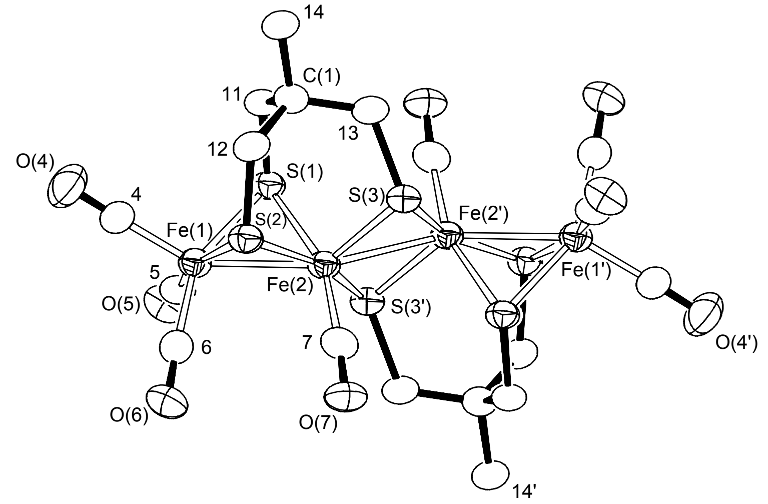

Figure II-6. ORTEP view of $[Fe_2(CO)_4\{CH_3C(CH_2S)_3\}]_2$ (**22**) depicted with 50% thermal ellipsoids. All hydrogen atoms have been omitted for clarity. Selected bond distances (Å) and angles (deg): Fe(1)-Fe(2) = 2.5384(16), Fe(2)-Fe(2') = 2.642(2), Fe(1)-S(1) = 2.2603(18), Fe(1)-S(2) = 2.254(2), Fe(2)-S(1) = 2.290(2), Fe(2)-S(2) = 2.246(2), Fe(2)-S(3) = 2.241(2), Fe(2)-S(3') = 2.224(2); Fe(1)-Fe(2)-Fe(2') = 146.74(6), Fe(1)-S(1)-Fe(2) = 67.81(6), Fe(1)-S(2)-Fe(2) = 68.68(6), Fe(2)-S(3)-Fe(2') = 72.56(7).

This molecule is thought to be obtained by oxidative elimination of dihydrogen and loss of CO from the parent $[Fe_2(CO)_5\{CH_3C(CH_2S)CH_2SH\}]$, but no study on the possible mechanism has been carried out.

Interestingly, looking at formal oxidation states of irons in the molecule, external irons can be considered as Fe(I), and internal irons as Fe(II). This observation shows interesting electronic similarities with the natural {2Fe2S}-subsite, its semi-reduced form as suggested by spectroscopists.[29] All previously synthesised complexes contain Fe(I)Fe(I) di-iron centres whereas here the presence of an Fe(II) suggests the possibility of synthesising mixed-valence compounds of relevance to [Fe]-hydrogenase.

The short distance between the two internal irons (2.642 Å) suggests a degree of metal-metal bonding. Thus, the overall electron configuration of the complex is a 66 electron structure with an 18-electron configuration for each metal.

Detailed electrochemistry and relevance to [Fe]-hydrogenase chemistry of **22** will be described in **Chapter III**.

II.6 Structural comparisons of different {2Fe3S}-complexes

In each complex, both iron atoms are five-coordinate with square pyramidal patterns (Scheme **II-9**). The square base is formed by two thiolates (S(1) and (S(2)) and two carbon atoms of carbonyl ligands. The top of the pyramid is represented by a carbonyl ligand for the distal iron Fe(1) and the thioether sulfur atom S(3) for the proximal iron Fe(2). The geometry of irons can also be approximated to octahedral geometry with a 'bent' metal-metal bond as described for [$Fe_2(CO)_6(\mu\text{-}S)_2$] by Seyferth and coworkers (see **I.7.a**, Scheme **I-13**).[55]

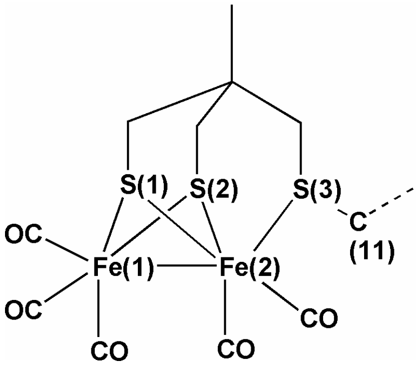

Scheme II-9. Atom labels for {2Fe3S}-complexes.

Metal-metal bonds Fe(1)-Fe(2) range from 2.495(2) Å (shortest) for the ethylpyridine-derivative **11** and 2.5165(8) Å (longest) for the aniline-derivative **15** (Table **II-1**). This difference of *ca.* 0.02 Å is rather small but is statistically significant (3σ criteria). The same range of *ca.* 0.02 Å is observed for the Fe(2)-S(3) bond lengths.

The electronic effect of aniline and nitrobenzene on metal centre bond lengths is not dramatic. A significant difference (statistical standard deviation > 3σ criteria) can be noted for the metal-metal bond and the S(3)-C(11) bond, whereas the metal-sulfur bond remains unchanged. NH_2 is a better donor than NO_2 and we expect it to push more electronic density onto the iron to strengthen the metal-metal bond, but we observe exactly the opposite. This is discussed further below.

The structural similarities between the {2Fe2S}-subsite of [Fe]-hydrogenase and the model complexes are evident. The average Fe-Fe bond lengths are similar to those distances estimated from the protein crystallographic data, as are the $Fe\text{-}S_{bridge}$ distances. However, the thioether-proximal iron distance (Fe(2)-S(3)) is shorter than the corresponding bond in the enzyme ($d_{average}$ = 2.25 Å / $d_{[Fe]\text{-}hydrogenase}$ = 2.5 Å). This is certainly due to the different nature of the iron-sulfur bond as in our models we are looking at thioethers coordinating the proximal iron where the "H-cluster" has a bridging thiolate (from a cysteine) linking two iron atoms.

Compound	Fe(1)-Fe(2)	Fe(2)-S(3)	S(3)-C(11)
$[Fe_2(CO)_5\{CH_3C(CH_2S)_2CH_2SCH_3\}]$ (23)[63]	2.5086(9)	2.2508(14)	1.792(5)
$[Fe_2(CO)_5\{CH_3C(CH_2S)_2CH_2SCH_2Ph\}]$ (24) [63]	2.4969(8)	2.2347(10)	1.808(4)
$[Fe_2(CO)_5\{CH_3C(CH_2S)_2CH_2SCH_2Py\}]$ (10)	2.5152(8)	2.2354(10)	1.824(4)
$[Fe_2(CO)_5\{CH_3C(CH_2S)_2CH_2SCH_2CH_2Py\}]$ (11)	2.495(2)	2.241(3)	1.816(10)
$[Fe_2(CO)_5\{CH_3C(CH_2S)_2CH_2SC_6H_4\text{-}p\text{-}NO_2\}]$ (14)	2.501(1)	2.2454(15)	1.793(5)
$[Fe_2(CO)_5\{CH_3C(CH_2S)_2CH_2SC_6H_4\text{-}p\text{-}NH_2\}]$ (15)	2.5165(8)	2.2452(8)	1.775(3)
$[Fe_2(CO)_5\{CH_3C(CH_2S)_2CH_2SCH_2CH_2OH\}]$ (20)	2.5006(10)	2.2551(9)	1.826(3)
$[Fe_2(CO)_4\{CH_3C(CH_2S)_3\}]_2$ (22)	2.5384(16)	2.241(2)	/
"H-cluster"[25]	2.6(1)	2.5(1)	/

Table II-1. Selected bond lengths (Å) for {2Fe3S}-complexes and {2Fe2S}-subsite of [Fe]-hydrogenase.

II.7 Infra-red spectra of carbonyl compounds: back-bonding

II.7.a General aspects

FTIR spectroscopy of carbonyl and cyanide ligands is commonly used in organometallic chemistry to probe the electronic environment around metal centres. It has also been very useful to characterise different redox states of [Fe]-hydrogenase as they exhibit very different spectra (see **I.5.c.γ**).[29]

The effect of the synergic bonding between the metal and CO, referred to as "back-bonding", has an influence on vibrational spectra of carbonyl complexes. The filled σ orbital of the carbon overlaps with a σ-type empty orbital of the metal (Scheme **II-10**). However, as the electron flow goes from the carbon to the metal, it increases the electronic density on the metal atom. Considering Pauling's electroneutrality principle, the metal attempts to reduce its overall charge by pushing electrons back to acceptor orbitals of the ligand thus the empty $p\pi^*$ orbital of the CO can accept the electronic density from $d\pi$ (or hybrid $dp\pi$) metal orbital.

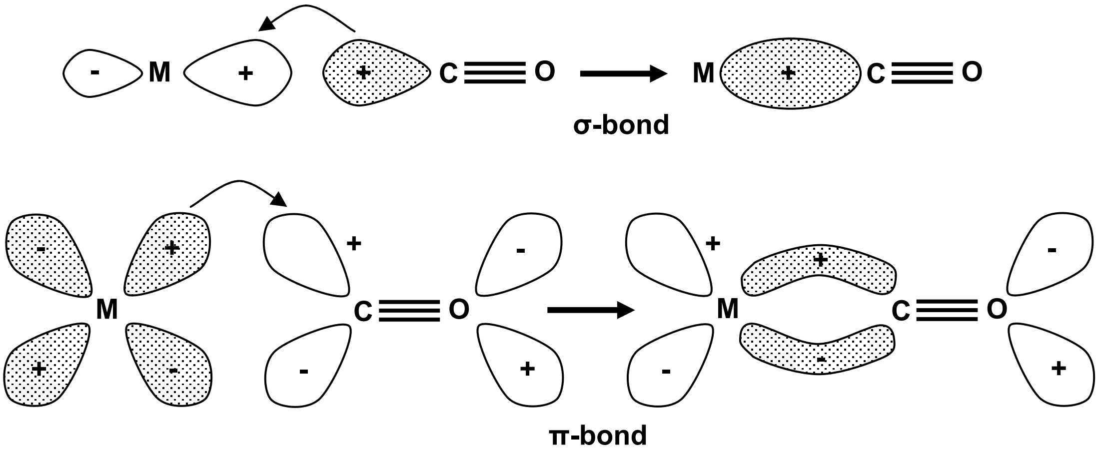

Scheme II-10. "Back-bonding" of the π-acceptor CO: formation of the metal ← carbon σ-bond using unshared electron pair on the C atom; formation of the metal → carbon π-bond.

Experimental ν(CO) provides a measure of the "net" σ-donor / π-acceptor role of the CO ligands coordinated to a metal. The more the back-donation from the metal to CO increases the more the metal-carbon bond becomes stronger (*i.e.* shorter) and the C≡O bond weaker (*i.e.* longer). Therefore, the vibrational spectra of metal carbonyl complexes will give information on the electronic structure of the metal centre and its environment. CN ligands behave in the same way but are less commonly used as their IR frequency intensities are not as strong as for CO frequencies. These considerations also explain why carbonyl and cyanide ligands help metals to sustain low oxidation states by accepting their charge excess by back-donation.

Terminal CO generally absorbs at higher frequencies (1850-2125 cm^{-1}; 2155 cm^{-1} for free CO) than a bridging CO (1700-1860 cm^{-1}) because more electron density is required to bind two metals and therefore the CO bond is weakened. Terminal CO frequencies can be quite low if co-ligands are good donors but poor π-acceptors or if the molecule is negatively charged. In both cases, the back-donation is much larger, increasing the strength of the metal-carbon bond and decreasing CO frequencies.

The charge effect on CO stretching wavenumbers can be illustrated by Table **II-2** with the concomitant decrease of the CO frequencies while the negative charge increases on the metal centre. This is consistent with the model proposed above as an increase in the charge on the metal atom delocalises the excess of electronic density by populating CO π* antibonding orbital thus weakening the CO bond.

Compound	**v(CO) (cm^{-1})**
$[Mn(CO)_6]^+$	2090
$Cr(CO)_6$	2000
$[V(CO)_6]^-$	1860
$[Ti(CO)_6]^{2-}$	1750

Table II-2. Influence of metal centre charge on CO frequencies.[84]

The relative importance of σ and π components of the bonding is difficult to attribute, and even for simple $M(CO)_x$ ($x = 4, 5, 6$) it is not theoretically feasible without substantial approximations.[85]

II.7.b {2Fe3S}-carbonyl complexes

The FTIR of the carbonyl region of $[Fe_2(CO)_6(pdt)]$ (pdt = propanedithiolate) shows three major bands (2072, 2033 and 1993 cm^{-1}).

The replacement of a carbonyl ligand (σ-donor, π-acceptor) by a thioether ligand (poor σ-donor, π-donor), as in $[Fe_2(CO)_5\{CH_3C(CH_2S)_2CH_2SCH_3\}]$ (**23**), results, as expected, in a general shift to lower frequencies (Table **II-3**).

The FTIR of the complexes in which the thioether possesses the $-CH_2SCH_2$**Y** structure (**Y** = H, CH_2Ph, CH_2Py, CH_2CH_2Py, CH_2CH_2Pyrrole, CH_2CH_2OH) shows that the CO bands are insensitive to the nature of the functionality. Not unexpectedly the methylene group essentially insulates the di-iron unit from the electronic influence of **Y**. This is reinforced by the very close similarity of reduction potentials as discussed in Chapter **III**.

Compound	Frequencies (cm^{-1})	Reference
[$Fe_2(CO)_6\{SCH_2CH_2CH_2S\}$]	2074, 2035, 1994	[86]
[$Fe_2(CO)_6\{SCH_2NHCH_2S\}$]	2076, 2036, 2008, 1989, 1979	[87]
[$Fe_2(CO)_5\{CH_3C(CH_2S)_2CH_2SCH_3\}$] (23)	2046, 1981, 1925	[63]
[$Fe_2(CO)_5\{CH_3C(CH_2S)_2CH_2SCH_2Ph\}$] (24)	2046, 1981, 1925	[63]
[$Fe_2(CO)_5\{CH_3C(CH_2S)_2CH_2SCH_2Py\}$] (10)	2046, 1982, 1926	this work
[$Fe_2(CO)_5\{CH_3C(CH_2S)_2CH_2SCH_2CH_2Py\}$] (11)	2049, 1983, 1927	this work
[$Fe_2(CO)_5\{CH_3C(CH_2S)_2CH_2SCH_2CH_2Pyrrole\}$] (21)	2049, 1984, 1926	this work
[$Fe_2(CO)_5\{CH_3C(CH_2S)_2CH_2SCH_2CH_2OH\}$] (20)	2048, 1983, 1926	this work
[$Fe_2(CO)_5\{CH_3C(CH_2S)_2CH_2SC_6H_4\text{-}p\text{-}NH_2\}$] (15)	2048, 1983, 1928	this work
[$Fe_2(CO)_5\{CH_3C(CH_2S)_2CH_2SC_6H_4\text{-}p\text{-}NH_3^+\}$] (25)	2051, 1987, 1932	this work
[$Fe_2(CO)_5\{CH_3C(CH_2S)_2CH_2S\ C_6H_4\text{-}p\text{-}NO_2\}$] (14)	2052, 1988, 1938	this work

Table II-3. Infrared frequencies of {2Fe3S}-complexes (ν(CO) region, in acetonitrile).

A small but nevertheless significant perturbation of ν(CO) values is evident in the arylthioether **14**, **15** and **25** complexes. As discussed above, two -$CH_2SC_6H_4$-*p*-**X** complexes were synthesised which have extreme electron withdrawing **X** = NO_2 (**14**) and electron donating properties **X** = NH_2 (**15**) (Hammet values: NO_2, σ_{para} = 0.81 σ^+_{para} = 0.79; NH_2, σ_{para} = -0.57 σ^+_{para} = -1.3). The carbonyl stretches for the **X** = NO_2 complex occur at higher frequencies than the **X** = NH_2 derivative, *ca.* +5cm^{-1}. This has some parallel with the crystal structure analysis where a weak effect of these groups on their relative bond lengths is observed. Protonation of the **X** = NH_2 derivative switches the releasing electronic effect of the group to that of a withdrawing group ($NH_2 \rightarrow NH_3^+$: σ_{para}, $-0.57 \rightarrow +0.60$)[82]. Thus, the arylammonium derivative **25** exhibits similar carbonyl frequencies to the **X** = NO_2 derivative.

II.8 Studies of dynamic / equilibrium properties of the thioether ligand

II.8.a NMR coalescence

Inversion of the two lone pairs of thioether ligands can be studied by NMR spectroscopy and energy barriers determined by this technique (Scheme **II-11**).

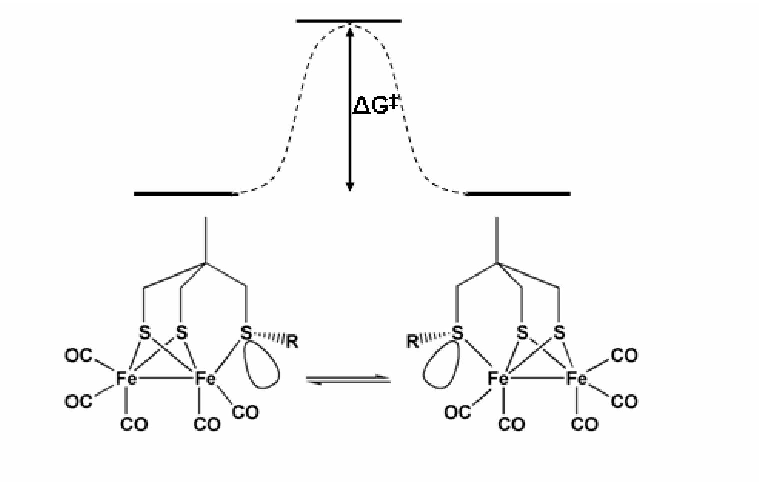

Scheme II-11. Schematic representation of the inversion of the two lone pairs of the thioether ligand on {2Fe3S}-complexes.

One of the important features of NMR is its ability to probe molecular motions over a wide range of timescales (picoseconds to several seconds) if they change nuclear spins. The nature of the NMR effect depends on the type of motion and the timescale. As NMR detects the molecular motion itself rather than the number of molecules in different states, it can probe chemical exchange even when the system is in equilibrium. This is because NMR involves individual nuclear spins which are located in particular sites in the molecule and therefore are not chemically equivalent so the chemical shift of a nuclear spin changes as it is "transported" from one side of the molecule to the other.

In our study, we looked at the coalescence of NMR signals by varying the temperature of the experiment. At "low" temperature, the exchange between two isomers is restricted so NMR signals for the two nuclei are well separated. As the temperature is raised, the rotation becomes more rapid and signals broaden. At higher temperature, nuclei are surrounded by an average environment as the exchange rate becomes very fast and only one resonance is detected, mid-way between the two separate signals (Scheme **II-12**).

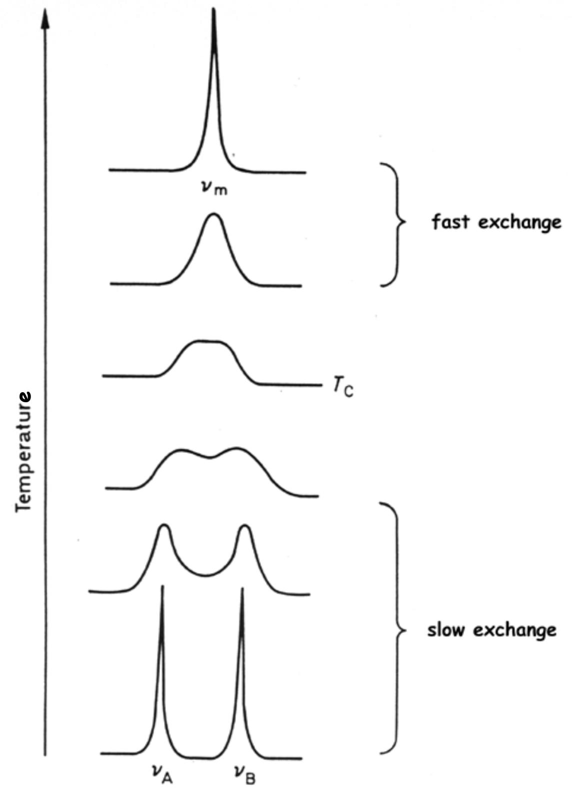

Scheme II-12. Effect of temperature on NMR signals for a simple exchange system.

From these studies we can extract the free energy activation barrier $\Delta G^{\ddagger}$:

- the temperature of coalescence T_c is measured when the average signal begins to split. At this temperature, the reaction rate is:

$$k_{T_c} = \frac{\pi}{\sqrt{2}} |\nu_A - \nu_B|$$

- the rate exchange for any reaction is described by the Eyring equation (N is Avogadro’s number and h the Plank’s constant):

$$k = \frac{R}{N.h}\, e^{-\frac{\Delta G^{\ddagger}}{RT}}$$

- inserting the reaction rate within the coalescence temperature we obtain:

$$\frac{\pi}{\sqrt{2}}|v_A - v_B| = \frac{RT}{N.h}\, e^{-\frac{\Delta G}{RT}}$$

- and this can be rearranged to give the free activation energy as a function of the coalescence temperature:

$$\Delta G^{\ddagger} = RT_c \cdot \ln \frac{RT_c\sqrt{2}}{\pi\, .\, N\, .\, h\, |v_A - v_B|}$$

- after numerical solution (with ν in Hz and T_c in Kelvin):

$$\Delta G^{\ddagger} = 19 \cdot 10^{-3} \cdot T_c\, (9.97 + \log T_c - \log |v_A - v_B|)$$

This method can give a good approximation of the energy barrier $\Delta G^{\ddagger}$ directly from the spectrum despite the difficulty in identifying the exact coalescence point corresponding to T_c. Computed simulation of spectra over a range of temperatures can also be used to determine thermodynamic parameters as $\Delta G^{\ddagger}$, $\Delta H^{\ddagger}$ or $\Delta S^{\ddagger}$ of inversion processes.

^{13}C NMR fluxional studies of the dithiolate and CN ligands had been carried out with $[Fe_2(CO)_4(CN)_2\{SCH_2CH_2CH_2S\}]^{2-}$ and showed the inversion of the propanedithiolate bridging ligand at T_c = -40ºC for this analogue to the "H-cluster" subsite.[60] Concomitant with the splitting of the $^{13}CH_2$ the bridging dithiolate, ^{13}CN signal splits also into two sets at the same temperature showing the cessation of the molecular dynamics to reveal the presence of two differentiated isomers.

Previous ^{1}H NMR fluxional studies on methyl- (**23**) and benzyl-derivatives (**24**) {2Fe3S}-complexes in the lab pointed out the complex molecular dynamics in these thioether-di-iron complexes.[63] Unlike the former example, the bridging dithiolate ligand does not exhibit flipping of the alkyl chain because the backbone is locked by the coordination of the thioether ligand.

Nevertheless, the fluxionality associated with the inversion of the two lone pairs of the thioether ligand has been identified by NMR coalescence. However, the complexity of the spectrum by varying the temperature needs more complex calculations than the use of the simple Eyring equation. Indeed, two independent spin systems can be identified for [$Fe_2(CO)_5\{CH_3C(CH_2S)_2CH_2SCH_3\}$] **23** (Figure **II-7**).

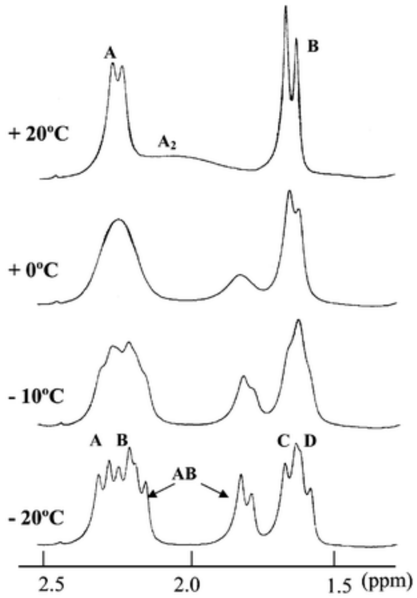

Figure II-7. Variable temperature ^1H NMR spectrum of [$Fe_2(CO)_5\{CH_3C(CH_2S)_2CH_2SCH_3\}$] (**23**) in CD_2Cl_2 (taken from reference [63]).

Two ABCD spin systems coalesce in two AB spin systems as the temperature is raised, plus an isolated AB pair which coalesces to an A_2 spin system. The interconverting spins systems are readily explained by inversion at the thioether sulfur (Scheme **II-13**).

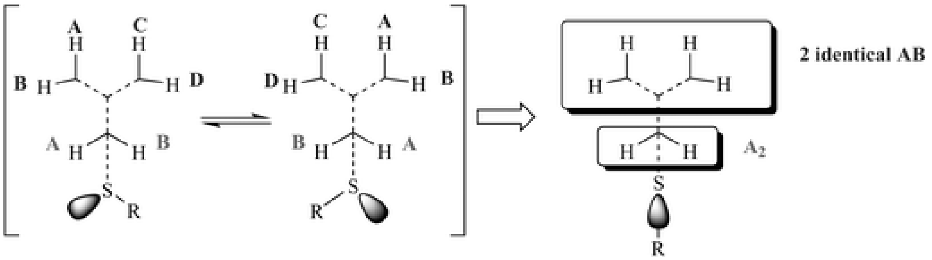

Scheme II-13. Schematic representation of the ABCD→AB and AB→A_2 systems for [$Fe_2(CO)_5\{CH_3C(CH_2S)_2CH_2SR\}$] (view from the apical methyl on top of the ligand, R = Me or Bz) (taken from reference [63]).

NMR experiments were performed in *d*-chloroform by Dr. S. A. Fairhurst (Figure **II-8**) and from the data activation energies $\Delta G^{\ddagger}$ for the AB↔A_2 spin system of different {2Fe3S}-complexes were calculated at T_c and these are given in Table **II-4**. Simulations of the NMR spectra were also performed and $\Delta G^{\ddagger}$ values (at T_c) are in very good agreement with the experimental data.

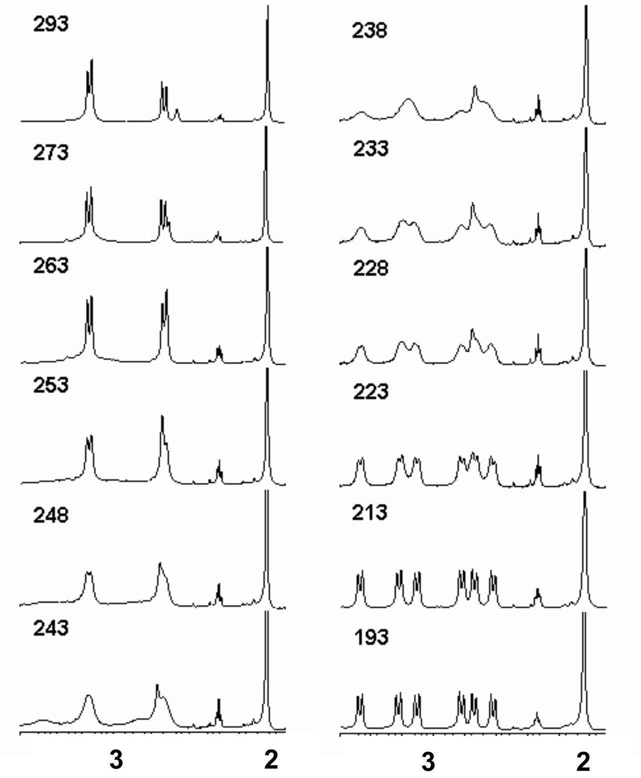

Figure II-8. Variable temperature (in K) ^1H NMR spectrum of [$Fe_2(CO)_5\{CH_3C(CH_2S)_2CH_2SC_6H_4\text{-}p\text{-}NH_2\}$] (**15**) in $CDCl_3$.

Simulation of the spectra over a range of temperatures provides further data. Given in Table **II.4**, are values of $\Delta H^{\ddagger}$ which are obtained from the Eyring plot (ln k/T *vs.* 1/T) and values of E_a obtained from an Arrhenius plot (ln k *vs.* 1/T), noting $\Delta H^{\ddagger} \approx E_a - RT$. In both cases, k values were estimated by simulation of the experimental spectra as illustrated for the plot in Figure **II-8**.

Compound	**Δv_{ab} (Hz)**	**T_c (K)**	**$\Delta G^{\ddagger}_{T_c}$ (kJ.mol^{-1})**	**$\Delta G^{\ddagger}_{T_c}$ simulated (kJ.mol^{-1})**	**$\Delta H^{\ddagger}$ (kJ.mol^{-1})**	**E_a (kJ.mol^{-1})**
$[Fe_2(CO)_5\{CH_3C(CH_2S)_2CH_2SCH_2C_6H_5\}]$ (24)	43	240	48.8 ± 0.5	48.78	85.6	87.6
$[Fe_2(CO)_5\{CH_3C(CH_2S)_2CH_2SC_6H_4\text{-}p\text{-}NH_2\}]$ (15)	323	243	45.8 ± 0.5	45.80	51.7	55.4
$[Fe_2(CO)_5\{CH_3C(CH_2S)_2CH_2SC_6H_4\text{-}p\text{-}NH_3^+\}]$ (25)	315	208	39.0 ± 0.5	38.98	14.2	16.2
$[Fe_2(CO)_5\{CH_3C(CH_2S)_2CH_2SC_6H_4\text{-}p\text{-}NO_2\}]$ (14)*	20-330	200	/	38-42	/	/

* the slow limit spectra was not possible to record due to the machine limitation, however coalescence at approximately 200 K was observed and a range of value for $\Delta G^{\ddagger}$ was obtained by simulating the slow limit spectra using the programme *gNMR*.

Table II-4. Determination of the free energy activation ($\Delta G^{\ddagger}$) parameter in $CDCl_3$; T_c is the coalescence temperature; Δv_{ab} is determined from the slow limit spectra.

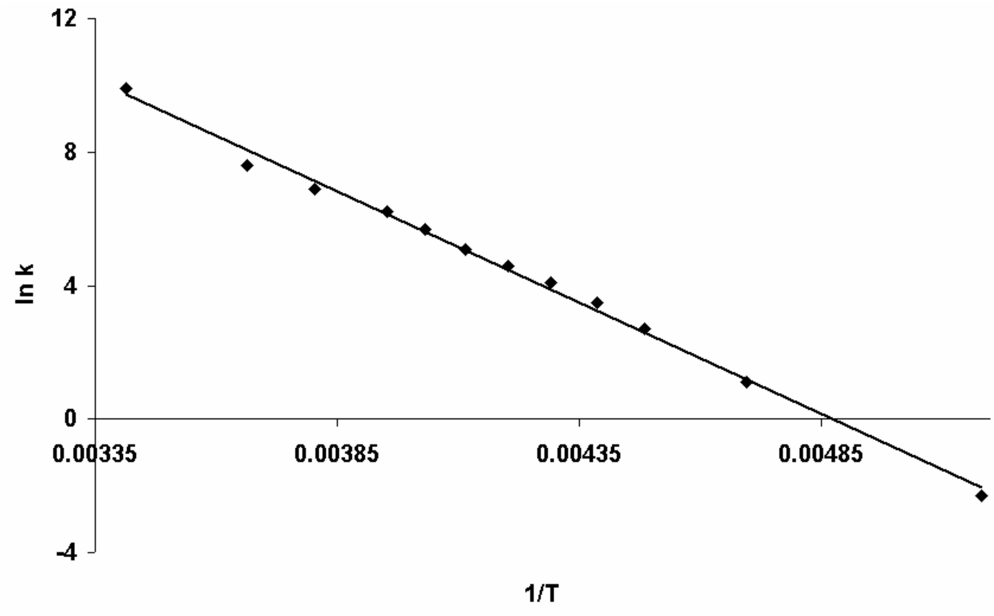

Figure II-8. Plot of ln k *vs.* 1/T from the simulation of the AB↔A2 spin system using *g*NMR for $[Fe_2(CO)_5\{CH_3C(CH_2S)_2CH_2SC_6H_4\text{-}p\text{-}NH_2\}]$ (**15**).

The results presented in Table **II-4** show a clear trend in the activation energy for the inversion of the thioether ligand. For the aryl compounds, the activation energy is lower when an electron-withdrawing group is in the *para*-position. Protonation of the aniline group can switch the electron donor character of the amine group to that of a group with a strong electron acceptor character, $-NH_3^+$. Obtaining an accurate figure for the *p*-nitro compound is problematic because the coalescence temperature, estimated to be about 200 K, is close to the freezing point of the solvent.

II.8.b Lability of the thioether ligand under CO

Earlier studies of alkyl and benzyl thioether complexes with the {2Fe3S}-core under CO at one atmosphere showed that they were unreactive.[88] CO at one atmosphere did not displace the thioether group to any significant extent. The aryl thioether group complexes **14**, **15** and **25** are considerably more reactive and equilibrate within a few hours with CO at one atmosphere as represented by Equation **II-1**.

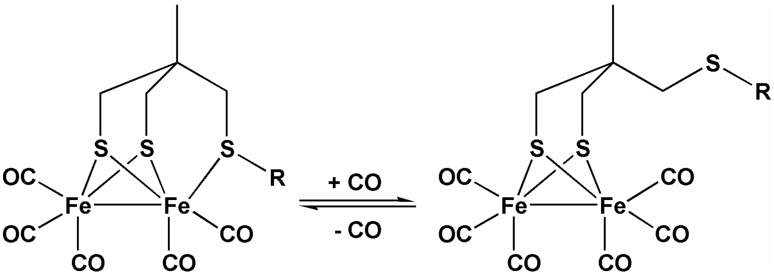

(II.1)

Measurements of K_{eq} was carried out by exposing a solution of a complex under CO atmosphere overnight (to let the system equilibrate) in acetonitrile at 20ºC and then to compare the infrared spectrum before and after the exposure to CO. Values measured are independent of the complex concentration as we compare absorptions. We chose to measure K_{eq} using the lowest CO frequency peak as it does not overlap with the other peaks from the starting or the final compound (1925 cm^{-1} for benzyl-derivative **24**, 1928 cm^{-1} for the aniline-derivative **15** and 1932 cm^{-1} for the nitrobenzene-derivative **14**) (Figure **II-9**). The pentacarbonyl complex can be recovered within a few minutes by bubbling dinitrogen into the complex solution

.

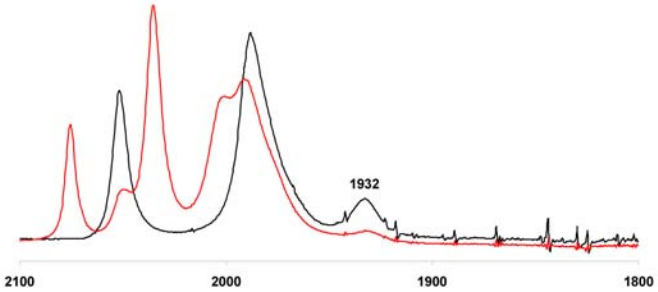

Figure II-9. FTIR of the nitrobenzene **14** complex before (black) and after (red) exposure to CO (in CH_3CN).

K_{eq} was determined as follow:

$$A + CO \overset{K_{eq}}{\rightleftarrows} B$$

$$K_{eq} = \frac{[B_{final}]}{[A_{final}].[CO]}$$

$$[A_{initial}] = [A_{final}] + [B_{final}]$$

$$K_{eq} = \frac{[A_{initial}] - [A_{final}]}{[A_{final}].[CO]}$$

$$K_{eq} = \left(\frac{[A_{initial}]}{[A_{final}]} - 1 \right) \cdot \frac{1}{[CO]}$$

We measure absorbance and not directly the concentration of the species, but as we are considering the ratio of concentration, this is equivalent to the ratio of absorbance (Beer-Lambert law). The saturating concentration of CO in acetonitrile is 13.4 mM at 20ºC.[65] Results are presented in Table **II-5**. Noting that the -SC_6H_4-*p*-NH_2 complex has FTIR and crystallographic data very similar to that of the benzyl thioether complex and that the activation energy associated with the fluctionality was not dramatically different prompted a closer examination of the equilibration of the benzyl thioether derivative with CO. We found that the hexacarbonyl and the pentacarbonyl are in a 1 : 24 equilibrium ratio under one atmosphere of CO (Table **II-5**). From this data ΔG° was calculated.

Compound	K_{eq} (L.mol^{-1})	ΔG°_{293} (kJ.mol^{-1})
$[Fe_2(CO)_5\{CH_3C(CH_2S)_2CH_2SC_6H_4\text{-}p\text{-}NO_2\}]$ (14)	362 ± 28	-14.4 ± 0.2
$[Fe_2(CO)_5\{CH_3C(CH_2S)_2CH_2SC_6H_4\text{-}p\text{-}NH_3^+\}]$ (25)	125 ± 19	-11.8 ± 0.4
$[Fe_2(CO)_5\{CH_3C(CH_2S)_2CH_2SC_6H_4\text{-}p\text{-}NH_2\}]$ (15)	13.7 ± 0.1	-6.38 ± 0.015
$[Fe_2(CO)_5\{CH_3C(CH_2S)_2CH_2SCH_2C_6H_5\}]$ (24)	3.21± 0.28	-2.84 ± 0.21

Table II-5. K_{eq} values measured for {2Fe3S}-complexes in saturated CO solution (13.4 mM) in acetonitrile at 20ºC.

Whereas only small differences have been observed in the crystal structures and infrared spectra, the equilibration experiments show that reversible carbonylation involving cleavage of the thioether bond is clearly affected by the nature of the thioether ligand. The CO substitution for the nitrobenzene derivative is *ca.* 8 kJ.mol^{-1} more favourable than for the aniline derivative which in turn is about 3.5 kJ.mol^{-1} more favourable than the benzyl thioether complex.

II.9 On the bonding and reactivity of the thioether ligand

II.9.a Free energy correlations between inversion and substitution reactions

Comparison of the carbonyl substitution data for the thioether derivatives appears at first sight straightforward. The greater the electron withdrawing effect of the group on the thioether the weaker the Fe-S$_{\text{thioether}}$ bond and the more extensive is the carbonylation *i.e.* the equilibrium in Equation **II.1** is shifted more to the right hand side the stronger the electron-withdrawing effect.

The detached thioether in all four cases must have little influence on bond strengths within the hexacarbonyl framework (Scheme **II.13**) and we can therefore consider the ground state hexacarbonyl products as equi-energetic. If we make the following assumptions:

(i) the contribution of solvation energy changes to ΔG° for the conversion of the neutral pentacarbonyl to the neutral hexacarbonyl are similar

(ii) the TΔS contribution to ΔG° is similar for each compound

then we can make the approximation that the differences in ΔG° between the compounds, ΔΔG°, can be taken as a direct measure of the *relative* bond enthalpy energy difference between the ground states of the parent {2Fe3S}-complexes (Scheme **II-14**).

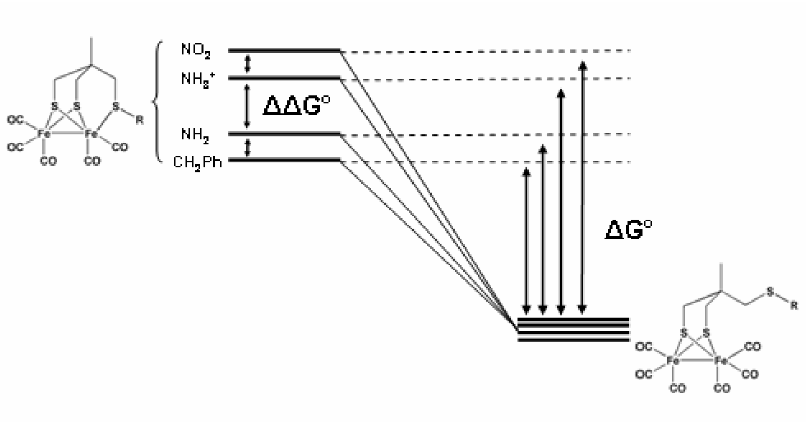

Scheme II-14. Energetic diagram of CO substitution.

We can now consider ΔG° for the carbonylation and the activation energy data for the inversion process as determined by NMR. Figure **II-10** shows a plot of ΔG°_{293} for the carbonyl substitution reaction *versus* Ea for the inversion. For the limited data there is a reasonable linear correlation as would be expected if ΔG°_{293} is dominated by the enthalpy term. There is a poor correlation between $\Delta G^{\ddagger}$ for the inversion and ΔG° for the carbonylation reaction. The $\Delta S^{\ddagger}$ term may vary significantly if ordering the transition state is important. However, estimation of $\Delta S^{\ddagger}$ is generally subject to considerable error.

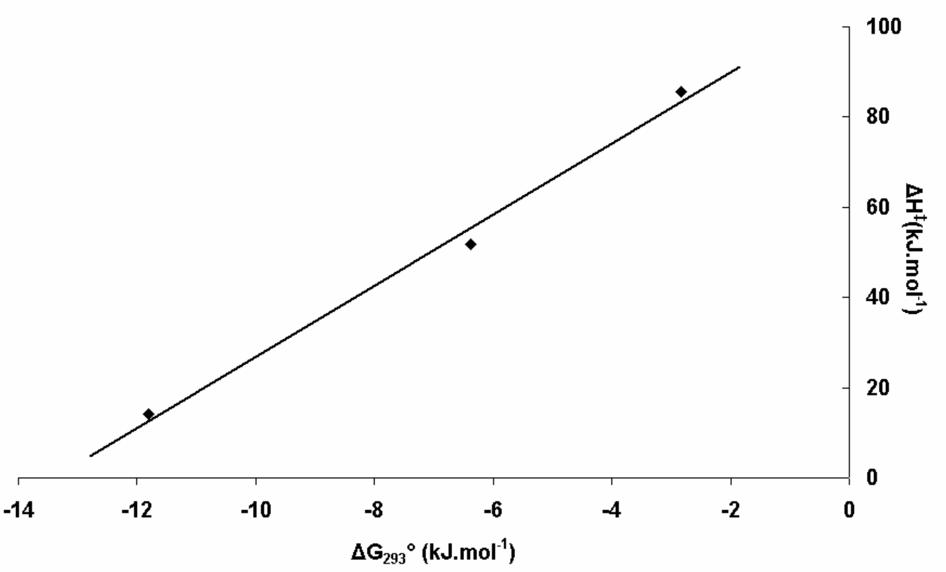

Figure II-10. Plot of ΔG°_{293} for the carbonyl substitution reaction *vs.* E_a for the inversion.

Although a little speculative at this stage because of limited data we believe that the transition state for the inversion involves the thioether either non-bonded or weakly bonded to the iron centre (Scheme **II-15**).

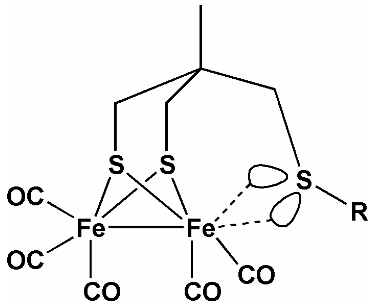

Scheme II-15. Postulated transition state for the inversion of the two lone pair electrons of the thioether ligand.

Detachment of the thioether may be involved in the intimate mechanism of the reversible carbonylation reaction. We know from experimental [65] and DFT [89] studies of the mechanism of cyanation of $[Fe_2(CO)_5\{CH_3C(CH_2S)_2CH_2SCH_3\}]$ that cyanide attack on the distal iron leads to thioether dissociation and that this almost certainly occurs via formation of a bridging CO. Subsequent recoordination of thioether to the monocyanide product is also a reversible reaction and leads to CO loss (Scheme **II-16**).

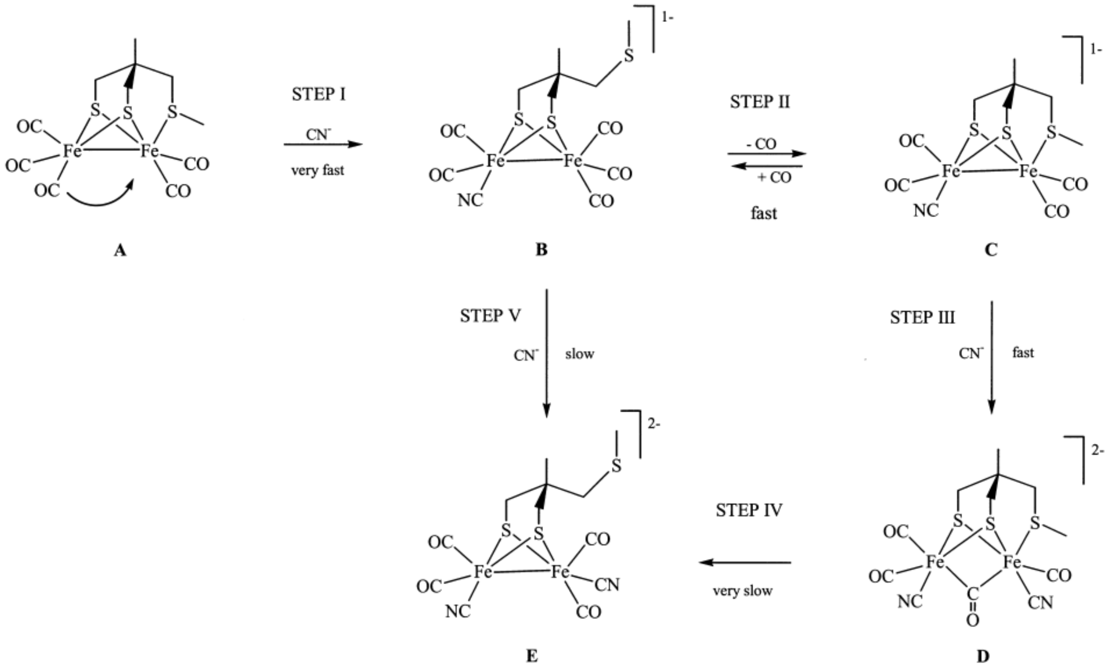

Scheme II-16. Summary of the cyanation chemistry of $[Fe_2(CO)_5\{CH_3C(CH_2S)_2CH_2SCH_3\}]$ (taken from reference [65]).

In our case we have not studied the intimate mechanism of the equilibration reaction with CO. It could involve

(i) addition of CO to the distal iron concomitant with CO transfer and decoordination of the thioether

(ii) addition of CO across the metal-metal bond followed by rearrangement with decoordination of the thioether

(iii) associative substitution by attack of CO on the thioether ligated iron

(iv) dissociative substitution by loss of thioether followed by CO ligation

These remarks suggest the possibility of having a vacant site on the proximal iron of the subsite of the “H-cluster” of the [Fe]-hydrogenase by decoordination of the cysteinate ligand, providing a potent site for protonation and/or dihydrogen coordination. This will be further discussed in Chapter **IV**.

II.9.b Back-bonding to the thioether ligand: possible influence on metal-metal bond strength

In section **II.6** above we noted that in the comparison between the nitro- and the amino-substituted thioether complexes the former had the shorter bond length which is counterintuitive and we now consider this in more detail.

It has been reported that a thioether ligand may accept electron density from filled *dπ*-orbitals of a transition metal centre and that the σ* orbitals of the C-S bond have a significant role in the description of the back-bonding.[90-92] Spatial overlapping of C-S σ* orbital and a donor t_{2g} orbital on the metal induces increased back-donation (Scheme **II-17**). By accepting electronic density in the anti-bonding σ* orbitals, the carbon-sulfur bond is lengthened, and *in extremis* can lead to complete C-S bond cleavage.[92]

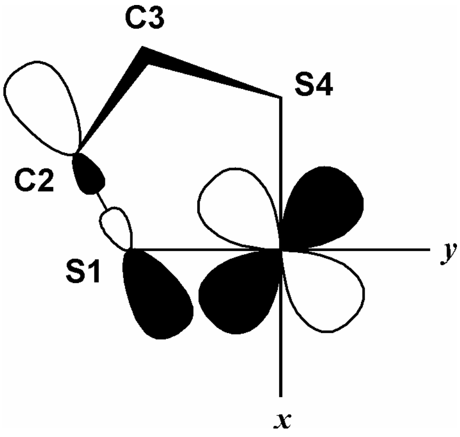

Scheme II-17. Spatial overlap between C-S σ* and metal t_{2g} orbitals (adapted from reference[92]).

If back-bonding is operative in our systems, then we might expect to see this in a comparison of the amino- and nitro-arylthioether complexes. As can be seen from Table **II.1**, the C-S bond is longer for the nitro derivative (2.501(1)) than it is for the amino derivative (2.5168(8)). However, the Fe-S thioether bond length is the same for both complexes. S(3)-C(10) distances for the aromatic thioethers do not differ significantly. An uncoordinated thioether group shows an S(3)-C(10) bond length of 1.799(4) in the thioacetyl complex described in **Chapter IV**. This is marginally shorter than in all the ligated thioether complexes, however, it must be noted that the thioacetyl group is electronically quite different from thioethers.

The depletion of electronic density on the sulfur atom by the nitro group induces a lowering in energy of the σ^* antibonding orbital and provides a better mixing between the filled metal $d\pi$ orbitals, resulting in a lengthening of the C-S bond.

The synergistic effect of this back-donation may enhance σ donation to the iron centre then more electron density transmitted to the metal-metal bond. If we consider the z axis being represented by the $S_{\text{thioether}}$-Fe_{proximal} bond, it is the orbital d_{z2} of the metal which can share electrons with the σ bonding orbital of the sulfur to form the Fe-S bond. The d_{z2} orbital is therefore more electron rich. The d_{z2} orbital is also involved in the formation of the bent metal-metal bond [55] and enhancing electronic density on this orbital will thus account for the shorter metal-metal bond distance.

The apparent contradictory observation that CO frequencies are lowered whereas the metal-metal bond is shorter follows from competition between the σ^* antibonding orbital of the thioether ligand and the π^* orbitals of the CO for electron density from the filled $d\pi$ orbitals (d_{xy}, d_{xz} and d_{yz}) of the metal. This is schematically illustrated in Scheme **II-18**.

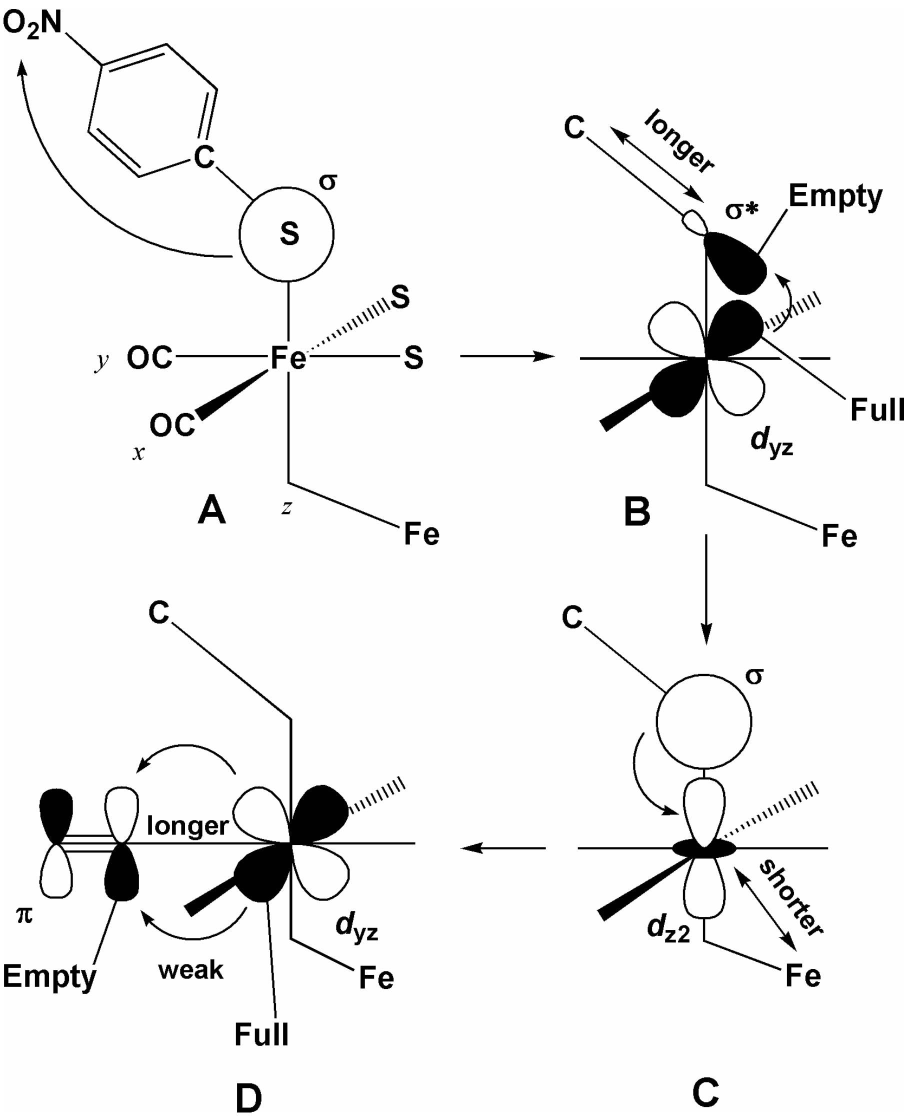

Scheme II-18. Diagram representing the electronic influence of a withdrawing group on the molecular orbitals: (A) the σ orbital of the sulfur is depleted by the electronic acceptor character of the nitro group; (B) the σ* orbital lowered in energy is accessible for the *d*π orbitals of the metal to accept electronic density, destabilising the C-S bond; (C) back-donation from the σ orbital of the sulfur to the d_{z2} orbital of the metal, increasing the electronic density on the metal centre and the metal-metal bond is shortened; (D) the depleted *d*π orbitals of the metal are less involved in back-donation into empty π orbitals of the CO due to the σ* orbital of the sulfur resulting in weakening of the metal-carbonyl bond.

II.10 General conclusions

In this chapter, we have shown that a range of functionalised {2Fe3S}-complexes can be synthesised.

The modifications of the thioether ligand by electron-donating and electron-withdrawing groups have begun to provide an understanding of how a thioether ligand can influence the structure, spectroscopy and reactivity of the di-iron unit.

An intriguing aspect of this is the sulfur inversion and the thermodynamic data for reversible carbonylation. There is a strong correlation between ground state energies estimated for the complexes and the activation energy for the inversion, and this has led to the conclusion that a non-bonded thioether transition state is involved in the inversion process. Extending the range of substituted arylthioether complexes should allow firmer conclusions on this.

Small differences in bond length data have been observed, notably a shortening of the Fe-Fe bond when an electron-withdrawing group is placed on an arylthioether together with a lengthening of the aromatic C-S bond. It has been argued that this is a consequence of a synergistic increase of the electron density in a d_{z2} orbital with metal-metal bonding character induced by back-donation from metal $d\pi$ orbitals into the thioether σ^* orbital. This is supported by the observation that the C-S bond is longer in the *p*-nitro arylthioether than in the *p*-amino analogue.

Ligand S K-edge spectroscopy will also provide strong evidence for the implication of the σ^* antibonding orbital of the C-$S_{thioether}$ bond in the coordination of the thioether ligand. Iron-sulfur complexes and proteins have been analysed by this technique [93] and evidence that the electronic environment has a strong influence on Fe-S bonds encouraged us to collaborate with R.K. Szilagyi from Montana University. Preliminary results have already given an interesting insight into the electronic state of our complexes and further studies are currently being carried out at the Stanford synchrotron.

II.10 Experimental

$CH_3C(CH_2OTs)_3$ (2).

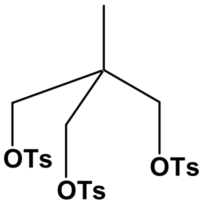

$CH_3C(CH_2OH)_3$ (**1**) (82.2 g, 680 mmol) was dissolved in pyridine (300 cm^3) and cooled down to 0°C. TsCl (429 g, 2.25 mol) dissolved in pyridine (500 cm^3) was added drop wise, and the mixture was stirred at RT overnight. The solution was poured into water (2500 cm^3), sulphuric acid (300 cm^3) and ice, and the precipitate was filtered, washed with water and then methanol until the pink colour disappeared to give a white powder (360 g, 619 mmol, 91%). δ_H (400 MHz; solvent $CDCl_3$; standard $SiMe_4$) 0.89 (3H, s, C*H₃*), 2.47 (9H, s, CH_3Ph), 3.76 (6H, s, 3×C*H₂*), 7.36 (6H, d, *J* 8.6 Hz, Ph), 7.71 (6H, d, *J* 8.3 Hz, Ph).

$CH_3C(CH_2SCN)_3$(3).

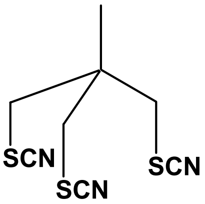

2 (60.2 g, 103 mmol) and KSCN (125 g, 1.3 mol) were stirred in DMF (250 cm^3) at 125°C for 8 hours. The mixture was poured into ice and left overnight at 4°C. The yellow precipitate was filtered and washed with water (2×500 cm^3), ethanol/diethyl ether (1:1) (2×50 cm^3) and finally with diethyl ether (2×50 cm^3) to give a yellow powder (20.0 g, 82 mmol, 79%). δ_H (400 MHz; solvent $CDCl_3$; standard $SiMe_4$) δ 1.41 (3H, s, C*H₃*), 3.25 (6H, s, 3×C*H₂*).

$CH_3C(CH_2SH)_3$, 1,1,1-tris(mercaptomethyl)ethane (4).

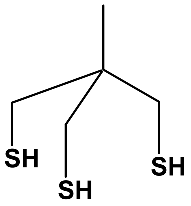

Lithium aluminium hydride (7.5 g, 198 mmol) was dissolved in diethyl ether (160 cm^3) under nitrogen. The mixture was cooled with an ice bath and **3** (15.4 g, 63 mmol) was added very carefully (violent "fizzing"). The reaction was then stirred under reflux overnight. The mixture was cooled in an ice bath and a degassed solution of H_2O/HCl (1:1) (70 cm^3) was added. Then a solution of toluene/HCl (1:1) (200 cm^3) was added, and the product was extracted with toluene (3×50 cm^3). The organic phase was dried with magnesium sulphate and solvents were removed to give a yellow oil (8.04 g, 48 mmol, 82%).δ_H (400 MHz; solvent $CDCl_3$; standard $SiMe_4$) 1.0 (3H, s, C*H_3*), 1.2 (3H, t, *J* 8.8 Hz, S*H*), 2.6 (6H, d, *J* 8.8 Hz, C*H_2*).

$CH_3C(CH_2S)_2CH_2SH$, (4-methyl-[1,2]dithiolan-4-yl)methanethiol (5).

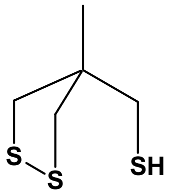

4 (3.90 g, 23.2 mmol) was dissolved in methanol (130 cm^3). Dimethyl disulfide (2.5 ml, 27.8 mmol) was added. Addition of potassium *tert*-butoxide (20 mg, 0.2 mmol) changes immediately the colour to yellow. The mixture was stirred for two hours and degassed regularly to liberate CH_3SH. Degassed ammonium chloride-saturated water solution (80 cm^3) was added, and the product was extracted with degassed diethyl ether (3×100 cm^3). The organic phase was dried with magnesium sulphate, filtered, and the product was purified by flash chromatography under nitrogen (ethyl acetate/hexane 1:1) to give a yellow oil (3.52 g, 21.2 mmol, 91%).δ_H (400 MHz; solvent $CDCl_3$; standard $SiMe_4$) 1.3 (3H, s, C*H_3*), 1.5 (1H, t, *J* 8.8 Hz, S*H*), 2.7 (2H, d, *J* 8.8 Hz, C*H_2*), 2.9 and 3.1 (2×2H, 2×d, *J* 11.5 Hz, C*H_2*).

$PyCH_2Br$, 2-Bromomethyl-pyridine.

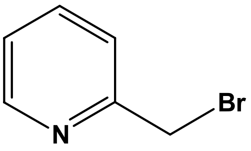

2-pyridylcarbinol (10.0 g, 89.8 mmol) was dissolved in HBr 48% (90 cm^3). The mixture was stirred at 150°C for 4 hours. The water was removed and the solid compound was stirred in ethanol and put in the fridge overnight. After filtration, a pale brown solid was obtained (10.2 g, 40.0 mmol, 45%). δ_H (400 MHz; solvent $CDCl_3$; standard $SiMe_4$) 4.9 (2H, s, CH_2Br), 7.9 (1H, t, Py), 8.0 (1H, d, Py), 8.5 (1H, t, Py), 8.7 (1H, d, Py).

$CH_3C(CH_2S)_2CH_2SCH_2Py$,

2-(((4-methyl-1,2-dithiolan-4-yl)methylthio)methyl)pyridine (6).

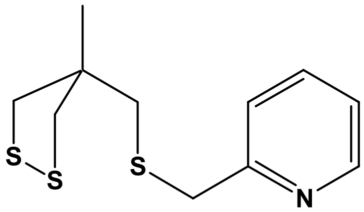

NaH (60% oil suspension, 0.27 g, 6.75 mmol) was washed with hexane and then dissolved in tetrahydrofuran (5 cm^3). **5** (0.87 g, 5.2 mmol) was dissolved in tetrahydrofuran, added to the solution of NaH and stirred at room temperature. 2-bromomethyl-pyridine was dissolved in diethyl ether, added to the mixture and stirred at room temperature for two hours. Excess of sodium hydride was quenched by ammonium chloride-saturated water and diethyl ether (30 cm^3) was added. The organic phase was washed with water, dried ($MgSO_4$) and purified by flash chromatography (chloroform/ethyl acetate 1:1) to give a yellow oil (0.48 g, 36%), (Found C, 51.34; H, 5.84; N, 5.43. $C_{11}H_{15}NS_3$, requires C, 51.32; H, 5.87; N, 5.44%); δ_H (400 MHz; solvent $CDCl_3$; standard $SiMe_4$) 1.26 (3H, s, CH_3), 2.79 (2H, s, CH_2SCH_2Py), 2.85 (2H, d, *J* 11.2 Hz, CH_2SS), 3.05 (2H, d, *J* 11.2 Hz, CH_2SS), 3.88

(2H, s, C*H₂*Py), 7.17 (1H, m, Py), 7.37 (1H, d, *J* 7.8 Hz, Py), 7.66 (1H, m, Py) and 8.55 (1H, d, *J* 4.2 Hz, Py); *m/z* 257 $(M)^+$, 165 $(M - CH_2Py)^+$, 119 $(M - CH_2SCH_2Py)^+$.

$MeC(CH_2SH)_2CH_2SCH_2Py$,
2-(((pyridin-2-yl)methylthio)methyl)-2-methylpropane-1,3-dithiol (7).

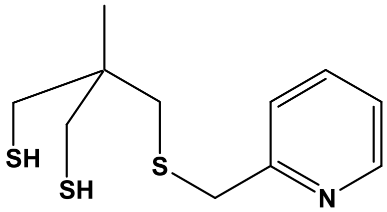

$LiAlH_4$ (0.52 g, 13.9 mmol) was dissolved in diethyl ether (100 cm^3) and cooled in an ice bath. 2-(4-Methyl-[1,2]dithiolan-4-ylmethylsulfanylmethyl)-pyridine (**6**) (1.20 g, 4.7 mmol) dissolved in diethyl ether was added carefully. The mixture was stirred at room temperature overnight. The reaction was then cooled in an ice bath and the excess of $LiAlH_4$ was quenched by degassed water (100 cm^3) and degassed sulphuric acid solution (50 cm^3; 10 % v/v). The aqueous phase was extracted with degassed diethyl ether. The organic phase was washed with degassed water, dried ($MgSO_4$) and the solvent removed to give a colourless oil (1.02 g, 84%), δ_H (400 MHz; solvent $CDCl_3$; standard $SiMe_4$) 1.00 (3H, s, CH_3), 1.23 (2H, t, *J* 9.0 Hz, 2×SH), 2.56 (4H, d, *J* 9.0 Hz, 2×CH_2), 2.64 (2H, s, C*H₂*SCH_2Py), 3.84 (2H, s, C*H₂*Py), 7.19 (1H, m, Py), 7.37 (1H, d, *J* 7.8 Hz, Py), 7.67 (1H, m, Py) and 8.54 (1H, d, *J* 3.9 Hz, Py); *m/z* 259 $(M)^+$, 167 $(M - CH_2Py)^+$, 119 $(M - CH_2SCH_2Py)^+$.

$Fe_2(CO)_5(CH3C(CH_2S)_2CH_2SCH_2Py)$ (10)

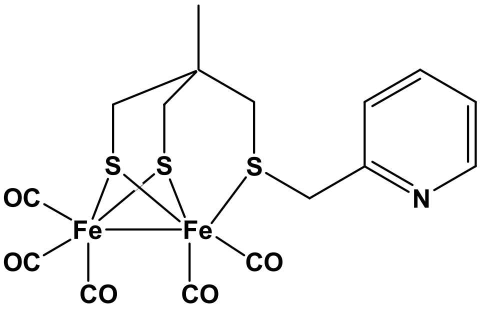

$[Fe_3(CO)_{12}]$ (1.11 g, 2.2 mmol) was dissolved in freshly distilled toluene (100 cm^3) and stirred. $CH_3C(CH_2SH)_2CH_2SCH_2Py$ (**7**) was dissolved in toluene, added to the iron complex and heated at 80°C for 90 min. The dark green mixture turned red brown. The toluene was removed and the compound was purified by flash chromatography under dinitrogen (degassed ethyl acetate) to give a red-brown powder (0.26 g, 24%). The powder was dissolved in acetonitrile (10 cm^3), and slow evaporation of the solvent under a stream of dinitrogen led to the formation of single crystals. (Found C, 37.97; H, 3.07; N, 2.68. $C_{16}H_{15}NO_5S_3Fe_2$, requires C, 37.74; H, 2.97; N, 2.75); ν_{max}/cm^{-1} (CO) 1926, 1982 and 2046 (acetonitrile); δ_H (400 MHz; solvent $CDCl_3$; standard $SiMe_4$) 0.88 (3H, br s, CH_3), 1.62 (2H, br d, *J* 13.4 Hz, CH_2SFe), 2.01 (2H, br s, CH_2SCH_2Py), 2.24 (2H, br d, *J* 13.4 Hz, CH_2SFe), 4.16 (2H, s, CH_2Py), 7.29 (1H, br s, Py), 7.49 (1H, br s, Py), 7.77 (1H, br s, Py) and 8.57 (1H, br s, Py); *m/z* 509 $(M)^+$, 481 $(M – CO)^+$, 453 $(M - 2CO)^+$, 425 $(M - 3CO)^+$, 397 $(M – 4CO)^+$, 369 $(M – 5CO)^+$, 323 $(Fe_2CH_3C(CH_2S)_3)^+$, 268 $(Fe_2SSCH_2Py)^+$, 176 $(Fe_2S_2)^+$; Mössbauer spectrum (solid, 77 K, referenced to 25 μm Fe-foil at 298 K): two doublets, isomer shifts at 0.044 and 0.093, quadrupole splittings of 0.954 and 0.247 $mm.s^{-1}$.

$Py(CH_2)_2OTs$, 2-(2-tosyloxyethyl)pyridine.

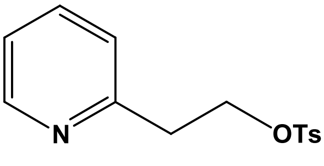

2-(2-hydroxyethyl)pyridine (4.9 g, 40 mmol) was dissolved in CH_2Cl_2 (70 cm^3). The solution was cooled at 0°C and triethylamine (8.0 g, 80 mmol) was added. *p*-toluenesulfonyl chloride (11.4 g, 60 mmol) was added in small aliquots over a 10 min period. The mixture was stirred overnight at room temperature. CH_2Cl_2 (200 cm^3) was added and the organic phase was washed with H_2O (100 cm^3), then with brine (100 cm^3) and dried ($MgSO_4$). The product was purified by column chromatography (hexane/ethyl acetate 1:1) to give a white solid (10.0 g, 36 mmol, 90%). δ_H (250 MHz; solvent $CDCl_3$; standard $SiMe_4$) 2.4 (3H, s, Ts), 3.1 (2H, t), 4.4 (2H, t), 7.1 (2H, m), 7.3 (2H, d, *J* 12.8 Hz), 7.6 (1H, t, *J* 8.8 Hz), 7.7 (2H, d, *J* 12.4 Hz), 8.4 (1H, d, *J* 8.8 Hz).

$CH_3C(CH_2S)_2CH_2SCH_2CH_2Py$,

2-(2-((4-methyl-1,2-dithiolan-4-yl)methylthio)ethyl)pyridine (8).

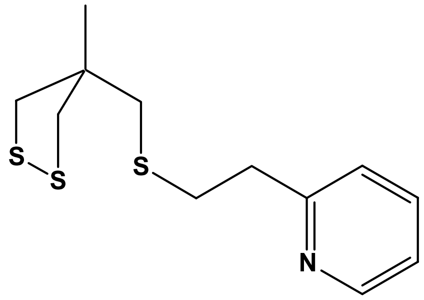

NaH (60% oil suspension, 0.60 g, 15.0 mmol) was washed with dry hexane and then dissolved in THF (100 cm^3). (4-methyl-[1,2]dithiolan-4-yl)methanethiol (**5**) (2.0 g, 12.0 mmol) was dissolved in THF (25 cm^3), added to the solution of NaH and stirred at room temperature. 2-(2-tosyloxyethyl)pyridine was dissolved in tetrahydrofuran (25 cm^3), added to the mixture and stirred at room temperature for 2h. Excess sodium hydride was quenched by ammonium chloride-saturated water and the product was extracted with diethyl ether. The organic phase was washed with distilled water, dried ($MgSO_4$) and purified by flash chromatography (chloroform/ethyl acetate 1:1) to give a yellow oil (2.3 g, 8.5 mmol, 71%). δ_H (400 MHz; solvent $CDCl_3$; standard $SiMe_4$) 1.29 (3H, s, CH_3), 2.78 (2H, s, $C\mathit{H_2}SCH_2CH_2Py$), 2.87 (2H, d, *J* 11.2 Hz, $C\mathit{H_2}SS$), 3.00 (2H, d, J 6.8 Hz, $C\mathit{H_2}CH_2Py$), 3.07 (2H, d, *J* 6.8 Hz, $CH_2C\mathit{H_2}Py$), 3.10 (2H, d, *J* 11.2 Hz, $C\mathit{H_2}SS$), 7.14 (1H, m, Py), 7.17 (1H, d, *J* 7.8 Hz, Py), 7.61 (1H, m, Py) and 8.55 (1H, d, *J* 4.8 Hz, Py); *m/z* 272 $(MH)^+$.

$CH_3C(CH_2SH)_2CH_2SCH_2CH_2Py$,

2-((2-(pyridin-2-yl)ethylthio)methyl)-2-methylpropane-1,3-dithiol (9).

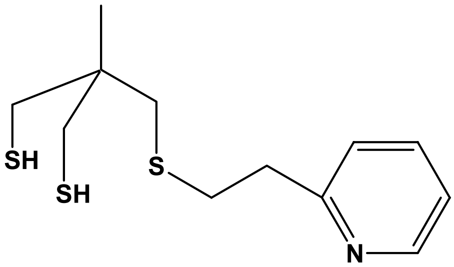

$LiAlH_4$ (0.8 g, 21.0 mmol) was dissolved in diethyl ether (100 cm^3) and cooled in an ice bath. 2-[2-(4-Methyl-[1,2]dithiolan-4-ylmethylsulfanyl)-ethyl]-pyridine (**8**) (2.3 g, 8.5 mmol) was dissolved in diethyl ether (100 cm^3) and added dropwise. The mixture was stirred at room temperature overnight. The reaction was then cooled in an ice bath and the excess $LiAlH_4$ was quenched by degassed water (100 cm^3). A few drops of H_2SO_4 were added, the organic phase became white and it was extracted until the aqueous phase became clear. The organic phase was dried ($MgSO_4$) and evaporated to give a white oil (2.0 g, 86%). δ_H (400 MHz; solvent $CDCl_3$; standard $SiMe_4$) 1.03 (3H, s, CH_3), 1.23 (2H, t,, *J* 7.1 Hz, 2×SH), 2.58 (4H, d, J 7.1 Hz, CH_2SH), 2.63 (2H, s, C*H*$_2$SCH$_2$CH$_2$Py), 2.96 (2H, d, J 6.8 Hz, C*H*$_2$CH$_2$Py), 3.09 (2H, d, *J* 6.8 Hz, CH$_2$C*H*$_2$Py), 7.14 (1H, m, Py), 7.17 (1H, d, *J* 7.8 Hz, Py), 7.61 (1H, m, Py) and 8.55 (1H, d, *J* 4.8 Hz, Py); *m/z* 274 $(MH)^+$.

$Fe_2(CO)_5(CH_3C(CH_2S)_2CH_2SCH_2CH_2Py)$ (11).

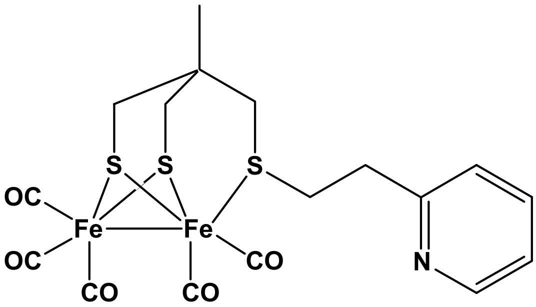

$[Fe_3(CO)_{12}]$ (4.15 g, 8.2 mmol) was dissolved in toluene (100 cm^3) and stirred. 2-Methyl-2-(2-pyridin-2-yl-ethylsulfanylmethyl)-propane-1,3-dithiol (**9**) (2.00 g, 7.3

mmol) was dissolved in dichloromethane and heated at 80°C for 90 min. The dark green mixture turned red brown. The toluene was removed and the compound was purified by flash chromatography under dinitrogen (degassed ethyl acetate) to give a red-brown powder (1.31 g, 34%). The powder was dissolved in acetonitrile (10 cm^3), and slow evaporation of the solvent under a stream of dinitrogen led to the formation of single crystals. (Found C, 38.27; H, 3.27; N, 2.66. $C_{17}H_{17}NO_5S_3Fe_2$, requires C, 39.03; H, 3.27; N, 2.68); ν_{max}/cm^{-1} (CO) 1927, 1983 and 2049 (acetonitrile); δ_H (400 MHz; solvent $CDCl_3$; standard $SiMe_4$) 0.89 (3H, br s, CH_3), 1.62 (2H, br d, *J* 14.0 Hz, CH_2SFe), 2.04 (2H, br s, CH_2SCH_2Py), 2.22 (2H, br d, *J* 14.0 Hz, CH_2SFe), 3.30 (4H, s, CH_2CH_2Py), 7.21 (1H, br s, Py), 7.29 (1H, br s, Py), 7.68 (1H, br s, Py) and 8.57 (1H, br s, Py); *m/z* 523 $(M)^+$, 467 $(M - 2CO)^+$, 439 $(M - 3CO)^+$, 411 $(M - 4CO)^+$, 383 $(M – 5CO)^+$, 176 $(Fe_2S_2)^+$; Mössbauer spectrum (solid, 77 K, referenced to 25 µm Fe-foil at 298 K): two doublets, isomer shifts at 0.025 and 0.105, quadrupole splittings of 1.002 and 0.228 $mm.s^{-1}$.

$CH_3C(CH_2S)_2CH_2SC6H4$-*p*-NO_2,
4-((4-nitrophenylthio)methyl)-4-methyl-1,2-dithiolane (12).

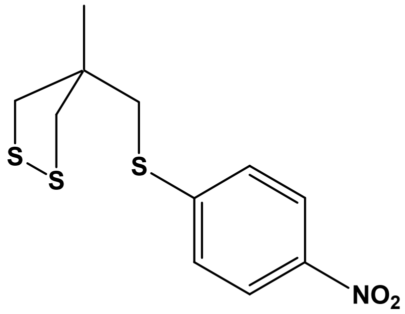

NaH (60% oil suspension, 0.33 g, 8.2 mmol) was washed with hexane and then dissolved in THF (50 cm^3) under a dinitrogen atmosphere. **5** (1.00 g, 6.0 mmol) was dissolved in THF (5 cm^3), added to the solution of NaH and stirred at room temperature. 4-bromo-nitrobenzene (1.49 g, 7.4 mmol) was dissolved in THF (5 cm^3), added to the mixture and stirred at 60°C overnight. Excess sodium hydride was quenched by ammonium chloride-saturated water and the product was extracted with dichloromethane. The organic phase was dried ($MgSO_4$) and purified by flash chromatography (hexane/chloroform 4:1) to give a yellow solid (0.86 g, 3.0 mmol, 50%). (Found C, 45.77; H, 4.59; N, 4.86; S, 32.30. $C_{11}H_{13}NO_2S_3$ requires C, 45.97; H, 4.56; N, 4.87; S, 33.46); δ_H (400 MHz; solvent $CDCl_3$; standard $SiMe_4$) 1.39 (3H, s, CH_3), 2.97 (2H, d, *J* 11.5 Hz, C*H*$_2$SS), 3.17 (2H, d, *J* 11.5 Hz, C*H*$_2$SS), 3.28 (2H, s, C*H*$_2$SPh), 7.41 (2H, d, *J* 8.8 Hz, Ph), 8.13 (2H, d, *J* 9.0 Hz, Ph).

$CH_3C(CH_2SH)_2CH_2SPhNH_2$,

2-((4-aminophenylthio)methyl)-2-methylpropane-1,3-dithiol (13).

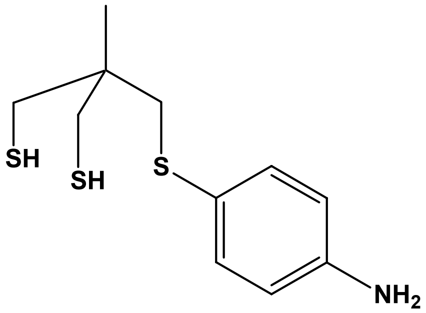

Pd/C (12 mg) and $NaBH_4$ (0.39 g, 10.3 mmol) were suspended in 2M NaOH (20 cm^3). **12** (0.28 g, 0.97 mmol) was added and the mixture stirred at 90°C overnight. The excess of $NaBH_4$ was quenched with 2 M HCl and the solution was neutralised with 2 M NaOH. The compound was then extracted with chloroform, dried over magnesium sulphate and purified by flash chromatography (chloroform/ethyl acetate 1:1) to give a yellow solid (0.24 g, 0.92 mmol, 95%). δ_H (400 MHz; solvent $CDCl_3$; standard $SiMe_4$) 1.04 (3H, s, CH_3), 1.18 (2H, t, *J* 9.0 Hz, 2×SH), 1.54 (2H, s, CC*H*$_2$SPh), 2.61 (4H, d, *J* 9.2 Hz, 2×C*H*$_2$SH), 3.71 (2H, br s, PhN*H*$_2$), 6.61 (2H, d, *J* 8.8 Hz, Ph), 7.26 (2H, d, *J* 8.8 Hz, Ph).

$Fe_2(CO)_5(CH_3C(CH_2S)_2CH_2SPhNO_2)$ (14).

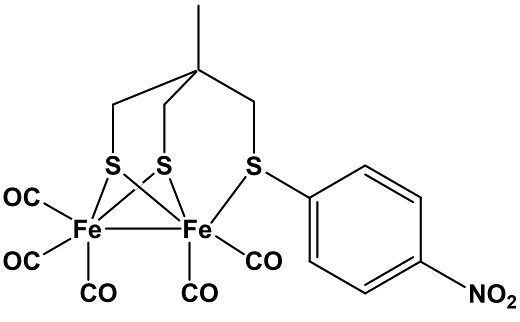

[$Fe_3(CO)_{12}$] (0.97 g, 1.9 mmol) was dissolved in toluene (50 cm^3). **12** (0.46 g, 1.6 mmol) was added to the solution. The dark green mixture turned red brown when it was heated at 90°C for 90 min. The solvent was removed and the compound was purified by flash chromatography under dinitrogen (diethyl ether/hexane 4:1) to give a red-brown powder (0.28 g, 0.52 mmol, 32%). (Found C, 35.74; H, 2.50; N, 2.67; S, 17.84. $Fe_2C_{16}H_{13}S_3O_7N$ requires C, 35.64; H, 2.43; N, 2.60; S, 17.84); ν_{max}/cm^{-1} (CO) 1933, 1988 and 2052 cm^{-1} (acetonitrile); δ_H (400 MHz; solvent $CDCl_3$; standard $SiMe_4$) 0.95 (3H, s, CH_3), 1.74 (2H, d, *J* 13.9 Hz, CH_2SFe), 2.32 (2H, d, *J* 13.9 Hz, CH_2SFe), 2.44 (2H, s, CCH_2SPh), 7.95 (2H, d, *J* 8.8 Hz, Ph), 8.33 (2H, d, *J* 8.8 Hz, Ph).

$Fe_2(CO)_5(CH_3C(CH_2S)_2CH_2SPhNH_2)$ (15).

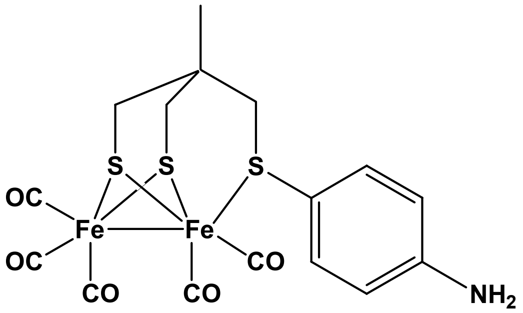

[$Fe_3(CO)_{12}$] (0.56 g, 1.1 mmol) was dissolved in toluene (20 cm^3) and stirred under nitrogen. **13** (0.24 g, 0.92 mmol) was added to the solution. The dark green mixture turned red brown when it was heated at 90°C for 90 min. The solvent was removed and the compound was purified by flash chromatography under dinitrogen (diethyl ether/hexane 1:1) to give a red-brown powder (0.26 g, 0.51 mmol, 55 %). (Found C, 37.76; H, 2.99; N, 2.66; S, 18.94. $Fe_2C_{16}H_{15}S_3O_5N$ requires C, 37.74; H, 2.97; N, 2.75; S, 18.89); ν_{max}/cm^{-1} (CO) 1928, 1983 and 2048 cm^{-1} (acetonitrile); δ_H (400 MHz; solvent $CDCl_3$; standard $SiMe_4$) 0.83 (3H, s, CH_3), 1.66 (2H, d, *J* 13.7 Hz, CH_2SPh), 2.25 (4H, d, *J* 13.4 Hz, 2×CH_2SFe), 3.95 (2H, s, NH_2), 7.95 (2H, d, *J* 8.8 Hz, Ph), 8.33 (2H, d, *J* 8.8 Hz, Ph).

$CH_3C(CH_2S)_2CH_2SCH_2CH_2$Pyrrole, 1-(2-((4-methyl-1,2-dithiolan-4-yl)methylthio)ethyl)pyrrole (18).

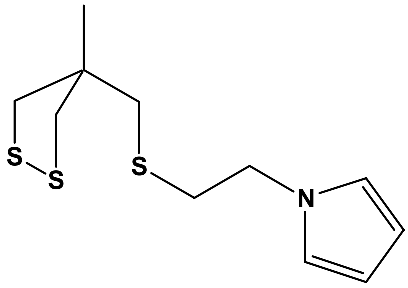

NaH (60% oil suspension, 0.24 g, 6.0 mmol) was washed with hexane and then dissolved in acetonitrile (50 cm^3). **1** (1.29 g, 7.8 mmol) was dissolved in acetonitrile (5 cm^3), added to the solution of NaH and stirred at room temperature. N-pyrrole ethanechloride (1.00 g, 7.8 mmol) was dissolved in acetonitrile (5 cm^3), added to the mixture and stirred at 60°C for 5h. Excess of sodium hydride was quenched by ammonium chloride-saturated water and the product was extracted with dichloromethane. The organic phase was dried ($MgSO_4$) and the solvent removed to give a reddish oily solid (1.50 g, 5.8 mmol, 74%). (Found C, 47.18; H, 6.07. $C_{11}H_{17}S_3N$ requires C, 47.06; H, 6.08); δ_H (400 MHz; solvent $CDCl_3$; standard $SiMe_4$) 1.24 (3H, s, CH_3), 2.56 (2H, s, CCH_2SCH_2), 2.87 (4H, m), 3.04 (2H, d, *J* 11.4 Hz, CH_2SS), 4.07 (2H, t, *J* 6.8, CH_2NPyrrole), 6.14 (2H, d, *J* 2.2 Hz, Pyrrole), 6.67 (2H, d, , *J* 2.2 Hz Pyrrole); *m/z* (EI-MS) 259 $(M)^+$, 165 $(M – CH_2CH_2Pyrrole)^+$.

$CH_3C(CH_2SH)_2CH_2SCH_2CH_2$Pyrrole, 2-((2-pyrrol-1-yl)ethylthio)methyl)-2-methylpropane-1,3-dithiol (19).

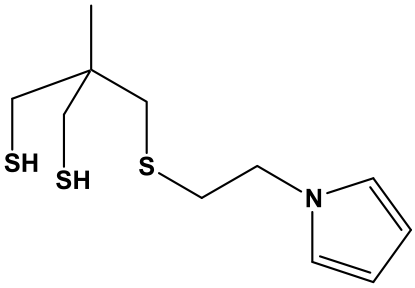

$LiAlH_4$ (0.49 g, 13.0 mmol) was dissolved in diethyl ether (50 cm^3) and cooled with an ice bath. **18** (1.4 g, 5.4 mmol) was dissolved in diethyl ether (50 cm^3) and added drop wise. The mixture was stirred at room temperature overnight. The reaction was then cooled in an ice bath and the excess of $LiAlH_4$ was quenched by degassed water (100 cm^3). A few drops of H_2SO_4 were added, the organic phase became white and it was extracted with diethyl ether until the aqueous phase became clear. The organic phase was dried ($MgSO_4$) and evaporated to give a white oil (1.02 g, 3.9 mmol, 72 %). (Found C, 46.50; H, 6.81. $C_{11}H_{19}S_3N$ requires C, 46.72; H, 6.74); δ_H (400 MHz; solvent $CDCl_3$; standard $SiMe_4$) 0.93 (3H, s, CH_3), 1.18 (2H, t, *J* 9.0 Hz, 2×SH), 2.40 (2H, s, CCH_2SCH_2), 2.49 (4H, d, *J* 9.0 Hz, 2×CH_2SH), 2.77 (2H, t, *J* 7.0 Hz, SCH_2CH_2Pyrrole), 3.99 (2H, t, *J* 7.0 Hz, SCH_2CH_2Pyrrole), 6.08 (2H, d, *J* 2.2 Hz, Pyrrole), 6.61 (2H, d, *J* 2.2 Hz, Pyrrole); *m/z* (EI-MS) 261 $(MH)^+$.

$Fe_2(CO)_5(CH_3C(CH_2S)_2CH_2SCH_2CH_2Pyrrole)$ (21).

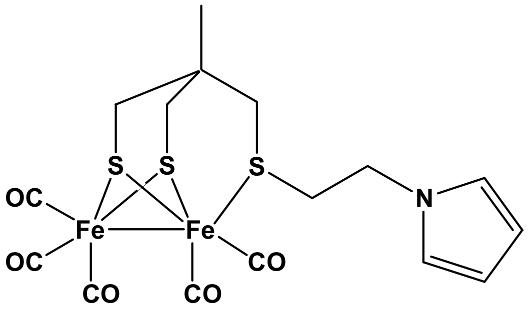

$[Fe_3(CO)_{12}]$ (2.01 g, 4.0 mmol) was dissolved in toluene (50 cm^3). **19** (1.03 g, 3.9 mmol) was added to the solution. The dark green mixture turned red brown when it was heated at 90°C for 2h. The solvent was removed and the compound was purified by flash chromatography under dinitrogen (hexane/ethyl acetate 2:1) to give a red-brown powder (1.18 g, 2.3 mmol, 59%). (Found C, 38.02; H, 3.49; N, 0.73; S, 19.32. $Fe_2C_{16}H_{17}S_3O_5N$ requires C, 37.59; H, 3.35; N, 2.74; S, 18.82); ν_{max}/cm^{-1} (CO) 1926, 1984 and 2049 cm^{-1} (acetonitrile); δ_H (400 MHz; solvent $CDCl_3$; standard $SiMe_4$) 0.67 (3H, s, CH_3), 1.50 (4H, d, *J* 13.9 Hz, 2×CH_2SFe), 2.04 (2H, d, *J* 14.2 Hz, CCH_2SCH_2), 3.14 (2H, t, *J* 6.1 Hz, SCH_2CH_2Pyrrole), 4.27 (2H, t, *J* 6.3 Hz, SCH_2CH_2Pyrrole), 6.13 (2H, d, *J* 2.0 Hz, Pyrrole), 6.68 (2H, d, *J* 1.9 Hz, Pyrrole) ; *m/z* (EI-MS) 511 $(MH)^+$, 455 $(M - 2CO)^+$, 399 $(M - 4CO)^+$, 371 $(M - 5CO)^+$.

$CH_3C(CH_2S)_2CH_2SCH_2CH_2OH$,

2-((4-methyl-1,2-dithiolan-4-yl)methylthio)ethanol (16).

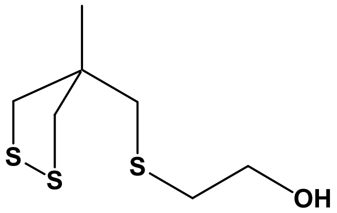

NaH (60% oil suspension, 0.24 g, 6.0 mmol) was washed with hexane and then dissolved in THF (50 cm^3). **5** (0.77 g, 4.6 mmol) was dissolved in THF (5 cm^3), added to the solution of NaH and stirred at room temperature. Iodoethanol (0.79 g, 4.6 mmol) was dissolved in THF (5 cm^3), added to the mixture and stirred at room temperature for 2h. Excess of sodium hydride was quenched by ammonium chloride-saturated water and the product was extracted with diethyl ether. The organic phase was dried ($MgSO_4$) and the solvent removed to give a yellow oil (0.82 g, 3.9 mmol, 84%). δ_H (400 MHz; solvent $CDCl_3$; standard $SiMe_4$) 1.32 (3H, s, CH_3), 2.07 (1H, t, *J* 6.1 Hz, CH_2OH), 2.79 (4H, m, CCH_2SCH_2), 2.91 (2H, d, *J* 11.2 Hz, CCH_2SS), 3.13 (2H, d, *J* 11.5 Hz, CCH_2SS), 3.75 (2H, q, *J* 5.6/6.1, CH_2CH_2OH).

$CH_3C(CH_2SH)_2CH_2SCH_2CH_2OH$ (17).

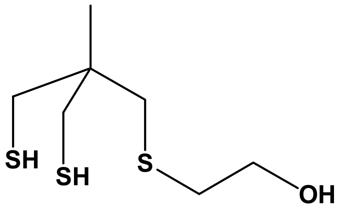

To an ice-cooled suspension of $LiAiH_4$ (0.42 g, 11 mmol) in dry THF (30 cm^3) was drop-wise added a solution of **16** (0.59 g, 2.8 mmol). After the addition, the mixture was warmed up to room temperature. The reaction was heated at 40°C overnight. To the cooled mixture was very carefully dropwise added degassed water (20 cm^3). After the mixture was stirred for about half an hour, dilute sulphuric acid (0.5 M, 40 cm^3) was added. The mixture was stirred for one hour before it was extracted with degassed ethyl acetate, dried with $MgSO_4$ and was purified by column chromatography (ethyl acetate/hexane 2:3)to give a colourless oil (0.37 g, 1.8 mmol, 63%). δ_H (400 MHz; solvent $CDCl_3$; standard $SiMe_4$) 1.30 (3H, t, *J* 9.0 Hz, CH_3), 2.15 (1H, t, OH), 2.62 (2H, d, *J* 8.8 Hz), 2.62 (2H, d, *J* 8.8 Hz,), 2.68 (2H, s, CCH_2SCH_2), 2.76 (8H, t, *J* 5.9 Hz), 3.75 (2H, qd, *J* 5.6 Hz), 3.81 (2H, s).

$Fe_2(CO)_5(CH_3C(CH_2S)_2CH_2SCH_2CH_2OH)$ (20).

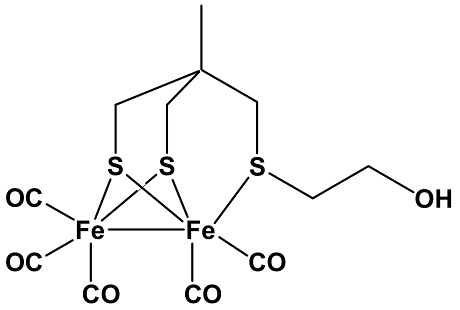

$[Fe_3(CO)_{12}]$ (1.95 g, 3.9 mmol) was dissolved in toluene (50 cm^3). **17** (0.82 g, 3.9 mmol) was added to the solution. The dark green mixture turned red brown when it was heated at 90°C for 3h. The solvent was removed and the compound was purified by flash chromatography under dinitrogen (hexane/ethyl acetate 3:1) to give a red-brown powder (0.90 g, 2.0 mmol, 50%). (Found C, 31.27; H, 3.13; S, 19.92. $Fe_2C_{12}H_{14}S_3O_6$ requires C, 31.19; H, 3.05; S, 20.81); ν_{max}/cm^{-1} (CO) 1926, 1983 and 2048 cm^{-1} (acetonitrile); δ_H (400 MHz; solvent $CDCl_3$; standard $SiMe_4$) 0.84 (s, 3H, CH_3), 1.57 (2H, d, *J* 13.9 Hz, CH_2SFe), 1.74 (1H, t, *J* 5.2 Hz, CH_2OH), 2.10 (2H, s, CCH_2SCH_2), 2.16 (2H, d, *J* 13.9Hz, CH_2SFe), 3.02 (2H, t, *J* 5.6 Hz, CH_2CH_2OH), 4.00 (2H, q, *J* 5.5 Hz, CH_2CH_2OH).

$Fe_4(CO)_8(CH_3C(CH_2S)_2)_2$.

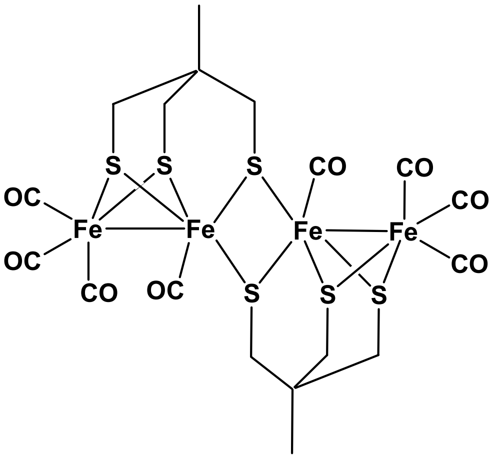

$Fe_3(CO)_{12}$ (3.0 g, 5.9 mmol) was dissolved in toluene (50 cm^3) and stirred. 1,1,1-tris(mercaptomethyl)ethane (**4**) (1.0 g, 5.9 mmol) was added and heated at 80°C for 2 h. After removing solvent, the solid was purified by flash chromatography (diethyl ether and then dichloromethane) to give a dark brown solid (0.27 g, 0.3 mmol, 10%). ν_{max}/cm^{-1} (CO) 2046, 1988 and 1947 cm^{-1} (dichloromethane); δ_H (400 MHz; solvent $CDCl_3$; standard $SiMe_4$) 0.94 (s, 6H, 2×CH_3), 1.16 (2H, d, *J* 14.2 Hz, 2×C*H*SFe), 1.59 (2H, d, *J* 14.2 Hz, 2×C*H*SFe), 1.97 (2H, d, *J* 13.9 Hz, 2×C*H*SFe), 2.13 (2H, d, *J* 13.2 Hz, 2×C*H*SFe), 2.77 (2H, d, *J* 13.7 Hz, 2×C*H*SFe), 3.54 (2H, d, *J* 13.7 Hz, 2×C*H*SFe).

- Chapter III -

Electrochemistry and proton reduction by {2Fe3S}-complexes

The ability of [Fe]-hydrogenase to function as a proton reducing / dihydrogen oxidising catalyst makes chemical models very attractive in term of electrocatalysis for reversible hydrogen fuel cells.[21,94]

Electrochemical methods can be used as a probe of molecular orbital energy levels of the metal centre. Indeed, reduction potential is directly connected to the LUMO (lowest unoccupied molecular orbital) whereas the HOMO (highest occupied molecular orbital) is related to the oxidation potential.[95-97] The effect of substituting one ligand for another on the redox potential can also give a valuable insight into electronic effects.[98] In addition, electrochemistry can provide an insight into the detailed mechanism of electron-transfer chemistry and pertinent to this study information on the capacity of metallo-systems to electrocatalyse proton reduction.[99]

III.1 Electrochemical behaviour of the {2Fe3S}-complexes

III.1.a General Features

Figure **III-1** shows a typical cyclic voltammogram of an $[Fe_2(CO)_5\{CH_3C(CH_2S)_2CH_2SR\}]$ complex. At room temperature, the voltammogram shows a partially reversible reduction (E_p = -1.25 V *vs.* Ag/AgCl) which gives rise to a major product oxidation peak detected at E_p = -0.96 V and a smaller product peak at E_p = -0.69 V. The voltammetry is simplified at low temperature (*ca.* -40°C). A fully reversible system is observed with i_p^{ox} / i_p^{red} close to unity. The difference in the peak current between the two temperatures is due to the decrease in the diffusion coefficient of the complex.

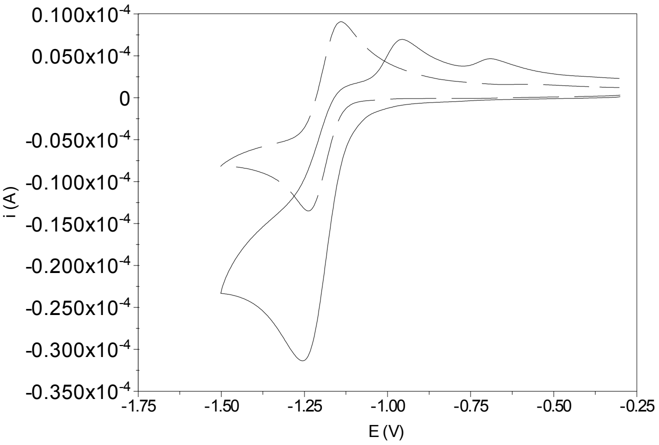

Figure III-1. Cyclic voltammogram of [$Fe_2(CO)_5\{CH_3C(CH_2S)_2CH_2SCH_2CH_2$-*N*-Pyrrole}] (**21**) (3 mM, 0.2 M [NBu_4][BF_4] in acetonitrile, 0.1 V.s^{-1}). A partially reversible process is observed at 20ºC (plain line) and becomes reversible (dashed line) at -40ºC.

The reduction process is diffusion-controlled as is evident from the linear relationship between the peak current and the square root of the scan-rate (Figure **III-2**).

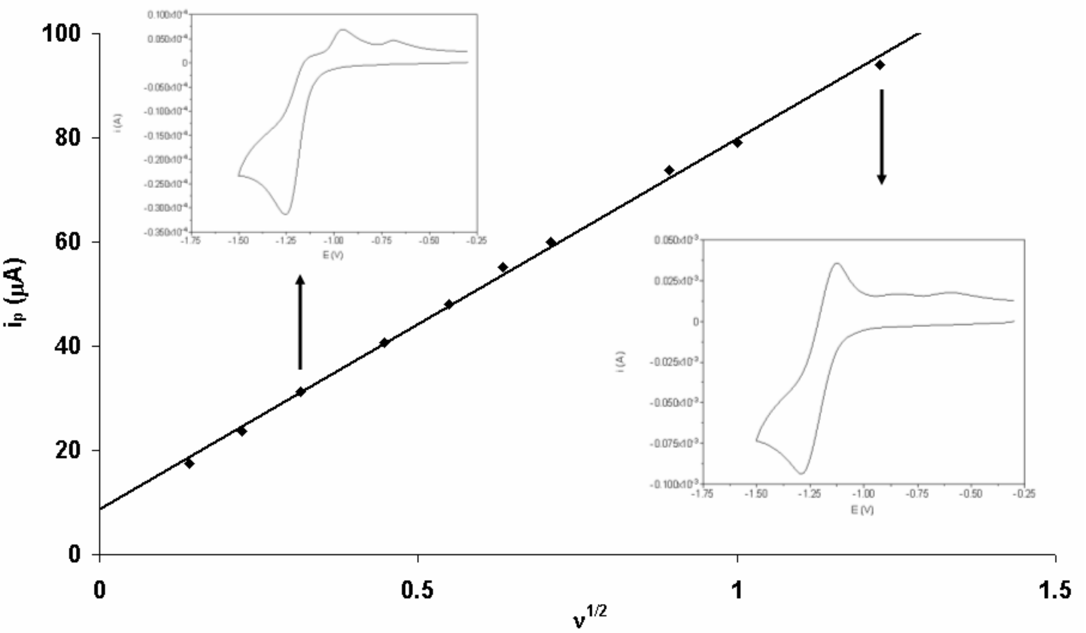

Figure III-2. Diffusion-controlled process of the primary reduction of [$Fe_2(CO)_5\{CH_3C(CH_2S)_2CH_2SCH_2CH_2$-*N*-Pyrrole}] (**21**) ($v^{½}$ *vs.* i_p) (R = 0.9979). Insets show the cyclic voltammograms at 0.1 (left) and 1.5 V.s^{-1} (right).

The increase in reversibility of the system at higher scan-rates is shown by Figure **III-3** (top) and the plot of i_p^{ox} / i_p^{red} (bottom).

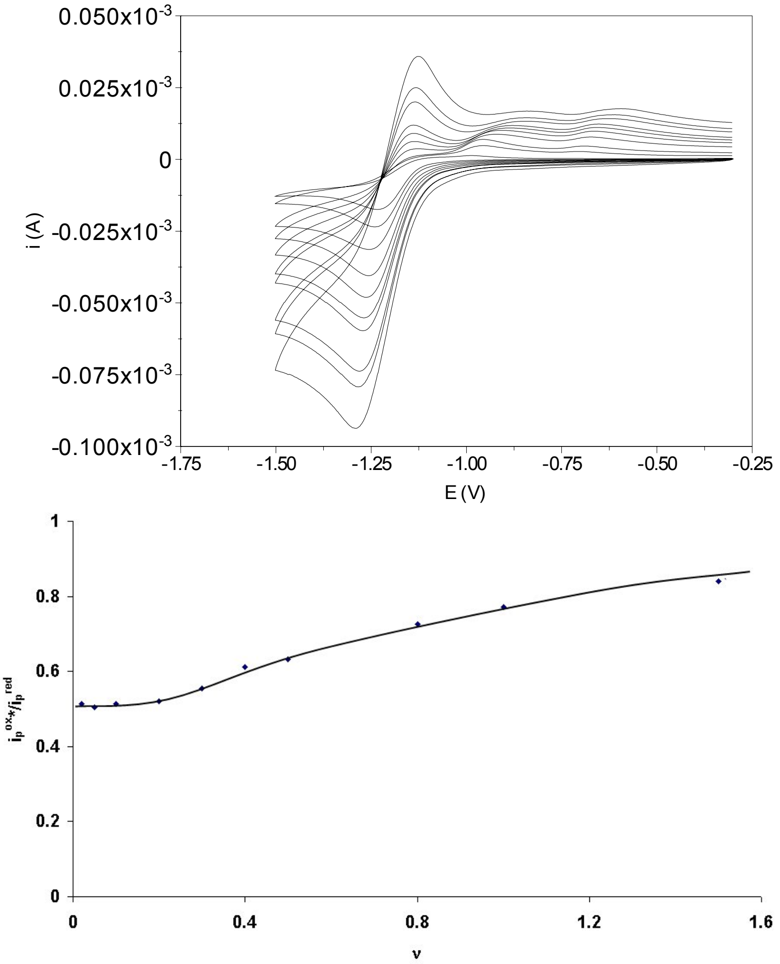

Figure III-3. Scan rate dependence of $[Fe_2(CO)_5\{CH_3C(CH_2S)_2CH_2SCH_2CH_2$-*N*-Pyrrole$\}]$ ($v = 0.02$ to $1.5\ V.s^{-1}$) (top). Plot of i_p^{ox} (0 measured at -1.35 V) / i_p^{red} *versus* v (bottom).

The variation in reversibility does not lead to a deviation in the linearity of the peak current function $i_{p\ corrected}^{red}/v^{1/2}$ *versus* v plot (Figure **III-4**). From this it can be concluded that although there is chemistry following the electron-transfer step this does not lead to a change in the electron-stoichiometry. The separation in the peak potentials $|E_p^{ox} - E_p^{red}| = \Delta E_p$ at the lower scan-rates, where the iR drop is less important, is close to 110 mV. Theoretically, for a fast reversible one-electron system at 298K ΔE_p is close to 60mV and for a corresponding two electron system *ca.* 30 mV.[100] We find that for ferrocene recorded under similar conditions ΔE_p = 117 mV (i_p^{ox} = 38 μA) whilst [$Fe_2(CO)_5\{CH_3C(CH_2S)_2CH_2SCH_2CH_2$-*N*-pyrrole}] has ΔE_p = 124 mV (i_p^{ox} = 48 μA). Thus, we conclude that the primary electron-transfer reaction is a single electron transfer.

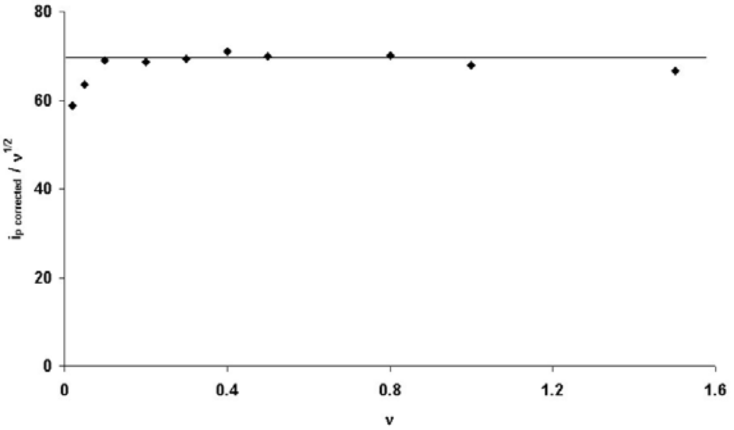

Figure III-4. Plot of $i_{p\ corrected}/v^{½}$ *versus* v where $i_{p\ corrected} = i_p - i_{p\ (v\ =\ 0)}$.

The chemistry following the single-electron reduction gives rise to the detection of two oxidation peaks in the voltammetry of each of the complexes. We have not investigated in detail the nature of this following chemistry. However, it is clear that a single electron transfer must generate a 37-electron product, with either the electron going to the metal-metal σ*-antibonding orbital or into the "electron-poor" $Fe(CO)_3$ centre. The addition of an anion to the {2Fe3S}-systems is known to lead to the cleavage of the Fe-$S_{thioether}$ bond by an associative mechanism involving attack on the distal iron.[65] It is possible that electron-addition to the {2Fe3S}-complex also results in cleavage of this bond to give a 18-electron / 17-electron Fe(I) / Fe(0) species. This anion may give rise to the first of the two detectable oxidation waves.

The electrochemical behaviour of all of the {2Fe3S}-complexes is essentially identical to the [$Fe_2(CO)_5\{CH_3C(CH_2S)_2CH_2SCH_2CH_2$-*N*-pyrrole}] (**21**) complex discussed in detail above.

III.1.b Relationship between redox potentials and structure

Table **III-1** shows data of the {2Fe3S}-complexes and {2Fe2S}-complex ([$Fe_2(CO)_6$(pdt)]). As reported earlier, substitution of a CO by an SMe ligand makes the di-iron unit harder to reduce by some 140 mV. This is due to the donor character of the thioether ligand which increases the electronic density on the proximal iron compared to CO ligand (π-acceptor).

Compound	E_p^{red} **(V)**	**Reference**
[$Fe_2(CO)_6\{SCH_2CH_2CH_2S\}$]	-1.12	[86]
[$Fe_2(CO)_5\{CH_3C(CH_2S)_2CH_2SCH_3\}$] (23)	-1.26	[63]
[$Fe_2(CO)_5\{CH_3C(CH_2S)_2CH_2SCH_2Py\}$] (10)	-1.24	This work
[$Fe_2(CO)_5\{CH_3C(CH_2S)_2CH_2SCH_2CH_2Py\}$] (11)	-1.26	This work
[$Fe_2(CO)_5\{CH_3C(CH_2S)_2CH_2SC_6H_4\text{-}p\text{-}NO_2\}$] (14)	-1.21	This work
[$Fe_2(CO)_5\{CH_3C(CH_2S)_2CH_2SC_6H_4\text{-}p\text{-}NH_2\}$] (15)	-1.25	This work
[$Fe_2(CO)_5\{CH_3C(CH_2S)_2CH_2SCH_2CH_2$-*N*-Pyrrole}] (21)	-1.25	This work
[$Fe_2(CO)_5\{CH_3C(CH_2S)_2CH_2SCH_2CH_2OH\}$] (20)	-1.27	This work

Table III-1. Primary redox potentials of {2Fe3S}-complexes in acetonitrile (vs. Ag/AgCl, CH_2Cl_2, 0.45 M [NBu_4][BF_4], 0.05 M [NBu_4]Cl).

Comparing the range of new synthetic {2Fe3S}-systems shown in Table **III.1**, we can see that there is only a minimal effect on the reduction potential as the nature of the thioether group is varied (10-20 mV). The exception is the nitrobenzene complex and it will be discussed below. The small effect of substituents on redox potentials is parallel to the infra-red and crystallographic data.

III.2 Electrocatalytic reduction of protons

III.2.a General aspects of electrocatalysis

The electrocatalysis mechanism (called EC' mechanism) can be summarised as:

$$O + ne^- \rightleftharpoons R$$

$$R + Z \longrightarrow O + Y$$

The catalytic process occurs as the reduced species *R* reacts with a substrate molecule *Z* oxidising back the starting material *O* and releasing a non-electroactive species *Y*. In a cyclic voltammetry experiment, electrocatalysis is characterised by an enhancement of the current as the regeneration of *O* permits its re-reduction to *R* and so on. The size of the catalytic current depends on the quantity of the substrate present in solution and on the rate of the reaction between *R* and *Z* (Scheme **III-1**).

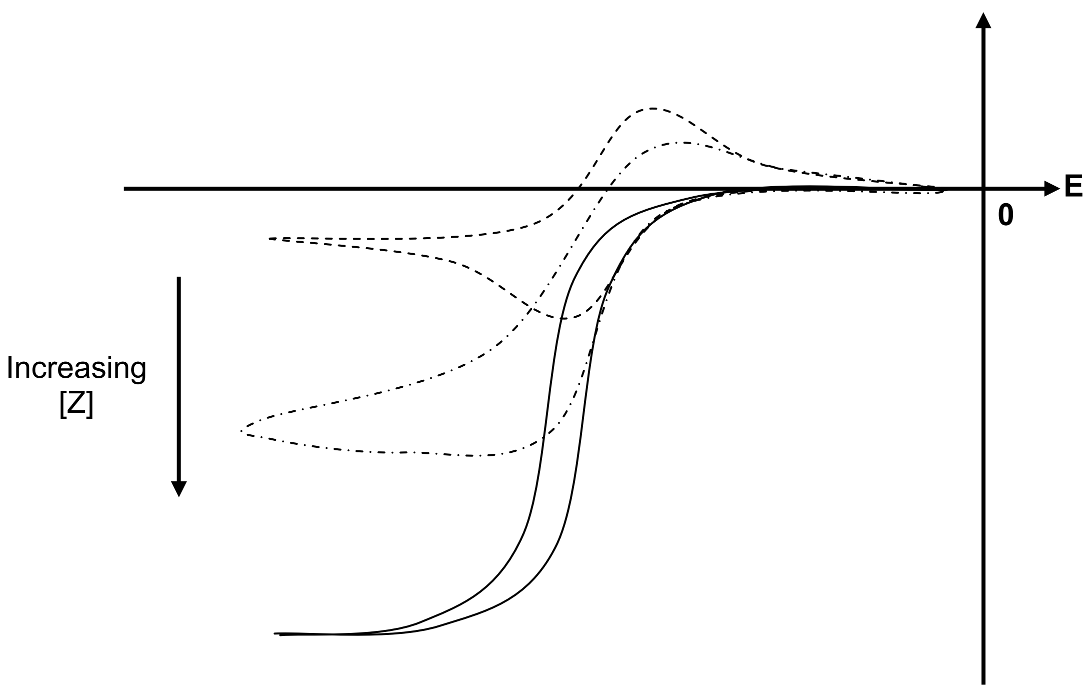

Scheme III-1. Typical cyclic voltammogram for an EC' process. No substrate (— —), [Z] increases (— - — - and —).

Here we discuss the electrochemistry of the {2Fe3S}-systems in the presence of protons and show that they are capable of electrocatalysis. We used 2,6-lutidinium tetrafluoroborate as the source of protons. Direct reduction of 2,6-lutidinium on vitreous carbon electrode occurs at E_p = -1.33 V as shown in Figure **III-5**.

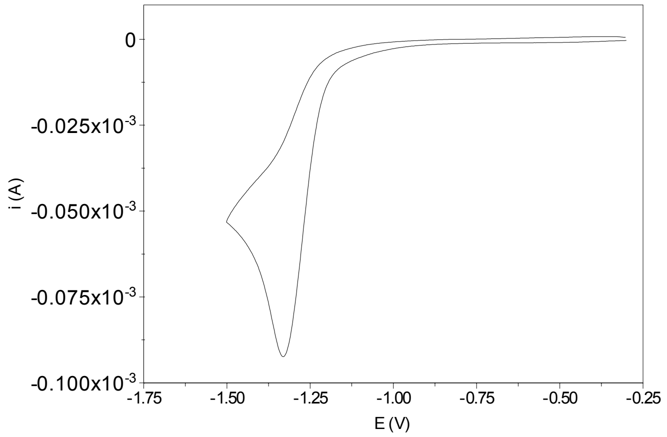

Figure III-5. Cyclic voltammogram of 2,6-lutidinium tetrafluoroborate (0.4 M, 0.2 M $[NBu_4][BF_4]$ in acetonitrile, 0.1 V.s^{-1}).

III.2.b {2Fe3S}-pyridine derivatives 10 and 11

Two pyridine-derivative complexes have been synthesised and fully characterised (see **II.2**). In both cases, the heterocycle is not coordinated to the metal centre. The protonation site presented by the pyridine offers the possibility of facilitating the proton transfer to the di-iron subsite during the catalytic turnover.

Both complexes show a similar electrochemical behaviour in acetonitrile with a partially reversible one-electron reduction occurring at E_p = -1.24 V (methyl-derivative) and E_p = -1.26 V (ethyl-derivative) (Figure **III-6**).

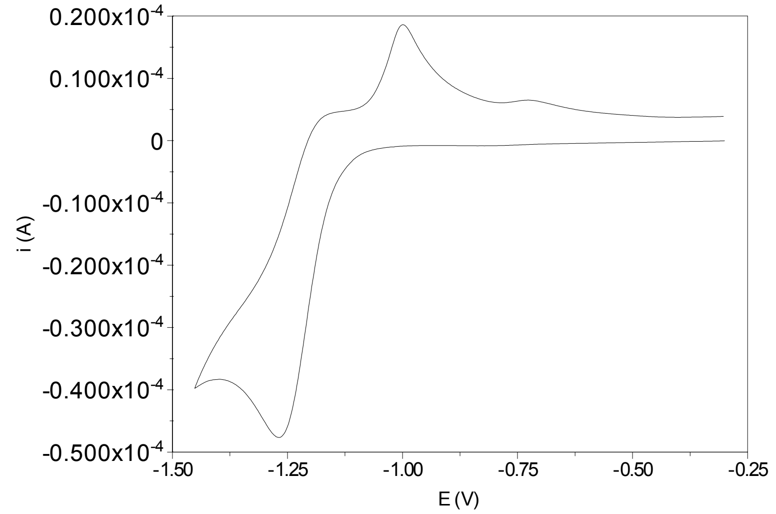

Figure III-6. Cyclic voltammogram of [$Fe_2(CO)_5\{CH_3C(CH_2S)_2CH_2SCH_2CH_2$-2-Py}] (**11**) (3 mM, 0.2 M [NBu_4][BF_4] in acetonitrile, 0.1 V.s^{-1}).

Addition of acid (2,6-lutidinium) to the complex in solution shows an increase of the current density response at the same potential where the irreversible reduction process occurs (E_p = -1.31 V). This can be attributed to the catalytic production of dihydrogen by the complex, which consumes more electrons than required for a normal electron-transfer and explains the large increase in the current (Figure **III-7**). The behaviour of this and related {2Fe3S}-systems in the presence of acid is complicated by adsorption and this is discussed further below. Cyclic voltammograms shown are for first-scans at freshly polished electrodes.

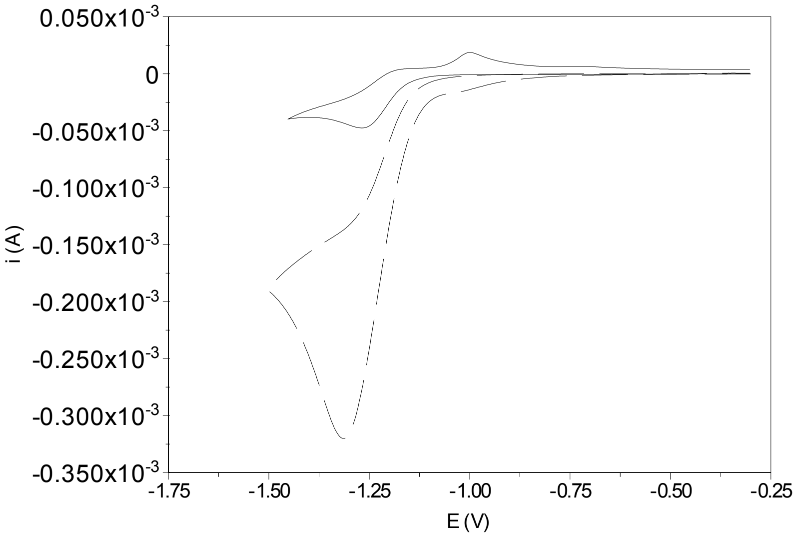

Figure III-7. Cyclic voltammogram of [$Fe_2(CO)_5\{CH_3C(CH_2S)_2CH_2SCH_2CH_2$-2-Py}] (3 mM, 0.2 M [$NBu_4$][$BF_4$] in acetonitrile, 0.1 V.s^{-1}) in the absence (—) and in the presence of 10 equivalents of 2,6-lutidinium (——).

Despite the small positive shift in potential observed compared with the acid alone in solution (+ 20 mV), the current response is more than three times greater in the presence of the complex (Figure **III-8**). The $i_{p\ max}$ value for 2,6-lutidinium on vitreous carbon alone occurs at E_p = -1.33 V (i = -93 μA). The identical current magnitude in the presence of the catalyst occurs at E_p = -1.18 V. At this potential the current in the absence of catalyst is ten times smaller the in the presence of the catalyst.

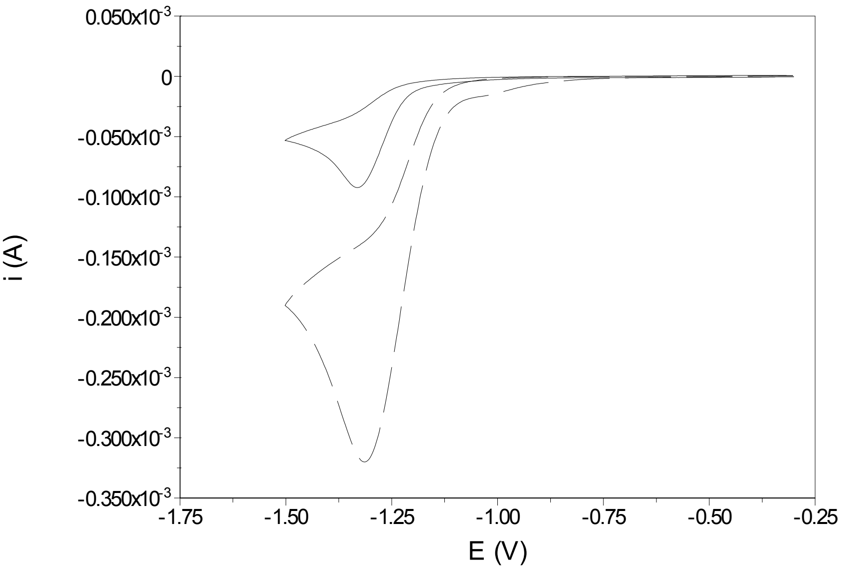

Figure III-8. Cyclic voltammogram of 2,6-lutidinium (30 mM) in the absence (—) and in the presence (— —) of [$Fe_2(CO)_5\{CH_3C(CH_2S)_2CH_2SCH_2CH_2$-2-Py}] (3 mM, 0.2 M [$NBu_4$][$BF_4$] in acetonitrile, 0.1 V.s^{-1}).

III.2.c {2Fe3S}-aniline derivative 15

Cyclic voltammetry of the aniline-derivative shows a similar behaviour to the pyridine complexes with a partially reversible one-electron process at E_p = -1.25 V, and the detection in the backward scan of two oxidative processes (Figure **III-9**).

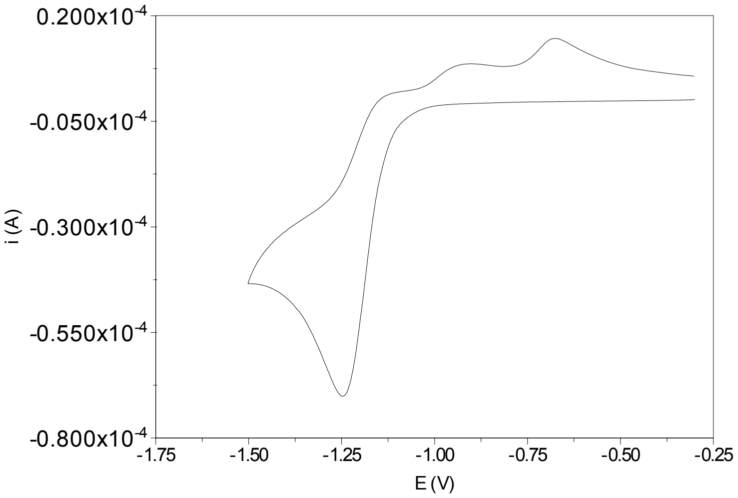

Figure III-9. Cyclic voltammogram of [$Fe_2(CO)_5\{CH_3C(CH_2S)_2CH_2SC_6H_4$-*p*-$NH_2$}] (**15**) (7 mM, 0.2 M [NBu_4][BF_4] in acetonitrile, 0.1 V.s^{-1}).

Under acidic conditions (2,6-lutidinium), the cyclic voltammogram shows a characteristic increase in the current density as the concentration of acid is increasing confirming the catalytic behaviour of our {2Fe3S}-complex for dihydrogen evolution (Figure **III-10**).

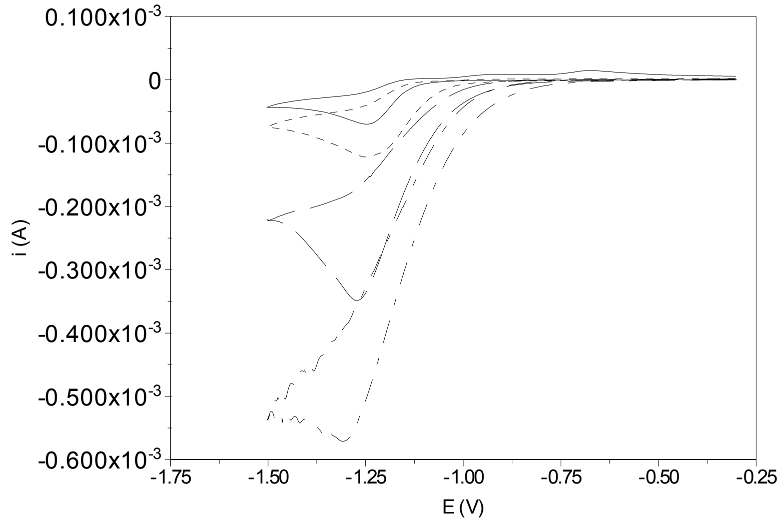

Figure III-10. Cyclic voltammogram of [$Fe_2(CO)_5\{CH_3C(CH_2S)_2CH_2SC_6H_4$-*p*-$NH_2\}$] (**15**) (7 mM, 0.2 M [NBu_4][BF_4] in acetonitrile, 0.1 V.s^{-1}) in absence of acid (—) and in presence of 1 (– – –), 5 (———) and 10 equivalents (— - — -) of 2,6-lutidinium.

Nevertheless, no improvement toward more positive potentials is observed and the proton reduction potential is at the same potential as the irreversible reduction of the complex in the absence of protons, showing that the di-iron centre has to be reduced first to accept one proton. The protonated complex can then be reduced a second time and then evolves dihydrogen.

These experiments correlated with observations carried out on the {2Fe3S}-pyridine complexes but do not provide more information about the actual proton reduction mechanism. The protonation site as well as the redox states and structural rearrangements, cannot be determined and further investigations will be needed to unravel this electrochemical process.

III.3 {2Fe3S}-nitrobenzene derivative 14

III.3.a Electrochemical studies

The nitrobenzene complex **14** shows a primary reversible reduction at $E_{½}$ = -0.85 V followed by a partially reversible process at E_p = -1.21 V (Figure **III-11**). This second system is rather similar to previous complexes, but the high reversibility of the primary electron-transfer step and its positive value is quite unlike the behaviour of the other {2Fe3S}-systems. For this reason we suspected that the primary reduction process was ligand centred on the nitrobenzene group.

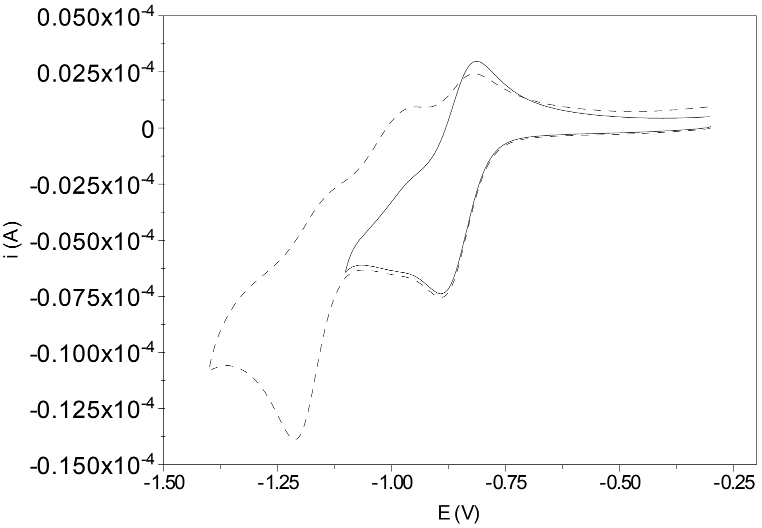

Figure III-11. Cyclic voltammogram of [$Fe_2(CO)_5\{CH_3C(CH_2S)_2CH_2SC_6H_4$-*p*-$NO_2\}$] (**14**) (2 mM, 0.2 M [NBu_4][BF_4] in acetonitrile, 0.1 V.s^{-1}).

Reversible one-electron reduction of nitrobenzene to give the radical anion in dry solvents is well established. Figure **III-11** shows the electrochemical response of nitrobenzene under the same conditions as recorded for the complex. The well-defined reversible one-electron reduction is evident at $E_{½}$ = -1.03 V. It occurs at a potential slightly more negative than the free ligand **12** (disulfide form) at $E_{½}$ = -0.98 V as is expected with an electropositive sulfur atom substituent in the *para*-position. The reduction of the nitrobenzene group is further shifted to a more positive potential

($E_{½}$ = -0.85 V) when the thioether is coordinated to the electron-withdrawing di-iron centre (**14**). We therefore conclude that the primary reduction of the complex is associated with the nitrobenzene group.

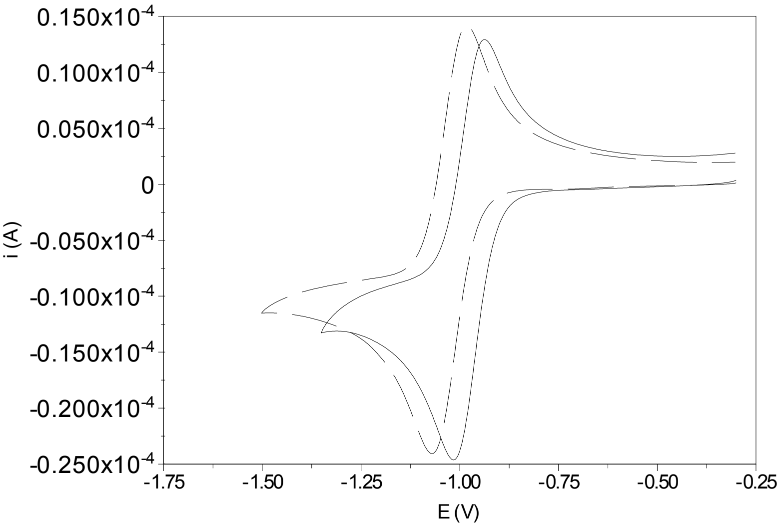

Figure III-12. Cyclic voltammogram of (— —) nitrobenzene (2 mM) and (—) $CH_3C(CH_2S)_2CH_2S(C_6H_4$-*p*-$NO_2)$ (**12**) (2 mM) (0.2 M $[NBu_4][BF_4]$ in acetonitrile, 0.1 V.s^{-1}).

A rather similar compound has been prepared by L. Sun and coworkers, $[Fe_2(CO)_6\{(\mu\text{-}SCH_2)_2N(C_6H_4\text{-}p\text{-}NO_2)\}]$, and the electrochemistry in the absence and in the presence of a proton source was reported (Figure **III-13**).[101] They observed a similar behaviour for the electrochemistry and proposed the assignation of that primary reduction to the couple [Fe(I)Fe(I)(N) / Fe(I)Fe(0)(N)], with N as the nitrogen of the bridging dithiolate ligand. In the light of our experiments, we suggest that the primary reversible reduction of $[Fe_2(CO)_6\{(\mu\text{-}SCH_2)_2N(C_6H_4\text{-}p\text{-}NO_2)\}]$ is not metal based.

Sun et al furthermore suggested that in the presence of acid, the primary reduction of their complex is shifted to more positive values because the [Fe(I)Fe(I)(NH) / Fe(I)Fe(0)(NH)] system is generated and this is followed by a second reduction to form dihydrogen. They argued that the introduction of nitrogen in the bridging dithiolate ligand may change the electrocatalytic process for proton reduction and that the presence of the nitrobenzene withdrawing group displaces the reduction potential to more positive values as the di-iron centre is easily reduced.

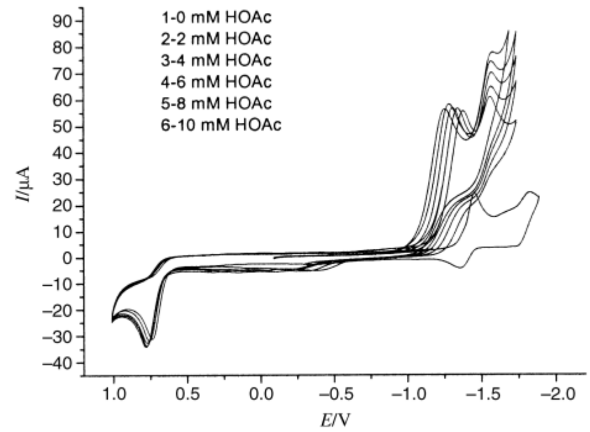

Figure III-13. Cyclic voltammogram of $[Fe_2(CO)_6\{(\mu\text{-}SCH_2)_2N(C_6H_4\text{-}p\text{-}NO_2)\}]$ (1.0 mmol) with HOAc (0-10 mmol) (*vs.* Ag/Ag^+) (taken from ref [101]).

We therefore examined the electrochemical behaviour of both our {2Fe3S}-complex and nitrobenzene in the presence of acetic acid.

The primary reduction of nitrobenzene in the presence of acetic acid becomes irreversible and is shifted to more positive potentials as the concentration of acid is increased as is expected with fast following chemistry (Figure **III-14**).

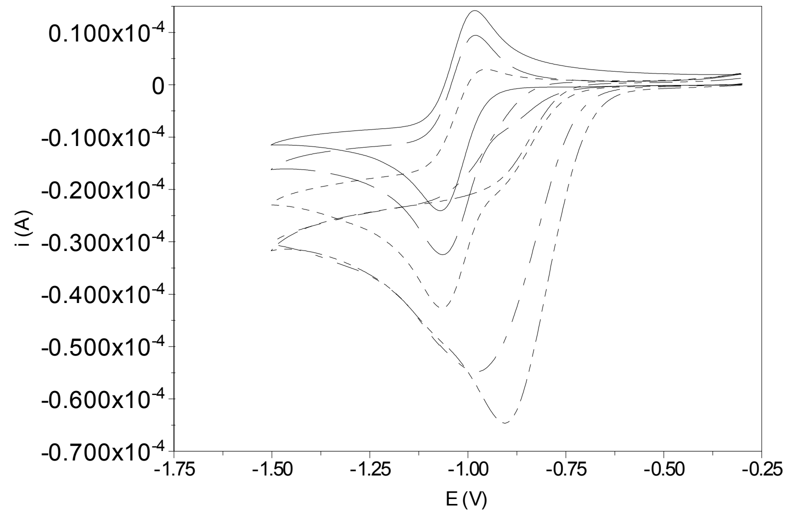

Figure III-14. Cyclic voltammogram of nitrobenzene (2 mM) in the absence and in the presence of acetic acid: 0 (—), 1 (— —), 5 (---), 15 (– - – -) and 30 equivalents (— - - —) (0.2 M $[NBu_4][BF_4]$ in acetonitrile, 0.1 V.s^{-1}).

This behaviour is directly paralleled by the electrochemistry of the {2Fe3S}-complex **14** under the same conditions (Figure **III-15**). The current response as a function of the acid concentration reaches a limit of about 2-3 times the peak current in the absence of acid.

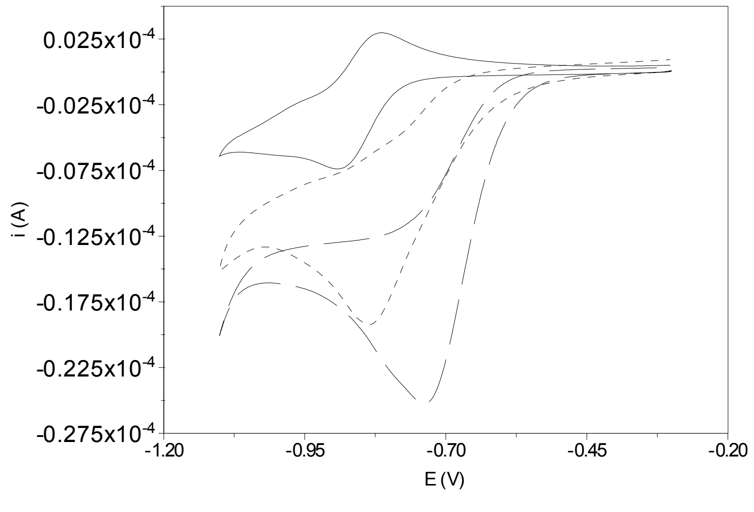

Figure III-15. Cyclic voltammogram of $[Fe_2(CO)_5\{CH_3C(CH_2S)_2CH_2SC_6H_4\text{-}p\text{-}NO_2\}]$ (**14**) (2 mM, 0.2 M $[NBu_4][BF_4]$ in acetonitrile, 0.1 V.s^{-1}) in the absence (—) and in the presence of acetic acid: (----) 1 equivalent; (— —) 10 equivalents.

Again we can see that the electrocatalytic reduction of protons as proposed by Sun et al (Figure **III-13**) is unlikely and their observations are better explained by proton-dependent reduction of the appended nitro group rather than of a hydride intermediate.

A plausible explanation would be that in the absence of protons, this process corresponds to the reduction of $Ph\text{-}NO_2 + e^- \rightarrow PhNO_2^-$. In the presence of a proton source, the current increases nearly three-fold compared to that in the absence of acid, implying a multi-electron process. The fate of a nitrobenzene radical anion in the presence of acid can include the formation of a nitroso species, which itself can undergo further reductive chemistry.[102]

In order to probe the mechanism of reduction of the {2Fe3S}-complex further, we carried out FTIR-spectroelectrochemical studies.

III.3.b Spectroelectrochemical studies

Infra-red spectroelectrochemistry (IR-SEC) was used as the nitro group has characteristic bands and therefore reduction and structural changes can be monitored by this technique.[103]

Experiments were carried out in acetonitrile and dichloromethane. In either solvent, the primary reduction of **14** at *ca.* -1.0 V gives rise to two species detected in the time-resolved difference FTIR spectra. In CH_2Cl_2, the first transient species is more stable and at short times well resolved spectra are obtained (Figure **III-16**).

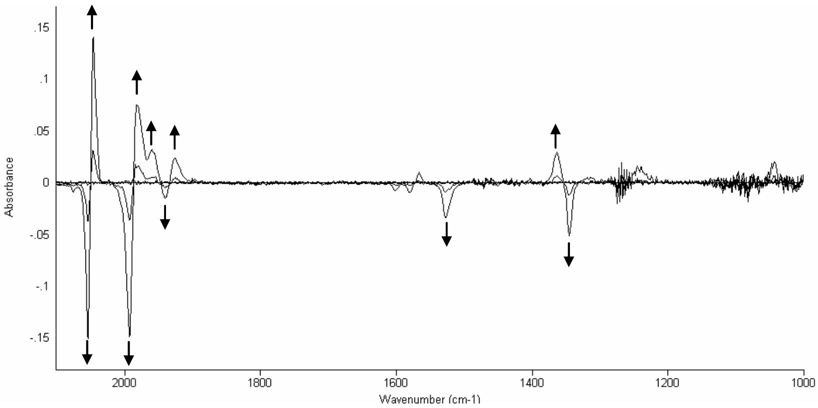

Figure III-16. IR-SEC of [$Fe_2(CO)_5\{CH_3C(CH_2S)_2CH_2SC_6H_4$-*p*-$NO_2\}$] (**14**) in CH_2Cl_2 under Ar (40 psi); potential applied: -1.0 V (*vs.* Ag wire); timeframe: 0 to 11 s.

In this spectrum, the two nitro bands (ν_{NO_2} = 1528, 1345 cm^{-1}) are depleted and a new band appears (1362 cm^{-1}). Correspondingly the terminal carbonyl bands (2054, 1991 and 1938 cm^{-1}) are depleted and new bands (2054, 2046, 1985, 1962 and 1929 cm^{-1}) are observed. The CO frequencies are slightly shifted down (*ca.* -8 cm^{-1}) showing that the di-iron centre has not been directly involved in the first reduction process but is affected by the modification of the nitrobenzene group. We therefore assigned the primary reduction to the generation of a thioether ligated radical anion.

On a longer time-scale further reduction takes place. Carbonyl frequencies are shifted to considerably lower values indicative of a process involving the di-iron centre (Figure **III-17**).

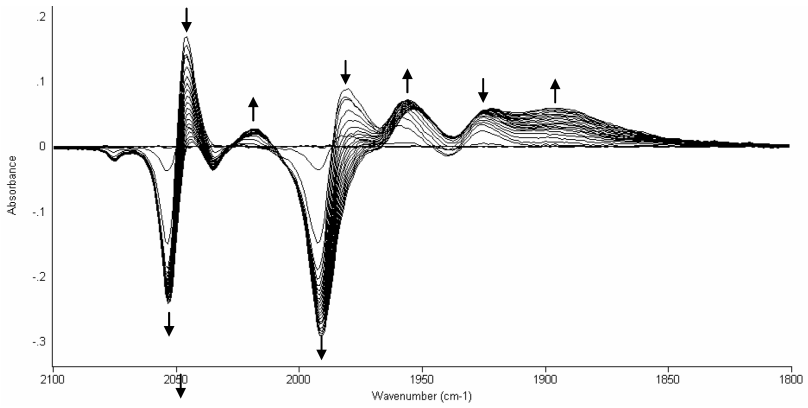

Figure III-17. IR-SEC of $[Fe_2(CO)_5\{CH_3C(CH_2S)_2CH_2SC_6H_4\text{-}p\text{-}NO_2\}]$ (**14**) in CH_2Cl_2 under Ar (40 psi); potential applied: -1.0 V (*vs.* Ag wire); timeframe: 0 to 60 s.

It is possible that the slow chemistry following the initial reduction (Scheme **III-3, Step 1**) leads to decoordination of the thioether group and subsequent reduction of the coordinatively unsaturated di-iron centre (Scheme **III-3, Step 2 and 3**). Considering the potential applied to generate these species, the direct electrochemical reduction of the di-iron centre is quite unfavourable. Therefore, we could envisage that an electron transfer from the nitrobenzene occurs, followed by the re-reduction of the nitro group. The resulting di-iron centre would therefore be 37-electrons (18e-19e). This unfavourable situation might be stabilised by the cleavage of a 2-electron donor ligand. The decoordination of the thioether ligand is the most plausible possibility and would leave the metal centre 35-electrons (18e-17e), a much more favourable situation.

A closer examination of the cyclic voltammogram shown in Figure **III-11**, shows evidence for the generation of an electroactive product at a potential slightly more negative than the primary process. This might be associated with thioether decoordination and intramolecular electron transfer. Consistent with this, the following reduction occurs near -1.0 V (*vs.* Ag/AgCl), a potential close to that for the free ligand.

In the presence of protons (2,6-lutidinium), the IR-SEC shows two weak bands appearing at 1492 and 1378 cm^{-1} (Figure **III-18**). The proton consumption in the reduction process is confirmed by the depletion of the 2,6-lutidinium bands replaced by 2,6-lutidine (between 1550 and 1650 cm^{-1}).

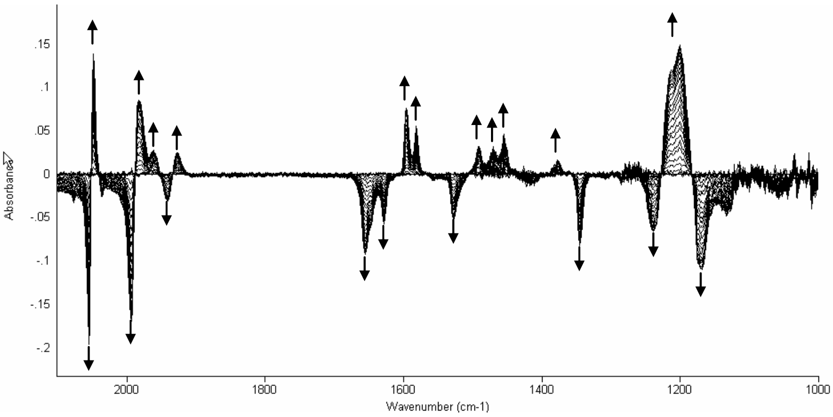

Figure III-18. IR-SEC of [$Fe_2(CO)_5\{CH_3C(CH_2S)_2CH_2SC_6H_4$-*p*-$NO_2\}$] (**14**) in presence of 2,6-lutidinium (TsO$^-$ as counter-cation) in CH_2Cl_2 under Ar (40 psi); potential applied: -0.9 V (*vs.* Ag wire); timeframe: 0 to 40 s.

Time profile bands (at ν = 1981, 1925 and 1376 cm^{-1}) share the same time dependence and this is consistent with them being due to a single species (Figure **III-19**).

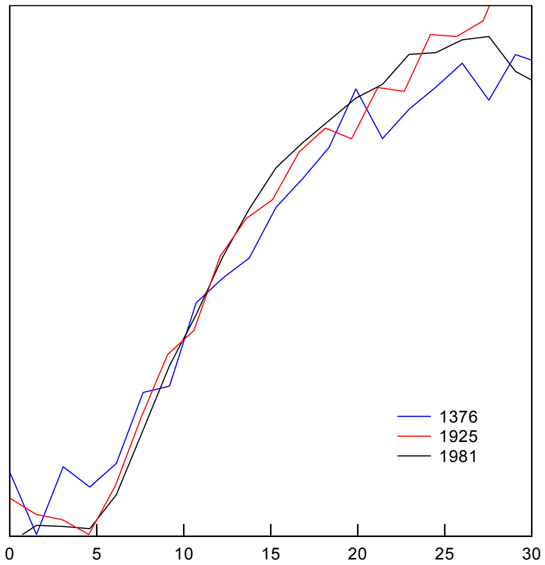

Figure III-19. Normalised time profile of infra-red bands of the IR-SEC from Figure **III.18**.

para-substituted nitrosobenzene derivatives show two main characteristic bands in solution at 1500-1520 and 1350-1380 cm^{-1}, although it has been the subject of some debate as to whether these are for the monomeric or dimeric form of the compound.[104,105]

However, the carbonyl bands shift to lower frequencies and this is rather surprising considering the strong withdrawing character of the nitroso group (Hammett σ = 0.91). The weak bands we see at 1492 and 1378 cm^{-1} may be associated with the formation of a nitroso group. The small shift in the carbonyl stretching frequencies to lower values and an infrared pattern characteristic of ligated thioether is more consistent with further reduction of the nitroso group to a more donating moiety. It is known that the reduction of nitroaromatic species can be quite complex and lead to a variety of products. This is best illustrated by the data of Steudel *et al* who have shown that it is possible to observe the nitrosobenzene radical anion under flow conditions but the fate of this species is quite diverse (Scheme **III-2**).[102] Notably, nitrosobenzene is easier to reduce than the nitrobenzene group ($E_{½\ \text{nitrosobenzene}} \approx$ -0.8 V [102] and $E_{½\ \text{nitrobenzene}} \approx$ -1.0 V $^{\text{this work}}$ *vs.* Ag/AgCl).[102]

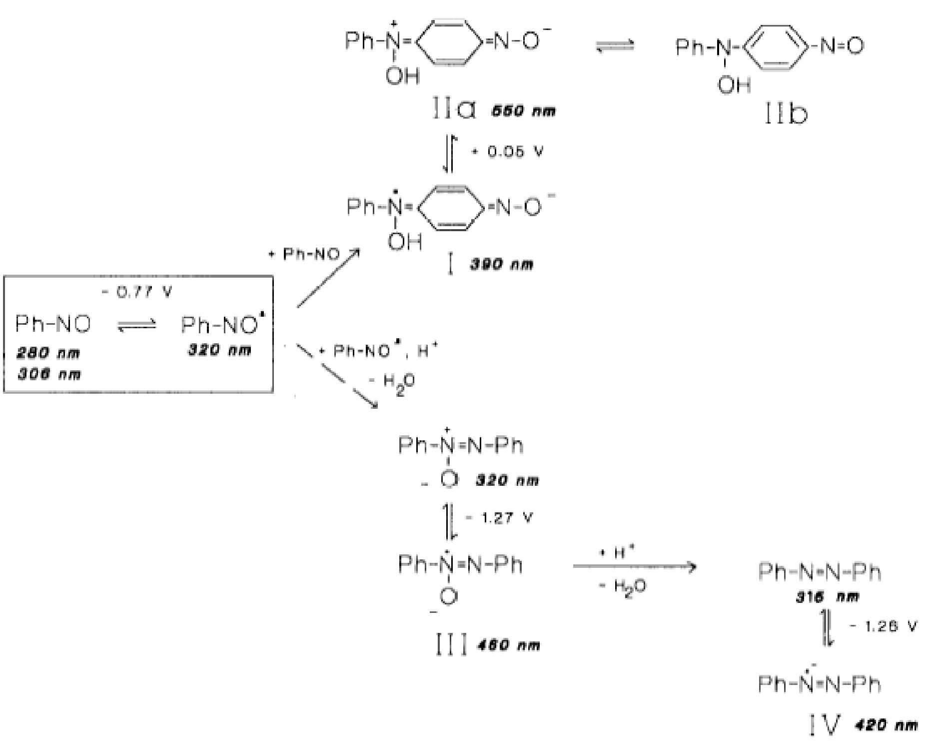

Scheme III-2. Schematic representation of the reaction mechanism after nitrosobenzene reduction (potentials quoted are *versus* Ag/AgCl) (taken from reference [102]).

In presence of CO (40 psi), the starting material is predominantly the hexacarbonyl complex $[Fe_2(CO)_6\{CH_3C(CH_2S)_2CH_2SC_6H_4\text{-}p\text{-}NO_2\}]$, as described in the previous chapter. Upon reduction in presence of the same acid (2,6-lutidinium), we observed the formation of a pentacarbonyl species (Figure **III-20**). This is without any doubt due to the more electron-releasing character of the reduced group formed in the *para*-position compared to the nitro substituent, which allows re-coordination of the thioether ligand with CO displacement following the reduction (Scheme **III-3, Step 4**). As discussed above for the reduction in presence of protons and in the absence of CO, possible reduced groups include hydroxylamide or other functions illustrated in Scheme **III-2**.

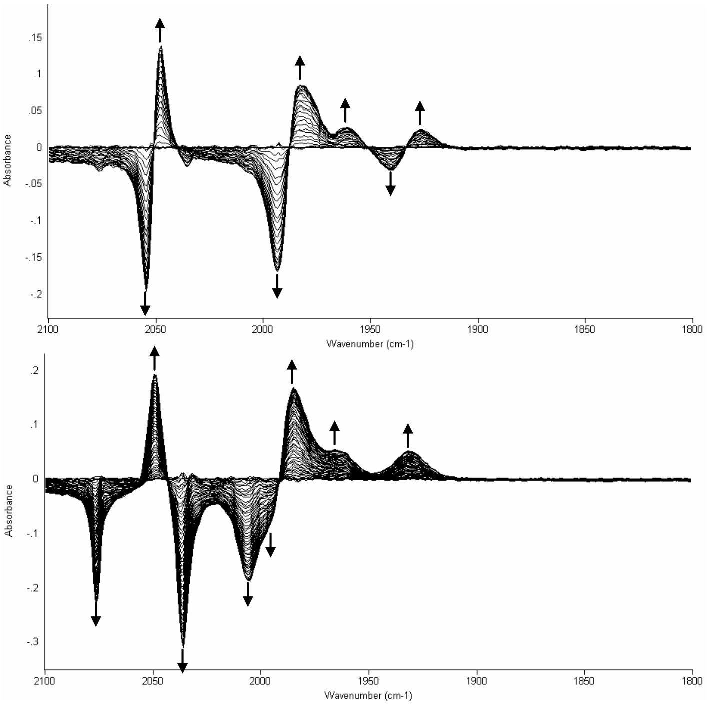

Figure III-20. IR-SEC of $[Fe_2(CO)_5\{CH_3C(CH_2S)_2CH_2SC_6H_4\text{-}p\text{-}NO_2\}]$ (**14**) in presence of 2,6-lutidinium in CH_2Cl_2; under Ar (40 psi) (top); under CO (40 psi) (bottom).

These observations are summarised in Scheme **III-3**. This system provides a tuneable system where electronic properties of the pendant ligand can be switched to electron-withdrawing / releasing and therefore allows the study of the electronic interaction between the metal centre and the thioether ligand. UV-vis-SEC studies as well as EPR measurements will be carried out to unravel the interesting chemistry of this complex.

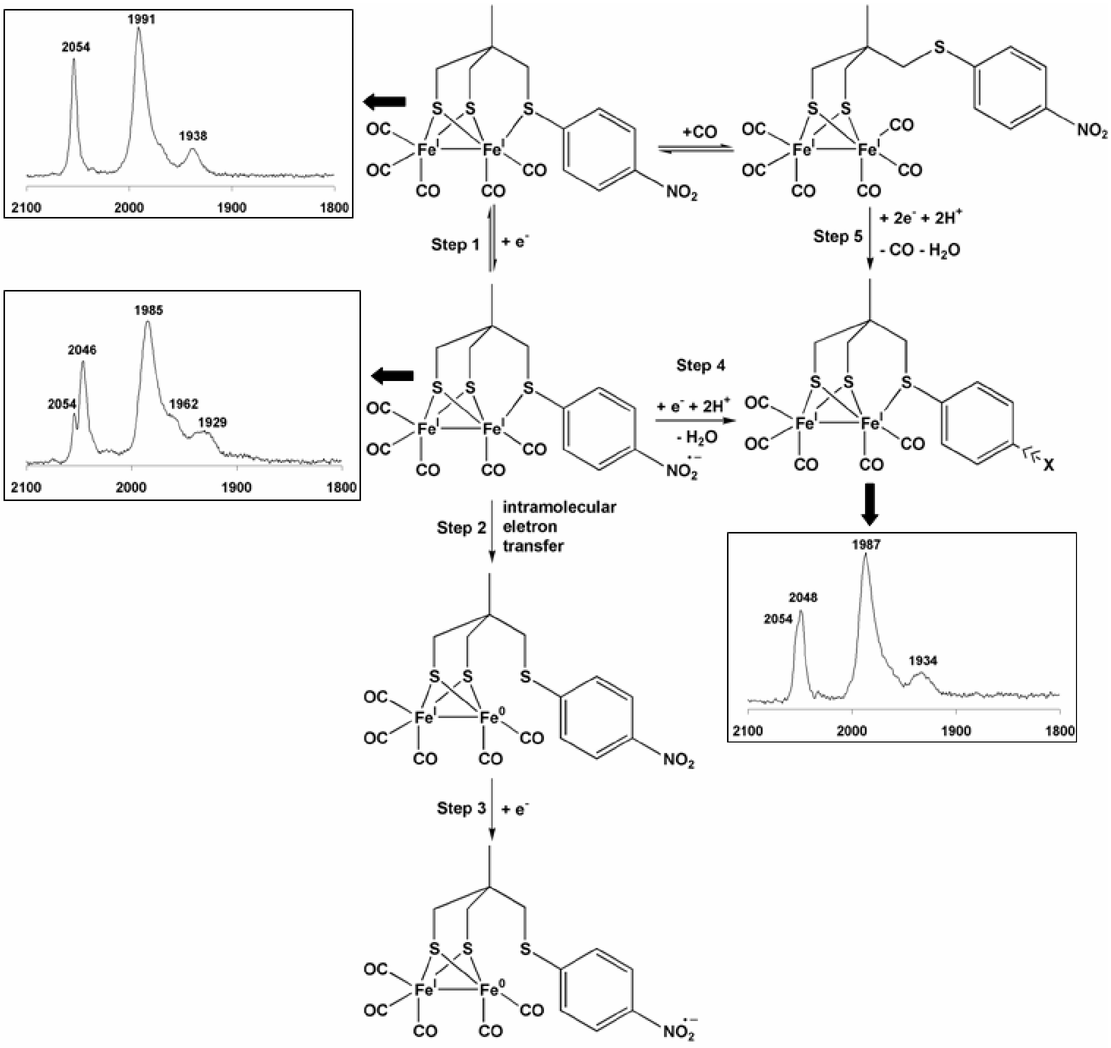

Scheme III-3. Schematic representation of the electrochemical behaviour of [$Fe_2(CO)_5\{CH_3C(CH_2S)_2CH_2SC_6H_4$-*p*-$NO_2\}$] (**14**) (the **X** group represents an electron-donating moiety).

III.4 Electrocatalysis of hydrogen evolution by the mixed-valence tetra-iron complex (22)

As described previously (see **II.5**) the formal oxidation state of the irons reached in [$Fe_2(CO)_4(CH_3C(CH_2S)_3]_2$ (**22**) can be considered as Fe(I)-Fe(II)-Fe(II)-Fe(I) and electronic similarities with the natural “H-cluster” have been also outlined as two {2Fe3S}-subunits fused by two bridging thiolates.

Higher oxidation states of di-iron centres are very interesting to prepare because a decrease in the electronic density would make the bi-metallic subunit easier to be reduced. As observed in the previous section, all the first reduction potentials of {2Fe3S}-complexes are restricted to potentials between -1.21 and -1.27 V (*vs.* Ag/AgCl). It is therefore reasonable to expect a shift toward more positive values of this first reduction wave for that higher oxidation state compound.

The cyclic voltammetry of the tetranuclear complex showed two successive one-electron reductions at $E_{½}$ = -0.70 (reversible) and -1.07 V (quasi-reversible) (*vs.* Ag/AgCl) (Figure **III-21**). A further irreversible one-electron reduction is also observed near -2.0 V.

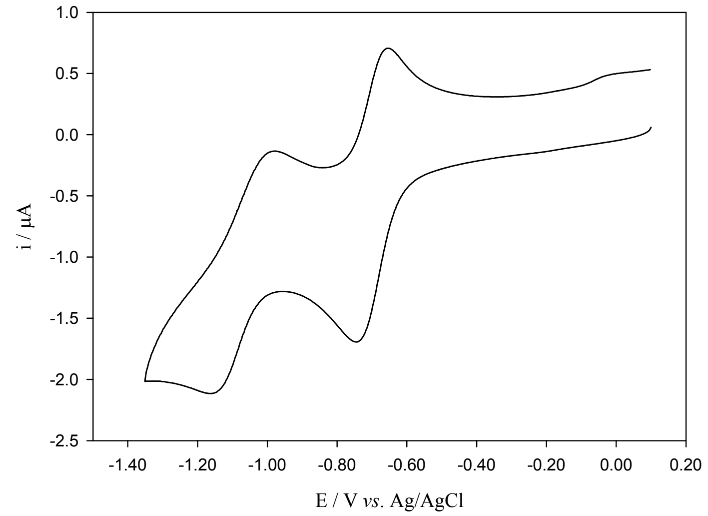

Figure III-21. Cyclic voltammogram of $[Fe_2(CO)_4(CH_3C(CH_2S)_3]_2$ (**22**) (1.5 mM, 0.5 M $[NBu_4][BF_4]$ in dichloromethane, 0.1 $V.s^{-1}$).

The large ΔE_p (175 mV) of the second quasi-reversible process corresponds to a slow electron-transfer and is indicative of structural or spin-state reorganisation accompanying the electron-transfer. Considering this observation, a cleavage of the central metal-metal bond after the second reduction would conserve the 18-electron configuration for each iron in the Fe(I)-Fe(I)-Fe(I)-Fe(I) assembly.

An increase in the current density is observed in the presence of acid (2,6-lutidinium) characteristic, as previously described, of the catalytic production of dihydrogen (Figure **III-22**). The formation of dihydrogen was confirmed by bulk electrolysis (-1.5 V) and gas chromatography of the head space. After the passage of 9 F.mole^{-1} hydrogen was formed with a current yield of 85 ± 5%. This reaction occurred by accessing the di-anionic Fe(I)-Fe(I)-Fe(I)-Fe(I) level. However acid also affects the primary one-electron reduction process (Figure **III-22, inset**).

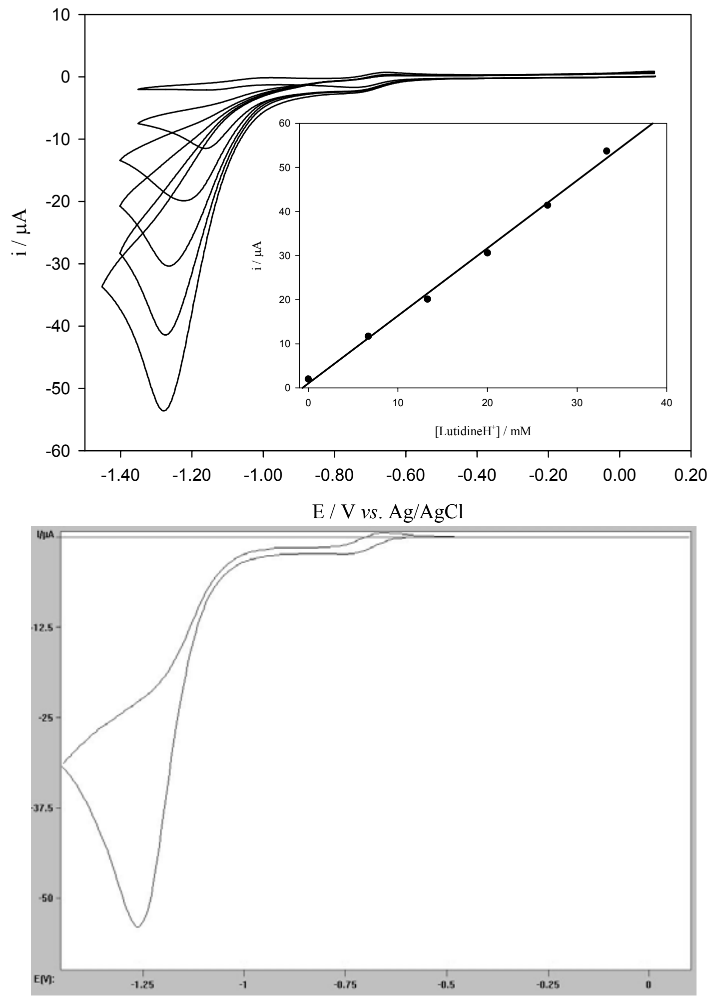

Figure III-22. (top) Cyclic voltammetry of $[Fe_2(CO)_4(CH_3C(CH_2S)_3]_2$ (**22**) (1.5 mM) in the presence of 2,6-lutidinium (0.5 M $[NBu_4][BF_4]$ in dichloromethane, 0.1 V.s^{-1}); (bottom) simulated cyclic voltammogram of $[Fe_2(CO)_4(CH_3C(CH_2S)_3]_2$ (1.5 mM) in the presence of 2,6-lutidinium (33 mM).

Thus, in the presence of acid, the first electron-transfer becomes partially reversible with a concomitant two-fold increase in the current, indicative of the formation of intermediate protonated species and this may provide slow electrocatalysis of proton reduction at a modest potential, near -0.75 V. Support for this comes from simulation of the cyclic voltammetry which is consistent with the mechanistic scheme for reduction of $[Fe_2(CO)_4(CH_3C(CH_2S)_3]_2$ as summarize by Scheme **III-4**.

This synthetic electrocatalyst is energetically inefficient with respect to the potential, where the reaction occurs at a fast rate ($E_p \approx -1.3$ V) and this overpotential is far below that for proton reduction on platinum under the same conditions ($E_p \approx -0.7$ V). That we have some evidence for slow electrocatalysis by this mixed-valence species at $E_p \approx -0.75$ V is intriguing.

A detailed spectroscopic study involving EPR and FTIR-SEC would provide useful information for a more complete understanding of this system.

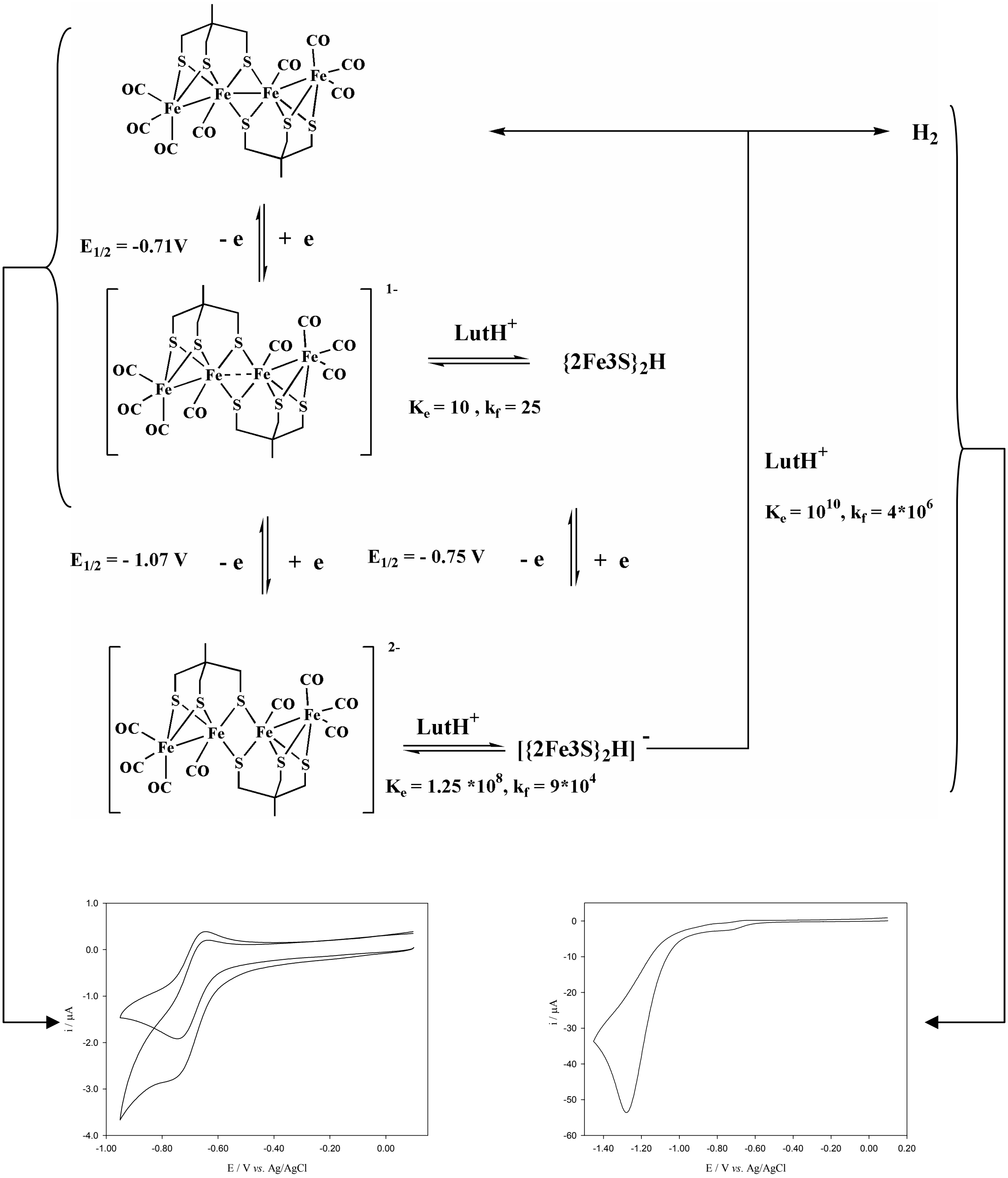

Scheme III-4. Mechanism for hydrogen evolution electrocatalysed by $[Fe_2(CO)_4(CH_3C(CH_2S)_3]_2$ (**22**). The equilibrium constants K_e (dimensionless) and the forward rate constants k_f ($mol^{-1}.L.s^{-1}$) were determined by digital simulation (Digisim 3.03a). The left-insert shows the experimental CV (1.5 mM, 0.1 $V.s^{-1}$) before and after addition of 2,6-lutidinium (33 mM); the right insert shows the overall response in the presence of the acid.

III.5 Surface deposition of a catalytic material

Experiments carried out with Dr. X. Liu in the lab showed an interesting surface behaviour of these pyridine-derivative complexes in the presence of protons, which could then be generalised to all {2Fe3S}-complexes but not to simple {2Fe2S}-systems.

A positive shift is observed after exposing the compound to acid (2,6-lutidinium) and to a repetitive slow scanning (10 mV.s^{-1}) between -0.3 and -1.5 V. The current density increases, showing that a catalytic process occurs at the electrode corresponding to the catalytic proton reduction into dihydrogen at a relatively positive potential considering {2Fe2S}- and {2Fe3S}-systems (Figure **III-23**). The second redox process corresponds to the {2Fe3S}-complex remaining in solution.

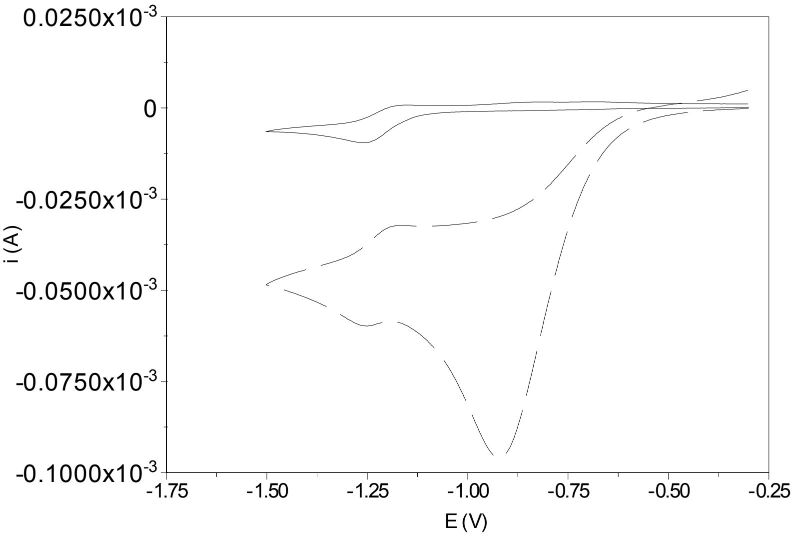

Figure III-23. Cyclic voltammogram of [$Fe_2(CO)_5\{CH_3C(CH_2S)_2CH_2SCH_2CH_2$-2-Py}] (**11**) (3 mM, 0.2 M [NBu_4][BF_4] in acetonitrile, 0.1 V.s^{-1}) in the absence (—) and after slow scanning in the presence of 10 equivalents of 2,6-lutidinium (——).

This positive shift can be cancelled by polishing the electrode (with 0.3 µm alumina particles on polishing cloth), proving the formation of a solid material catalyst on the electrode surface by a reductive mechanism. The coating was examined by scanning electron microscopy (SEM) (Figure **III-24**). An irregular deposition of a surface bound material is evident. The morphology may be a result of shrinking after solvent loss, but the characteristics are not unlike those observed for electrodeposited poly(pyrrole).

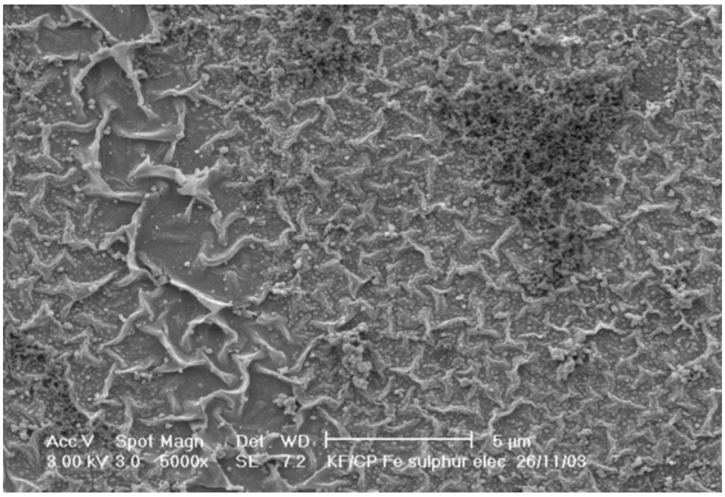

Figure III-24. Scanning electron microscopy image of the coated glassy carbon electrode (obtained by electrochemical reduction of {2Fe3S}-complex).

Reflectance infrared spectroscopy of the coated surface did not show any carbonyl bands in the region 2100-1700 cm^{-1}, and attempts to evaluate the ratio Fe/S in that material by energy dispersive X-ray analysis (EDX) or X-ray photoelectron spectroscopy (XPS) showed the presence of iron and sulfur but the Fe/S ratios varied widely. Although the nature of the coating and its uniformity are ill-defined, there is clearly an interesting electrocatalytic behaviour that requires further investigation.

- Chapter IV -

Synthesis of the “H-cluster” Framework

The major challenge following on from the work done on {2Fe3S}-subsite model complexes is now to build a free-standing analogue of the entire “H-cluster”. This type of assembly would provide an insight into the interplay between the di-iron centre and the iron-sulfur cubane, as well as provide a structural model to understand the enzymatic catalytic machinery.

This chapter describes work towards this goal and reports the synthesis, spectroscopic and electrochemical studies of an assembly which possesses the ‘Fe_6S_{10}’ framework of the “H-cluster”.

IV.1 {Fe_4S_4}-cluster and the trithiol ligand

As we described in previous chapters, the chemistry involved in the synthesis of this type of model complex will be based on the functionalisation of our “classic” tripodal thiol ligand.

Therefore, first attempts were carried out to link the trithiol ligand to an {Fe_4S_4}-cubane type cluster. We have seen that iron-sulfur chemistry has been well developed during the last 30 years and a large range of different clusters is available (see **I.6**). {Fe_4S_4}-clusters with mercaptan ligands on irons of the cubane are easily synthesisable, and introduction of new ligands is just done by exchanging present ligands with other organic thiols.[106]

Because of the high coordinating power of mercaptans with {Fe_4S_4}-clusters, we decided not to use the trithiol ligand directly, because of the possibility of multiple substitutions and polymerisation, but instead used its disulfide protected form (**5**). Experiments were carried out with Dr. S. Ibrahim by reacting the protected disulfide with $[Fe_4S_4(SR)_4][NBu_4]_2$ (R = Et or Ph), and led to the desired $[Fe_4S_4(CH_3C(CH_2S)_3)_4][NBu_4]_2$ characterised by ES-MS and electrochemistry (Scheme **IV-1**).

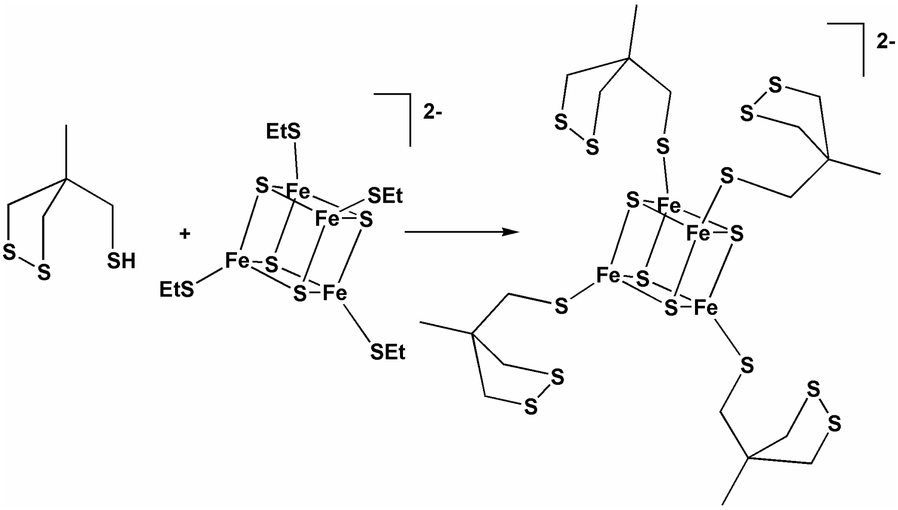

Scheme IV-4. Synthesis of $[Fe_4S_4(CH_3C(CH_2S)_3)_4][NBu_4]_2$.

As direct reduction of this disulfide is not possible, again because of potential polymerisation problems, we tried to react $[Fe_3(CO)_{12}]$ with the cluster synthesised, an approach we have successfully used for synthesis of the *p*-nitrobenzene derivative (see **II.3.b**). Unfortunately, monitoring these reactions by FTIR gave no evidence for an introduction of the di-iron motif on one or several disulfide ligands despite several attempts under a variety of conditions.

IV.2 $[Fe_2(CO)_6(CH_3C(CH_2S)_2CH_2SCOCH_3)]$: an activated di-iron subsite

The reverse procedure can be envisaged to solve this problem:

- synthesis of an activated form of the di-iron carbonyl subsite
- then react it with an iron-sulfur cubane

We considered preparing a thiol analogue $[Fe_2(CO)_5\{CH_3C(CH_2S)_2CH_2\mathbf{SH}\}]$, but as we have seen in a previous chapter that the reaction of the trithiol ligand with $[Fe_3(CO)_{12}]$ can easily lead to the formation of a dimer (see **II.6**). The synthesis of such a complex and its reaction with an iron-sulfur cluster as the usual procedure for the mercapto iron-sulfur cluster preparation is therefore compromised.

It has been reported in the seventies by Holm and coworkers that halide iron-sulfur clusters can be prepared from $[Fe_4S_4(SEt)_4]^{2-}$ and benzoyl chloride, releasing ethylthiobenzoate (Equation **IV-1**).[107] Following this observation, we designed the synthesis of a thioester activated di-iron centre able to reproduce such reactivity.

$$[Fe_4S_4(SEt)_4]^{2-} + Ph\text{-}CO\text{-}Cl \longrightarrow [Fe_4S_4Cl_4]^{2-} + Ph\text{-}CO\text{-}SEt \quad (\textbf{IV-1})$$

The trithiol ligand **4** reacts with anhydride acetic under basic conditions to give the thioester dithiol compound together with di- and tri-functionalised materials. Column chromatography allowed isolation of the clean mono-substituted target ligand in moderate yield. The reaction of the thioacetyl ligand in toluene with $[Fe_3(CO)_{12}]$ led to the di-iron complex **27** (Scheme **IV-2**).

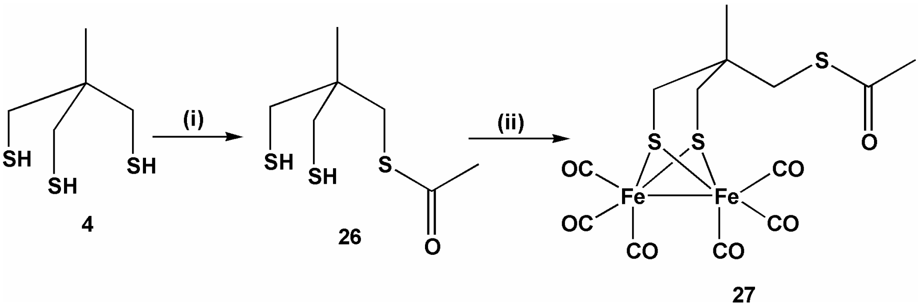

Scheme IV-2. Synthesis of the {2Fe3S}-thioester complex **27**. (i) Acetic anhydride, $NaHCO_3$, diethyl ether, RT, 31%; (ii) $[Fe_3(CO)_{12}]$, toluene, 80°C, 50%.

Surprisingly, as revealed by FT-IR and X-ray crystallography, the sulfur of the thioester does not coordinate the proximal iron as observed in previous {2Fe3S}-complexes (Figure **IV-1**).[63] Undoubtedly, this is due to the electron-withdrawing effect of the acyl group on the sulfur which lowers its nucleophilicity and the thioester can not displace a carbonyl ligand to give a pentacarbonyl complex. This is interesting in the context of the equilibrium discussed in **Chapter II**. The thioacetyl complex can be considered as representing at one extreme the hexacarbonyl / pentacarbonyl equilibrium and at the other the methyl thioether complex.

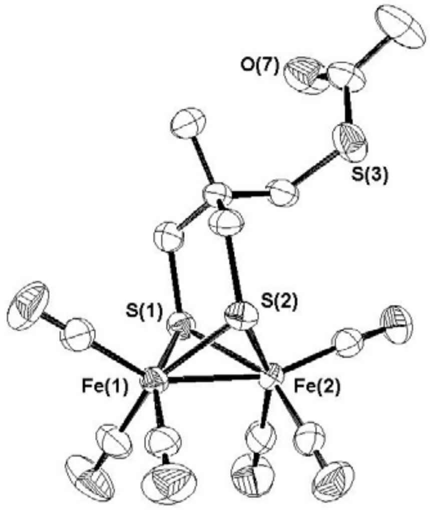

Figure IV-1. X-ray structure of [$Fe_2(CO)_6\{CH_3C(CH_2S)_2CH_2SC(O)CH_3\}$] (**27**). Selected bond lengths (Å) and angles (°): Fe(1)-Fe(2) = 2.4911(9), Fe(1)-S(1) = 2.2615(10), Fe(1)-S(2) = 2.2546(10), Fe(2)-S(1) = 2.2558(10), Fe(2)-S(2) = 2.2756(10), Fe(1)-S(1)-Fe(2) = 66.94 (3), Fe(1)-S(2)-Fe(2) = 66.72 (3).

The key bond distance and bond angle data obtained from the X-ray analysis is given in Figure **IV-1**. There are no significant differences in these values compared with those of related hexacarbonyl (Fe-Fe length for the [$Fe_2(CO)_6\{S(CH_2)_3S\}$] is 2.5103(11) Å).[59]

IV.3 Multiple subsites around the {Fe_4S_4}-core

The reaction of the thioester activated di-iron complex with [$Fe_4S_4(SPh)_4$][NBu_4]$_2$ showed a significant negative shift of the carbonyl frequencies in the infra-red region corresponding to a modification in the coordination sphere of the proximal iron. Work-up of the black material obtained after the reaction between the two compounds overnight in acetonitrile eliminated the resulting by-product $PhSCOCH_3$ ($\nu_{CO\ thioester}$ = 1707 cm^{-1}; $\nu_{CO\ thioester\ complex}$ = 1697 cm^{-1}) (Scheme **IV-3**).

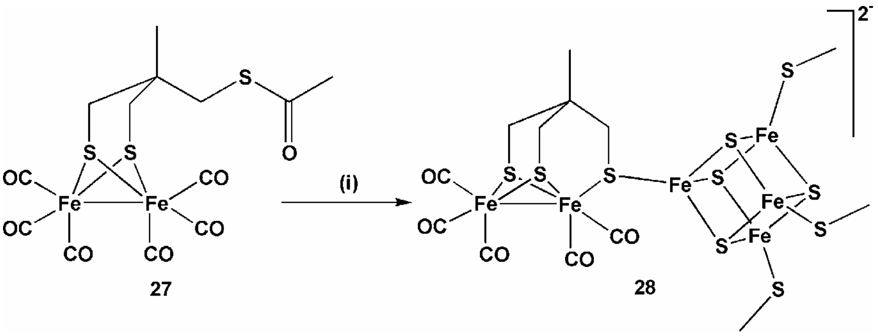

Scheme IV-3. Synthesis of $[Fe_4S_4(SR)_{4-n}\{Fe_2(CO)_5(CH_3C(CH_2S)_3\}_n]^{2-}$ (**28**) (n = 1 to 4; R = SEt or Ph). (i) $[Fe_4S_4(SR)_4][NBu_4]_2$, CH_3CN, RT.

Depending on the conditions used, negative ion electrospray mass spectrometry (ES-MS) in acetonitrile showed different substitution patterns. Complete substitution of the $\{Fe_4S_4\}$-core by {2Fe3S}-subsites is possible if a large excess of the parent di-iron complex is utilised (>5 equivalents) to give $[Fe_4S_4\{Fe_2(CO)_5(CH_3C(CH_2S)_3\}_4]^{2-}$. ES-MS shows the formation of a dianion at *m/z* = 1009.6 with the corresponding isotopic distribution pattern. The monoanion cannot be observed due to the limitation of the machine (max. *m/z* = 2000).

The electrochemistry (0.1 M $[NBu_4][BF_4]$ – CH_2Cl_2, 100 mV.s^{-1}) shows two processes with a first reversible reduction at $E_{½}$ = -0.65 V corresponding to the reduction of the cluster (couple $\{Fe_4S_4\}^{2+}/\{Fe_4S_4\}^{+}$) and a second multi-electron process (E_p = -1.58 V) probably due to the irreversible reduction of the subsites around the iron-sulfur core (Figure **IV-2**). The primary reversible reduction of $[Fe_4S_4(SEt)_4]^{2-}$ occurs at -1.15 V under the same conditions, attesting to the strong electron-withdrawing properties of the di-iron subsites.

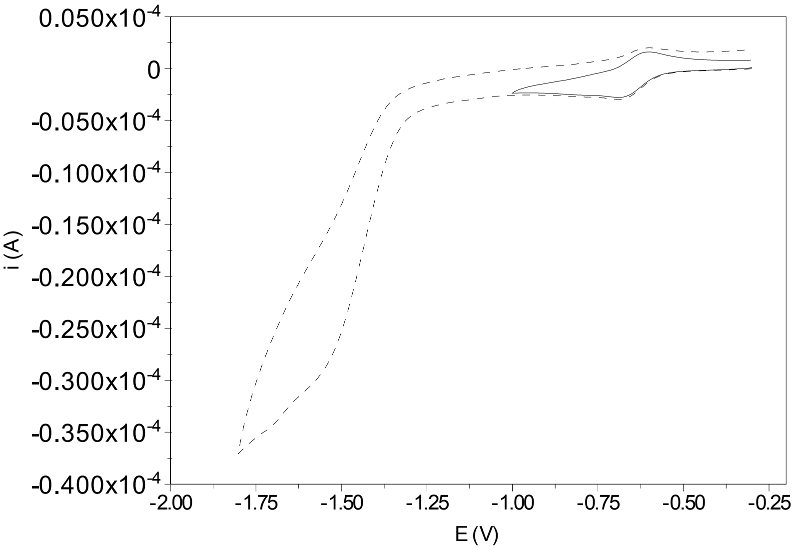

Figure IV-2. Cyclic voltamogramm of $[Fe_4S_4\{Fe_2(CO)_5(CH_3C(CH_2S)_3\}_4]^{2-}$ (**28**) (0.1 M $[NBu_4][BF_4]$ – CH_2Cl_2, 0.1 $V.s^{-1}$).

Mono-, di-, and tri-substituted $\{Fe_4S_4\}$-core can be prepared by using less equivalents of the thioester complex. These are again characterised by ES-MS, but it appears that we can only get a mixture of different substitutions (Figure **IV-3**).

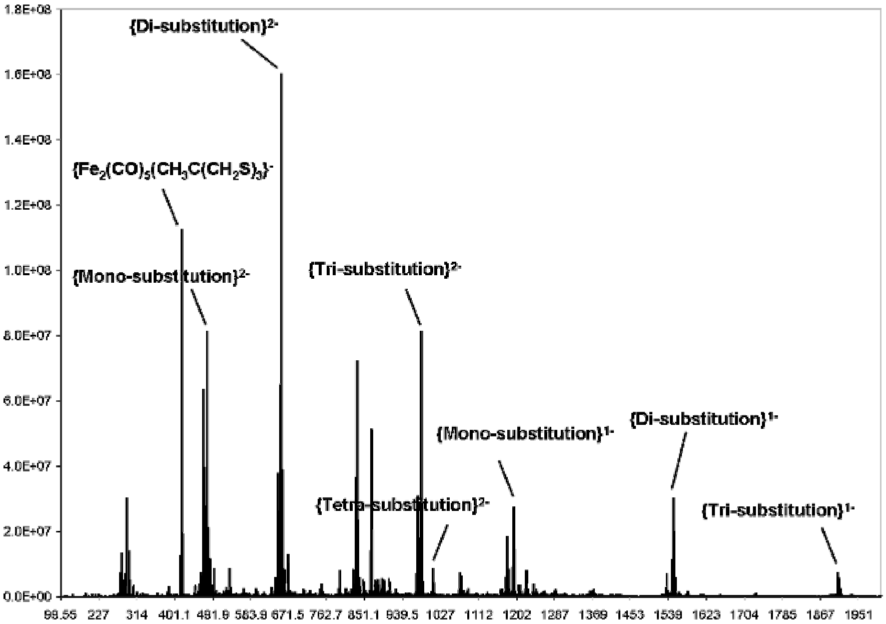

Figure IV-3. ES-MS spectrum of the reaction between $[Fe_4S_4(SEt)_4]^{2-}$ and four equivalents of $[Fe_2(CO)_6\{CH_3C(CH_2S)_2CH_2SC(O)CH_3\}]$ (**27**).

From the point of view of the “H-cluster” framework, the mono-substituted complex $[Fe_4S_4(SEt)_3\{Fe_2(CO)_5(CH_3C(CH_2S)_3\}]^{2-}$ is very interesting as the environment around the $\{Fe_4S_4\}$-core is rather similar to the “H-cluster” itself with its three cysteines from the protein backbone and the {2Fe2S}-subsite on the fourth iron. The problem of purification and isolation of this di-anionic species is problematic as all of the different complexes seem to co-precipitate rather than crystallise. Attempts to separate the mixture by column chromatography using a Sephadex size exclusion column swollen in acetonitrile in a glove box were unsuccessful. The materials ran down the column at the same rate.

Although it was not possible to separate the solid material, gas phase ion-trapping is possible and this allowed measurement of the photoelectron spectroscopy (PES) on the parent and mono-substituted clusters. This was carried out by LS Wang and coworkers at the Pacific Northwest National Laboratory, WA (see section **VII.5**). Previous PES studies on $\{Fe_4S_4\}$-cubane clusters have probed the intrinsic electronic structure of Fe-S clusters by comparison of clusters with different ligands (-SEt, -SH, -Cl, -Br, -I) (Figure **IV-4**) .[108]

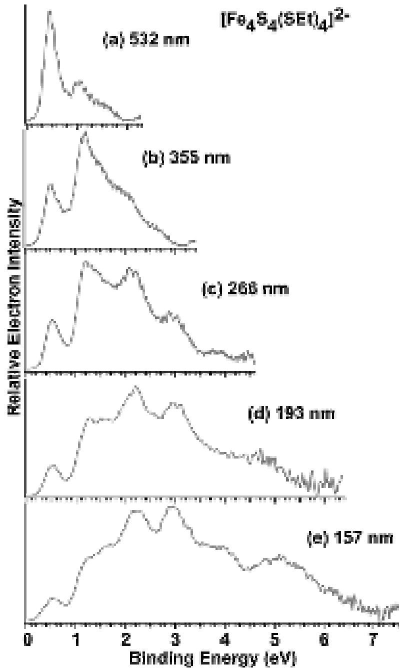

Figure IV-4. Photoelectron spectra of $[Fe_4S_4(SC_2H_5)_4]^{2-}$ at (a) 532 nm (2.331 eV), (b) 355 nm (3.496 eV), (c) 266 nm (4.661 eV), (d) 193 nm (6.424 eV), and (e) 157 nm (7.866 eV) (taken from ref [108]).

The PES of isolated $[Fe_4S_4(SEt)_3\{Fe_2(CO)_5(CH_3C(CH_2S)_3\}]^{2-}$ (Figure **IV-5**) reveals similar features with the $[Fe_4S_4(SC_2H_5)_4]^{2-}$ spectrum, but is shifted by about 0.6 eV to higher energy (from 0.29 to 0.89 eV at 355 nm). This implies a stabilisation of the highest-energy orbitals of the cubane core by the replacement of one ethanethiolate ligand by one {2Fe3S}-subsite. The gap between the first two bands is very similar to what was observed with $[Fe_4S_4(SEt)_4]^{2-}$, which means that the valence orbitals are still located on the cubane cluster.

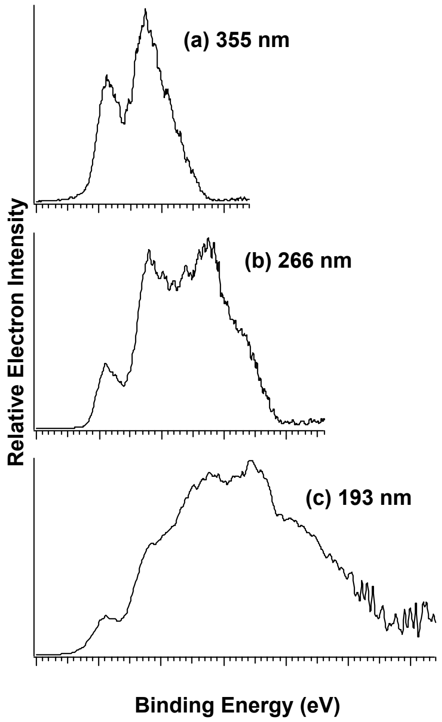

Figure IV-5. Photoelectron spectra of $[Fe_4S_4(SEt)_3\{Fe_2(CH_3C(CH_2S)_3(CO)_5\}]^{2-}$ (**28**): $^{-}$**a**, at 355 nm (3.496 eV); **b**, at 266 nm (4.661 eV); **c**, at 193 nm (6.424 eV).

These experiments outline the fundamental reciprocal electronic influence between the $\{Fe_4S_4\}$-cubane cluster and the {2Fe3S}-subsite.

IV.4 The "H-cluster" model (HCM)

Given the multiple substitution problems discussed above, we looked for another strategy to synthesise a well-defined cluster subsite assembly by a clean procedure. Having established in principle that it was experimentally possible to form a thiolate bridge between the $\{Fe_4S_4\}$-core and the di-iron centre using a thioester-activated complex, which is to our knowledge the first example of such a bonding type in iron-sulfur cluster chemistry (see **I.6**), we decided to focus on protecting three of the four cubane sites from substitution.

Providing a unique site for reactivity of a single thiolate with our activated {2Fe3S}-subsite led us to synthesise a polydentate ligand to build a site-differentiated cluster (see **I.6.b**). The ligand (LS_3) designed by Stack and Holm [43] was the most appropriate target as it has been used for many different studies of model cubane complexes related to the active sites of redox proteins and enzymes such as sulfite reductase,[42,46,109] biotin synthase [110] or "C-cluster" and "A-cluster" of carbon monoxide dehydrogenase.[48,49]

IV.4.a Synthesis of the "Holm ligand"

The starting material is the 1,3,5-trifluorobenzene (**29**) which reacts with Br_2 to lead to the formation of the 1,3,5-trifluoro-2,4,6-tribromobenzene (**30**) (Scheme **IV-4**).[111] Bromine atoms are then substituted with *p*-tolylthiocuprate [112] to give the 1,3,5-tris(*p*-tolylthio)-2,4,6-trifluorobenzene (**33**).[113]

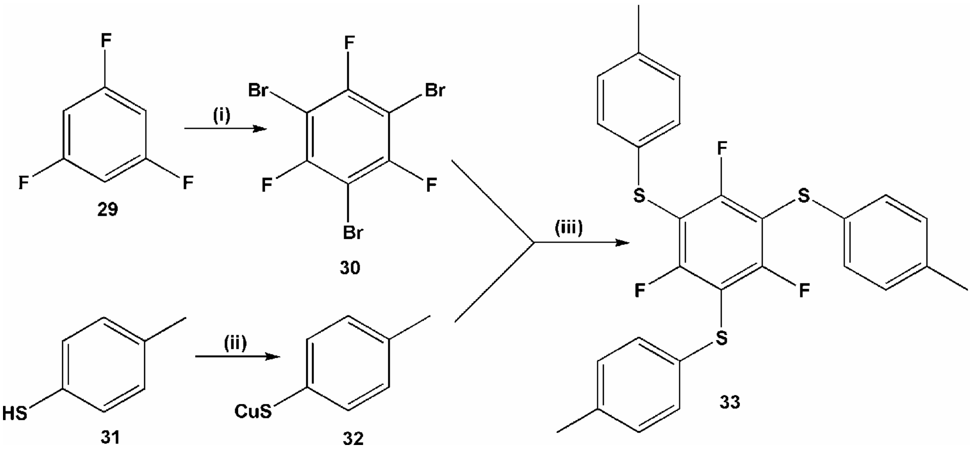

Scheme IV-4. (i) Br_2, Al powder, 60°C, 72%; (ii) Cu_2O, ethanol, 78°C, 94%; (iii) DMF, 140°C, 52%.

The second part of the ligand is the synthesis of the thiolated arm which will coordinate the {Fe_4S_4}-cubane cluster (Scheme **IV-5**). The starting material is the *m*-xylene (**34**), and the reaction with chlorosulfonic acid followed by deprotection with hydrochloric acid gives the 4,6-dimethylbenzene-1,3-dithiol (**36**).[114] The protection with chloromethylmethylether followed by the deprotection of one of the two thioether group leads to the monoprotected thiol (**37**).[113] The ambiguously described procedure for this step in the original literature [113] caused several failed attempts over an extended period.

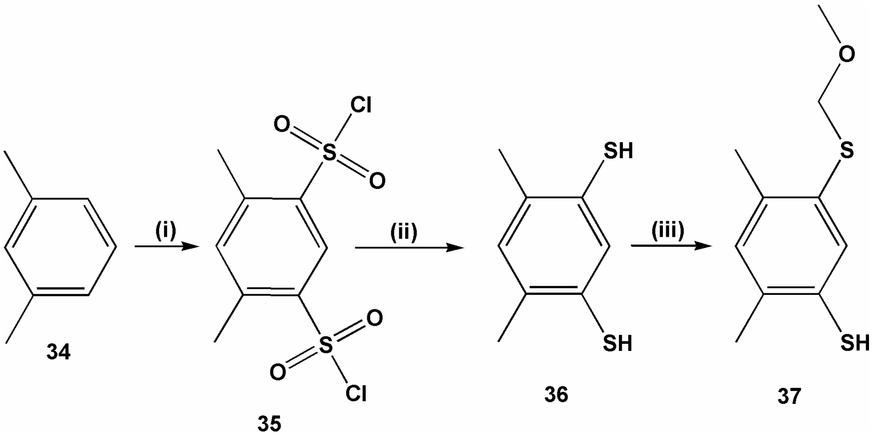

Scheme IV-5. (i) $ClSO_3H$, 150°C, 80%; (ii) Sn, HCl, 100°C, 61%; (iii) 2 eq. NaH, 2 eq. $ClCH_2OCH_3$, DMF, RT, then 1 eq. CH_3CH_2SNa, 34%.

The coupling reaction between three equivalents of the monothiol **37** and the trifluorobenzene compound **33** under basic conditions [115] followed by the deprotection of the thioether group by mercury acetate / H_2S gives an analytically pure yellow solid **39** (Scheme **IV-6**).[110]

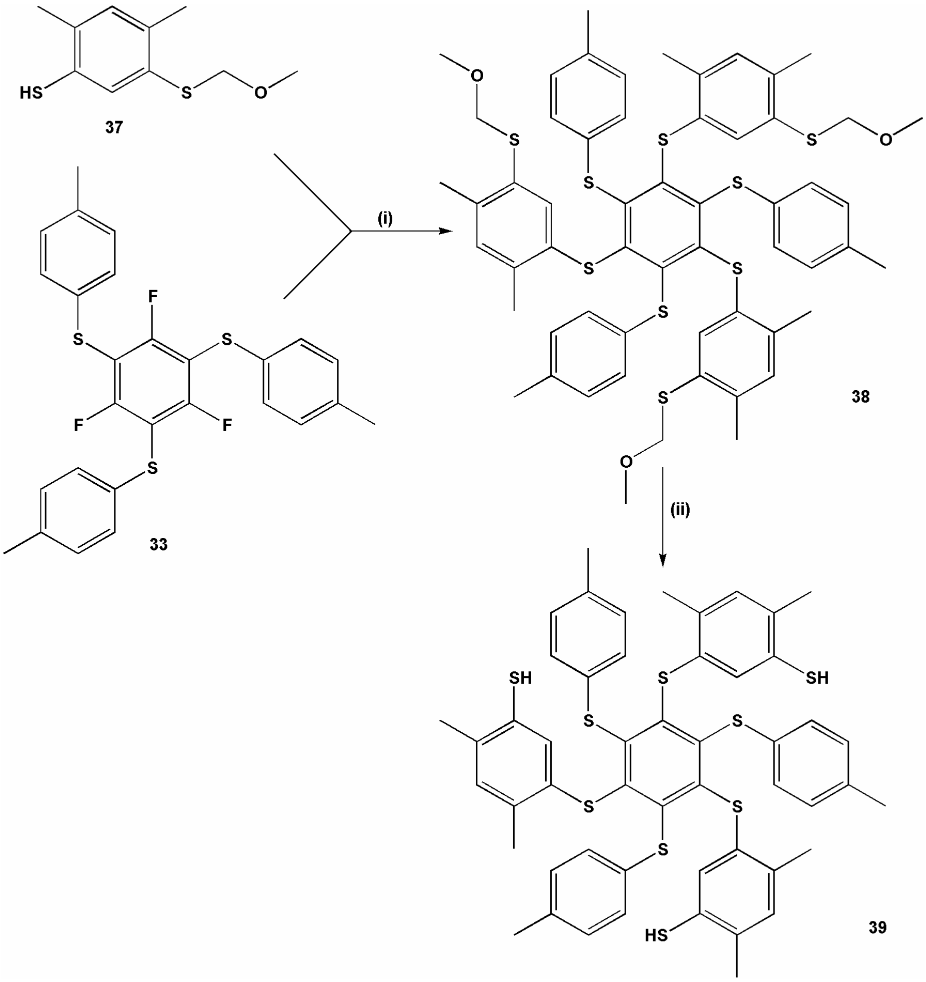

Scheme IV-6. (i) NaH, THF then DMEU, 85°C, 50%; (ii) $Hg(OAc)_2$, chloroform / ethanol, RT then H_2S, 56%.

IV.4.b Synthesis and properties of the "Holm cluster"

The procedure for the synthesis of the site-differentiated $\{Fe_4S_4\}$-cubane follows the usual preparation of mercapto derivative clusters (Scheme **IV-7**). The equilibrium is greatly in favour of the ligand substitution because of the chelate effect of the ligand itself (three coordinating sites are present) and also the volatility of the by-product (ethanethiol, bp = 35°C).

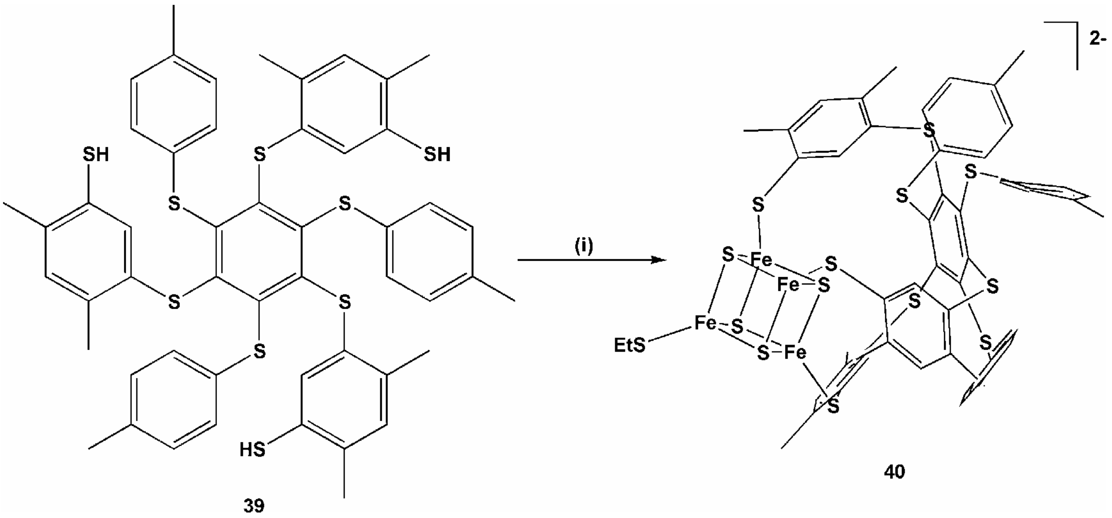

Scheme IV-7. (i) $[Fe_4S_4(SEt)_4][NBu_4]_2$, dichloromethane/acetonitrile, RT, 64%.

The electrochemistry of the complex **40** shows two one-electron processes (Figure **IV-6**). The first reversible reduction at $E_{½}$ = -0.98 V (in acetonitrile, *vs.* Ag/AgCl) corresponds to the $\{Fe_4S_4\}^{2+}/\{Fe_4S_4\}^{+}$ couple, and the second partially reversible reduction at E_p = -1.77 V corresponds to the $\{Fe_4S_4\}^{+}/\{Fe_4S_4\}^{0}$ couple.

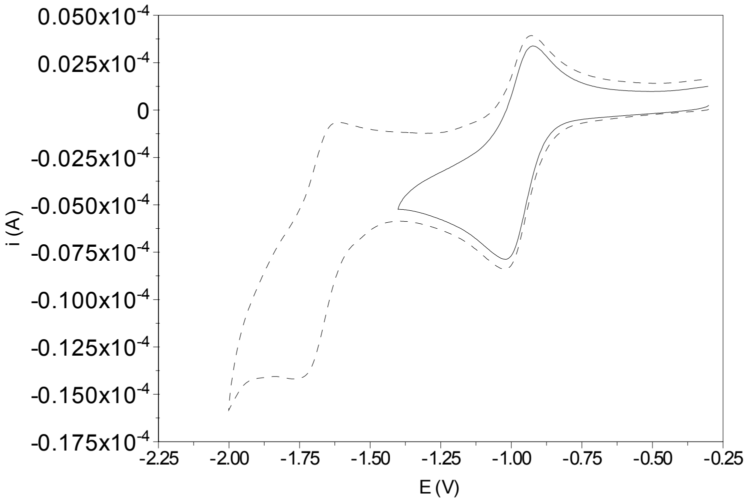

Figure IV-6. Cyclic voltammogram of $[Fe_4S_4(SEt)(LS_3)][NBu_4]_2$ (**40**) (0.2 M $[NBu_4][BF_4]$ – CH_3CN, 0.1 V.s^{-1}).

These two reduction processes occur at higher relative potentials than the parent cluster $[Fe_4S_4(SEt)_4][NBu_4]_2$ ($E_{½}$ = -1.17 V for the first reversible reduction, in

CH_2Cl_2). This is because the three arylthiolate ligands are more electron-withdrawing than the ethylthiolate ligands on the iron-sulfur cubane. The $[Fe_4S_4(SPh)_4][NBu_4]_2$ cluster can be reduced at even more positive potential as it possesses four phenylthiolate ligands around the iron-sulfur cubane ($E_{½}$ = -0.86 V for the first reversible reduction, in CH_3CN). As is well established, the cubane electrochemistry is sensitive to the nature of the thiolate substituents.[116]

The oxidative cyclic voltammetry shows two irreversible processes at E_p^{ox} = +0.25 and +0.45 V (Figure **IV-7**). Oxidation can become partially-reversible particularly for some tetrathiolate $\{Fe_4S_4\}$-cubane clusters with strong withdrawing ligands such as $-SC_6F_5$.[116]

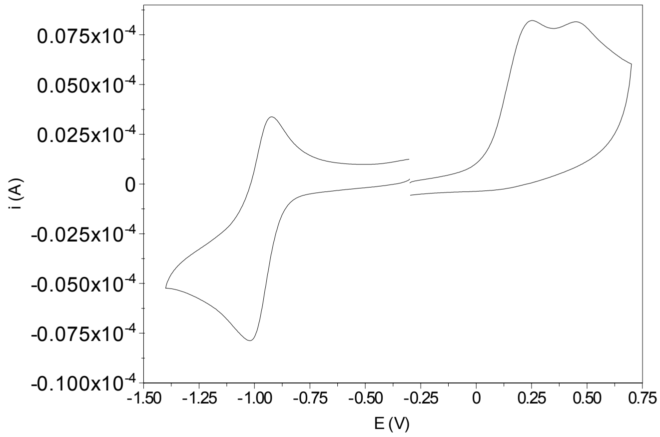

Figure IV-7. Cyclic voltamogramm of $[Fe_4S_4(SEt)(LS_3)][NBu_4]_2$ (**40**) (0.2 M $[NBu_4][BF_4]$ – CH_3CN, 0.1 V.s^{-1}, both scans were recorded separately).

A useful spectroscopic property is the effect of the $\{Fe_4S_4\}$-cubane on the chemical shift of the proximal C*H₂* of alkylthiolate ligands in ^{1}H-NMR spectra (e.g. Me, Et, n-Pr, CH_2Ph). There is an isotropic shift which is due to the presence of a paramagnetic $[Fe_4S_4]^{2+}$ core and the antiferromagnetic properties of these clusters.[117] Isotropic shifts originate from the thermal occupation of excited states of the spin ladder (with S > 0) and therefore is dependent on the temperature but has a small solvent dependence. In the “Holm cluster”, the chemical shift for the C*H₂* of the ethanethiolate is found at

12.58 ppm (in $CDCl_3$ at 20°C) compared to 10.1 ppm for the parent cluster $[Fe_4S_4(SEt)_4][Ph_4As]_2$ (in CD_3CN at 22°C).[117]

IV.4.c “H-cluster” model (HCM)

The activated di-iron thioesther complex **27** reacts cleanly with one equivalent of the “Holm cluster” **40** over a 12h period at room temperature in acetonitrile, to give after work-up, analytically pure $[Fe_4S_4(LS_3)\{Fe_2(CO)_5(CH_3C(CH_2S)_3)\}][NBu_4]_2$, **HCM** (Scheme **IV-8**).

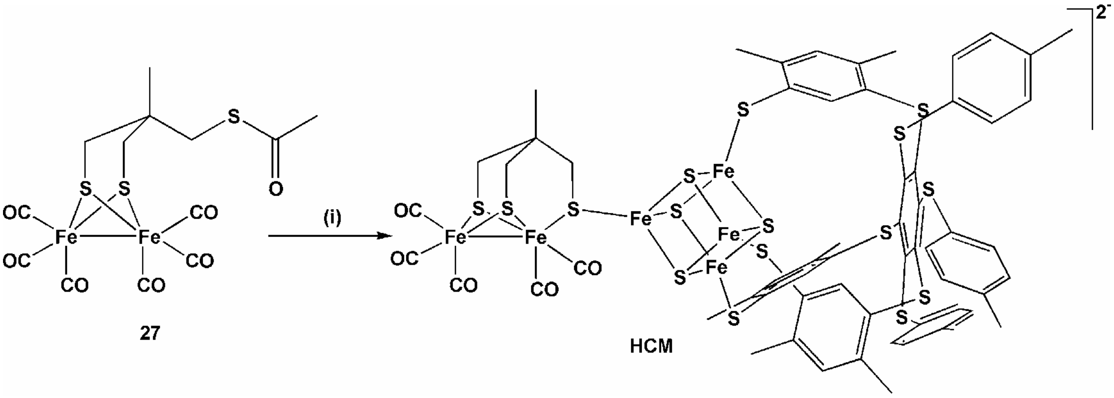

Scheme IV-8. Synthesis of $[Fe_4S_4(LS_3)\{Fe_2(CO)_5(CH_3C(CH_2S)_3)\}][NBu_4]_2$ (**HCM**). (i) $[Fe_4S_4(SEt)(LS_3)][NBu_4]_2$ (**40**), CH_3CN, RT, 40%.

ES-MS in acetonitrile showed peaks centred at $m/z = 856.9$ and at $m/z = 1957.3$.

A good method to determine the relative charge of anions detected by mass spectrometry is the correlation of the isotopic distribution pattern with the peak separation. Each atom is present in nature in several isotopic forms, *e.g.* four for iron and sulfur. Thus, the mass spectrometry spectrum represents the statistical distribution of atomic masses of the elements present in the charged molecule. The difference between each isotope being one, an isotopic pattern with a peak difference of one would be singly charged ($z = 1$) because the spectrum shows the m/z ratio.

The isotopic distribution pattern recorded for the compound is consistent with doubly (*m/z* = 859.9, $[Fe_4S_4(LS_3)\{Fe_2(CO)_5(CH_3C(CH_2S)_3)\}]^{2-}$) and singly (*m/z* = 1957.3, $[Fe_4S_4(LS_3)\{Fe_2(CO)_5(CH_3C(CH_2S)_3)\}]^{2-}[NBu_4]^{+}$) charged species (Figure **IV-8**).

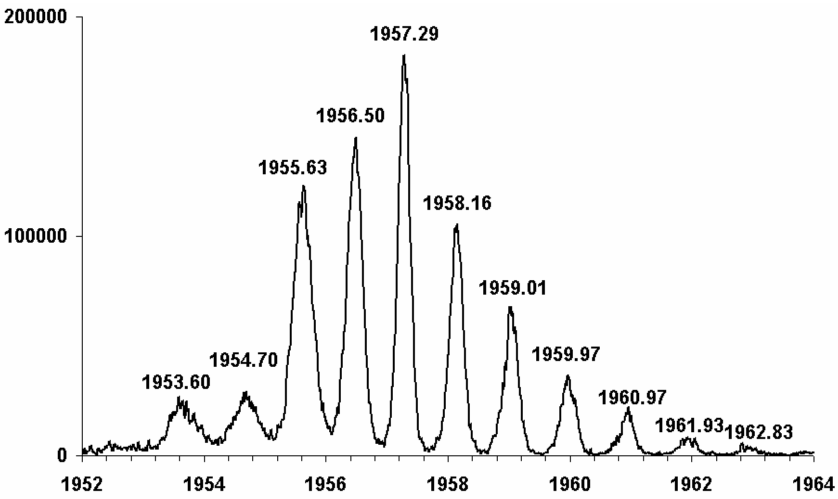

Figure IV-8. Isotopic distribution pattern corresponding to the singly charged $\{[Fe_4S_4(LS_3)\{Fe_2(CO)_5(CH_3C(CH_2S)_3)\}][NBu_4]\}^-$ (**HCM**).

IV.4.c.α FTIR spectroscopy

FTIR of ν(CO) shows the "classical" pattern for pentacarbonyl {2Fe3S}-complexes (2035(m), 1970(s) and 1912 (w) cm^{-1}) as the $\{Fe_4S_4\}$-cubane cluster re-coordinates onto the proximal iron. This is due to its stronger electron donor effect compared to the {2Fe3S}-hexacarbonyl thioacetyl parent complex **27** (Figure **IV-9**).

The electronic communication between the di-iron centre and the iron-sulfur cubane is evident as the ν(CO) frequencies of the subsite are shifted to the lower values by *ca.* 15 cm^{-1}. Notably, as outlined in **Chapter III**, this shift has to be compared to the very weak influence of strong withdrawing / donating groups on the ν(CO) frequencies in the usual {2Fe3S}-subsite model complexes (Δν(CO) *ca.* 5cm^{-1} between NO_2 and NH_2 derivatives) and highlights the difference in electronic properties of the thioether ligand *versus* the thiolate ligand.

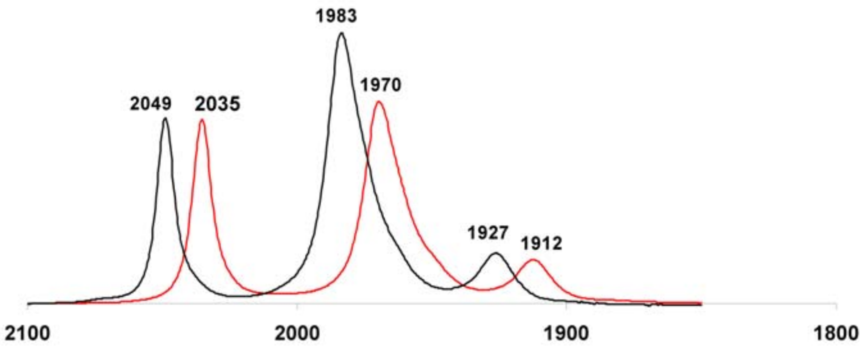

Figure IV-9. FTIR in acetonitrile of the **HCM** (red) and the complex $[Fe_2(CO)_5\{CH_3C(CH_2S)_2CH_2SCH_3\}]$ (**black**).

IV.4.c.β Mössbauer spectroscopy

As described in **section I.5.c.γ**, Mössbauer parameters for the enzymatic "H-cluster" have been recorded for different enzymes.[30,32] From the comparison with previous $\{Fe_4S_4\}$-cubane complex [31] data and {2Fe3S}-complex data,[63] parameters recorded on our "H-cluster assembly" should provide an insight on the electronic communication between the di-iron subsite and the $\{Fe_4S_4\}$-cubane.

The solid-state Mössbauer spectrum recorded at 77 K shows four overlapping quadrupole split doublets (Figure **IV-10**). This is consistent with four differentiated iron sites: two from the di-iron subsite (Fe_{distal} and $Fe_{proximal}$) and two associated with the $\{Fe_4S_4\}$-cubane.

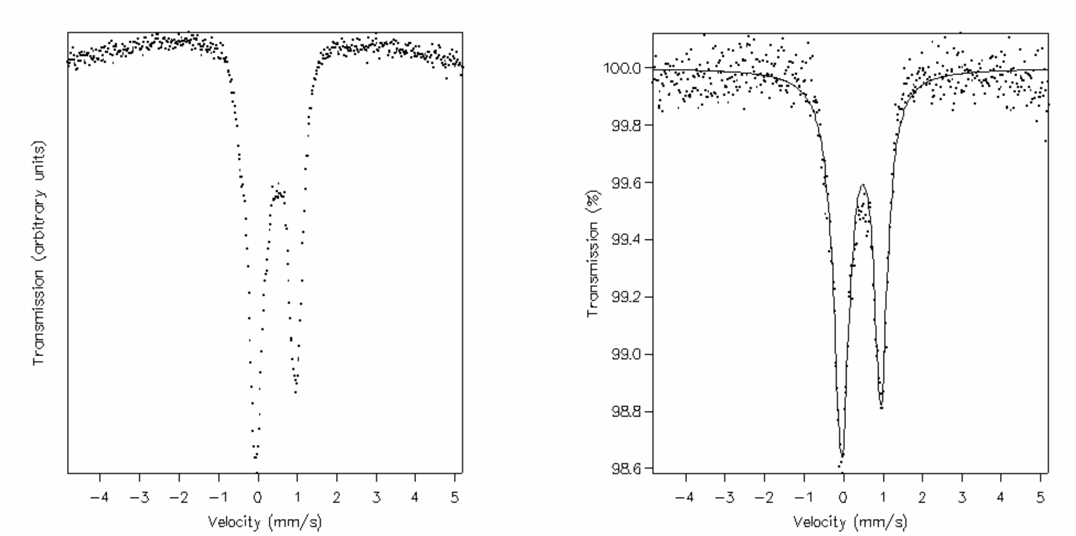

Figure IV-10. Solid state Mössbauer spectrum recorded at 77 K of **HCM** (fitted spectrum on the right).

Di-iron subsite parameters for the distal iron are consistent with previous model complexes (i.s. = 0.04, q.s. = 1.00 mm.s^{-1}).[63] Without any doubt, the doublet corresponding to the i.s. = 0.04, q.s. = 0.50 mm.s^{-1} parameters can be assigned to the proximal iron of the di-iron subsite. The binding of a thiolato ligand (instead of a CO ligand for the distal iron) causes a decrease in the q.s. parameter, due to the replacement of a π-acceptor by a non-π-acceptor. Interestingly, it does not seem that there is any difference for the s-electron density (i.s.) between the distal and the proximal iron, contrary to "classical" {2Fe3S}-pentacarbonyl complexes.

Mössbauer parameters for synthetic models of iron-sulfur protein model complexes have been intensively studied. The attribution of the two other doublets can be associated with the site-differentiated cluster (i.s. = 0.47 and 0.45; q.s. = 1.14 and 0.87 mm.s^{-1} at 77 K) as the values measured for the [Fe$_4$S$_4$(LS$_3$)(SPh)$_4$]$^{2-}$ are in the same range (i.s. = 0.37 and 0.37; q.s. = 1.40 and 1.04 mm.s^{-1} at 77 K).[118]

Comparison of these data with data recorded with the enzyme provides interesting information (Table **IV-1**). 77 K corrected data of Mössbauer parameters of the reduced state of CpII [Fe]-hydrogenase (recorded at 4.2 K) [30] show three doublets, two for the site-differentiated cubane (i.s. = 0.49 and 0.49; q.s. = 1.37 and 0.87 mm.s^{-1}) and one for the di-iron subsite (i.s. = 0.10; q.s. = 0.89 mm.s^{-1}). These similarities seem to confirm the +2 state of the {Fe_4S_4}-cubane cluster for H_{red}. Mössbauer parameters for the di-iron subsite do not provide such a similarity as we observed two doublets, probably due to a lack of resolution for the spectrum of the enzyme. Nevertheless, the parameters recorded are in the range of what we should expect for that type of Fe(I)-Fe(I) complex. These data seem to confirm that the reduced state of the {2Fe3S}-subsite would be more likely Fe(I)-Fe(I) than Fe(II)-Fe(II).

Compound	**i.s.**	**q.s.**
$[Fe_2(CO)_6\{SCH_2CH_2CH_2S\}]$[21]	0.04	0.87
	0.03	0.70
$[Fe_2(CO)_5\{CH_3C(CH_2S)_2CH_2SCH_2Ph\}]$[3]	0.04	1.00
	0.13	0.28
$[Fe_4S_4(LS_3)\{Fe_2(CO)_5(CH_3C(CH_2)_3)\}][NBu_4]_2$	0.04	1.00
	0.04	0.50
	0.47	1.14
	0.45	0.87
“H-cluster” (CpII)[18]	0.10	0.89
	0.49	1.37
	0.49	0.87

Table IV-1. Solid state Mössbauer parameters (mm.s^{-1}) for iron-sulfur assemblies at 77 K.

IV.4.c.γ DFT calculation

Attempts to get an X-ray crystal structure were unsuccessful. In order to probe the stability of the isolated **HCM**, DFT calculations were carried out. Full geometry optimisation of an *in silico* model of the **HCM**, $[Fe_4S_4(SCH_3)_3\{Fe_2(CO)_5(CH_3C(CH_2S)_3)\}]^{2-}$, was carried out in the density functional theory (DFT) framework using the BP86 pure functional [119,120] and an all-electron valence triple-ζ basis set with polarisation functions on all atoms.[121] This was done by

L. De Gioia and M. Bruschi at the University of Milan. The author did not perform the *in silico* calculations but the results are included here for completeness.

The calculated structure is fully consistent with the proposed experimental structure (Figure **IV-11**). The bridging thiolate coordinates almost symmetrically the $\{Fe_4S_4\}$-cubane cluster and the {2Fe2S}-subunit ($Fe_{cubane}S$ = 2.340 and $Fe_{subsite}S$ = 2.312 Å). The Fe-Fe distance (2.6 Å) in the di-iron subunit is indicative of a metal-metal bond and is consistent with previous observed data for {2Fe3S}-complexes (see **II.6**). Electronic property analysis reveals that the redox state of the di-iron subunit can be described as Fe(I)-Fe(I), as suggested by ES-MS and Mössbauer spectroscopy.

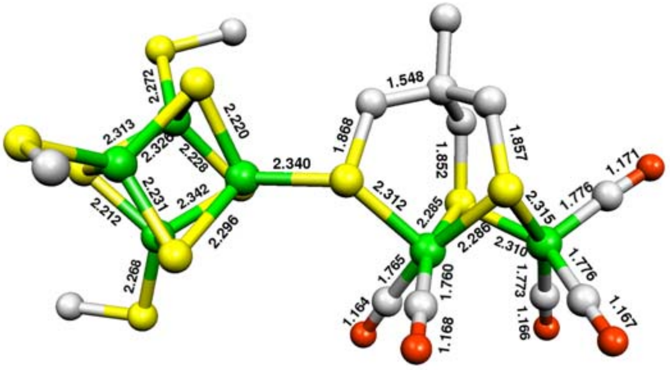

Figure IV-11. Structure of $[Fe_4S_4(SCH_3)_3\{Fe_2(CO)_5(CH_3C(CH_2S)_3)\}]^{2-}$, derived from DFT calculations (bond lengths in Å).

IV.4.c.δ Electrochemistry

The inductive effect of the iron-sulfur cubane has shown its influence on CO frequencies by lowering ν(CO) by *ca.* 15 cm^{-1}, and an effect has also been observed on the Mössbauer spectrum with a smaller i.s. compared to the thioether {2Fe3S}-complexes due to the increase of s-electron density on the proximal iron.

Electrochemistry of **HCM** should support these observations and provide an insight into the interplay between the $\{Fe_4S_4\}$-cubane cluster and the {2Fe2S}-subsite. Experiments were carried out in acetonitrile (0.2 M $[NBu_4][BF_4]$ in CH_3CN).

The primary reversible one-electron reduction occurs at $E_{½}$ = -0.86 V and corresponds to the $\{Fe_4S_4\}^{2+}/\{Fe_4S_4\}^{+}$ couple (Figure **IV-12**). Under identical conditions, the parent cluster $[Fe_4S_4(LS_3)(SEt)][NBu_4]_2$ is reduced at $E_{½}$ = -0.98 V (see **IV.4.b**). This implies that the energy of the cubane's lowest unoccupied molecular orbital (LUMO) is substantially lowered due to the presence of the {2Fe3S}-subsite probably because of an electronic density transfer through the thiolato bridge linking the two FeS clusters as suggested by IR-spectroscopy, and therefore the cubane can be reduced at more positive potentials.

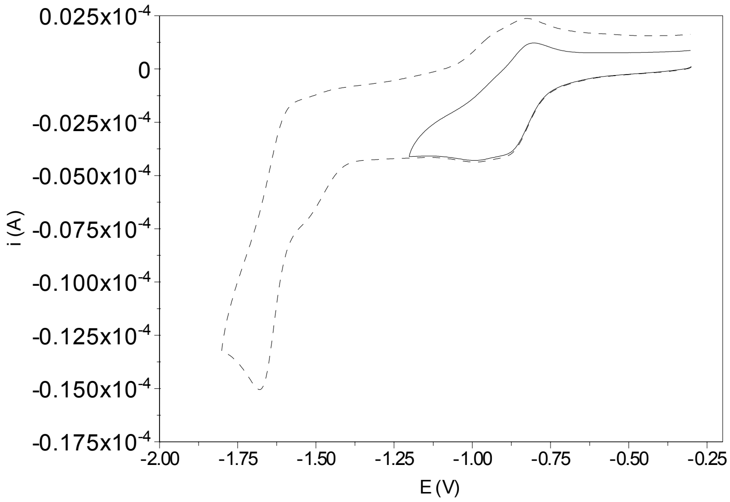

Figure IV-12. Cyclic voltammogram of $[Fe_4S_4(LS_3)\{Fe_2(CO)_5(CH_3C(CH_2)_3)\}][NBu_4]_2$ (**HCM**) (0.2 M $[NBu_4][BF_4]$ – CH_3CN, 0.1 V.s^{-1}).

The formal replacement of EtS by $\{Fe_2(CO)_5(CH_3C(CH_2S)_3\}$ reveals a $\Delta E_{½}$ of +120 mV, which fits well with the $\Delta E_{½}$ of +500 mV observed for the replacement of four EtS ligands by four di-iron subsites and outlines the electronic communication between the two parts (see **IV.3**).

A closer look to the first reduction shows two different processes (Figure **IV-13**). At slow scan rate (20 mV.s^{-1}), both systems are partially reversible, as when the scan rate is increased process I becomes more reversible.

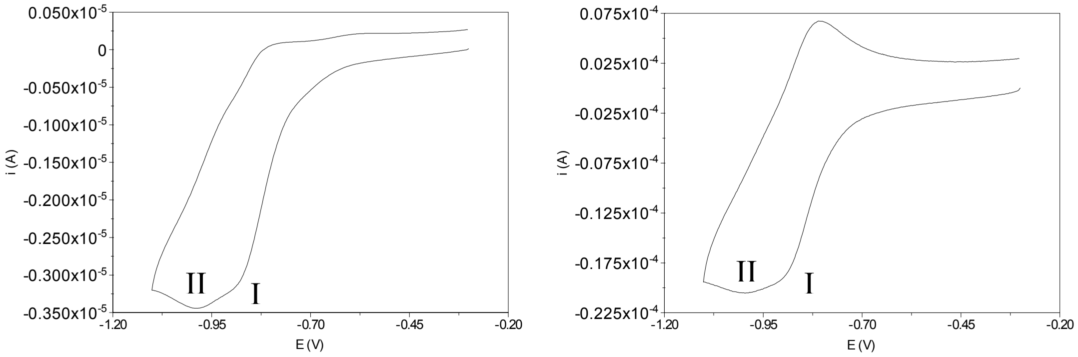

Figure IV-13. Cyclic voltammogram of **HCM** at 20 mV.s^{-1} (left) and 1 V.s^{-1} (right) (0.2 M [NBu$_4$][BF$_4$] – CH$_3$CN, 0.1 V.s^{-1}).

Repetitive cyclic voltammetry over 10 cycles shows the build-up of a reversible system at -0.96 V for the process II (Figure **IV-14**), which is close to that of the cluster [Fe$_4$S$_4$(LS$_3$)(SEt)][NBu$_4$]$_2$ (under the same conditions).

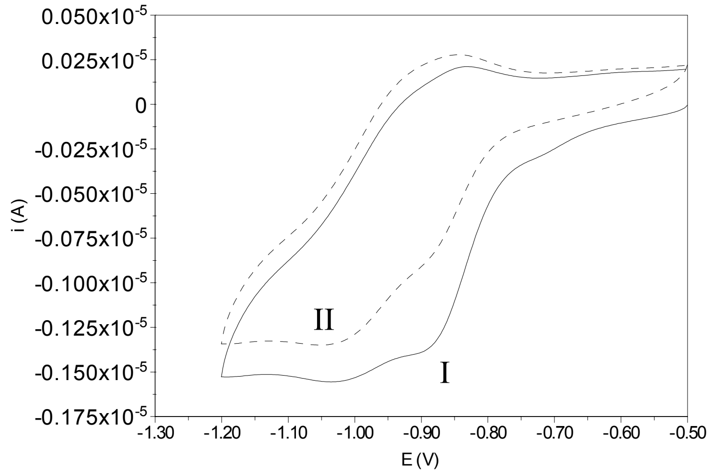

Figure IV-14. Cyclic voltammogram of **HCM** at 30 mV.s-1 (dashed line represents the 10th scan) (0.2 M [NBu$_4$][BF$_4$] – CH$_3$CN, 0.1 V.s^{-1}).

If the bridge is opened following electron-transfer, then the product would have a very similar structure to the ethylthiolate complex and thus have a similar reduction potential. This mechanism provides the basis for a digitally simulated voltammogram (Figure **IV-15**) which fits reasonably the observed experimental data.

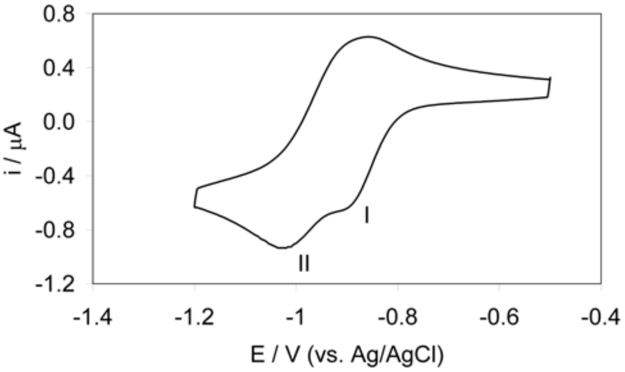

Figure IV-15. Simulated (Digisim 3.03a) repetitive scan (10th cycle) voltammograms of **HCM** at 30 mV.s^{-1} showing interconverting redox processes I and II.

We therefore suggest that the mechanism of reduction of HCM can be represented as shown in Scheme **IV-9**. After the reduction of the $\{Fe_4S_4\}$-cubane cluster at -0.87 V (process I), the mechanism involves an intramolecular electron-transfer to the {2Fe2S}-subsite in concert with reversible opening of the μ-S bridge. The cubane cluster therefore returns to the +2 state and is in a similar configuration to the parent cluster $[Fe_4S_4(LS_3)(SEt)]^{2+}$, and another reduction is then possible for the $\{Fe_4S_4\}^{2+}/\{Fe_4S_4\}^{+}$ couple which occurs at -0.96 V (process II), close to that for the ethylthiolate cubane cluster.

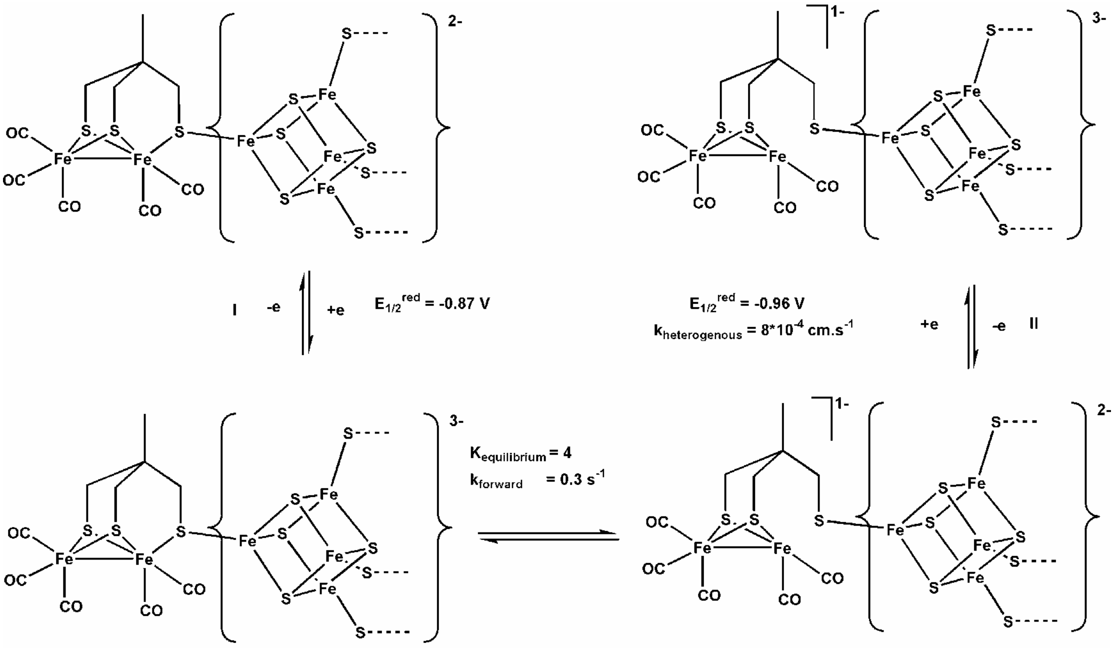

Scheme IV-9. Proposed pathways for redox interconversions between μ-S and alkylthiolate forms of cubane for **HCM**. The thermodynamic and kinetic parameters are those used in the simulation.

Oxidation of the **HCM** complex showed two irreversible processes at E_p^{ox} = 0.27 and 0.47 V. This cyclic voltammetry is nearly identical (shift of +20 mV) to the parent {Fe_4S_4}-cubane cluster (Figure **IV-16**) and therefore seems to indicate that only the cubane is involved in the oxidative process.

FTIR-SEC described below will investigate these oxidative features.

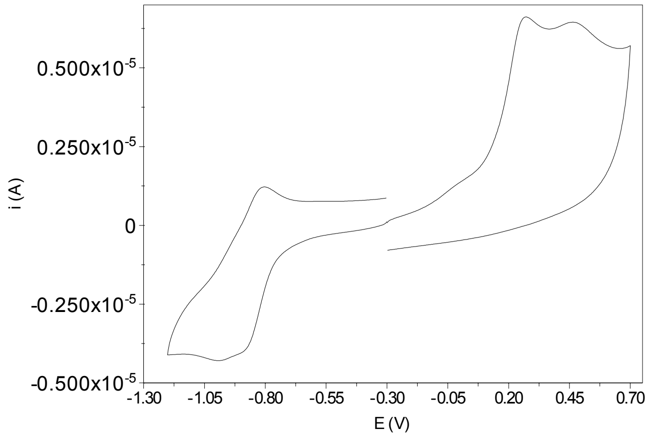

Figure IV-16. Cyclic voltamogramm of $[Fe_4S_4(LS_3)\{Fe_2(CO)_5(CH_3C(CH_2S)_3)\}][NBu_4]_2$ (**HCM**) (0.2 M $[NBu_4][BF_4]$ – CH_3CN, 0.1 V.s^{-1}, both scans were recorded separately).

IV.4.c.ε Electrocatalysis of proton reduction

As described in **Chapter III**, most of the {2Fe2S}- and {2Fe3S}-complexes are able to catalyse dihydrogen evolution from protons, albeit at low reduction potentials. The current-potential curve for the proton reduction in the presence of **HCM** (E_p = -1.06 V) is displaced by *ca.* 270 mV more positive from that measured in the absence of the catalyst (E_p = -1.33 V) (Figure **IV-17**).

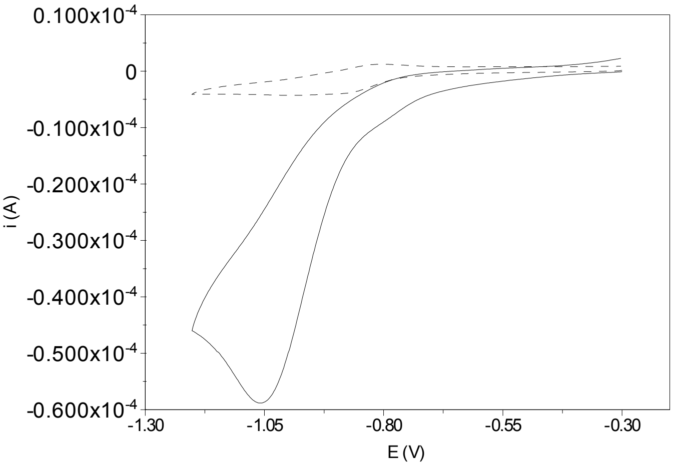

Figure IV-17. Cyclic voltammogram of **HCM** (2 mM) showing the electrocatalytic response in the absence (···) and in the presence (–) of 2,6-lutidinium as a source of protons (20 mM, 0.2 M $[NBu_4][BF_4]$ – CH_3CN, 0.1 V.s^{-1}).

The shape of the cyclic voltammograms in the presence of protons seems to show two processes. A primary reduction of the complex occurs at slightly more positive potential than for **HCM** in the absence of protons ($E_p \approx$ -0.80 V), suggesting a reduction of a protonated form of **HCM**.

The following reduction takes place at roughly the same potential (*ca.* -1.0 V) as the first reduction of **HCM** at low concentration of acid, the E_p is then displaced to a more negative values when the amount of acid increases due to *i*R drop.

Comparing previous {2Fe2S}- and {2Fe3S}-model complexes of the subsite of [Fe]-hydrogenase, this potential for proton reduction is, to our knowledge, the most positive, but still far below platinum ($E_p \approx$ -0.72 V, same conditions).

IV.4.c.ζ FTIR-Spectroelectrochemistry

The author studied the spectroelectrochemistry of the model of the "H-cluster" at the University of Melbourne with Dr. S. Best and S. Borg. The reduction and oxidation of **HCM** in the absence and presence of CO and in the presence of an acid source was examined by FTIR-SEC.

Reduction at a potential corresponding to the primary process led to the detection of two infrared-active species, **R1** and **R2** (Figure **IV-18**). **R1** is first formed and rapidly converts to a more reduced compound, **R2**.

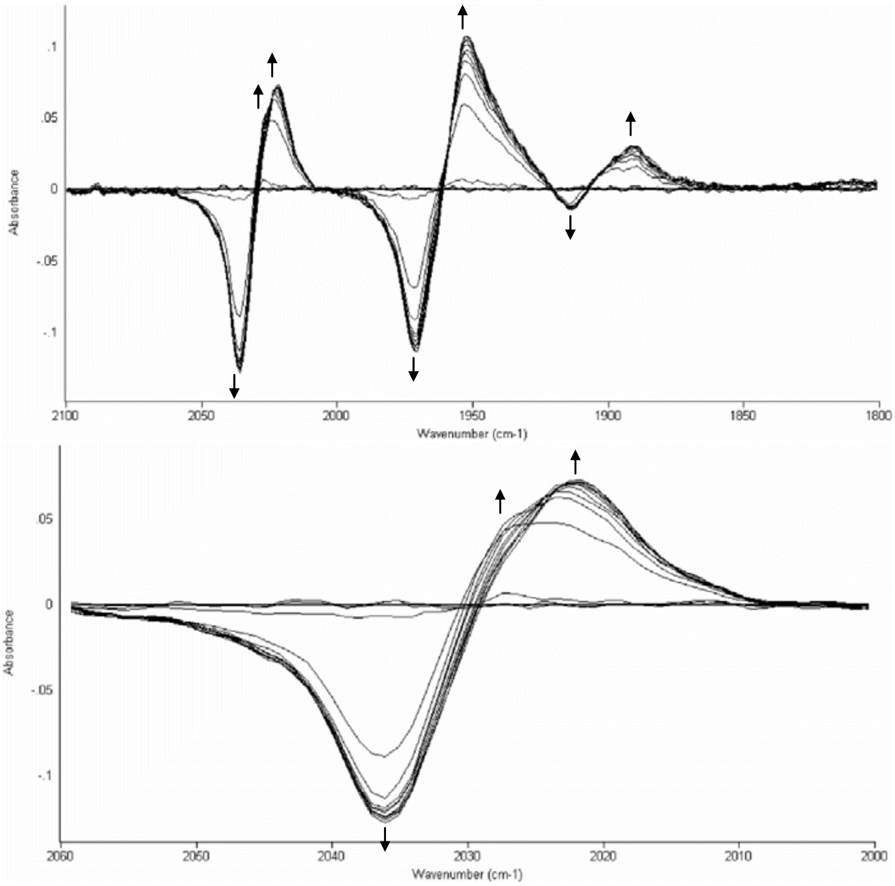

Figure IV-18. IR-SEC of **HCM** in CH_3CN under Ar (40 psi); potential applied: -0.9 V (*vs.* Ag wire); timeframe: 0 to 19 s.

Re-oxidation of the **R1** / **R2** system at -0.6 V showed that **R1** is rapidly converted back to the starting material whereas a longer time is required for the conversion of **R2** back to the parent complex (Figure **IV-19**).

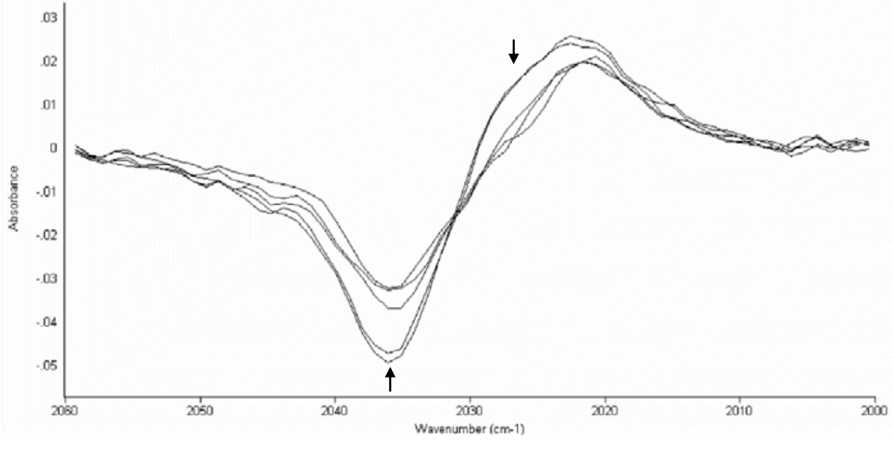

Figure IV-19. IR-SEC of **HCM** in CH_3CN under Ar (40 psi); potential applied: 0 V after reduction at -0.6 V (*vs.* Ag wire); timeframe: 10 to 15 s.

The absorption spectra of **R1** and **R2** can be obtained from the difference spectra and are shown in Figure **IV-20**.

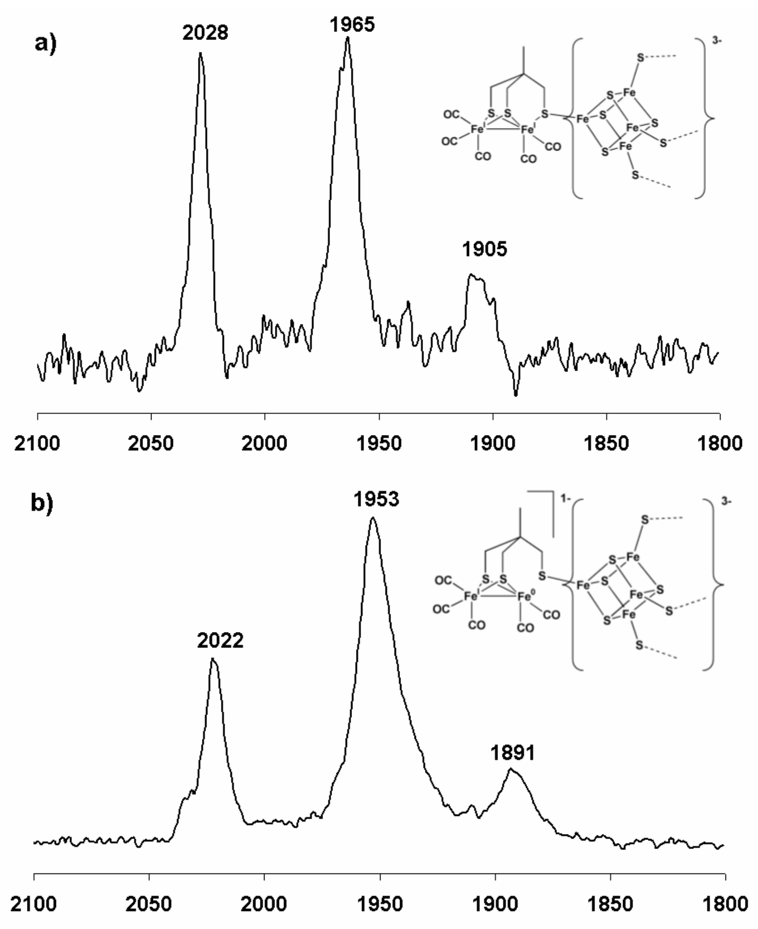

Figure IV-20. IR-spectra in CH_3CN obtained from IR-SEC of **HCM** a) the one-electron reduced species (**R1**) and b) the two-electron reduced species (**R2**).

Inspection of Figure **IV-20(a)** shows that **HCM** and **R1** have a similar pattern and are therefore likely to have a similar geometry i.e. the $Fe_{proximal}$ – $S_{thiolate}$ – Fe_{cubane} arrangement is retained. The shift in ν(CO) frequencies between **HCM** and **R1** is ca. 7 cm^{-1}. This small value is consistent with the primary electron transfer taking place on the cubane, which influences the subsite frequencies by an enhanced donor effect. As noted in Chapter **II**, the inductive effect on ν(CO) can be small.

The subsequent process generating **R2** gives a spectral pattern rather closer to that of a thioether system than to the parent **HCM** complex. The overall shift in frequency on going from **HCM** to **R2** is 17 cm^{-1}.

One possible interpretation of this chemistry is that an electron is added to the di-iron centre with cleavage of the proximal iron-thiolate bond as suggested in section **IV.4.c.δ** on the basis of redox potentials. The infrared pattern similar to that of a thioether-ligated system might then be explained by the odd electron on the proximal iron site occupying the same position as a thioether group. However, the reduced centre does not interact with CO as we might have expected. Closer examination of the electron counting on each metal indicates that the reduced di-iron centre would be 18e$^-$ / 19e$^-$ with the thiolate coordinated. This unfavourable situation is stabilised by the de-coordination of the thiolate ligation, resulting in a 18e$^-$ / 17e$^-$ configuration. Even in the presence of a good electron acceptor ligand, such as CO, it is most unlikely that the substitution can take place to recover the unfavourable 18e$^-$ / 19e$^-$, and therefore no interaction with CO is observed.

An alternative explanation is that the Fe$_{\text{proximal}}$ –S$_{\text{thiolate}}$ – Fe$_{\text{cubane}}$ linkage remains intact and the electron enters a metal-metal antibonding orbital.

Oxidation of **HCM** gives a single product **O1** (Figure **IV-21**), and the shift to higher frequencies observed is ~ 19 cm^{-1}.

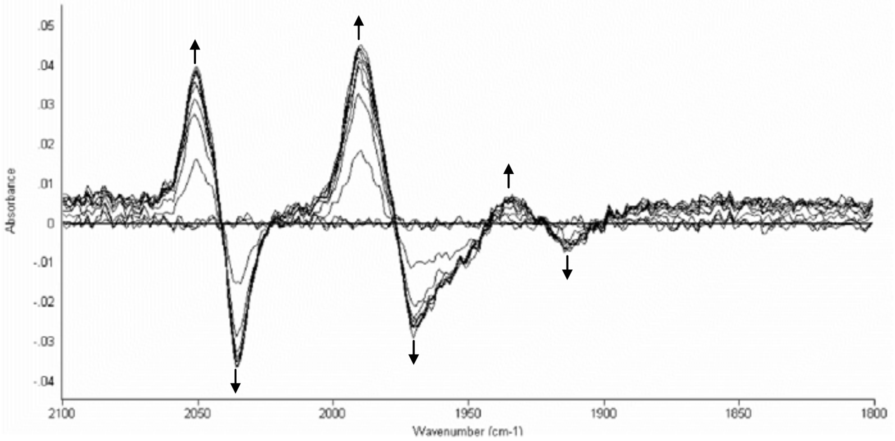

Figure IV-21. IR-SEC of **HCM** in CH$_3$CN under Ar (40 psi); potential applied: +0.8 V (*vs.* Ag wire); timeframe: 0 to 18 s.

Similarities in pattern and intensities suggest that there is no structural change during the oxidation (Figure **IV-22**) involving the di-iron unit, and that the sulfur of the thiolate ligand remains coordinated. Considering the cyclic voltammetry described above and the relatively small shift in frequencies observed for the CO bands, we can also propose that this process involves the removal of a single electron from the cubane. Notably i_p^{ox} for the oxidation process is close to i_p^{red} for the reduction process of the cluster centre.

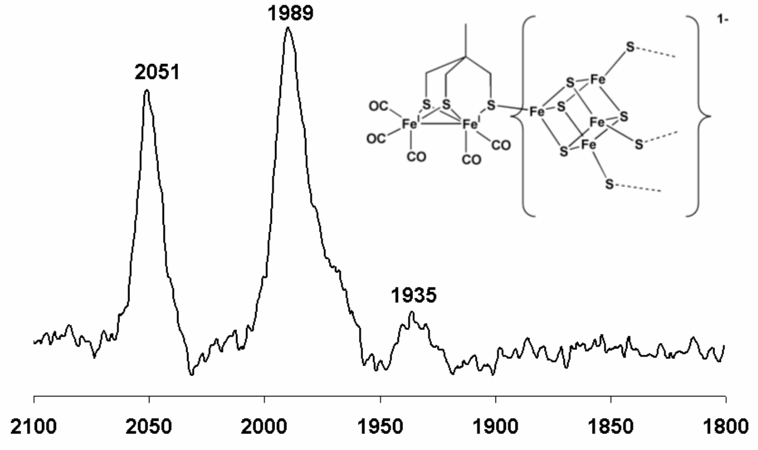

Figure IV-22. IR-spectra in CH_3CN obtained from IR-SEC of the oxidised species **O1** formed from **HCM**.

Oxidation under CO reveals the formation of new ν(CO) bands at long-times (Figure **IV-23**). These occur at 2073 and 1934 cm^{-1} and are very close to those measured for the {2Fe2S}-hexacarbonyl complexes (2074, 2035 and 1994 cm^{-1}). It seems likely therefore that oxidation of the cluster makes the proximal Fe-S bond weaker and CO can add this metal centre. This is strikingly similar to the NO_2, NH_2 and NH_3^+ chemistry described in Chapter **II**.

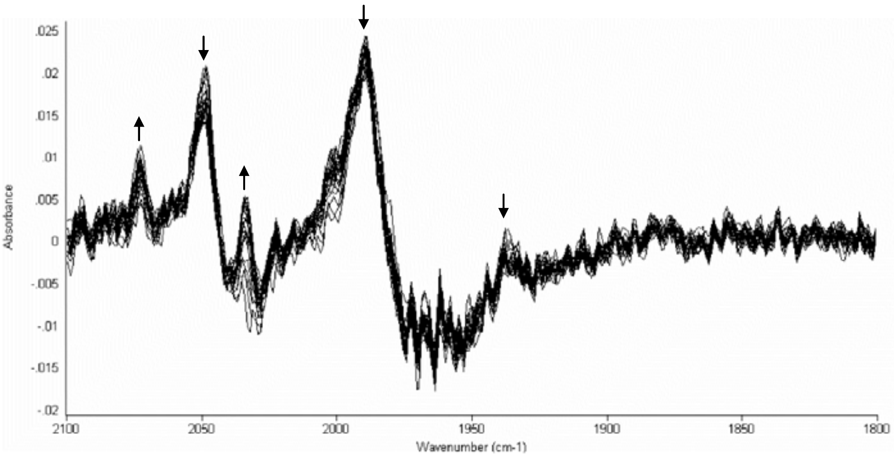

Figure IV-23. IR-SEC of **HCM** in CH_3CN under CO (40 psi); potential applied: +0.6 V (*vs.* Ag wire); timeframe: 60 to 386 s.

This is an interesting observation as a vacant site can be generated by oxidation and therefore addition of H_2 and oxidation into protons might be envisaged. Notably, experiments under a H_2 atmosphere showed a very good dihydrogen uptake, but it was thought to be due to the platinum counter electrode. Thus a counter electrode has to be designed (in carbon) to avoid signals due to Pt. These experiments will be carried out very soon in Melbourne.

In the presence of acid (2,6-lutidinium), different species were observed during the turnover evolving dihydrogen. In the early stages of reduction (-0.9 V), a slightly oxidised product **RH** appears which might be a protonated compound as its spectrum is rather different from the starting material or **O1** (Figure **IV-24**). Then, as the acid concentration is depleted in the thin layer, **R1** is observed and when no acid remains the two-electron reduced **R2** is detected.

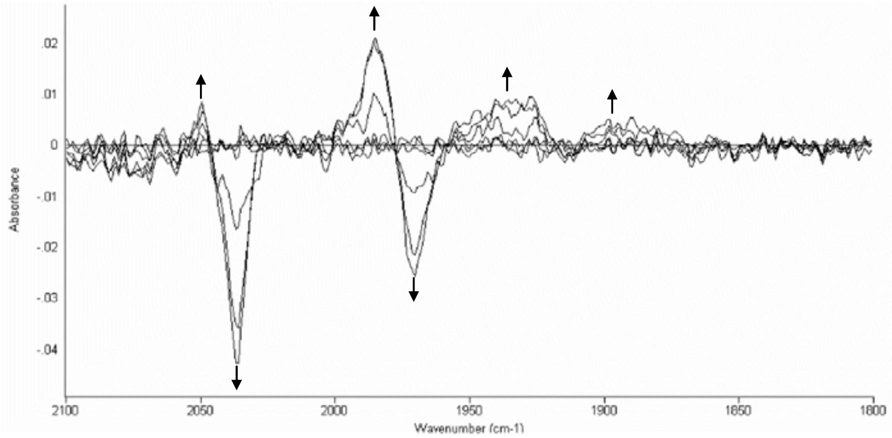

Figure IV-24. IR-SEC of **HCM** in CH_3CN under Ar (40 psi) and in presence of 2,6-lutidinium; potential applied: -0.9 V (*vs.* Ag wire); timeframe: 0 to 9 s.

The infra-red spectrum obtained after subtraction of **HCM** shows a different pattern and suggests structural modification of the molecule (Figure **IV-25**).

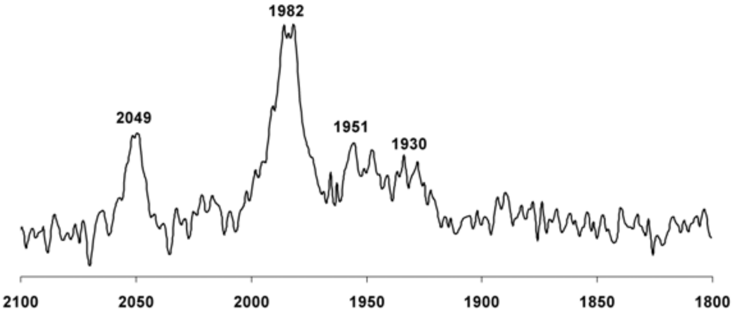

Figure IV-25. IR-spectra in CH_3CN obtained from IR-SEC of **HCM** one-electron reduced protonated specie **RH**.

In presence of higher acid concentration (>10 eq.) and without any electrochemistry applied, an oxidised species is observed with exactly the same spectrum as the oxidised species **O1** obtained by electrochemical oxidation. This suggests that protons are able to oxidise **HCM** presumably releasing dihydrogen without any potential applied. The FeS cubane would act as a battery, providing the extra electron to release protons. This process might not be very efficient in terms of catalysis, but further investigations will be carried out to understand this interesting observation.

IV.4.c.η Summary of redox reactions of **HCM**

A mechanism summarising the data from electrochemistry and IR-SEC can be proposed in Scheme **IV-10**. Some features will need more investigation, for example, the nature of the protonated species **RH**, whether the thiolate ligand is cleaved, and the mechanism of dihydrogen uptake by the oxidised compound **O1**.

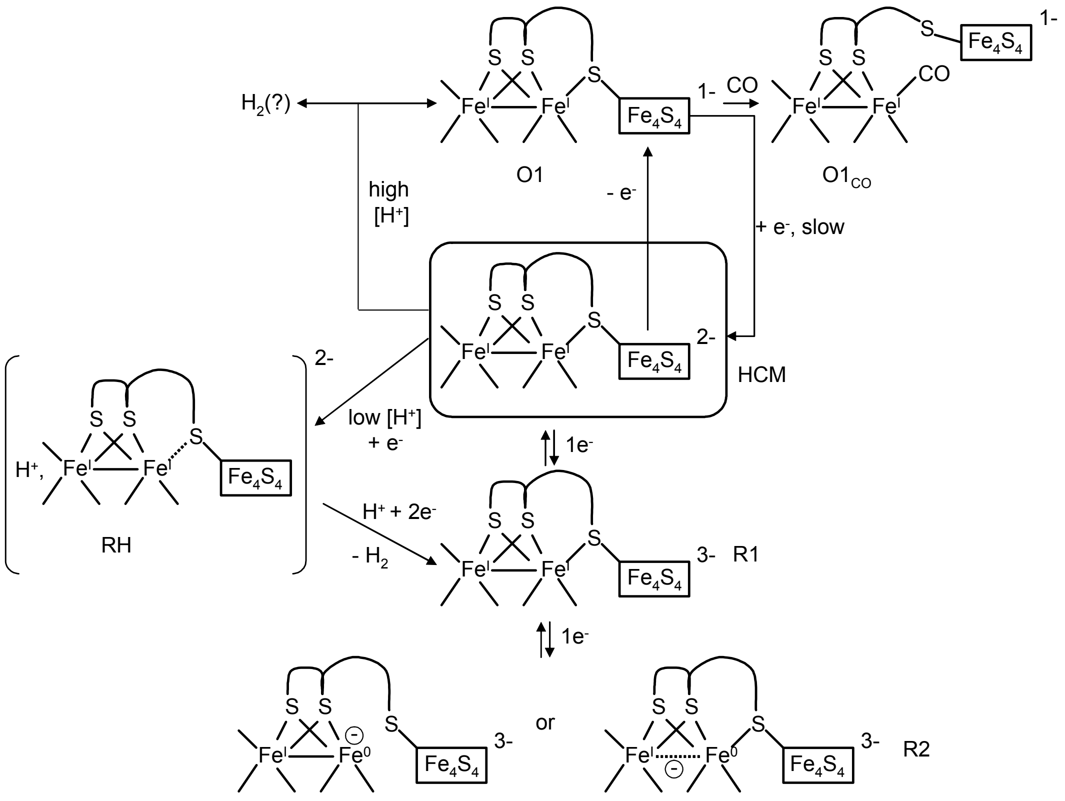

Scheme 10. Proposed mechanism for reduction / oxidation of **HCM** in the presence / absence of CO or acid.

IV.5 Relevance to the natural system

The synthesis of this analogue to the "H-cluster" is the first assembly describing the coupling between an {Fe_4S_4}-cubane cluster and the {2Fe2S}-subsite linked by a μ-S thiolate bridge. As discussed in the first chapter, not much is known about the mechanism of dihydrogen evolution / uptake by the enzyme and the synthesis of this close model allows us to envisage a possible and relevant pathway for this “simple” reaction.

The interesting chemistry developed, coupled with powerful spectroscopic techniques provided us with a first glimpse of the interplay between the FeS cubane and the di-iron centre. This study outlined the fundamental role of the functionality brought by the thioether ligand, whereas all the other systems studied to date are more focused on changing ligands around the di-iron centre or functionalising the dithiolate bridging ligand.[74,75,101,122]

The clear limitation of the present “H-cluster” model is the absence of the cyanide ligand. Unfortunately, generation of the cyanide derivative of **HCM** has not been successful, despite numerous attempts. The introduction of two more negative charges to this dianion species has been problematic and new strategies have to be designed. Oxidative addition of cyanide to the two irons of the subsite would be ideal to reach the Fe(II)-Fe(II) state (similar to H_{ox}-CO) and should permit the two cyanides to be retained. Such experiments will probably provide a better model and a clearer understanding of the intimate mechanism of dihydrogen evolution / uptake.

IV.X Experimental

$CH_3C(CH_2SH)CH_2SCOCH_3$,

Thioacetic acid (3-mercapto-2-mercaptomethyl-2-methyl-propyl) ester (26).

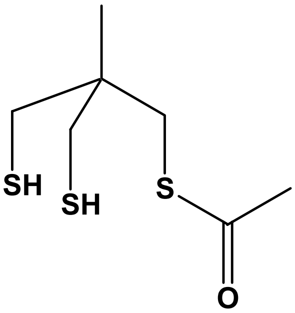

1,1,1-tris(mercaptomethyl)ethane 4 (2.69 g, 16.0 mmol) was dissolved in diethyl ether (50 cm^3). Acetic anhydride (2.2 cm^3, 24.0 mmol) and then sodium hydrogen carbonate (2.0 g, 24.0 mmol) were added and stirred overnight at room temperature. Degassed water was added and the product was extracted with diethyl ether. The organic phase was dried ($MgSO_4$) and then evaporated. The compound was purified by flash chromatography (hexane/chloroform) to give a colourless oil (1.04 g, 31%); ν_{max}/cm^{-1} (SH) 2570, (C=O) 1691 cm^{-1} (nujol); δ_H (400 MHz; solvent $CDCl_3$; standard $SiMe_4$) 1.01 (3H, s, CH_3C), 1.30 (2H, t, *J* 9.0 Hz, 2×SH), 2.37 (3H, s, CH_3CO), 2.56 (2H, d, *J* 2.4 Hz, CH_2SH), 2.59 (2H, d, *J* 2.6 Hz, CH_2SH) and 3.05 (2H, s, CH_2CO); *m/z* 210 $(M)^+$, 167 $(M - CH_3CO)^+$, 133 $(M - CH_3COS)$.

$Fe_2(CO)_6(CH_3C(CH_2S)_2CH_2SCOCH_3)$ (27).

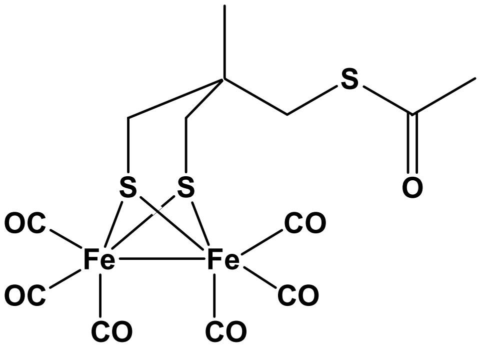

$[Fe_3(CO)_{12}]$ (4.91 g, 9.8 mmol) was dissolved in toluene (60 cm^3) and stirred. **26** (1.75 g, 8.3 mmol) was added and heated at 80°C for 90 min. The dark green mixture turned red. The toluene was removed and the compound was purified by flash chromatography under dinitrogen (degassed hexane/ethyl acetate 95:5) to give a red powder (2.00 g, 50%). The powder was dissolved in acetonitrile (10 cm^3), and slow evaporation of the solvent under a stream of dinitrogen led to the formation of single crystals. (Found C, 32.26; H, 2.48. $C_{13}H_{12}S_3O_7Fe_2$, requires C, 31.99; H, 2.48); ν_{max}/cm^{-1} (CO) 2076, 2037, 2001 and 1697 cm^{-1} (acetonitrile); δ_H (400 MHz; solvent $CDCl_3$; standard $SiMe_4$) 1.03 (3H, s, CH_3C), 2.12 (4H, br, 2×CH_2SFe), 2.36 (3H, s, CH_3CO) and 2.88 (2H, s, CH_2CO); *m/z* 488 $(M)^+$, 460 $(M - CO)^+$, 432 $(M - 2CO)^+$, 404 $(M - 3CO)^+$, 376 $(M - 4CO)^+$, 348 $(M - 5CO)^+$, 320 $(M - 6CO)^+$.

$[Fe_4S_4(Fe_2(CO)_5CH_3C(CH_2S)_3)_4][NBu_4]_2$ (28).

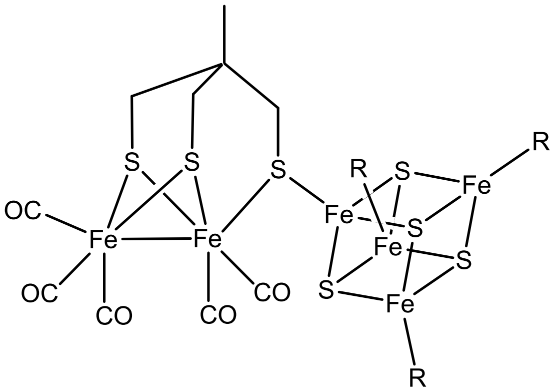

$[Fe_4S_4(SEt)_4][NBu_4]_2$ (106 mg, 0.098 mmol) was dissolved in acetonitrile (15 cm^3) and **27** was added and the mixture was stirred at RT overnight. The solvent was pumped off and the dark brown solid was washed with toluene (200 mg, 0.080 mmol, 82%). ν_{max}/cm^{-1} (CO) 2034, 1970 and 1912 (acetonitrile); m/z 1010 $(M)^{2-}$; Mössbauer spectrum (solid, referenced to 25 μm Fe-foil at 298 K): 80 K: three doublets, isomer shifts at 0.58, 0.39 and 0.20, quadrupole splittings of 0.94, 0.92 and 1.00 $mm.s^{-1}$; 298 K: three doublets, isomer shifts at 0.51, 0.33 and 0.18, quadrupole splittings of 0.93, 0.89 and 0.95 $mm.s^{-1}$.

$C_6F_3Br_3$, 1,3,5-tribromo-2,4,6-trifluorobenzene (30).[111]

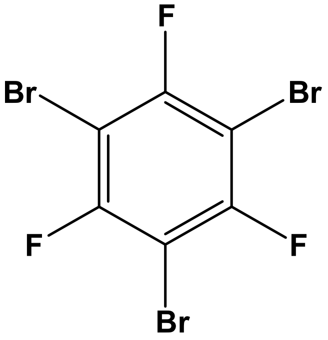

To a solution of bromine (40 cm^3, 780 mmol) aluminium powder was added (0.79 g, 29 mmol). 1,3,6-trifluorobenzene (11.75 cm^3, 110 mmol) was added dropwise with the mixture in an ice bath to cool the reaction (white fumes of HBr evolve). The mixture was heated at 60°C for 1h and then poured into H_2O (100 cm^3). The product was extracted with diethyl ether, dried ($MgSO_4$), filtered and the solvent was removed. The pale orange solid was washed with cold ethanol to give a white solid (30.47 g, 82 mmol, 72%). δ_F (400 MHz; solvent $CDCl_3$; standard $SiMe_4$) -95.79 (s).

Cu_2O, copper oxide.

In a beaker, copper sulphate (69 g, 432 mmol) was dissolved in H_2O (1000 cm^3) and 10 drops of H_2SO_4 were added. In another beaker, $Na_2C_4H_4O_6.(H_2O)_2$ (350 g, 1.5 mol) was dissolved in H_2O (1000 cm^3), and NaOH (100 g, 2.5 mol) was added. The two beakers were mixed and D-glucose was added (54 g, 300 mmol). The mixture was boiled until it becomes red and then filtered, washed with hot water and cold ethanol and dried in the oven to give a red powder (28.2 g, 197 mmol, 91%).

$CH_3C_6H_4SCu$, *p*-tolylthiocuprate (32).[112]

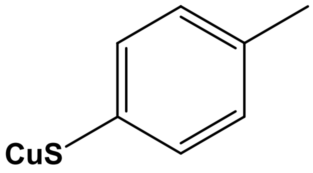

Freshly distilled *p*-thiocresol (40.0 g, 322 mmol) was dissolved in ethanol (400 cm^3) under a nitrogen atmosphere. Copper oxide (28.2 g, 197 mmol) was added and the mixture was stirred under reflux for 3 days. The insoluble solid was filtered, washed with ethanol and acetone and dried under vacuum to give a white solid (57.0 g, 305 mmol, 94%).

$C_6F_3(SC_6H_4CH_3)$, 1,3,5-tris(p-tolylthio)-2,4,6-trifluorobenzene (33).[113]

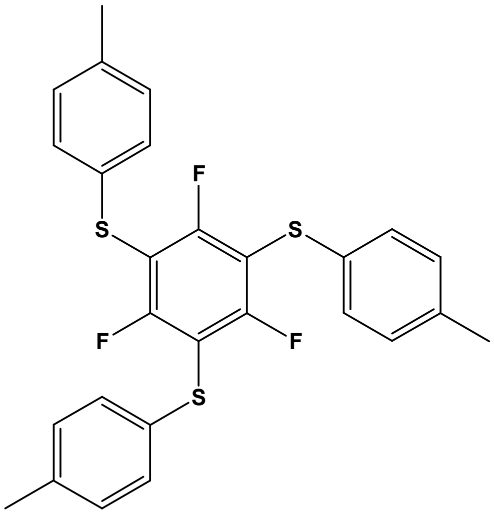

30 (30.5 g, 82 mmol) and **32** (57.0 g, 305 mmol) were dissolved in DMF (500 cm^3) under a nitrogen atmosphere. The slurry was stirred mechanically at 140°C for 36 h. The mixture was poured into ice (1500 cm^3) and HCl 37 % (250 cm^3). The product was extracted with diethyl ether, filtered, washed with K_2CO_3 10 % and NaCl saturated solution, dried ($MgSO_4$) and the solvent was removed to give a white solid (18.8 g, 42 mmol, 52%). δ_H (400 MHz; solvent $CDCl_3$; standard $SiMe_4$) 2.30 (9H, s, 3×CH_3), 7.05 (6H, d, *J* 8.1 Hz, 6×Ph), 7.18 (6H, d, *J* 8.1 Hz, 6×Ph); δ_F (400 MHz; solvent $CDCl_3$; standard $SiMe_4$) -91.60 (s).

$(CH_3)_2C_6H_2(SO_2Cl)_2$, 4,6-dimethylbenzene-1,3-disulfonyl dichloride (35).

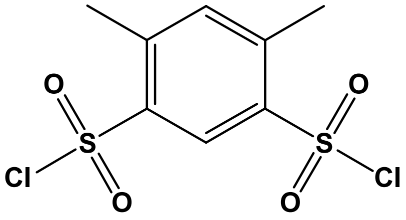

m-xylene (15 cm^3, 122 mmol) was added drop wise to chlorosulfonic acid (100 cm^3, 1.5 mol) at room temperature. The mixture was stirred under reflux (150°C) for 90 min. The dark red solution was then poured into ice (1500 cm^3) and left overnight to complete the precipitation. The solid was then filtered, washed with water and dried under vacuum to give a white solid (32.0 g, 105 mmol, 86%). δ_H (400 MHz; solvent $CDCl_3$; standard $SiMe_4$) 2.87 (6H, s, 2×C*H*$_3$), 7.52 (1H, s, Ph), 8.72 (1H, s, Ph).

$(CH_3)_2C_6H_2(SH)_2$, 4,6-dimethylbenzene-1,3-dithiol (36).[114]

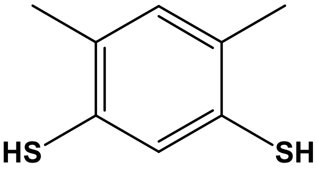

Granulated tin (300 g, 2.53 mol) was dissolved in HCl 37% (800 cm^3) and stirred mechanically. Portions of **35** (30.0 g, 99 mmol) were added and the mixture was stirred under reflux for 2 h. The product was purified by steam distillation, filtered and washed with H_2O to give a white solid (10.3 g, 60 mmol, 61%). δ_H (400 MHz; solvent $CDCl_3$; standard $SiMe_4$) 2.25 (6H, s, 2×C*H*$_3$), 3.21 (2H, s, 2×S*H*), 6.96 (1H, s, Ph), 7.23 (1H, s, Ph); ν_{max}/cm^{-1} (SH) 2559 cm^{-1} (nujol).

$(CH_3)_2C_6H_2(SH)(SCH_2OCH_3)$,

4,6-dimethyl-3-((methoxymethyl)thio)benzenethiol (37).[113]

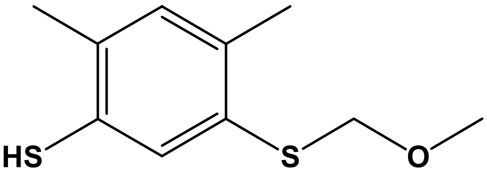

Sodium hydride (60% oil suspension, 2.0 g, 50 mmol) was washed with dry hexane and dissolved in DMF (150 cm^3). **36** (4.0 g, 23 mmol) was added and the solution was stirred for 3 h at RT. Chloromethyl methyl ether (3.8 cm^3, 51 mmol) was then added and after a further 6 h of stirring, NaSEt (1.94 g, 23 mmol) was added and the mixture was heated to 120°C for 3 h. DMF was removed by distillation under ambient pressure leaving a reddish oil, which was dissolved in ether (50 cm^3). Extraction with 5% aqueous NaOH (3×30 cm^3), immediate acidification with 2M AcOH (100 cm^3), extraction into ether (3×30 cm^3), drying of the organic phase ($MgSO_4$) and solvent removal gave the crude monoprotected thiol as a red oil. The product was then purified by flash chromatography (100% hexane then hexane/ether 19:1) to give a colourless oil (2.20 g, 17.7 mmol, 77%). δ_H (400 MHz; solvent $CDCl_3$; standard $SiMe_4$) 2.27 (3H, s, $^{Ph}CH_3$), 2.32 (3H, s, $^{Ph}CH_3$), 3.27 (1H, s, S*H*), 3.43 (3H, s, OCH_3), 4.91 (2H, s, SCH_2O), 6.98 (1H, s, Ph), 7.46 (1H, s, Ph); ν_{max}/cm^{-1} (SH) 2562 cm^{-1} (neat).

$L(SCH_2OCH_3)_3$, 1,3,5-tris(4,6-dimethyl-3-(methoxymethylthio)phenylthio)-2,4,6-tris(*p*-tolylthio)benzene (38).[115]

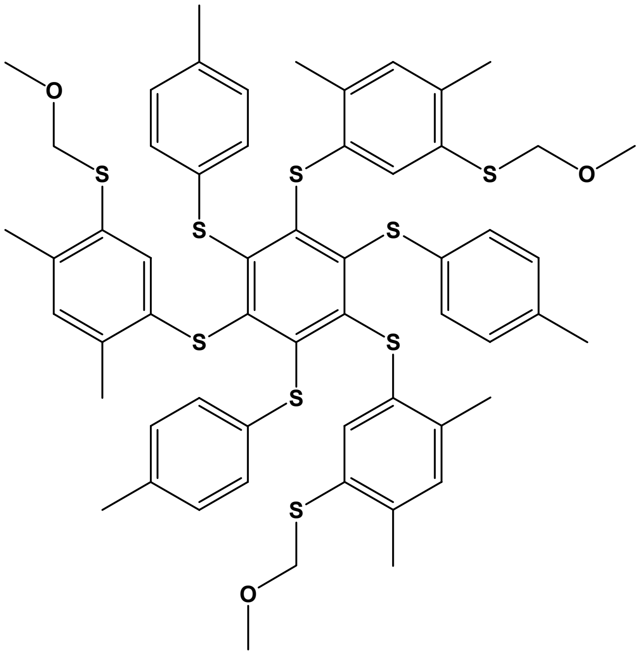

Sodium hydride (60% oil suspension, 0.73 g, 15 mmol) was washed with dry hexane and dissolved in THF. **37** (3.16 g, 14.7 mmol) was added and the orange solution was stirred for 1 h. The THF was then pumped off, the gummy residue was dissolved in 1,3-dimethyl-2-imidazolidinone (DMEU) (30 cm^3) and **33** (1.72 g, 3.9 mmol) was added rapidly. The mixture was stirred for 4 days at 85°C. Diethyl ether (150 cm^3) was then added and the solution was washed with 10% aqueous K_2CO_3 (3×100 cm^3), dried ($MgSO_4$) and the solvent removed to give a brown oil. Flash chromatography of this oil (diethyl ether/hexane, 5% to 20% of diethyl ether) gave an yellow oil (2.1 g, 1.9 mmol, 50%).

L(SH)$_3$,

1,3,5-tris(4,6-dimethyl-3-mercaptophenylthio)-2,4,6-tris(*p*-tolylthio)benzene (39).[110]

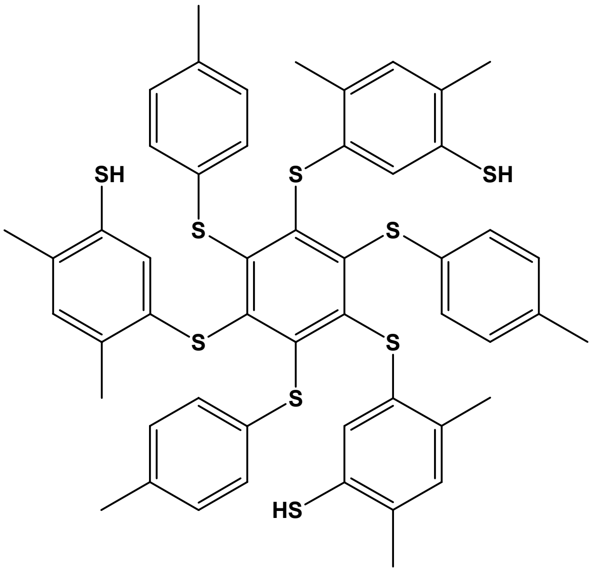

38(0.57 g, 0.53 mmol) was dissolved in degassed chloroform (30 cm^3) and ethanol (2 cm^3). Hg(OAc)$_2$ (0.68 g, 2.12 mmol) was added and the solution was stirred at RT overnight. The solution was then placed under an H_2S atmosphere and bubbled with H_2S for 20 min to consume the excess of the mercury compound. During this time, the solution changed from yellow to orange to brown, and finally to a black-coloured suspension. The mixture was then sparged for 45 min to remove the excess of H_2S and the solution was filtered through a Celite column and eluted with warm chloroform until no yellow colour remained. The solvent was removed under vacuum and the crude solid was washed with warm acetonitrile (5×20 cm^3) to give a yellow solid (0.28 g, 0.3 mmol, 56%). δ_H (400 MHz; solvent $CDCl_3$; standard $SiMe_4$) 2.16 (3H, s, C*H$_3$*), 2.17 (3H, s, C*H$_3$*), 2.27 (3H, s, C*H$_3$*), 3.07 (1H, s, S*H*), 6.44 (1H, s, Ph), 6.84 (1H, s, Ph), 6.85 (2H, d, *J* 12.1 Hz, Ph), 6.96 (2H, d, *J* 11.7 Hz, Ph).

[$Fe_4S_4(LS_3)(SEt)][NBu_4]_2$ (40).[110]

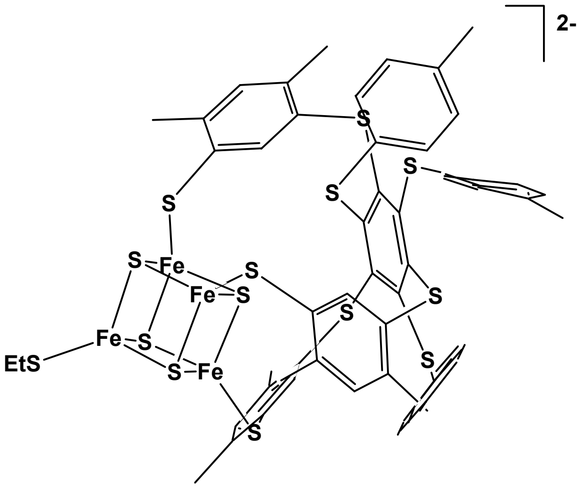

39 (0.26 g, 0.27 mmol) was dissolved in dichloromethane (100 cm^3) on warming at 35°C until the solution became clear. The solution was cooled at RT and $[Fe_4S_4(SEt)_4][NBu_4]_2$ (0.27 g, 0.27 mmol) dissolved in acetonitrile (60 cm^3) was added. The solution was stirred for 30 min at ambient pressure and for a further hour under dynamic vacuum. The solvent was removed under vacuum and the crude product was washed with ether (5×20 cm^3). The product obtained was a black solid (0.32 g, 0.17 mmol, 64%). δ_H (400 MHz; solvent $CDCl_3$; standard $SiMe_4$) 3.48 (3H, s, C*H₃*), 3.92 (3H, s, C*H₃*), 5.00 (1H, br s, Ph), 6.90 (4 H, br, Ph), 7.96 (1H, s, Ph), 12.58 (2H, br, S$CH_2$$CH_3$); ES-MS: m/z 1599.6 (M + $[NBu_4])^-$, 679.1 $(M)^{2-}$; Cyclic voltammogram (CH_3CN, $[BF_4][NBu_4]$ 0.2 M): E° = -1.13 V (reversible), -1.96 V (irreversible).

$[Fe_4S_4(LS_3)(Fe_2(CO)_5CH_3C(CH_2S)_3)][NBu_4]_2$ (HCM).

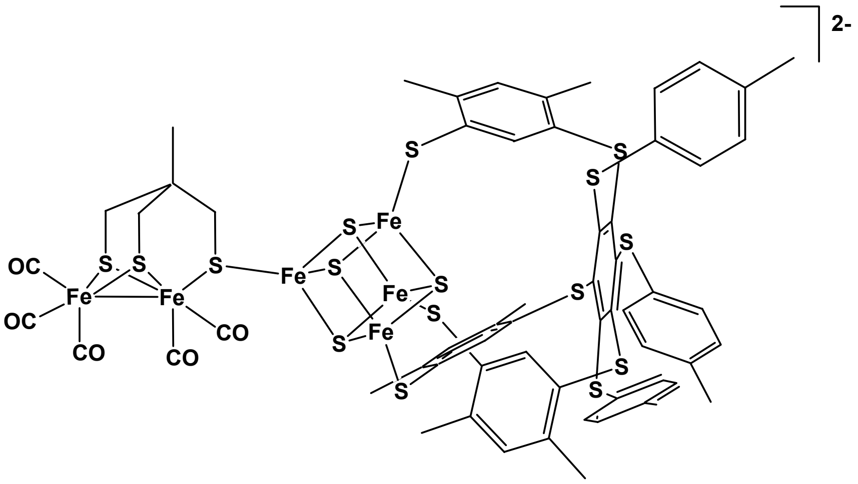

40 (31 mg, 16.8 μmol) was dissolved in acetonitrile (5 cm^3). **27** (11 mg, 22.5 μmol) was added to the black solution and stirred at RT overnight. The solvent was then pumped off and the solid was washed with ether (3×20 cm^3). A black solid was obtained (15 mg, 6.8 μmol, 40%). (Found C, 50.58; H, 5.84; N, 1.04; S, 21.60. $Fe_6C_{93}H_{126}S_{16}N_2O_5$ requires C, 50.77; H, 5.77; N, 1.27; S, 23.32); ν_{max}/cm^{-1} (CO) 2035, 1970 and 1912 cm^{-1} (acetonitrile); ES-MS: m/z 1957.1 $(M + [NBu_4])^-$, 1285.8 $(M - \text{subsite})^-$, 857.0 $(M)^{2-}$, 417.0 $(\text{subsite})^-$; δ_H (400 MHz; solvent $CDCl_3$; standard $SiMe_4$) 4.83 (1H, br, ^{2}H), 5.84 (1H, br, SCH_2C), 6.69 (2H, $^{3'}$H), 7.02 (2H, $^{2'}$H), 8.06 (1H, ^{5}H).

- Chapter V -

Toward new assemblies related to the "H-cluster"

V.1 {2Fe3S}-subsites and electropolymers

V.1.a Fuel cells

The building of an electrode assembly capable of performing dihydrogen evolution / uptake is particularly attractive in the context of electrocatalysts for hydrogen fuel cells, which are critical to the development of the "hydrogen economy".[123]

The principle of fuel cells is rather similar to batteries in the sense that electrical energy is generated by conversion of chemical energy by electrochemical reaction at anode and cathode electrodes (Scheme **V-1**). Differences are in the location of the chemical energy storage and the conversion. Batteries function as closed systems, energy storage and conversion occur in the same compartment. In fuel cells, the components for the redox reaction are stored outside the cell (*e.g.* dioxygen from air or from a tank), therefore energy storage and energy conversion are locally separated.

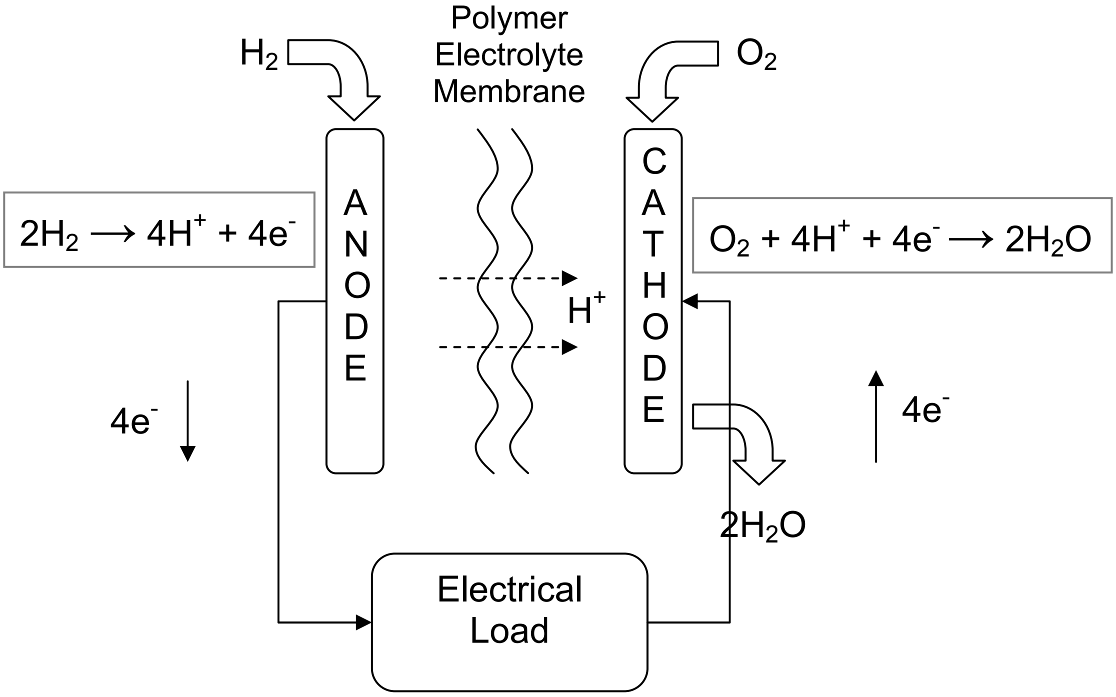

Scheme V-1. Schematic representation of a H_2/O_2 fuel cell.

Advantages of fuel cells compared with batteries are: energy conversion is more efficient; non-polluting sources of energy can be utilised; and a low maintenance is needed. Nevertheless some issues remain as fuel cells are currently expensive, impurities in the gas stream shorten the life of fuel cells and they have limited availability and low durability. The commercial potential of fuel cells depends in part on the ability to reduce the cost of expensive catalysts, for example platinum-based materials, which are currently the most favoured electrocatalysts for dihydrogen oxidation and dioxygen reduction.

Fuel cells would be an ideal solution for motor vehicles or portable electronic devices, and are currently used for long space missions where high energy densities and cryogenic storage of dihydrogen represent a cost saving by lowering the weight of the launch vehicle.

The basic reaction of a H_2/O_2 fuel cell is described by Equation **V-1**.

$$H_2 + \tfrac{1}{2}O_2 \rightleftarrows H_2O \ (\Delta H^o = -285.15\ \text{kJ.mol}^{-1}) \qquad (\mathbf{V\text{-}1})$$

The chemical energy (H_2 and O_2) is converted into electrical energy by controlled electrochemical reactions at each electrode of the cell. The main obstacle to the use of dihydrogen as energy carrier is that it is not a readily available fuel. As we have seen in **Chapter III**, the main source of dihydrogen comes from hydrocarbon reforming and although it is not “green”, a transition to a “hydrogen economy” will involve in the longer term dihydrogen generated from wind, solar, hydroelectric, tidal or nuclear energy. However, any trace amount of CO, CO_2 and H_2S found in this type of dihydrogen gas has to be removed as it causes an irreversible block of the platinum catalyst and thus poisons the electrode.

The design of material not based on precious metals would be a major step toward the use of dihydrogen as a fuel.

V.1.b Kinetics of electrode processes

The rate of an electrochemical reaction at an electrode is controlled by the kinetics of electron-transfer at the solution electrode interface, or if this is fast, the rate at which material diffuses to the electrode (*i.e.* mass-transfer).

The Butler-Volmer equation (**V-2**) is a fundamental electrode kinetic equation and describes the variation of the observed current *i* as a function of the overpotential applied η and the transfer coefficient α.

$$i = i_0[e^{-\alpha n f \eta} - e^{(1-\alpha) n f \eta}] \qquad \textbf{(V-2)}$$

with i_0: exchange current density

α: transfer coefficient

η: overpotential ($E - E_{eq}$)

f: *F*/*RT*

This equation has important implications for electrocatalysts as it correlates the resulting current to the overpotential applied. Two cases can be considered: a large value of i_0 and a small value of i_0. When i_0 is large, little or no overpotential is required to perform the desired reaction (Figure **V-1**). Moreover, if a small overpotential is applied, the resulting current will be largely increased. In the case of small i_0 values, a high overpotential will be required to induce a moderate current flow.

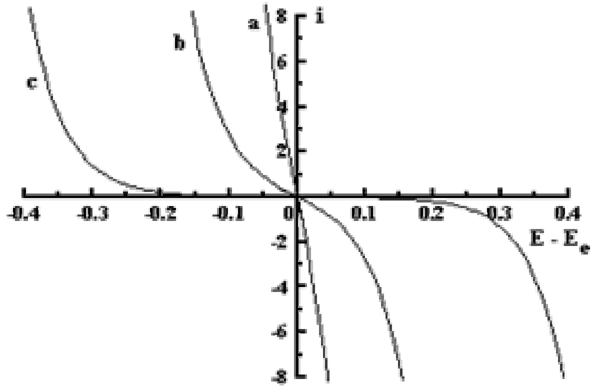

Figure V-1. Variation of the current as a function of the overpotential for (a) a large value of i_0, (b) an intermediate value of i_0 and (c) a small value of i_0 (α = 0.5).

This model illustrates what is required of an efficient electrocatalyst. If an electrode has to transfer an electron to a reactant molecule O but possesses an intrinsic small i_0 value, this charge transfer will be highly unfavourable due to the high overpotential needed for this process. However, an appropriate electrode, or a surface-modified electrode, with a higher i_0 value would then change this process to a kinetically favourable electron transfer. The exchange current density i_0 reflects the electrocatalytic performance of a surface towards a specific reaction**.**

For the reaction we are interested in, the reduction of protons can be achieved by a carbon electrode as well as a platinum electrode, but at very different potential. The ability of a material to perform this reaction at relatively low overpotential will depend on its affinity for the transient species generated (*i.e.* how well the transition state is stabilised, in this case the hydride). This can be schematised as the plot of the exchange current density as a function of the metal-hydride bond strength (Figure **V-2**). If that bond is too weak, this will not favour protons binding to the metal, but in contrast if that bond is too strong, the coupling of H atoms to the surface to form dihydrogen will be unfavourable. Therefore, the resulting material has to be a compromise between these two opposite effects. From this plot, noble metals are the best candidates for catalysis in dihydrogen evolution, and metallic iron is 2 orders of magnitude below platinum in terms of catalytic efficiency.

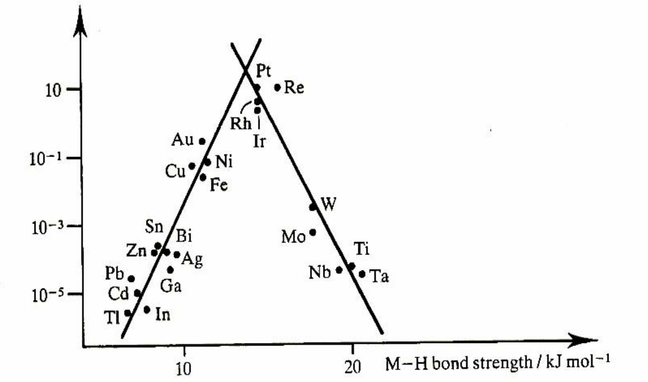

Figure V-2. Exchange current density (A.m^{-2}) as a function of metal-hydride strength (kJ.mol^{-1}).

However, [Fe]-hydrogenase can perform that reaction as efficiently as platinum but with just iron, inorganic sulphur, thiolates, CO and CN ligands. As for noble metals like platinum, the enzyme is able to stabilize the transition state of the catalytic cycle and therefore lowers the energy required to drive that reaction in the desired direction.

Building a surface-modified electrode could be a possibility to introduce our model complexes on a carbon electrode providing a reasonably cheap material capable of dihydrogen evolution / uptake by heterogeneous catalysis. The efficiency of such electrocatalyst will depend on the considerations made above.

An example of a chemically modified glassy carbon electrode supporting a di-iron complex {2Fe2S} relevant to [Fe]-hydrogenase chemistry has been recently described.[124] Grafting of 4-aminophenyl groups on the electrode surface followed by the reaction with a di-iron complex possessing an activated ester group to form an amide bond provides a way toward the formation of a monolayer material. However, this film does not withstand acidic conditions upon reduction as the amide bond is hydrolysed and studies of proton reduction cannot be carried out.

These considerations outline the importance of designing new types of stable catalysts to carry out these redox reactions and incorporate them on an electrode or on a supporting electropolymer capable of fast electron-transfer relay.

V.1.c The poly(pyrrole) framework

Most polymers are unable to carry electricity and their insulating properties have been extensively applied, notably with plastics (*e.g.* the insulating polymer around electrical wire). However, during the past two decades, a new class of organic polymers has been developed and exhibits remarkable conducting properties. Their alternate structures of π-conjugated systems and double bonds along the polymeric chain give them interesting electrical properties. Polymerisation occurs by electrochemical oxidation at potentials that form free radicals.

Poly(pyrrole) is a conductive polymer due to hopping of electrons through the polymer. Chemical oxidation of pyrroles leads to fine poly(pyrrole) powders, but electrochemical oxidation provides free-standing poly(pyrrole) films (Scheme **V-2**). These radicals are adsorbed on the electrode surface and multiple rearrangements lead to the polymer network. The growth of this polymer depends on its electrical character, and the growth of conductive polymers is virtually unlimited. The electrode potential and the reaction time allow the control of the thickness of the film and can be generated by cycling the potential or using a fixed potential.

Electrode coatings can be done on platinum or, more interestingly in term of fuel cells, on glassy carbon electrodes.

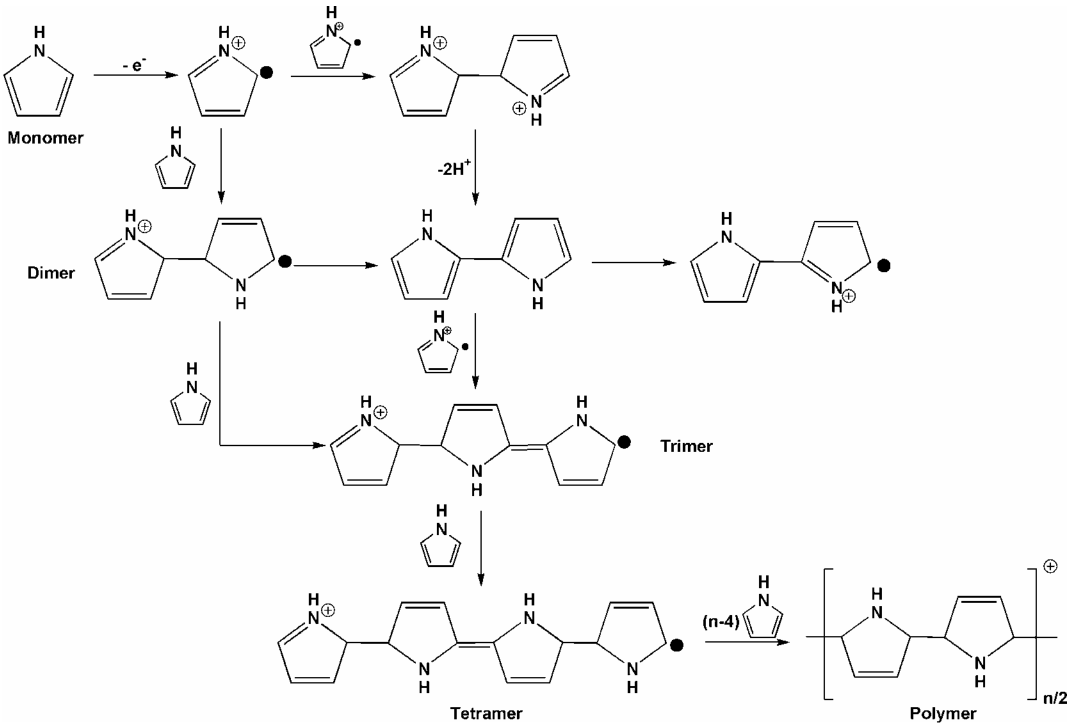

Scheme V-2. Scheme of the radical polymerisation of a pyrrole monomer.

V.1.d {2Fe3S}-pyrrole polymerisation

The functionalisation of poly(pyrrole) has been shown in the lab to be a successful method to introduce iron-sulfur analogues into an electropolymer.[125-127] Synthesis of cysteinyl-pyrrole derivatives followed by oxidative polymerisation led to the formation of an electropolymer with functional thiol groups. Exchange reaction occurs with {Fe_4S_4}-clusters and incorporation of cubanes into the polymer framework can be characterised by electrochemistry.

It was therefore evident that the most straightforward route toward the synthesis of an electropolymer functionalised with a di-iron subsite would be the synthesis of an {2Fe3S}-pyrrole complex (**21**). Studies of electropolymerisation and incorporation of subsites into polymers in general was carried out with Dr. S. K. Ibrahim.

The synthesis of the ligand and the complex have been described previously together with its reductive electrochemistry (see **II.4**).

Attempts to produce electropolymers *via* the approach outlined in Scheme **V-3** were undertaken. The pyrrole-derivative complex was oxidised in an acetonitrile electrolyte and the current response is shown in Figure **V-3**.

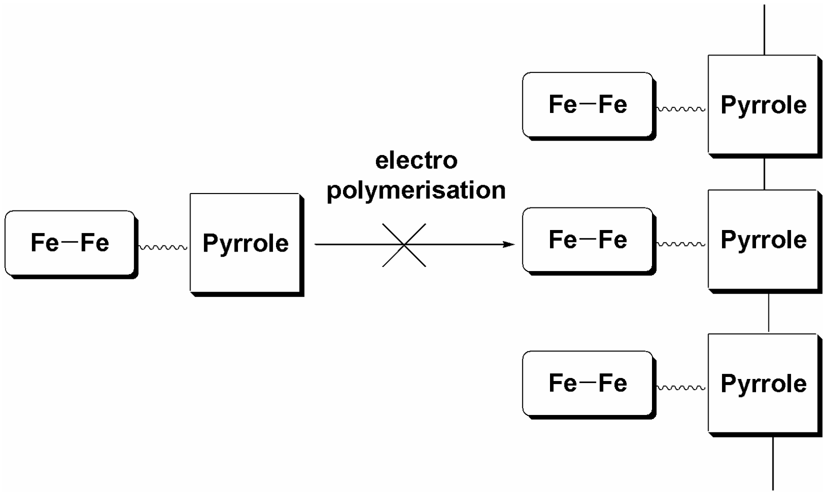

Scheme V-3. Schematic representation of the electropolymerisation of the pyrrole-derivative complex.

We did not observe the growth of a poly(pyrrole) film. Thus the “direct” strategy failed because the di-iron subsite is irreversibly oxidised before the oxidative polymerisation of the pyrrole can occur (Figure **V-3**). This could be expected because of the quite high potential which is required for poly(pyrrole) formation (*ca.* +1.0 V) compared to the first oxidation of the di-iron centre (*ca.* +0.75 V).

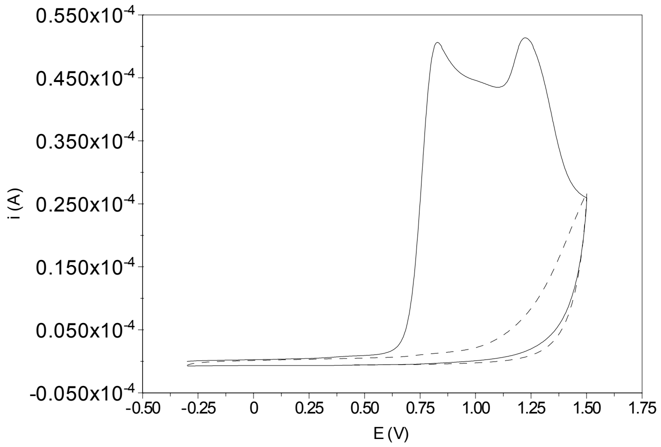

Figure V-3. Cyclic voltammogram of [$Fe_2(CO)_5\{CH_3(CH_2S)_2CH_2SCH_2CH_2$-N-Pyrrole}] (**21**) in acetonitrile (0.2 M [NBu_4][BF_4]). The first scan shows the primary oxidation of the di-iron complex followed by the oxidation of the pyrrole (plain line) and the second scan shows that the complex has been irreversibly destroyed (dashed line).

V.1.e Post-polymerisation

V.1.e.α {2Fe3S}-pentacarbonyl polymers

As discussed above, the direct approach failed, therefore another strategy was adopted utilising post-polymerisation modification procedures. A polymer containing a reactive group is used to bind covalently by chemical procedures a redox sensitive group.[125] For example, active ester polymers possessing pentafluoro or ortho/para-nitrobenzene groups react cleanly and rapidly with amine or alcohol groups to give amide or ester moieties, respectively.

The synthesis of the {2Fe3S}-ethanol subsite derivative **20** was thus successfully achieved as described above (see **II.4**).

The synthesis and electropolymerisation of the pentafluorophenolate "active ester" monomer were carried out by an established method [125] (0.6 V *vs.* Fc^+/Fc in CH_3CN 0.05 M [NBu_4][BF_4]) and give conducting films of the polymer of *ca.* 100 nm thickness (golden-yellow in the reduced-state).

The reaction of the alcohol-derivative complex **20** with the active ester polymer in basic conditions was monitored by diffuse reflectance FTIR spectroscopy. The characteristic depletion of the pentafluorophenolate ester band at 1784 cm^{-1} together with the appearance of another ester band at 1736 cm^{-1} corresponded well with the replacement of the high frequency of an ester band due to a strong withdrawing group (the pentafluorobenzene) by a C=O frequency for alkyl ester (Scheme **V-4**). Intense ν(C≡O) stretches are also observed between 1900 and 2100 cm^{-1} and confirm the covalent attachment of the di-iron complex to the poly(pyrrole) backbone.

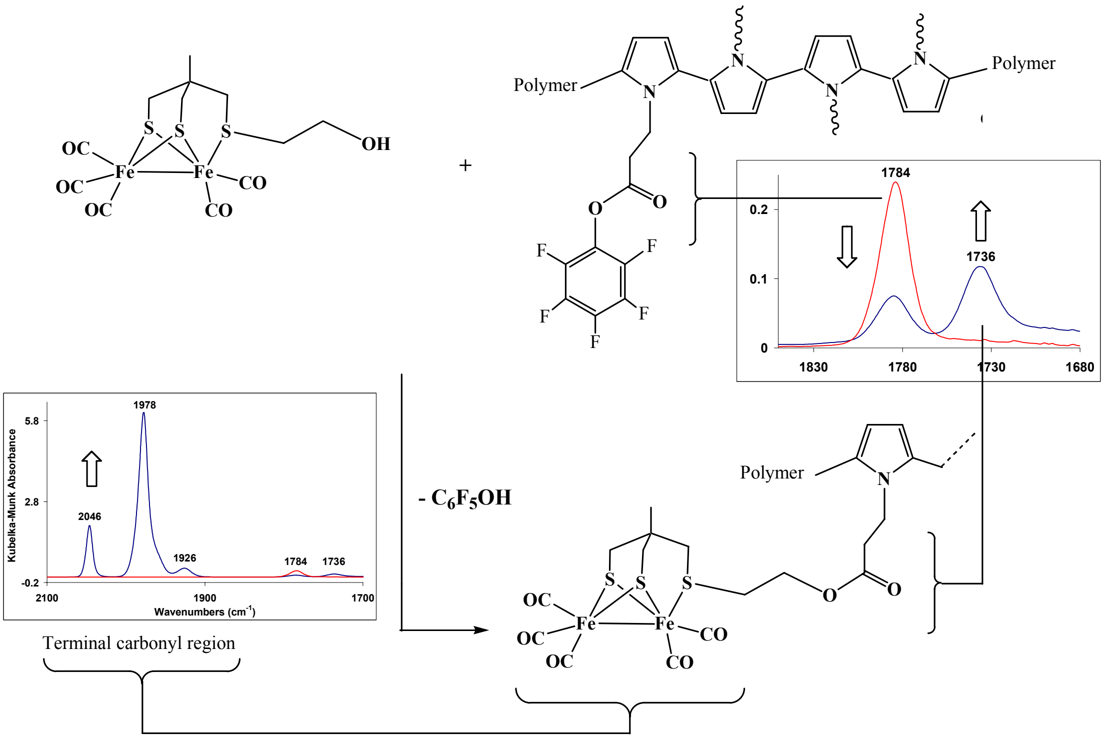

Scheme V-4. Reaction of {2Fe3S}-ethanol complex **20** with the active ester poly(pyrrole). Red FTIR spectrum shows the carbonyl spectrum before the reaction and blue spectrum shows the partial reaction.

The exposure of the poly(pyrrole) to the di-iron complex was carried out for 16 h at room temperature and showed a complete trans-esterification characterised by reflectance FTIR.

Cyclic voltammogram of the free {2Fe3S}-ethanol complex shows a similar behaviour to previously derived {2Fe3S}-systems and exhibits a primary quasi-reversible reduction potential at $E_{p/2}$ = -1.27 V (in CH_3CN, 0.2 $[NBu_4][BF_4]$) (Figure **V-4(a)**). In the same conditions, the di-iron electropolymer shows a similar reduction wave at $E_{p/2}$ = -1.22 V.

V.1.e.β Proton reduction by modified poly(pyrrole)

In the presence of protons, the catalytic reduction response takes place at $E_{p/2}$ = -1.20 V (Figure **V-4(b)**), a potential *ca.* 120 mV more positive than the potential observed for reduction of protons by the poly(pyrrole) electropolymer ($E_{p/2}$ = -1.32 V) and *ca.* 90 mV more positive than the unmodified glassy carbon electrode. Even if this material electrocatalyses proton reduction at a high overpotential, at an equivalent concentration of acid the current density for proton reduction on the di-iron electropolymer can be estimated to be six times higher than for the poly(pyrrole) electropolymer (measured at E = -1.20 V).

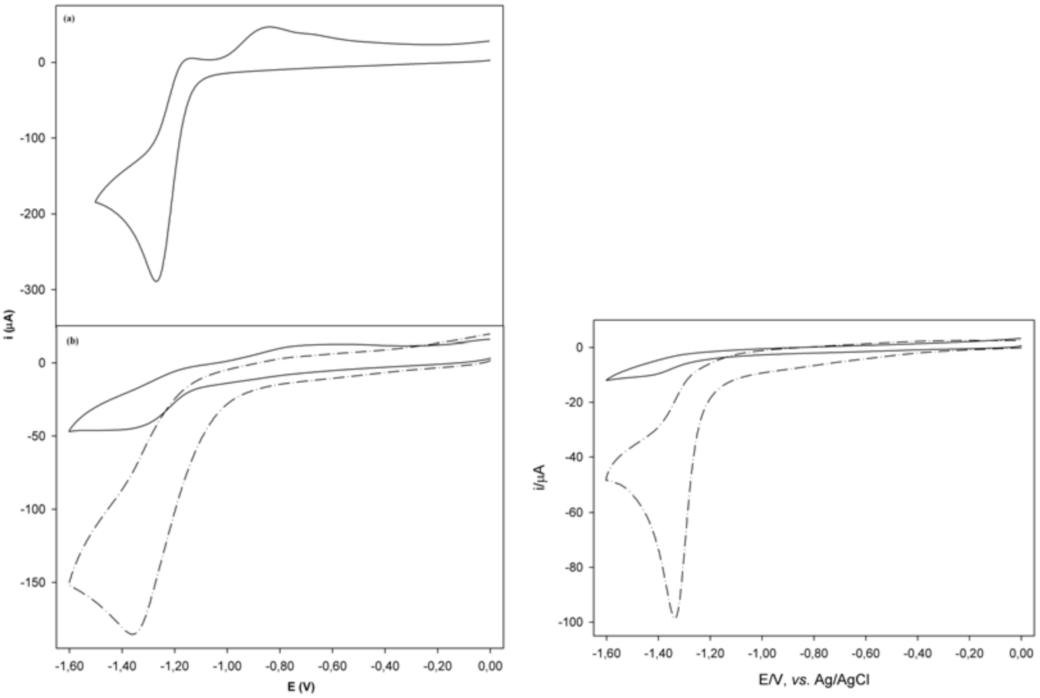

Figure V-4. Electrochemical behaviour of solution- and polymer-bound di-iron subsite analogues in acetonitrile (0.2 M [NBu$_4$][BF$_4$]). Right: (a): cyclic voltammetry of {2Fe3S}-ethanol at vitreous carbon electrode (15 mM; 0.1 V.s^{-1}; electrode area 0.77 cm^2); (b) cyclic voltammetry of di-iron poly(pyrrole) in the absence (solid line) and the presence (dashed line) of [LuH$^+$] = 16 mM (0.1 V.s^{-1}; electrode area 0.77 cm^2; film thickness 0.8 – 1 µm). Left: Electrochemical behaviour of [LuH$^+$] = 33 mM at uncoated vitreous carbon electrode (dashed line; 0.1 V.s^{-1}; nominal electrode area 0.126 cm^2 ; RT) and at the same electrode coated with the poly(pyrrole) electropolymer at a film thickness *ca.* 0.5 -1 µm (solid line; 0.1 V.s^{-1}).

V.1.e.γ Cyanation of di-iron subsite complexes

As described in the introduction, cyanation of {2Fe3S}-pentacarbonyl complexes follows a mechanism resembling a dicyanide species involving transient monocyanide and a bridging carbonyl mode.[65] In the di-iron poly(pyrrole) film, the reaction with [NBu$_4$][CN] just led to a limited reaction due to the tendency of this type of polymer to exclude cations, which are necessary to maintain charge neutrality within the film.

A new poly(pyrrole) film was then prepared by co-electropolymerisation of the pentafluorophenolate pyrrole used previously and a cationic tetra-alkylammonium pyrrole monomer to form a positively charged film able to sustain negatively charged complexes. The ratio of the two monomer precursors can be changed to allow more or less negative charge to penetrate into the polymer.

At low concentration of the cation monomer precursor in the film, the monocyanation is the predominant reaction as observed with ν(CO) and ν(CN) bands similar to those characterised for $[Fe_2(CO)_4(CN)\{CH_3C(CH_2S)_2CH_2SCH_3\}]^-$ in solution (Scheme **V-5(b)**).[63] Increasing the presence of the cation into the polymer allows more negative charge to penetrate and therefore a di-substitution by cyanide ligands can be observed corresponding to IR frequencies of $[Fe_2(CO)_4(CN)_2\{CH_3C(CH_2S)_2CH_2SCH_3\}]^{2-}$ (Scheme **V-5(c)**). Interestingly, a simple $[Fe_2(CO)_4(CN)_2(pdt)]^{2-}$ can be introduced within the polymer film by simple anion-exchange with BF_4^- at high concentration of the cation precursor and exhibits similar features to free {2Fe2S}-dicyanide complexes (Scheme **V-5(d)**).[58]

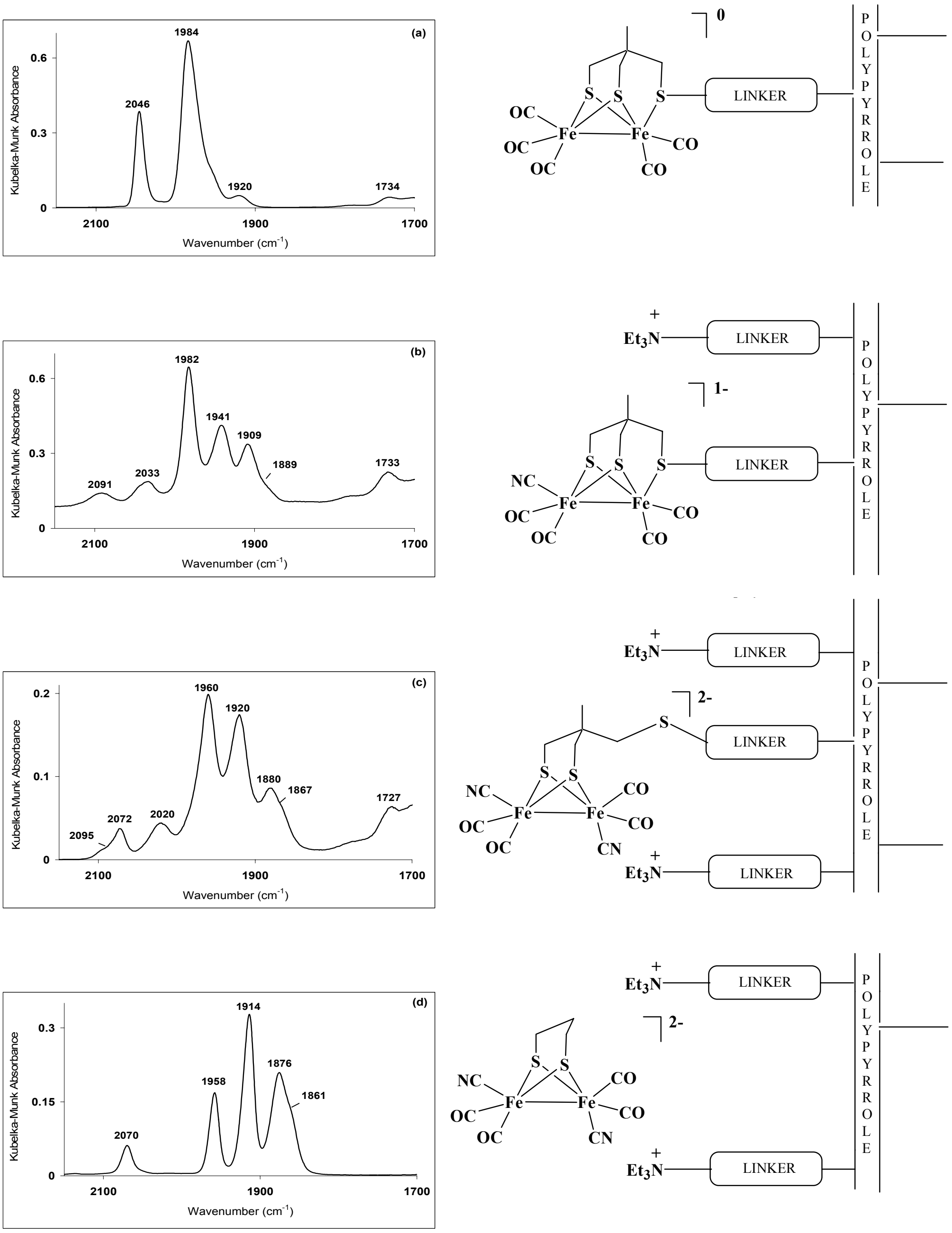

Scheme V-5. Diffuse reflectance FTIR data for CO and CN frequencies of di-iron subsite models on poly(pyrrole) polymer: (a) covalently linked {2Fe3S}-pentacarbonyl; (b) covalently linked {2Fe3S}-monocyanide; (c) covalently linked {2Fe3S}-dicyanide; (d) electrostatically linked {2Fe2S}-dicyanide.

These experiments demonstrate that it is possible to incorporate our {2Fe3S}-subsite model complexes into an electropolymer film grown on platinum or a glassy carbon electrode and this opens the way for experiments on dihydrogen evolution / uptake.

V.2 Replacing iron by cobalt: a route toward stable Co(I)-Co(II) and / or Co(II)-Co(II) "H-cluster" analogues?

Taking all the findings of our di-iron systems together, only Fe(I)-Fe(I) oxidation states are accessible, even if a transient Fe(I)-Fe(II) species has been observed and characterised by FTIR and electrochemistry presenting similar spectroscopic features to the semi-reduced form of the "H-cluster".[128] However, the lack of data on higher oxidation state model complexes led us to envisage the insertion of other metals hopefully to provide stabilisation of these inaccessible redox states. The recent synthesis of a di-ruthenium complex [$Ru_2(CO)_4(PCy_3)_2$(pdt)] demonstrated the first addition of H_2 on a [Fe]-hydrogenase with terminal and bridging hydride crystal structures reported and outlined the study of these bridging thiolate systems with new metals.[69]

As described previously, the trithiol ligand can react with different carbonyl-metals (e.g. Ir, Hg, Rh) [78-80] (see **II.1**) but no reactivity of other metals than iron has been studied with the dithiol-thioether ligand. When considering the objectives in terms of the "hydrogen economy", expensive metals like ruthenium or rhenium cannot be envisaged as alternatives to platinum and therefore reactivity of our ligand with cobalt carbonyl complexes has been carried out.

Cobaloximes have been recently examined in order to electrocatalyse proton reduction at moderate potential,[129] but this type of assembly does not exhibit any structural or spectroscopic feature of the active site of the enzyme and can therefore only be considered as functional models for hydrogenases.

V.2.a Cobalt-carbonyl complexes

Cobalt seems to be an interesting metal to consider as it just differs from iron by one extra electron in its *d* orbitals. A trend toward the series Ti, V, Cr, Mn, Fe, Co and Ni shows a decrease in the stability of very high oxidation states as Z increases, and a stabilisation of the +2 state relatively to the +3 state.

Cobalt carbonyl complexes have been well characterised and can form low-valence carbonyl complexes (*e.g.* $Co_2(CO)_8$) as well as high-valence carbonyl complexes (e.g. $[Co_6(CO)_{15}H]^-$). Oxidation states for the low-valence type vary from -1 to +1 and usually contain many carbonyl groups to help the stabilisation of these low oxidation states. Metal-metal bonds in these complexes are relatively long (>2.80 Å).

The starting material considered in this study is the di-cobalt octacarbonyl $[Co_2(CO)_8]$. This represents one of the simplest binuclear carbonyls as it satisfies the 18-electron rule due to the odd atomic number of cobalt. Thus, $Co(CO)_4$ is a radical 17-electron configuration, but it dimerises to complete its valence shell by a metal-metal bond. Three isomers exist in solution but only two structures are known (Scheme **V-6**).[85] The doubled-bridged structure (Scheme **V-6(b)**) predominates in solution at low temperature and is the only one contained in the crystalline form. This form is slightly favoured compared to the non-bridged form (ΔG^o difference is only a few kJ.mol^{-1}) because of the higher coordination number around the metal given by the bridged isomer and the metal-metal bond, and the smaller steric effect due to this arrangement.

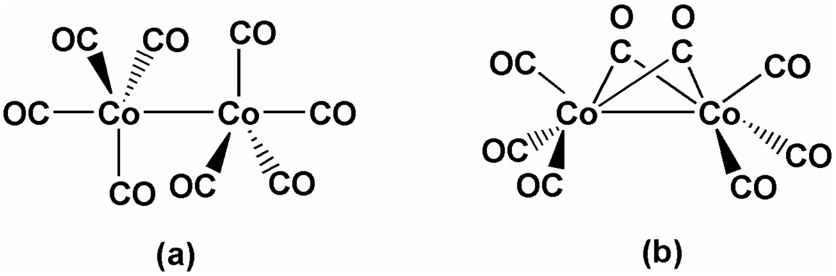

Scheme V-6. Structures of dinuclear cobalt complex $[Co_2(CO)_8]$ (adapted from reference [85]).

$[Co_2(CO)_8]$ is also known to be a good catalyst for the hydroformylation of alkenes into aldehydes containing one more carbon.[130] The active catalyst $[CoH(CO)_4]$ is obtained at a high pressure of dihydrogen, and under high pressure of CO and can introduce a carbonyl on a terminal alkene.

Carbonyl ligands can be displaced by phosphines or phosphites to lead to mono-substitution (e.g. $[Co_2(CO)_7(PY_3)]$) or di-substitutions (e.g. $[Co_2(CO)_6(PY_3)_2]$) as observed for iron-carbonyl complexes.[131]

V.2.b Cobalt-carbonyl clusters

The high reactivity of $[Co_2(CO)_8]$ toward various reactants under mild conditions yields a wide variety of cobalt-carbonyl derivatives. Reaction with elemental sulfur (in heptane at 35ºC) leads to several $Co_x(CO)_yS_z$ clusters: $[Co_3(\mu_3\text{-}S)(CO)_9]$ (obtained also with several mercaptans and disulfides, and also with CS_2), $[Co_3(\mu_3\text{-}S)(\mu_4\text{-}S_2)(CO)_7]$, $[Co_4(\mu_4\text{-}S)_2(CO)_{10}]$ and $[Co_6(\mu_3\text{-}S)_8(CO)_6.3S_8]$.[132] This simple experiment shows the high affinity of cobalt complexes for sulfur, similar to previous observations made for iron but also a tendency to form polynuclear products.

Bridging thiolate compounds with di-cobalt metal centres and CO ligands are also known but the literature is much less abundant than for the corresponding di-iron complexes.[133] As far as we know, only two complexes of the type {2Co2S} have been synthesised and characterised involving strongly withdrawing thio-ligands: $[Co_2(CO)_6(SC_6F_5)_2]$ and $[Co_2(CO)_6(SC_6Cl_5)_2]$.

V.2.c Reaction of $[Co_2(CO)_8]$ and $CH_3C(CH_2SH)_2CH_2SCH_3$

As for the preliminary studies for a {2Fe3S}-model complex of the subsite of the "H-cluster" of [Fe]-hydrogenase,[64] we decided to investigate the reactivity of the dithiol-methylthioether ligand (**42**) with di-cobalt octacarbonyl. The high reactivity of the cobalt complex and the well known coordination behaviour of the dithiol ligand suggested that we might make $[Co_2(CO)_5\{CH_3C(CH_2S)_2CH_2SCH_3\}]$ under the same conditions (Scheme **V-7**).

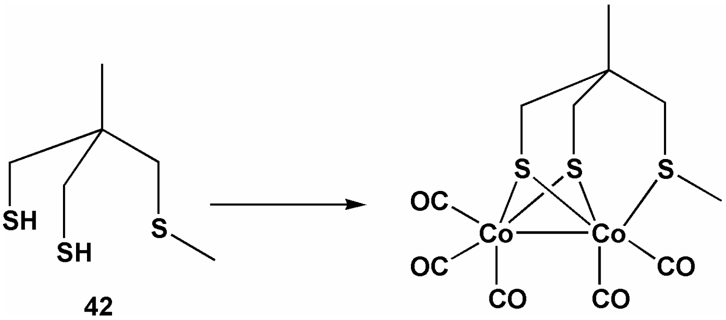

Scheme V-7. Postulated reaction between $CH_3C(CH_2SH)_2CH_2SCH_3$ and $[Co_2(CO)_8]$.

At 85ºC in toluene for 90 minutes, the dark red mixture turned dark brown and after evaporation of the solvent, the brown isolated solid was purified by column chromatography (diethyl ether and ethyl acetate) (Scheme **V-8**).

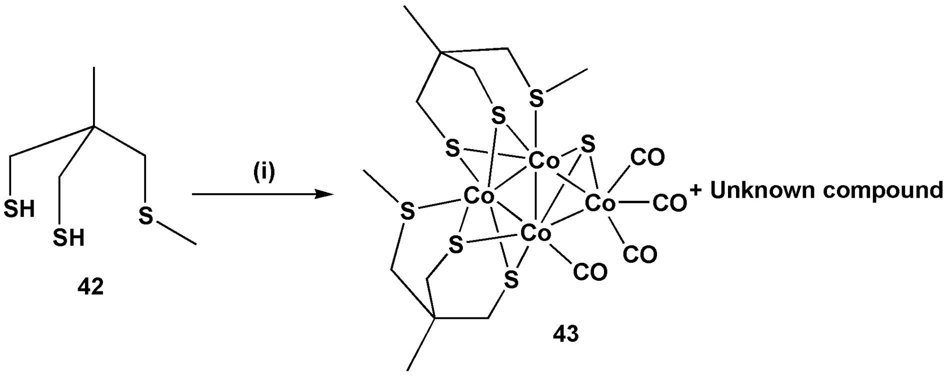

Scheme V-8. Synthesis of the tetracobalt-carbonyl complex **43**. (i) $[Co_2(CO)_8]$, toluene, 70°C.

Two major compounds can be isolated. Both of them exhibit CO frequencies in their infra-red spectra (ν(CO) = 2017(s), 2005(s), 1796(br) and 1705(br); 2047(sh), 2023(s), 2005(s), 1977(w) and 1942(sh) cm^{-1}), but only the more polar compound gave crystals suitable for X-ray diffraction after slow evaporation of the solvent (Figure **V-5**). From infra-red data, the unknown cobalt-carbonyl compound seems to possess two bridging carbonyl ligands (ν(CO) 1796 and 1705 cm^{-1}).

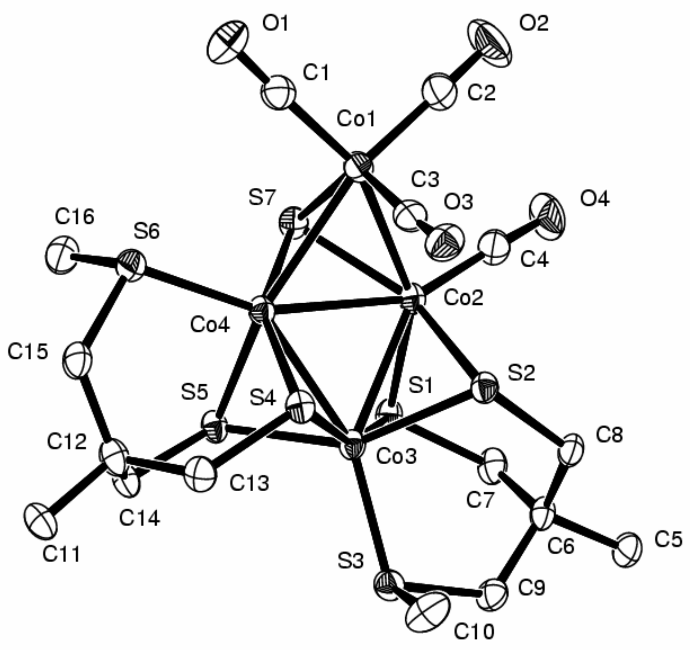

Figure V-5. ORTEP view of [$Co_4\{CH_3C(CH_2S_2)CH_2SCH_3\}_2(\mu_3\text{-}S)(CO)_4$] (**43**) depicted with 50% thermal ellipsoids. All hydrogen atoms have been omitted for clarity. Selected bond distances (Å) and angles (deg): Co(1)-Co(2) = 2.5631(9), Co(1)-Co(4) = 2.6076(9), Co(2)-Co(3) = 2.5470(9), Co(2)-Co(4) = 2.6035(8), Co(3)-Co(4) = 2.4645(9), Co(1)-S(7) = 2.1842(13), Co(2)-S(7) = 2.1736(14), Co(4)-S(7) = 2.1506(13), Co(2)-Co(1)-Co(4) = 60.46(2), Co(3)-Co(2)-Co(4) = 57.16(2), Co(1)-Co(2)-Co(4) = 60.62(2), Co(4)-Co(3)-Co(2) = 62.57(3), Co(3)-Co(4)-Co(2) = 60.27(2), Co(2)-Co(4)-Co(1) = 58.92(2), Co(3)-Co(2)-Co(1) = 111.25(3), Co(3)-Co(4)-Co(1) = 112.49(3).

The structure obtained was unexpected. The tendency of cobalt-carbonyl complexes to form larger clusters is described in the literature on this type of assembly as outlined above.[132,134,135]

The rhombus shape of the four octahedral cobalts is held by two dithiolate ligands. The sum of all the angles of the two triangles in the rhombus is exactly equal to 360° which confirms the planarity of the four-metal centre. Thioether groups also complete the coordination sphere of the metals. Only four CO ligands remain with three supported by one single cobalt. The average length of cobalt-cobalt bonds is 2.55 Å, but range from 2.46 to 2.60 Å. These bond lengths are similar to what we found for metal-metal bonds in the di-iron complexes.

Surprisingly, a μ_3-sulfur bridges three cobalts. The extra sulfur found in the crystal structure might come from desulfurisation of thiolate ligands which have not reacted with the cobalt carbonyl complex.

Bimetallic clusters Mo/Co with carbonyl and sulfur ligands reported by Curtis and co-workers showed also this tendency to pick up sulfur from thiolates in solution.[136] The cluster $[Cp'_2Mo_2Co_2S_3(CO)_4]$ can react with organic sulfur compounds (*e.g.* ^{t}BuSH, PhSH or thiophene) to give the bimetallic cubane cluster $[Cp'_2Mo_2Co_2S_4(CO)_2]$. Products of this reaction are parent hydrocarbon compounds for thiols and saturated and unsaturated hydrocarbons for the thiophene.

This reaction, called hydrodesulfurisation (HDS), has a fundamental role for the petroleum industry as it removes undesired thiols and thiophene compounds from fossil fuels and converts them into suitable hydrocarbons. This is highly relevant for the environment as these derivatives present in fuels are considered as major air pollutants. New environmental standards to reduce the emission of sulfur oxides produced during the combustion require 20 ppm sulfur content in gasoline whereas a 10-20,000 ppm level is found naturally in petroleum. Some precious metal catalysts used in subsequent re-forming reactions are also sulfur-sensitive and this process would prevent this poisoning.

Common catalysts for the HDS process are based on Co/Mo/S compositions (and related Ni/W/S systems) at high temperature (*ca.* 400ºC). Thiols (and thiophenes) can adsorb on the catalyst surface and it is thought that the molybdenum forms a Mo=S bond and releases the hydrocarbon. The catalyst is then regenerated with dihydrogen to form H_2S, which can then be transformed into sulphuric acid.

The mechanism and role of each component of the catalyst during the process are still unresolved, as well are the problem of thiophenes [137] which are more difficult to desulfurise than thiols or alkyl sulfides due to the stability of their aromatic ring.

Metal complexes activating C-S bonds of thiols or thiophenes have been investigated as well as Mo/Co/S clusters to mimic the environment of the catalyst.[136]

The molecule described here would be the first example as far as we know of a cobalt-carbonyl complex able to do similar chemistry. Unfortunately, the lack of structural information for the precursor of this product does not allow postulation of a plausible mechanism. The other compound purified in the column might be the initial compound, as another experiment carried out at lower temperature (85ºC) gave more of the unknown product compared to the tetracobalt complex characterised.

Redox states of cobalts deduced from the crystal structure give formally two Co(I) and two Co(II), confirming that high oxidation states might be accessible by utilising cobalt as a metal centre.

Electrochemistry of **43** showed three processes for the reduction of the rhombic tetra-cobalt complex (Figure **V-6**). The primary reduction ($E_{½}$ = -0.93 V) seems to correspond to a one-electron reversible process, the two other reductions being irreversible and probably also involving a single electron (E_p = -1.47 and -1.68 V).

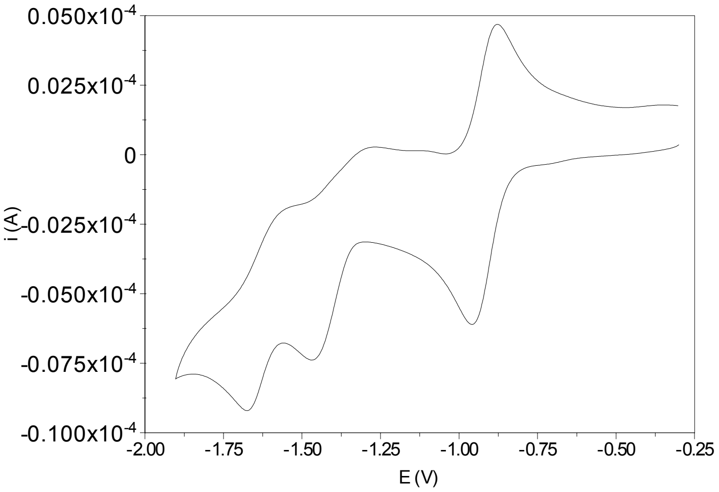

Figure V-6. Cyclic voltammogram of [$Co_4\{CH_3C(CH_2S_2)CH_2SCH_3\}_2(\mu_3$-S)$(CO)_4$] (**43**) in acetonitrile (4 mM, 0.2 M [NBu_4][BF_4], 0.1 V.s^{-1}).

Looking at the effect of protons on the electrochemical response gives a nice current response as the acid concentration rises (Figure **V-7**). The reduction of protons by the cobalt complex occurs at a more positive potential than that observed for the di-iron complexes.

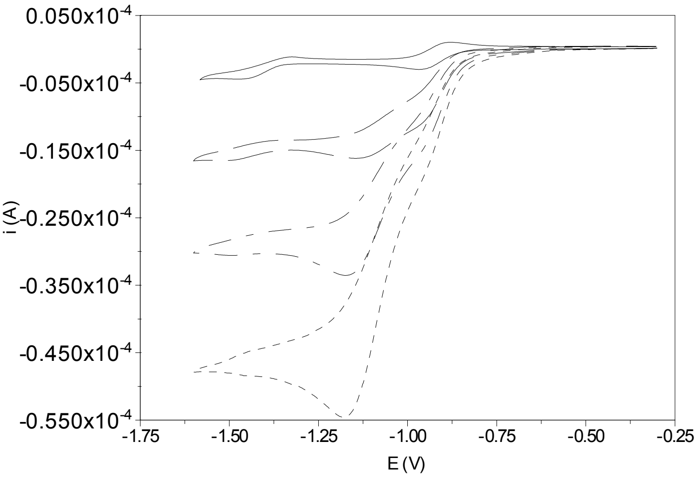

Figure V-7. Cyclic voltammogram of $[Co_4(CO)_4(\mu_3\text{-}S)\{CH_3C(CH_2S_2)CH_2SCH_3\}_2]$ (**43**) (4 mM, 0.2 M $[NBu_4][BF_4]$ in acetonitrile, 0.02 V.s^{-1}) in the absence of acid (—) and in the presence of 10 (——— – –), 20 (— - — -) and 30 equivalents (– – –) of 2,6-lutidinium.

A linear current response as a function of acid concentration is observed up to more than 30 equivalents of acid (Figure **V-8**). This outlines the relative stability of this cobalt complex toward acid concentration.

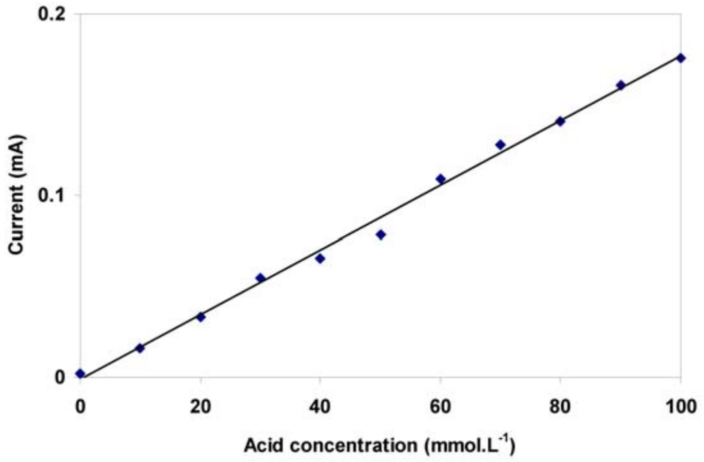

Figure V-8. Current response (measured at -1.17 V) of [$Co_4(CO)_4(\mu_3$-S){$CH_3C(CH_2S_2)CH_2SCH_3$}$_2$] (**43**) (4 mM, 0.2 M [NBu_4][BF_4] in acetonitrile, 0.02 V.s^{-1}) in function of acid concentration (2,6-lutidinium).

The lack of information on similar complexes for dihydrogen evolution does not allow us to postulate a mechanism corresponding to the observations described above (as far as we are aware the behaviour of a Co/S/CO complex in the presence of acid has not been reported).

Nevertheless, more attention will be focused on the possible precursor of the complex crystallised, which would provide us with more insight into the desulfurisation process.

V.X Experimental

$CH_3C(CH_2S)_2CH_2SCH_3$, (4-mmethyl-[1,2] dithiolan-4-yl)-methanethiol (44).[64]

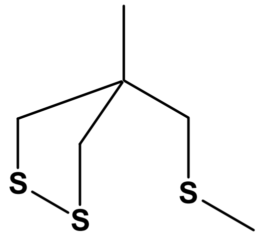

NaH (60% in oil suspension, 0.37 g, 9 mmol) was washed with hexane and then dissolved in THF (50 cm^3). **4** (1.50 g, 8.9 mmol) dissolved in THF was added and the mixture stirred at RT for 30 min. Iodomethyl (0.60 cm^3, 9 mmol) was then added and the solution was stirred for a further one hour. The reaction was quenched with NH_4Cl saturated water (50 cm^3), diethyl ether was added, the organic phase was washed with distilled water, dried over $MgSO_4$ and solvent removed under vacuum to give a yellow oil ($CH_3C(CH_2S)_2CH_2SCH_3$). δ_H (400 MHz; solvent $CDCl_3$; standard $SiMe_4$) 1.31 (3H, s, CCH_3), 2.19 (3H, s, SCH_3), 2.76 (2H, s, CH_2SCH_3), 2.90 (2H, d, *J* 11.4 Hz, CH_2SH), 3.13 (2H, d, *J* 11.4 Hz, CH_2SH).

$CH_3C(CH_2SH)_2CH_2SCH_3$, 2-methyl-2-methylsulfanylmethyl-propane-1,3-dithiol.[64]

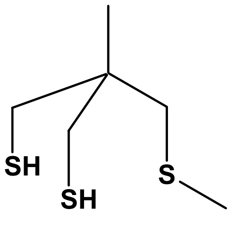

Disulfide compound **44** was dissolved in diethyl ether and $LiAlH_4$ (0.68 g, 18 mmol) was added cautiously to the mixture and then stirred at RT overnight. Degassed water (50 cm^3) and then degassed H_2SO_4 (50 cm^3 10% solution) were carefully added and the organic phase was washed with water, dried over $MgSO_4$ and the solvent removed under vacuum to give a colourless oil (0.50 g, 2.7 mmol, 30%). δ_H (400 MHz; solvent

$CDCl_3$; standard $SiMe_4$) 1.05 (3H, s, C*H*$_3$), 1.28 (2H, t, *J* 9.0 Hz, 2×S*H*), 2.15 (3H, s, SC*H*$_3$), 2.61 (4H, d, *J* 9.0 Hz, 2×C*H*$_2$SH), 2.62 (2H, s, C*H*$_2$SCH$_3$).

$[Co_4(CO)_4(\mu_3\text{-}S)\{CH_3C(CH_2S)_2CH_2SCH_3\}_2]$ (43).

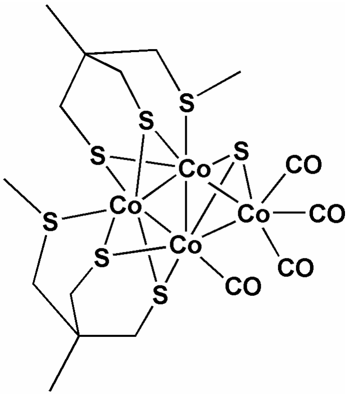

42 (0.50 g, 2.7 mmol) was dissolved in toluene (100 cm^3) and dicobalt-octacarbonyl $[Co_2(CO)_8]$ (0.95 g, 2.8 mmol) was added. The mixture was stirred at 70ºC for 90 min and then the solvent was removed under vacuum. The product was purified by flash column chromatography (gradient hexane 100% to diethyl ether / ethyl acetate 1:1) to give a dark brown solid. Crystals are obtained by slow evaporation of the compound dissolved in acetonitrile. ν_{max}/cm^{-1} (CO) 2047(sh), 2023(s), 2005(s), 1977(w) and (1942 (sh) cm^{-1} (acetonitrile); δ_H (400 MHz; solvent $CDCl_3$; standard $SiMe_4$) 1.15 (6H, s, 2×CC*H*$_3$), 1.80-2.40 (12H, m, 6×CH$_2$), 2.51 (6H, s, 2×SC*H*$_3$).

-Chapter VI-

Summary and future work

The work presented in this thesis can be summarised as follows.

- *The syntheses of six new functionalised {2Fe3S}-assemblies related to the subsite of the "H-cluster" of [Fe]-hydrogenase are described and the X-ray crystallographic structures of five of these molecules have been established.*

- *Spectroscopic, dynamic and equilibrium properties of the new complexes have been investigated and this has begun to provide a deeper understanding of the electronic factors which influence thioether lability / inversion and the transmission of electronic effects via the thioether unit.*

- *All of the {2Fe3S}-complexes electrocatalyse proton reduction but at potentials considerably more negative than that observed for platinum.*

- *The subsite of the "H-cluster" in the* $H_{ox\text{-}active}$ *state possesses a Fe(I)-Fe(II) unit. A new type of structure possessing two fused subsite units has been synthesised. The formal oxidation state of the iron centres are* Fe^{I}-Fe^{II}-Fe^{II}-Fe^{I}. *This species has been shown to catalyse proton reduction.*

- *The "H-cluster" possesses a redox active group, the* $\{Fe_4S_4\}$*-cubane, attached by a thiolate bridge to the di-iron subsite. One of the new molecules synthesised possesses an electroactive p-nitrobenzene group similarly attached by a sulfur bridge to a di-iron unit. The effect of one-electron reduction of this group on the di-iron unit has been explored by electrochemical and spectroelectrochemical methods.*

- *The design and synthesis of the first model of the entire "H-cluster" of the [Fe]-hydrogenase has been described, as well as its spectroscopic and electrochemical characterisation. The electron transfer chemistry of this system has been studied by electrochemical and spectroelectrochemical methods and electronic and mechanistic aspects of the interplay between subsite and cluster explored. The model assembly electrocatalyses dihydrogen evolution at low potential. Preliminary dihydrogen uptake studies by this assembly have been carried out in Melbourne and suggest that this system can also catalyse dihydrogen uptake.*

- *Synthetic systems might be developed which electrocatalyse dihydrogen evolution / uptake at low overpotentials and it would therefore be attractive to immobilise the catalysts at an electrode. An approach for incorporating subsite analogues into surface bound electropolymers has been established.*

This research may open the way for future studies towards the following.

- *A deeper understanding of the mechanism of action of [Fe]-hydrogenase. This would be facilitated by work on cyanation of the model "H-cluster" which would provide a closer analogue of the natural site and allow further studies of the electronic interactions between subsite and cluster and the potential for electrocatalysis.*

- *The assembly of new solid state materials for electrocatalysis. This is likely to require the synthesis of new ligands / polymers possessing both functionality for covalent binding of subsites, electron transfer relays, proton transfer relays and possibly hemi-labile ligands. It is particularly attractive to envisage catalytic sites embedded in a conducting polymer. Incorporating subsites within a functionalised polymeric environment may also provide a means of stabilising Fe(I)-Fe(II) assemblies.*

Finally, while exploratory work on extending the chemistry of the dithiolate thioether ligands to provide di-cobalt analogues of the di-iron subsite analogues proved unsuccessful, a novel polynuclear cobalt cluster has been synthesised and its formation most probably involves hydrodesulfurisation of the dithiolate thioether ligand.

-Chapter VII-

Materials and methods

VII.1 General

All manipulations were performed under an inert atmosphere of N_2 using the Schlenk technique. Solvents were dried and distilled under N_2 following standard procedures (Na for toluene, hexane, diethyl ether and pentane, Na/benzophenone for tetrahydrofuran, P_2O_5 for dichloromethane, Mg for methanol and CaH_2 for acetonitrile). Chemical compounds were purchased from Aldrich, Fluka and Avocado and unless otherwise stated were used as supplied without further purification.

Micro-analysis was performed by Medac Ltd, Surrey. ESI Mass spectrometry analysis was performed at the University of Sussex, Brighton.

NMR spectroscopy was recorded on a JEOL Lambda 400 MHz and FT-IR on a Shimadzu FTIR-8300. NMR coalescence experiments were carried out with S. A. Fairhurst from the Department of Biological Chemistry.

ES-MS analysis was performed on an LCQ DecaXP plus from Thermo Finnigan. The spray chamber conditions are: 50 units sheath gas, 5.0 kV spray voltage and 150°C for the capillary temperature. Sample dissolved in acetonitrile is introduced by Hamilton syringe at a flow of 1 to 10 µL per min depending on the concentration, into a flow of 200 to 300 µL per min of degassed acetonitrile. Experiments were carried out and discussed with L. Hill from the Department of Metabolic Biology.

VII.2 Mössbauer spectroscopy

This technique gives precise information about the chemical, structural and magnetic properties of inorganic complexes. The "Mössbauer Effect" was described by Rudolph Mössbauer, who first observed the recoilless gamma ray emission and absorption (or fluorescence) of nuclei in 1957 and received the Nobel Prize in Physics in 1961 for his work.

For the nuclei the recoil energy is much greater than for the atom fluorescence and therefore put the emission and absorption out of step. However, in the solid state at low temperature the recoil energy is practically zero, so the gamma rays emitted and absorbed are back in step and a resonance can be observed (the "Mössbauer Effect"). Only a few nuclei can be analysed by this spectroscopy and the most studied is ^{57}Fe, which has both a very low energy gamma rays and long-lived excited state. The typical source of gamma ray for ^{57}Fe Mössbauer spectroscopy is ^{57}Co which decays to ^{57}Fe* with a half-life of ≈ 200 days. After 10^{-7} s, ^{57}Fe decays from the $I = {}^{5}/_{2}$ state to the $I = {}^{3}/_{2}$ state (emitting a gamma ray with energy of 123 keV), then from the $I = {}^{3}/_{2}$ state to the $I = {}^{1}/_{2}$ state (emitting a gamma ray with energy of 14.4 keV) (Scheme **VII-1**). From this second decay results the resonance absorption peak and the sample will have different resonant absorption energy if it is in a different coordination than the source. Two parameters are analysed from a spectrum, the **isomer shift** (i.s.) and the **quadrupole splitting** (q.s.).

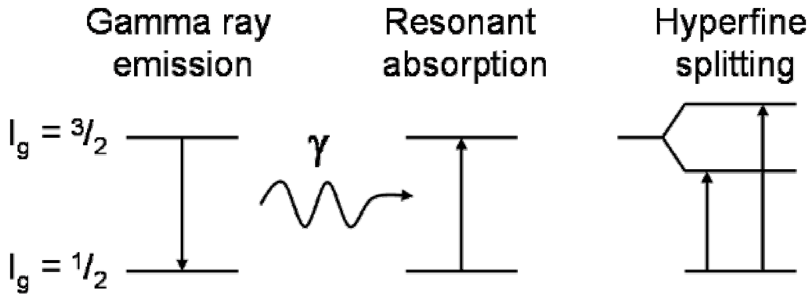

Scheme VII-1. Fluorescence of gamma ray of the nucleus ^{57}Fe. The hyperfine splitting is due to the nuclear quadrupole splitting.

The more *d* electrons that are present, the more the nucleus is shielded from *s* electrons, therefore adding *d* electrons can alter the absorption energy. The **isomer shift** results from this effect and is referenced as Fe foil in this thesis. It provides useful information on the valency, the ligand bonding or the oxidation state of Fe (Table **VII-1**).

d configuration	Isomer shift (mm.s^{-1})	Oxidation state
d^2	-0.9 to -0.8	Fe(VI)
d^4	-0.2 to 0.0	Fe(IV)
low spin d^5, d^6	0.0 to 0.3	Fe(II)
high spin d^5	0.3 to 0.7	Fe(III)
high spin d^6	1.0 to 1.5	Fe(II)

Table VII-1. Examples of typical i.s. for Fe.

The nuclear **quadrupole splitting** (resulting for the "Zeeman Effect") is due to the non-spherical charge distribution around the excited nucleus. This parameter gives information about the symmetry around the Fe and its electronic structure (Table **VI-2**).

Quadrupole splitting δ (mm.s^{-1})	Oxidation state
0.0 to 0.2	Fe(III) low spin
0.0 to 0.5	Fe(III) high spin
0.2 to 0.8	Fe(II) low spin
0.6	Fe(III) octahedral
1.9 to 3.1	Fe(II) high spin

Table VII-2. Examples of typical q.s. for Fe.

Mössbauer spectra were recorded on an ES-Technology MS-105 spectrometer with a 925 MBq ^{57}Co source in a rhodium matrix at 77 K. Spectra were referenced against a 25 µm iron foil at 298 K. Parameters were obtained by fitting the data with Lorentzian lines. Experiments were carried out and discussed with J.E. Barclay and D.J. Evans from the Department of Biological Chemistry.

VII.3 Electrochemistry

For the general charge transfer reaction (Equation **VII-1**) where n is the number of electrons transferred, the potential at the electrode under equilibrium is given by the Nernst equation (Equation **VII-2**). The equilibrium potential E results from the standard electrode potential of the reaction $E°$ and concentrations of the oxidised species O and the reduced species R at the electrode surface.

$$\mathrm{O} + ne^- \rightleftharpoons \mathrm{R} \qquad \textbf{(VII-1)}$$

$$E = E° + \frac{RT}{nF} \ln \frac{[\mathrm{O}]}{[\mathrm{R}]} \qquad \textbf{(VII-2)}$$

Cyclic voltammetry has been used in this thesis to study intrinsic electronic properties of models of the “H-cluster” of [Fe]-hydrogenase. The variation of the applied potential over two electrodes as a function of time is monitored and the current response is plotted against the potential (Scheme **VII-2**).

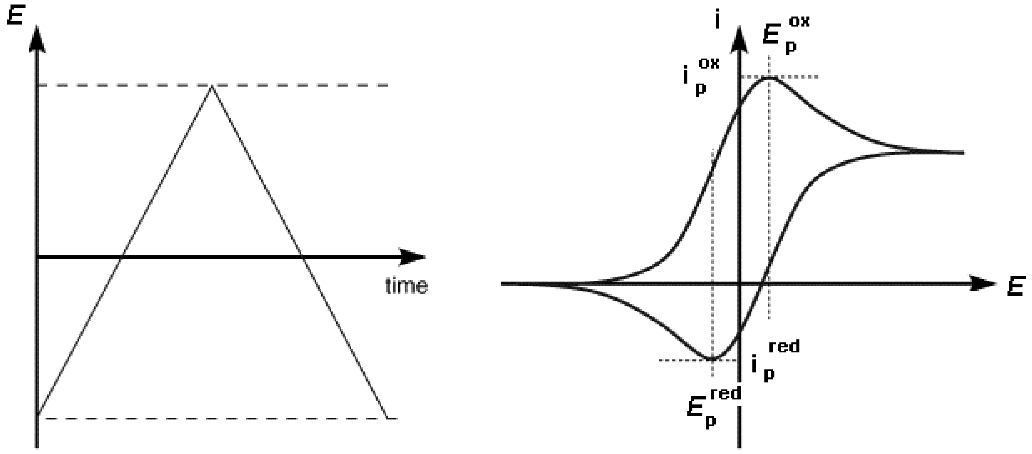

Scheme VII-2. Potential step applied during the experiment (left) and the current response (right).

Oxidative current is depicted as a positive wave and reductive current is depicted as a negative wave. If the solution is not stirred, upon oxidation a layer of oxidised species is formed close to the electrode surface. As the reduced species is depleted in the diffusion layer close to the electrode, the current then decreases after reaching a maximum (i_p^{ox}). In the case of a reversible system, the backward scan will resemble the forward scan and the reduced species will be regenerated (ratio $i_p^{ox} / i_p^{red} = 1$), if the oxidised and reduced species are stable on the timescale of the experiment. A loss in the reversibility of the system is characteristic of fast chemical reactions occurring during the experiment (EC process). More complex reaction schemes may be solved with the aid of computing a simulation of complex cyclic voltammograms.

The relationship between the current response and the scan rate is described by the Randles-Sevčik equation (**VII-3**), where v is the scan rate ($V.s^{-1}$), k is a constant (2.69×10^5 at 298 K), n the number of electron transferred per molecule, A the electrode area (cm^2), D_o the diffusion coefficient ($cm^2.s^{-1}$) and C_o^* the bulk concentration of the electroactive species ($mol.cm^{-3}$).

$$i_p = kn^{3/2}AD_o^{1/2}v^{1/2}C_o^* \quad \textbf{(VII-3)}$$

The peak current is therefore proportional to the square root of the scan rate and the concentration of the electroactive molecule.

Multiple electron processes can occur, and the number of electrons n involved can be predicted from the Nernst equation (**VII-2**). From the potential peak separation, a theoretical ΔE_p of $59/n$ mV should be observed. This is independent of the scan rate and concentration, but many factors may influence ΔE_p and the prediction of n has to be carefully considered. The half potential $E_{½}$ can be determined between the peak potentials and is a value close to the standard potential $E°$.

In the case of irreversible processes, the forward reaction has a much larger rate constant than the backward reaction and therefore the ΔE_p will be greater than $59/n$ mV and will increase with the scan rate. As a half potential cannot be observed, E_p^{ox} and E_p^{red} are reported.

Because of the small area of the working electrode (< 0.1 cm^2) and the large volume of the electrolyte solution (≈ 3 cm^3), the bulk concentration of electroactive species in solution is assumed to remain constant, even after multiples cyclic voltammetry experiments.

Experiments were carried out in a three-compartment glass cell with a vitreous carbon disk as working electrode (electrode area = 1 mm^2), a carbon strip as counting electrode and a Ag/AgCl reference electrode (Ag/AgCl, CH_2Cl_2, 0.45 M $[NBu_4][BF_4]$, 0.05 M $[NBu_4]Cl$). All electrodes were cleaned before use and the working electrode was polished with 9 μm alumina particles on polishing cloth. All potentials measured in this thesis are with reference to Ag/AgCl ($\{Fc^+/Fc\}$ = 0.52 V in CH_3CN and 0.57 V in CH_2Cl_2). The supporting electrolyte (0.2 M $[NBu_4][BF_4]$) was purged with N_2 or Ar before the experiments. Experiments in acidic conditions were carried out using 2,6-lutidinium (tetrafluoroborate as counter-cation) prepared in diethyl ether from 2,6-lutidine and HBF_4 (purchased from Aldrich).

Cyclic voltammetry experiments were controlled using an Autolab PGSTAT 30 with GPES version 4.9 software and digital simulations were performed using Digisim version 3.0 software.

VII.4 IR-Spectroelectrochemistry

Studying infra-red absorption features of metal-carbonyl complexes in their different redox states may be achieved using the reflection-absorption spectroelectrochemistry technique of thin film solution.[103]

The thin layer of the complex of interest is trapped between an electrode and an optically transparent window of calcium fluoride. Typical concentrations of the solution are 1 mL of 1 to 5 mM.

The working electrode (vitreous carbon) is highly polished beforehand, and the reflectance, while lower than platinum, is sufficient to carry out IR-SEC experiments. The thickness of the film is typically 20 μm and can be controlled by a micrometer which is also used to refresh the solution after each experiment.

The cell is composed of stainless steel and electrodes are wrapped in a Teflon sample holder (Scheme **VII-3**). This allows experiments to be performed at high pressure (*ca.* 40 psi) and with different gases (Ar, $^{12,13}CO$, H_2).

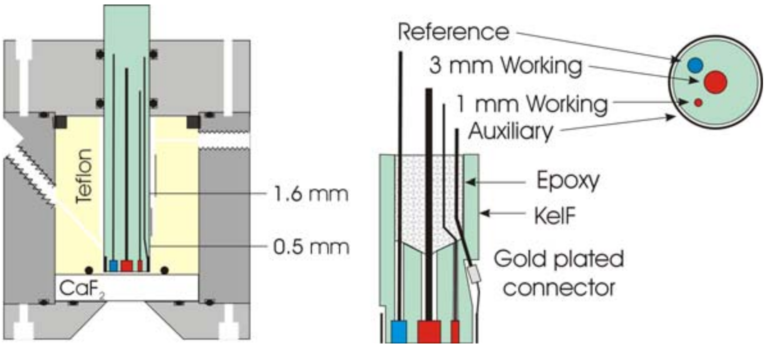

Scheme VII-3. Schematic diagram of a high pressure IR-SEC cell; cell body (right) and multi-electrode assembly (left).

Electrogeneration of reduced and oxidised species is monitored by IR spectral changes. Differential absorbance spectra were calculated using the spectrum recorded immediately before the application of the potential step as a reference. The negative bands correspond to the starting material being depleted from the thin layer and positive bands refer to species generated. The spectrum of the starting material is then used to subtract negative bands as a product can overlap the same absorptions.
Experiments were carried out with Stacey Borg during a one-month visit in 2005 at the School of Chemistry of the University of Melbourne (Australia) under the supervision of Dr. Stephen Best.

VII.5 Gas-phase photoelectron spectroscopy

This experimental technique is used to study the electronic structure and chemical bonding of isolated molecules without perturbation of solvents or the crystal field. Proteins can also be analysed and properties of iron-sulfur clusters and their interactions with the protein backbone can be elucidated.[138]

Photoelectron spectroscopy (PES) has been developed from the photoelectric effect, which postulates that the energy required for the ejection of a photoelectron is directly related to the binding energy of that electron (i.e. by conservation of energy). A spectrum can be generated from that property using high energy photons and an accurate measure of the kinetic energy of the photo-generated electrons.

This kinetic energy of the photoelectron (E_k) is directly related to its initial state binding energy (E_b) through the Einstein expression of the law of conservation of energy (Equation **VII-4**).

$$E_k = h\nu - E_b \qquad \textbf{(VII-4)}$$

Synchrotron radiations produced by accelerating free electrons in a magnetic field allow a continuous spectrum from infrared to the X-ray region for PES. Tunability of the source enables selection of the wavelength most appropriate for the experiment.

The chamber used for photoemission work is maintained under ultra high vacuum ($\leq 5\times10^{-9}$ Pa). These conditions permit the mean free path of electrons, ions and photons, to be increased and adsorbed gases to be removed from the sample, which prevents sample and detector contamination. Photoelectrons are then separated according to their kinetic energies upon reaching the detector.

The PES spectrum is then a continuous record of electron count integrated over a time constant (≈ 1 s), plotted as a function of electron kinetic energy and is normalised to the incident photon flux. PES data are normally reported in terms of the binding energy of the photoelectrons (calculated from Equation **VII-4**). Absolute binding energies are obtained through direct calibration using an internal reference standard.

PES can probe different orbital energy levels. The core level PES excites electrons from the atomic core level and the valence level PES probes the valence electrons of the complexes. The valence level PES can be accomplished at higher resolution using much lower energy photons in the ultraviolet region. These two types of spectrum are complimentary to each other and provide information about the electronic structure of metal complexes.

PES experiments described in this thesis have been carried out using an experimental apparatus equipped with an electrospray ion source and a time-of-flight mass spectrometer. This apparatus permits selection of single charged species by classical mass spectrometry techniques and its analysis by PES. Experiments were carried out on compounds synthesised by the author by Lai-Sheng Wang and X. Yang at the Pacific Northwest National Laboratory, WA.

VII.6 DFT calculations

Theoretical modelling of transition metal complexes have found favour recently due to their potential application in the determination of mechanism, structure and spectroscopic characterisation.[139] Chemical and physical properties can be predicted from fundamental principles by various computational techniques. These calculations on "simple" organic / inorganic molecules can be extended to biological systems and provide information about reaction mechanism from spectroscopic and structural data provided by biochemical studies.[140]

"Ab initio" methods (from the Latin "from the beginning") are derived from purely theoretical principles without inclusion of experimental data. The most common one is the Hartree Fock calculation (HF), but approximations coming from this method led to the consideration of other methods expressing the total energy in terms of the total electron density rather than the wavefunction as the Density Functional Theory (DFT). In general, "ab initio" calculations give very good qualitative results and can give increasingly accurate quantitative results as the molecules become smaller.

Computational transition metal chemistry is now almost synonymous with DFT for medium-sized molecules. The development of model studies of metal complexes correlated with computers getting cheaper and faster led to the large improvement of calculations by computers.

DFT structure optimisations were carried out using the BP86 pure functional [119,120] and an all-electron valence triple-ζ basis set with polarization functions on all atoms (TZVP).[121]

Calculations were carried out on various systems in collaboration with L. De Gioia and M. Bruschi at the University of Milano and discussed in depth at meetings in Reading (08/2005).

-Chapter VIII-

Appendix

VIII.1 X-ray structure data of [$Fe_2(CO)_5\{CH_3C(CH_2S)_2CH_2SCH_2$-2-Py}] (10) (from S. C. Davis).

Crystals were dark orange prisms. A single crystal of size 0.67 × 0.24 × 0.14 mm (corresponding to the *c, b* and *a* axes of the unit cell) was selected and mounted on a glass fibre and coated in epoxy resin for photographic examination and data collection. Diffraction data were measured on an Enraf-Nonius CAD4 diffractometer with monochromated Mo-K_α radiation. Cell parameters were refined using least-squares methods from the settings of 25 reflections in the range 10 to 11 degrees in theta. Each reflection was centred in 4 orientations. 4502 unique reflections were collected to theta of 27^o, with 2791 having intensities greater than $2\sigma_I$. 3 Reflections were chosen to monitor any decay in intensities (measured every 10000 seconds) and any change in orientation (measured every 300 reflections). There were no changes in either. Photographs and diffractometer data showed a monoclinic crystal in the space group $P2_1/c$ (no. 14) with cell dimensions *a* = 8.2456(9) Å, *b* = 20.884(3) Å, *c* = 12.168(5) Å, β = 99.02(2) ^{o} and V = 2069.5(10) $Å^3$.

The data were corrected for Lorentz-polarisation effects, for absorption by semi-empirical psi-scan methods, and for negative intensities by Bayesian statistical methods. The structure was solved using direct methods in the SHELXS-97 program and refined on F^2 using full-matrix least-squares procedures in SHELX-97.

The refinement process showed the structure of [$Fe_2(CO)_5\{CH_3C(CH_2S)_2CH_2SCH_2$-2-Py}] in the asymmetric unit. All non-hydrogen atoms were refined with anisotropic displacement parameters. Hydrogen coordinates were included in idealised positions and subsequently refined freely. All isotropic displacement parameters were refined freely. Convergence was reached with R_1 = 0.074 and wR_2 = 0.103 for all data weighted $w = 1 / [\sigma^2(F_o^2) + (0.043P)^2]$ where $P = (F_o^2 + 2F_c^2)/3$; for the 2791 observed data $R_1 = 0.040$ and $wR_2 = 0.084$.

In the final difference map the residual electron density was 0.46 $e^-/Å^3$ for the largest peak, which was close to an Fe atom.

Table VIII-1. Bond lengths (Å).

Fe(1) - Fe(2)	2.5152(8)	Fe(1) - S(1)	2.2677(11)
Fe(2) - S(1)	2.2533(13)	Fe(1) - S(2)	2.2472(13)
Fe(2) - S(2)	2.2514(11)	Fe(1) - C(1)	1.787(5)
Fe(2) - S(3)	2.2354(10)	Fe(1) - C(2)	1.782(6)
Fe(2) - C(4)	1.763(4)	Fe(1) - C(3A)	1.69(3)
Fe(2) - C(5)	1.761(4)	Fe(1) - C(3B)	1.88(2)
S(1) - C(11)	1.825(4)	C(1) - O(1)	1.132(5)
C(11) - C(14)	1.529(5)	S(2) - C(12)	1.818(4)
C(2) - O(2)	1.132(6)	C(12) - C(14)	1.527(5)
S(3) - C(13)	1.827(4)	C(3A) - O(3A)	1.16(3)
C(13) - C(14)	1.527(5)	C(14) - C(15)	1.527(6)
C(3B) - O(3B)	1.11(2)	S(3) - C(31)	1.824(4)
C(31) - C(322)	1.497(5)	C(4) - O(4)	1.139(4)
N(321) - C(322)	1.328(4)	N(321) - C(326)	1.350(5)
C(5) - O(5)	1.145(4)	C(322) - C(323)	1.373(5)
C(323) - C(324)	1.372(6)	C(324) - C(325)	1.365(6)
C(325) - C(326)	1.344(6)		

Table VIII-2. Bond angles (°).

S(2)-Fe(1)-S(1)	85.88(4)	S(2)-Fe(2)-S(1)	86.12(4)
C(1)-Fe(1)-S(1)	159.6(2)	S(3)-Fe(2)-S(1)	95.80(4)

C(2)-Fe(1)-S(1)	101.3(2)	C(4)-Fe(2)-S(1)	165.91(13)
C(3A)-Fe(1)-S(1)	89.3(8)	C(5)-Fe(2)-S(1)	89.32(14)
C(3B)-Fe(1)-S(1)	87.4(6)	S(3)-Fe(2)-S(2)	97.55(4)
C(1)-Fe(1)-S(2)	87.36(15)	C(4)-Fe(2)-S(2)	89.38(12)
C(2)-Fe(1)-S(2)	104.8(2)	C(5)-Fe(2)-S(2)	159.23(14)
C(3A)-Fe(1)-S(2)	166.2(7)	C(4)-Fe(2)-S(3)	98.03(13)
C(3B)-Fe(1)-S(2)	146.1(5)	C(5)-Fe(2)-S(3)	103.07(14)
C(2)-Fe(1)-C(1)	99.0(3)	C(5)-Fe(2)-C(4)	90.2(2)
C(3A)-Fe(1)-C(1)	92.8(8)	C(1)-Fe(1)-C(3B)	87.6(6)
C(3A)-Fe(1)-C(2)	88.8(7)	C(2)-Fe(1)-C(3B)	109.0(5)

VIII.2 X-ray structure data of [$Fe_2(CO)_5\{CH_3C(CH_2S)_2CH_2SCH_2CH_2$-2-Py}] (11) (from S. C. Davis).

Crystals were black rhombohedrons (dark red in thin section). A single crystal of size 0.34 × 0.24 × 0.24 mm was selected, mounted on a glass fibre and coated in epoxy resin for photographic examination and the data collection. Diffraction data were measured on an Enraf-Nonius CAD4 diffractometer with monochromated Mo-K_α radiation. Cell parameters were refined using least-squares methods from the settings of 24 reflections in the range 10 to 11 degrees in theta. Each reflection was centred in 4 orientations. 6046 Unique reflections were collected to theta of 30°, with 4393 having intensities greater than $2\sigma_I$. 3 Reflections were chosen to monitor any decay in intensities (measured every 10000 seconds) and any change in orientation (measured every 300 reflections). There were no changes in either. Diffractometer data showed a triclinic crystal. The space group I1 (equivalent to no. 2) was chosen to give angles closest to 90°; cell dimensions were a = 7.799(2) Å, b = 11.862(4) Å, c = 22.632(6) Å, α = 90.58(2)°, β = 96.33(3)°, γ = 90.81(3)° and V = 2080.6(11) $Å^3$.

The data were corrected for Lorentz-polarisation effects, for absorption by semi-empirical psi-scan methods, and for negative intensities by Bayesian statistical methods. The structure was solved using direct methods in the SHELXS-97 program and refined on F^2 using full-matrix least-squares procedures in SHELX-97.

The refinement process showed the structure of two molecules of $[Fe_2(CO)_5\{CH_3C(CH_2S)_2CH_2SCH_2CH_2\text{-2-Py}\}]$ in the asymmetric unit. All non-hydrogen atoms were refined with anisotropic displacement parameters. Hydrogen coordinates were included in idealised positions with isotropic displacement parameters refined freely. Convergence was reached with $R_1 = 0.045$ and $wR_2 = 0.088$ for all data weighted $w = 1 / [\sigma^2(F_o^2) + (0.041P)^2]$ where $P = (F_o^2 + 2F_c^2)/3$; for the 4393 observed data $R_1 = 0.033$ and $wR_2 = 0.078$.

In the final difference map the residual electron density was 0.44 $e^-/Å^3$ for the largest peak, which was close to an Fe atom.

Table VIII-3. Bond lengths (Å).

Fe(1) - Fe(2)	2.495(2)	Fe(1) - S(1)	2.253(3)
Fe(1) - S(2)	2.264(3)	Fe(1) - C(1)	1.781(15)
Fe(1) - C(2)	1.767(8)	Fe(1) - C(3)	1.804(11)
Fe(2) - S(1)	2.240(3)	Fe(2) - S(2)	2.257(3)
Fe(2) - S(3)	2.241(3)	Fe(2) - C(4)	1.752(12)
Fe(2) - C(5)	1.771(8)	S(1) - C(11)	1.797(11)
C(11) - C(14)	1.516(15)	S(2) - C(12)	1.811(10)
C(12) - C(14)	1.529(15)	S(3) - C(13)	1.818(11)
C(13) - C(14)	1.593(14)	C(14) - C(15)	1.619(13)
S(3) - C(31)	1.816(10)	C(31) - C(32)	1.422(15)
C(32) - C(331)	1.456(16)	C(331) - N(332)	1.416(14)
C(331) - C(336)	1.407(14)	N(332) - C(333)	1.324(16)
C(333) - C(334)	1.257(18)	C(334) - C(335)	1.40(2)
C(335) - C(336)	1.404(16)	C(1) - O(1)	1.212(16)
C(2) - O(2)	1.142(14)	C(3) - O(3)	1.119(13)

C(4) - O(4)	1.198(15)	C(5) - O(5)	1.135(12)

Table VIII-4. Bond angles (°).

S(1)-Fe(1)-S(2)	86.21(11)	S(1)-Fe(2)-S(2)	86.71(11)
S(1)-Fe(2)-S(3)	94.79(11)	S(3)-Fe(2)-S(2)	98.39(11)
Fe(2)-S(1)-Fe(1)	67.46(9)	Fe(2)-S(2)-Fe(1)	66.98(9)
C(1)-Fe(1)-S(1)	150.9(5)	C(2)-Fe(1)-S(1)	107.4(4)
C(3)-Fe(1)-S(1)	86.1(4)	C(1)-Fe(1)-S(2)	86.6(4)
C(2)-Fe(1)-S(2)	102.3(4)	C(3)-Fe(1)-S(2)	157.9(4)
C(2)-Fe(1)-C(1)	101.6(6)	C(1)-Fe(1)-C(3)	90.1(6)
C(2)-Fe(1)-C(3)	99.8(5)	C(4)-Fe(2)-S(1)	160.6(4)
C(5)-Fe(2)-S(1)	88.5(3)	C(4)-Fe(2)-S(2)	87.4(4)
C(5)-Fe(2)-S(2)	158.4(4)	C(4)-Fe(2)-S(3)	104.4(4)
C(5)-Fe(2)-S(3)	103.0(3)	C(4)-Fe(2)-C(5)	90.2(5)
C(11)-S(1)-Fe(1)	113.5(4)	C(11)-S(1)-Fe(2)	110.4(3)
C(12)-S(2)-Fe(1)	110.4(3)	C(12)-S(2)-Fe(2)	111.4(4)
C(13)-S(3)-Fe(2)	108.3(3)	C(31)-S(3)-Fe(2)	107.9(4)
C(31)-S(3)-C(13)	101.5(5)	C(14)-C(11)-S(1)	117.3(7)
C(14)-C(12)-S(2)	115.7(7)	C(14)-C(13)-S(3)	118.5(7)
C(11)-C(14)-C(12)	113.5(9)	C(11)-C(14)-C(13)	113.7(9)
C(11)-C(14)-C(15)	106.7(8)	C(12)-C(14)-C(13)	113.5(8)
C(12)-C(14)-C(15)	106.1(9)	C(13)-C(14)-C(15)	102.0(8)
C(32)-C(31)-S(3)	115.0(8)	C(31)-C(32)-C(331)	119.9(10)
N(332)-C(331)-C(32)	114.9(9)	C(336)-C(331)-C(32)	123.7(11)
C(336)-C(331)-N(332)	121.2(11)	C(333)-N(332)-C(331)	113.7(11)
C(334)-C(333)-N(332)	131.0(14)	C(333)-C(334)-C(335)	117.3(11)
C(336)-C(335)-C(334)	119.6(10)	C(335)-C(336)-C(331)	117.1(12)
O(1)-C(1)-Fe(1)	177.7(13)	O(2)-C(2)-Fe(1)	175.5(12)

O(3)-C(3)-Fe(1)	173.6(12)	O(4)-C(4)-Fe(2)	174.2(10)
O(5)-C(5)-Fe(2)	177.6(10)		

VIII.5 X-ray structure data of [$Fe_2(CO)_5\{CH_3C(CH_2S)_2CH_2SC_6H_4$-*p*-$NO_2\}$] (14) (from P. Hitchcock).

Temperature 173(2) K	Wavelength 0.71073 Å
Crystal system Orthorhombic	Space group Pbca (No.61)
Unit cell dimensions:	a = 12.8465(3) Å α= 90°.
	b = 16.3268(5) Å β= 90°.
	c = 19.9719(6) Å γ = 90°.
Volume	4189.0(2) $Å^3$.
Z	8
Density (calculated)	1.71 Mg/m^3
Absorption coefficient	1.72 mm^{-1}. F(000) 2176
Crystal size	0.30 x 0.20 x 0.08 mm^3
Theta range for data collection	3.41 to 25.98°.
Index ranges	-15<=h<=15, -20<=k<=20, -24<=l<=24
Reflections collected	56192
Independent reflections	4090 [R(int) = 0.121]
Reflections with I>2sigma(I)	2802
Completeness to theta = 25.98°	99.5 %
Tmax. and Tmin.	0.907 and 0.811
Refinement method	Full-matrix least-squares on F2
Data / restraints / parameters	4090 / 0 / 262
Goodness-of-fit on F2	1.105
Final R indices [I>2sigma(I)]	R1 = 0.061, wR2 = 0.113
R indices (all data)	R1 = 0.101, wR2 = 0.127
Largest diff. peak and hole	0.64 and -0.40 e.$Å^{-3}$

The diffraction was very weak at higher angle.

Data collection KappaCCD, Program package WinGX, Abs correction MULTISCAN

Refinement using SHELXL-97, Drawing using ORTEP-3 for Windows.

Table VIII-5. Bond lengths (Å).

Fe(1)-C(2)	1.768(7)	Fe(1)-C(1)	1.785(7)
Fe(1)-S(3)	2.2454(15)	Fe(1)-S(1)	2.2508(15)
Fe(1)-S(2)	2.2693(15)	Fe(1)-Fe(2)	2.501(1)
Fe(2)-C(3)	1.767(7)	Fe(2)-C(4)	1.784(6)
Fe(2)-C(5)	1.811(7)	Fe(2)-S(2)	2.2623(15)
Fe(2)-S(1)	2.2614(15)	S(1)-C(9)	1.823(5)
S(2)-C(8)	1.820(5)	S(3)-C(11)	1.793(5)
S(3)-C(10)	1.836(5)	O(1)-C(1)	1.143(7)
O(2)-C(2)	1.149(7)	O(3)-C(3)	1.136(7)
O(4)-C(4)	1.128(7)	O(5)-C(5)	1.126(7)
O(6)-N	1.187(9)	O(7)-N	1.198(9)
N-C(14)	1.476(8)	C(6)-C(8)	1.521(7)
C(6)-C(9)	1.530(7)	C(6)-C(7)	1.546(8)
C(6)-C(10)	1.548(7)	C(11)-C(12)	1.371(8)
C(11)-C(16)	1.388(7)	C(12)-C(13)	1.375(8)
C(13)-C(14)	1.365(9)	C(14)-C(15)	1.371(9)
C(15)-C(16)	1.388(8)		

Table VIII-6. Bond angles (°).

C(2)-Fe(1)-C(1)	91.2(3)	C(2)-Fe(1)-S(3)	101.2(2)
C(1)-Fe(1)-S(3)	103.07(19)	C(2)-Fe(1)-S(1)	159.1(2)
C(1)-Fe(1)-S(1)	88.7(2)	S(3)-Fe(1)-S(1)	99.25(6)
C(2)-Fe(1)-S(2)	88.2(2)	C(1)-Fe(1)-S(2)	163.7(2)

S(3)-Fe(1)-S(2)	93.01(6)	S(1)-Fe(1)-S(2)	86.14(5)
C(3)-Fe(2)-C(4)	88.7(3)	C(3)-Fe(2)-C(5)	100.4(3)
C(4)-Fe(2)-C(5)	99.4(3)	C(3)-Fe(2)-S(2)	151.6(2)
C(4)-Fe(2)-S(2)	86.5(2)	C(5)-Fe(2)-S(2)	108.0(2)
C(3)-Fe(2)-S(1)	89.1(2)	C(4)-Fe(2)-S(1)	159.9(2)
C(5)-Fe(2)-S(1)	100.6(2)	S(2)-Fe(2)-S(1)	86.06(5)
C(9)-S(1)-Fe(1)	110.76(18)	C(9)-S(1)-Fe(2)	112.30(19)
Fe(1)-S(1)-Fe(2)	67.33(4)	C(8)-S(2)-Fe(2)	112.23(19)
C(8)-S(2)-Fe(1)	110.92(17)	Fe(2)-S(2)-Fe(1)	67.00(5)
C(11)-S(3)-C(10)	100.3(2)	C(11)-S(3)-Fe(1)	113.80(18)
C(10)-S(3)-Fe(1)	108.11(17)	O(6)-N-O(7)	122.4(7)
O(6)-N-C(14)	119.2(7)	O(7)-N-C(14)	118.4(8)
O(1)-C(1)-Fe(1)	178.6(6)	O(2)-C(2)-Fe(1)	176.0(7)
O(3)-C(3)-Fe(2)	177.8(7)	O(4)-C(4)-Fe(2)	178.5(7)
O(5)-C(5)-Fe(2)	175.9(7)	C(8)-C(6)-C(9)	112.0(4)
C(8)-C(6)-C(7)	107.4(5)	C(9)-C(6)-C(7)	106.3(5)
C(8)-C(6)-C(10)	112.3(5)	C(9)-C(6)-C(10)	114.0(5)
C(7)-C(6)-C(10)	104.1(4)	C(6)-C(8)-S(2)	117.7(4)
C(6)-C(9)-S(1)	118.0(4)	C(6)-C(10)-S(3)	120.9(4)
C(12)-C(11)-C(16)	120.2(5)	C(12)-C(11)-S(3)	123.5(4)
C(16)-C(11)-S(3)	116.3(4)	C(11)-C(12)-C(13)	120.3(6)
C(14)-C(13)-C(12)	118.9(6)	C(13)-C(14)-C(15)	122.5(6)
C(13)-C(14)-N	119.0(7)	C(15)-C(14)-N	118.6(7)
C(14)-C(15)-C(16)	118.4(6)	C(15)-C(16)-C(11)	119.7(6)

VIII.5 X-ray structure data of [$Fe_2(CO)_5\{CH_3C(CH_2S)_2CH_2SC_6H_4$-*p*-$NH_2\}$] (15) (from S. C. Davies).

Crystals were orange-brown blocks. A single crystal of size 0.40 × 0.29 × 0.24 mm (corresponding to the *c, a* and *b* axes) was selected, mounted on a glass fibre and coated in silicone grease for photographic examination and the data collection. Diffraction data were measured on an Enraf-Nonius CAD4 diffractometer with monochromated Mo-K_α radiation. Cell parameters were refined using least-squares methods from the settings of 25 reflections in the range 10 to 11 degrees in theta. Each reflection was centred in 4 orientations. 3517 Unique reflections were collected to theta of 25°, with 2632 having intensities greater than $2\sigma_I$. 3 Reflections were chosen to monitor any decay in intensities (measured every 10000 seconds) and any change in orientation (measured every 300 reflections). There was slight decay of the crystal with an overall decrease in intensities of 1.11%. Diffractometer data showed a monoclinic crystal in the space group $P2_1/c$ (equivalent to no. 14) with cell dimensions $a = 8.797(3)$ Å, $b = 12.528(4)$ Å, $c = 18.181(4)$ Å, $\beta = 94.30(2)$ ° and V = 1998.0(10) Å^3.

The data were corrected for Lorentz-polarisation effects, for decay of the intensities, for absorption by semi-empirical psi-scan methods, and for negative intensities by Bayesian statistical methods. The structure was solved using direct methods in the SHELXS-97 program and refined on F^2 using full-matrix least-squares procedures in SHELXL-97.

The refinement process showed one [$Fe_2(CO)_5\{CH_3C(CH_2S)_2CH_2SC_6H_4$-*p*-$NH_2\}$] molecule in the unit cell. All non-hydrogen atoms were refined with anisotropic thermal parameters. Hydrogen coordinates were included in idealised positions and subsequently refined freely. All hydrogen isotropic thermal parameters were refined freely. Convergence was reached with $R_1 = 0.043$ and $wR_2 = 0.066$ for all data weighted $w = 1 / [\sigma^2(F_o^2) + (0.029P)^2]$ where $P = (F_o^2 + 2F_c^2)/3$; for the 2632 observed data $R_1 = 0.027$ and $wR_2 = 0.059$.

In the final difference map the residual electron density was 0.30 $e^-/Å^3$ for the largest peak, which was close to a S atom.

Table VIII-7. Bond lengths (Å).

Fe(1) - Fe(2)	2.5165(8)	Fe(1) - S(1)	2.2574(9)
Fe(2) - S(1)	2.2555(9)	Fe(1) - S(2)	2.2580(10)
Fe(2) - S(2)	2.2501(10)	Fe(1) - C(1)	1.771(4)
Fe(2) - S(3)	2.2452(8)	Fe(1) - C(2)	1.798(4)
Fe(2) - C(4)	1.778(3)	Fe(1) - C(3)	1.778(3)
Fe(2) - C(5)	1.767(3)	S(1) - C(11)	1.824(3)
C(1) - O(1)	1.136(4)	S(2) - C(12)	1.817(3)
S(3) - C(13)	1.838(3)	C(2) - O(2)	1.138(4)
S(3) - C(31)	1.775(3)	C(3) - O(3)	1.142(4)
C(11) - C(14)	1.514(4)	C(12) - C(14)	1.509(4)
C(4) - O(4)	1.139(3)	C(13) - C(14)	1.533(4)
C(14) - C(15)	1.543(4)	C(5) - O(5)	1.143(3)
C(31) - C(32)	1.382(4)	C(34) - C(35)	1.377(4)
C(31) - C(36)	1.381(4)	C(34) - N(31)	1.387(4)
C(32) - C(33)	1.377(4)	C(35) - C(36)	1.374(4)
C(33) - C(34)	1.389(4)		

Table VIII-8. Bond angles (°).

Fe(2)-S(1)-Fe(1)	67.78(3)	Fe(2)-S(2)-Fe(1)	67.86(2)
S(1)-Fe(1)-S(2)	85.70(3)	S(2)-Fe(2)-S(1)	85.93(3)
C(1)-Fe(1)-S(1)	162.28(13)	S(3)-Fe(2)-S(1)	87.18(3)
C(2)-Fe(1)-S(1)	96.86(11)	S(3)-Fe(2)-S(2)	102.85(3)
C(3)-Fe(1)-S(1)	88.10(10)	C(4)-Fe(2)-S(1)	165.52(9)

C(1)-Fe(1)-S(2)	86.27(11)	C(5)-Fe(2)-S(1)	91.93(10)
C(2)-Fe(1)-S(2)	108.68(11)	C(4)-Fe(2)-S(2)	86.96(9)
C(3)-Fe(1)-S(2)	149.06(12)	C(5)-Fe(2)-S(2)	158.24(10)
C(1)-Fe(1)-C(2)	100.7(2)	C(4)-Fe(2)-S(3)	106.71(10)
C(1)-Fe(1)-C(3)	90.72(14)	C(5)-Fe(2)-S(3)	98.66(10)
C(3)-Fe(1)-C(2)	102.2(2)	C(5)-Fe(2)-C(4)	90.01(13)
C(11)-S(1)-Fe(1)	111.98(12)	O(1)-C(1)-Fe(1)	178.6(4)
C(11)-S(1)-Fe(2)	109.73(10)	O(2)-C(2)-Fe(1)	176.1(4)
C(12)-S(2)-Fe(1)	112.02(12)	C(12)-S(2)-Fe(2)	110.63(11)
O(3)-C(3)-Fe(1)	178.0(3)	C(13)-S(3)-Fe(2)	107.15(11)
O(4)-C(4)-Fe(2)	177.9(3)	C(31)-S(3)-Fe(2)	116.60(9)
C(31)-S(3)-C(13)	101.86(14)	O(5)-C(5)-Fe(2)	177.5(3)
C(14)-C(11)-S(1)	119.1(2)	C(32)-C(31)-S(3)	123.7(2)
C(14)-C(12)-S(2)	118.5(2)	C(36)-C(31)-S(3)	117.5(2)
C(14)-C(13)-S(3)	118.3(2)	C(36)-C(31)-C(32)	118.7(3)
C(12)-C(14)-C(11)	110.9(2)	C(33)-C(32)-C(31)	120.2(3)
C(11)-C(14)-C(13)	113.8(3)	C(32)-C(33)-C(34)	121.2(3)
C(11)-C(14)-C(15)	107.8(3)	C(35)-C(34)-C(33)	118.0(3)
C(12)-C(14)-C(13)	112.2(3)	N(31)-C(34)-C(33)	121.5(3)
C(12)-C(14)-C(15)	106.3(3)	C(35)-C(34)-N(31)	120.5(3)
C(13)-C(14)-C(15)	105.3(2)	C(36)-C(35)-C(34)	121.0(3)
C(35)-C(36)-C(31)	120.9(3)		

VIII.5 X-ray structure data of [$Fe_2(CO)_5\{CH_3C(CH_2S)_2CH_2SCH_2CH_2OH\}$] (20) (from S. C. Davis).

Crystals were brown plates. A single crystal of size 0.48 × 0.07 × 0.07 mm (corresponding to the *a, b* and *c* axes) was selected, mounted on a glass fibre and coated in epoxy resin for photographic examination and data collection. Diffraction data were measured on an Enraf-Nonius CAD4 diffractometer with monochromated Mo-K_α radiation. Cell parameters were refined using least-squares methods from the settings of 25 reflections in the range 10 to 11 degrees in theta. Each reflection was centred in 4 orientations. 3445 Unique reflections were collected to theta of 26^o, with 2476 having intensities greater than $2\sigma_I$. 3 Reflections were chosen to monitor any decay in intensities (measured every 10000 seconds) and any change in orientation (measured every 300 reflections). There was slight decay of the crystal with an overall decrease in intensities of 3.33%. Diffractometer data showed a triclinic crystal in the space group P-1 (no. 2) with cell dimensions a = 9.514(3) Å, b = 9.7026(14) Å, c = 10.640(3) Å, $\alpha = 68.978(15)^o$, $\beta = 79.44(2)^o$, $\gamma = 75.12(2)^o$ and V = 881.5(4) Å^3.

The data were corrected for Lorentz-polarisation effects, for decay of the intensities, for absorption by semi-empirical psi-scan methods, and for negative intensities by Bayesian statistical methods. The structure was solved using direct methods in the SHELXS-97 program and refined on F^2 using full-matrix least-squares procedures in SHELXL-97.

The refinement process showed one $[Fe_2(CO)_5\{CH_3C(CH_2S)_2CH_2SCH_2CH_2OH\}]$ molecule in the asymmetric unit. All non-hydrogen atoms were refined with anisotropic thermal parameters. Hydrogen coordinates were included in idealised positions except the hydroxyl H which was geometrically constrained. All hydrogen isotropic thermal parameters were refined freely. Convergence was reached with R_1 = 0.051 and wR_2 = 0.071 for all data weighted $w = 1 / [\sigma^2(F_o^2) + (0.015P)^2]$ where $P = (F_o^2 + 2F_c^2)/3$; for the 2476 observed data R_1 = 0.032 and wR_2 = 0.062.

In the final difference map the residual electron density was 0.30 e$^-$/Å^3 for the largest peak, which was close to an Fe atom.

Table VIII-9. Bond lengths (Å).

Fe(1) - Fe(2)	2.5006(10)	Fe(1) - S(1)	2.2660(9)
Fe(2) - S(1)	2.2588(11)	Fe(1) - S(2)	2.2569(11)

Fe(2) - S(2)	2.2496(11)	Fe(1) - C(1)	1.782(4)
Fe(2) - S(3)	2.2551(9)	Fe(1) - C(2)	1.794(4)
Fe(2) - C(4)	1.765(3)	Fe(1) - C(3)	1.792(4)
Fe(2) - C(5)	1.762(4)	S(1) - C(11)	1.830(3)
C(1) - O(1)	1.145(4)	S(2) - C(12)	1.817(3)
S(3) - C(13)	1.826(3)	C(2) - O(2A)	1.19(2)
S(3) - C(31)	1.826(3)	C(2) - O(2B)	1.16(2)
C(11) - C(14)	1.519(4)	C(3) - O(3)	1.137(4)
C(12) - C(14)	1.521(4)	C(13) - C(14)	1.537(4)
C(4) - O(4)	1.149(4)	C(14) - C(15)	1.545(4)
C(31) - C(32)	1.514(4)	C(5) - O(5)	1.146(4)
C(32) - O(33)	1.402(4)		

Table VIII-10. Bond angles (°).

S(2)-Fe(1)-S(1)	85.35(4)	S(2)-Fe(2)-S(1)	85.69(4)
C(1)-Fe(1)-S(1)	154.45(11)	S(3)-Fe(2)-S(1)	94.91(4)
C(2)-Fe(1)-S(1)	104.72(14)	C(4)-Fe(2)-S(1)	161.13(10)
C(3)-Fe(1)-S(1)	87.03(11)	C(5)-Fe(2)-S(1)	90.29(11)
C(1)-Fe(1)-S(2)	86.94(12)	S(2)-Fe(2)-S(3)	98.11(4)
C(2)-Fe(1)-S(2)	102.70(14)	C(4)-Fe(2)-S(2)	87.64(12)
C(3)-Fe(1)-S(2)	157.76(12)	C(5)-Fe(2)-S(2)	159.26(11)
C(1)-Fe(1)-C(2)	100.7(2)	C(4)-Fe(2)-S(3)	103.50(10)
C(1)-Fe(1)-C(3)	91.1(2)	C(5)-Fe(2)-S(3)	102.50(11)
C(3)-Fe(1)-C(2)	99.4(2)	C(5)-Fe(2)-C(4)	89.7(2)
Fe(2)-S(1)-Fe(1)	67.10(3)	Fe(2)-S(2)-Fe(1)	67.41(4)
C(11)-S(1)-Fe(1)	113.92(11)	C(14)-C(11)-S(1)	118.8(2)
C(11)-S(1)-Fe(2)	109.55(11)	C(14)-C(12)-S(2)	117.4(2)
C(12)-S(2)-Fe(1)	112.09(13)	C(14)-C(13)-S(3)	122.1(2)

C(12)-S(2)-Fe(2)	111.55(11)	C(11)-C(14)-C(12)	111.0(3)
C(13)-S(3)-Fe(2)	106.74(10)	C(11)-C(14)-C(13)	114.8(3)
C(31)-S(3)-Fe(2)	108.65(11)	C(11)-C(14)-C(15)	107.7(3)
C(13)-S(3)-C(31)	101.2(2)	C(12)-C(14)-C(13)	111.4(3)
C(12)-C(14)-C(15)	106.4(3)	O(1)-C(1)-Fe(1)	177.9(3)
C(13)-C(14)-C(15)	105.0(2)	C(32)-C(31)-S(3)	112.9(2)
O(2A)-C(2)-Fe(1)	162.5(8)	O(33)-C(32)-C(31)	112.1(3)
O(2B)-C(2)-Fe(1)	166.4(8)	O(3)-C(3)-Fe(1)	179.1(3)
O(4)-C(4)-Fe(2)	176.5(3)	O(5)-C(5)-Fe(2)	177.0(3)

VIII.6 X-ray structure data of [$Fe_2(CO)_4\{CH_3C(CH_2S)_3\}]_2$ (22) (from D. L. Hughes).

Crystals are deep red, wafer-thin needles. From a sample under oil, one, *ca* 0.75 × 0.07 × 0.01 mm, was mounted on a glass fibre and fixed in the cold nitrogen stream on a Rigaku R-Axis IIc image plate diffractometer equipped with a rotating anode X-ray source (Mo-Kα radiation) and graphite monochromator. Using 4° oscillations, 48 exposures of 58 min. each were made. Total no. of reflections recorded, to θ_{max} = 25.4°, was 7931 of which 4696 were unique (Rint = 0.098); 3056 were 'observed' with $I > 2\sigma_I$.

Data were processed using the DENZO/SCALEPACK programs. The structure was determined by the direct methods routines in the SHELXS program (2A) and refined by full-matrix least-squares methods, on F^2's, in SHELXL (2B). There are two independent molecules in the cell, each of which lies across a centre of symmetry. The non-hydrogen atoms were refined with anisotropic thermal parameters. Hydrogen atoms were included in idealised positions and their Uiso values were set to ride on the Ueq values of the parent carbon atoms. At the conclusion of the refinement, wR_2 = 0.135 and R_1 = 0.085 (2B) for all 4696 reflections weighted $w = [\sigma^2(F_o^2) + (0.0563P)^2]^{-1}$ with $P = (F_o^2 + 2F_c^2)/3$; for the 'observed' data only, R_1 = 0.054.

In the final difference map, the highest peaks (to *ca* 0.51 e$Å^{-3}$) were close to the iron atoms.

Table VIII-11. Bond lengths (Å).

Fe(1) - Fe(2)	2.5384(16)	Fe(1) - S(1)	2.2603(18)
Fe(1) - S(2)	2.254(2)	Fe(1) - C(4)	1.772(8)
Fe(1) - C(5)	1.794(8)	Fe(1) - C(6)	1.796(6)
Fe(2) - Fe(2')	2.642(2)	Fe(2) - S(1)	2.290(2)
Fe(2) - S(2)	2.246(2)	Fe(2) - S(3)	2.241(2)
Fe(2) - S(3')	2.224(2)	Fe(2) - C(7)	1.768(7)
S(1) - C(11)	1.826(6)	C(11) - C(1)	1.526(9)
S(2) - C(12)	1.830(6)	C(12) - C(1)	1.542(8)
C(1) - C(13)	1.554(10)	C(1) - C(14)	1.531(8)
C(13) - S(3)	1.840(6)	C(4) - O(4)	1.171(9)
C(5) - O(5)	1.164(8)	C(6) - O(6)	1.158(7)
C(7) - O(7)	1.166(7)		

Table VIII-12. Bond angles (°).

Fe(1)-Fe(2)-Fe(2')	146.74(6)	S(2)-Fe(2)-S(1)	85.60(8)
S(3)-Fe(2)-S(1)	100.83(7)	S(3')-Fe(2)-S(1)	84.44(8)
C(7)-Fe(2)-S(1)	159.0(2)	S(3)-Fe(2)-S(2)	91.82(8)
S(3')-Fe(2)-S(2)	159.66(8)	C(7)-Fe(2)-S(2)	88.5(2)
S(3')-Fe(2)-S(3)	107.44(7)	C(7)-Fe(2)-S(3)	99.5(2)
C(7)-Fe(2)-S(3')	94.5(2)	Fe(1)-S(1)-Fe(2)	67.81(6)
C(11)-S(1)-Fe(1)	110.8(2)	C(11)-S(1)-Fe(2)	110.9(2)
C(1)-C(11)-S(1)	117.3(4)	Fe(2)-S(2)-Fe(1)	68.68(6)
C(12)-S(2)-Fe(1)	113.9(2)	C(12)-S(2)-Fe(2)	108.6(2)

C(1)-C(12)-S(2)	119.9(4)	C(11)-C(1)-C(12)	110.8(5)
C(11)-C(1)-C(13)	113.0(5)	C(11)-C(1)-C(14)	107.9(5)
C(12)-C(1)-C(13)	113.0(5)	C(14)-C(1)-C(12)	106.6(5)
C(14)-C(1)-C(13)	105.1(5)	C(1)-C(13)-S(3)	118.9(4)
Fe(2')-S(3)-Fe(2)	72.56(7)	C(13)-S(3)-Fe(2)	107.7(2)
C(13)-S(3)-Fe(2')	117.0(2)	O(4)-C(4)-Fe(1)	175.9(7)
O(5)-C(5)-Fe(1)	176.7(6)	O(6)-C(6)-Fe(1)	177.4(7)
O(7)-C(7)-Fe(2)	175.2(6)		

VIII.7 X-ray structure data of [$Fe_2(CO)_6\{CH_3C(CH_2S)_2CH_2SCOCH_3\}$] (27) (from S. C. Davies).

Crystals were orange cubic blocks. A single crystal of size 0.29 × 0.21 × 0.07 mm (corresponding to the *b, c* and *a* axes of the unit cell) was mounted on a glass fibre and coated in epoxy resin for photographic examination and the data collection. Diffraction data were measured on an Enraf-Nonius CAD4 diffractometer with monochromated Mo-K_α radiation. Cell parameters were refined using least-squares methods from the settings of 25 reflections in the range 10 to 11 degrees in theta. Each reflection was centred in 4 orientations. 4522 Unique reflections were collected to theta of 28°, with 2926 having intensities greater than $2\sigma_I$. 3 Reflections were chosen to monitor any decay in intensities (measured every 10000 seconds) and any change in orientation (measured every 300 reflections). There were no changes in either. Photographs and diffractometer data showed a monoclinic crystal in the space group $P2_1/c$ (no. 14) with cell dimensions a = 9.815(2) Å, b = 8.868(3) Å, c = 21.635(5) Å, β = 94.35(2) ° and V = 1877.7(8) $Å^3$.

The data were corrected for Lorentz-polarisation effects, for absorption by semi-empirical psi-scan methods, and for negative intensities by Bayesian statistical methods. The structure was solved using direct methods in the SHELXS program and refined on F^2 using full-matrix least-squares procedures in SHELX-97.

The refinement process showed the structure of four molecules of $[Fe_2(CO)_6\{CH_3C(CH_2S)_2CH_2SCOCH_3\}]$ in the unit cell. All non-hydrogen atoms were refined with anisotropic displacement parameters. Hydrogen coordinates were refined freely except those of the methyl carbon, with two alternate orientations located from electron density maps which were then geometrically constrained using a rotating model. All isotropic displacement parameters were refined freely except those of the disordered hydrogens, which were set to be $1.5 \times U_{eq}$ of the parent atom. Convergence was reached with $R_1 = 0.068$ and $wR_2 = 0.094$ for all data weighted $w = 1 / [\sigma^2(F_o^2) + (0.031P)^2]$ where $P = (F_o^2 + 2F_c^2)/3$; for the 2926 observed data $R_1 = 0.038$ and $wR_2 = 0.077$.

In the final difference map the residual electron density was $0.53e^-/Å^3$ for the largest peak, which was close to an Fe atom.

Table VIII-13. Bond lengths (Å).

Fe(1) - Fe(2)	2.4911(9)	Fe(1) - S(1)	2.2615(10)
Fe(2) - S(1)	2.2558(10)	Fe(1) - S(2)	2.2546(10)
Fe(2) - S(2)	2.2756(10)	Fe(1) - C(11)	1.797(4)
Fe(2) - C(21)	1.806(4)	Fe(1) - C(12)	1.794(4)
Fe(2) - C(22)	1.783(4)	Fe(1) - C(13)	1.791(4)
Fe(2) - C(23)	1.799(4)	S(1) - C(1)	1.826(3)
C(11) - O(11)	1.134(4)	S(2) - C(2)	1.827(3)
C(1) - C(3)	1.528(5)	C(12) - O(12)	1.133(4)
C(2) - C(3)	1.534(4)	C(3) - C(31)	1.533(4)
C(13) - O(13)	1.130(4)	C(3) - C(32)	1.535(4)
C(32) - S(3)	1.799(4)	C(21) - O(21)	1.135(4)
S(3) - C(33)	1.771(4)	C(33) - O(33)	1.178(5)
C(22) - O(22)	1.136(4)	C(33) - C(34)	1.499(5)
C(23) - O(23)	1.135(4)		

Table VIII-14. Bond angles (°).

S(2)-Fe(1)-S(1)	83.75(4)	S(1)-Fe(2)-S(2)	83.40(4)
C(11)-Fe(1)-S(2)	102.99(12)	C(21)-Fe(2)-S(1)	107.16(11)
C(12)-Fe(1)-S(2)	158.34(12)	C(22)-Fe(2)-S(1)	87.37(12)
C(13)-Fe(1)-S(2)	87.76(13)	C(23)-Fe(2)-S(1)	155.89(12)
C(11)-Fe(1)-S(1)	101.86(12)	C(21)-Fe(2)-S(2)	113.02(12)
C(12)-Fe(1)-S(1)	88.65(13)	C(22)-Fe(2)-S(2)	151.18(12)
C(13)-Fe(1)-S(1)	158.96(13)	C(23)-Fe(2)-S(2)	87.32(13)
C(12)-Fe(1)-C(11)	98.4(2)	C(22)-Fe(2)-C(21)	95.8(2)
C(13)-Fe(1)-C(11)	98.8(2)	C(23)-Fe(2)-C(21)	97.0(2)
C(13)-Fe(1)-C(12)	92.3(2)	C(22)-Fe(2)-C(23)	90.2(2)
Fe(2)-S(1)-Fe(1)	66.94(3)	Fe(1)-S(2)-Fe(2)	66.72(3)
C(1)-S(1)-Fe(1)	111.79(12)	C(1)-S(1)-Fe(2)	116.95(11)
C(2)-S(2)-Fe(1)	108.36(12)	C(2)-S(2)-Fe(2)	118.94(11)
C(3)-C(1)-S(1)	122.6(2)	O(11)-C(11)-Fe(1)	178.2(4)
C(3)-C(2)-S(2)	120.4(2)	C(1)-C(3)-C(31)	107.4(3)
O(12)-C(12)-Fe(1)	179.7(4)	C(1)-C(3)-C(2)	111.6(3)
C(31)-C(3)-C(2)	107.7(3)	O(13)-C(13)-Fe(1)	179.6(4)
C(1)-C(3)-C(32)	113.9(3)	C(31)-C(3)-C(32)	109.3(3)
O(21)-C(21)-Fe(2)	176.4(3)	C(2)-C(3)-C(32)	106.7(3)
C(3)-C(32)-S(3)	117.2(2)	O(22)-C(22)-Fe(2)	178.3(3)
C(33)-S(3)-C(32)	100.8(2)	O(33)-C(33)-C(34)	124.0(4)
O(23)-C(23)-Fe(2)	176.4(4)	O(33)-C(33)-S(3)	123.5(3)
C(34)-C(33)-S(3)	112.4(3)		

VIII.8 X-ray structure data of $[Co_4(CO)_4(\mu_3\text{-}S)\{CH_3C(CH_2S)_2CH_2SCH_3\}_2]$ (43) (from P. Hitchcock).

Temperature	173(2) K	
Wavelength	0.71073 Å	
Crystal system	Triclinic	
Space group	$P\bar{1}$ (No.2)	
Unit cell dimensions	a = 10.5510(4) Å	α= 93.966(2)°.
	b = 10.8810(4) Å	β= 92.485(2)°.
	c = 12.1472(3) Å	γ = 100.447(2)°.
Volume	1365.94(8) Å^3	
Z	2	
Density (calculated)	1.90 Mg/m^3	
Absorption coefficient	2.95 mm^{-1}	
F(000)	788	
Crystal size	0.20 x 0.10 x 0.05 mm^3	
Theta range for data collection	3.55 to 26.09°.	
Index ranges	-12<=h<=13, -13<=k<=13, -15<=l<=14	
Reflections collected	18722	
Independent reflections	5362 [R(int) = 0.052]	
Reflections with I>2sigma(I)	4229	
Completeness to theta = 26.09°	99.2 %	
Tmax. and Tmin.	0.745 and 0.666	
Refinement method	Full-matrix least-squares on F^2	
Data / restraints / parameters	5362 / 0 / 307	
Goodness-of-fit on F^2	1.338	
Final R indices [I>2sigma(I)]	R1 = 0.043, wR2 = 0.105	
R indices (all data)	R1 = 0.061, wR2 = 0.111	
Largest diff. peak and hole	2.03 and -0.99 e.Å^{-3} (near solvate	

atoms)

There is a poorly defined molecule of CH_3CN solvate for which the H atoms were not located and were omitted.

Data collection KappaCCD , Program package WinGX, Abs correction MULTISCAN.

Refinement using SHELXL-97, Drawing using ORTEP-3 for Windows.

Table VIII-15. Bond lengths (Å).

Co(1)-C(1)	1.776(6)	Co(1)-C(3)	1.780(6)
Co(1)-C(2)	1.804(6)	Co(1)-S(7)	2.1842(13)
Co(1)-Co(2)	2.5631(9)	Co(1)-Co(4)	2.6076(9)
Co(2)-C(4)	1.757(5)	Co(2)-S(7)	2.1736(14)
Co(2)-S(1)	2.2188(14)	Co(2)-S(2)	2.2437(14)
Co(2)-Co(3)	2.5470(9)	Co(2)-Co(4)	2.6035(8)
Co(3)-S(3)	2.1928(14)	Co(3)-S(5)	2.2275(13)
Co(3)-S(1)	2.2340(13)	Co(3)-S(2)	2.2375(13)
Co(3)-S(4)	2.2442(13)	Co(3)-Co(4)	2.4645(9)
Co(4)-S(7)	2.1506(13)	Co(4)-S(6)	2.1890(14)
Co(4)-S(5)	2.2050(13)	Co(4)-S(4)	2.2513(13)
S(1)-C(7)	1.816(5)	S(2)-C(8)	1.827(5)
S(3)-C(10)	1.798(5)	S(3)-C(9)	1.829(5)
S(4)-C(13)	1.837(5)	S(5)-C(14)	1.830(5)
S(6)-C(16)	1.812(5)	S(6)-C(15)	1.827(5)
O(1)-C(1)	1.149(6)	O(2)-C(2)	1.134(6)
O(3)-C(3)	1.154(6)	O(4)-C(4)	1.141(6)
C(5)-C(6)	1.549(6)	C(6)-C(8)	1.529(7)
C(6)-C(7)	1.536(7)	C(6)-C(9)	1.542(7)
C(11)-C(12)	1.541(6)	C(12)-C(13)	1.512(7)

C(12)-C(14)	1.516(7)	C(12)-C(15)	1.557(7)
N(1S)-C(2S)	1.195(9)	C(1S)-C(2S)	1.350(10)

Table VIII-16. Bond angles (°).

C(1)-Co(1)-C(3)	102.9(2)	C(1)-Co(1)-C(2)	102.1(2)
C(3)-Co(1)-C(2)	105.7(2)	C(1)-Co(1)-S(7)	104.87(16)
C(3)-Co(1)-S(7)	132.94(17)	C(2)-Co(1)-S(7)	104.60(18)
C(1)-Co(1)-Co(2)	156.25(16)	C(3)-Co(1)-Co(2)	88.72(16)
C(2)-Co(1)-Co(2)	94.31(18)	S(7)-Co(1)-Co(2)	53.78(4)
C(1)-Co(1)-Co(4)	99.24(16)	C(3)-Co(1)-Co(4)	86.23(16)
C(2)-Co(1)-Co(4)	152.32(18)	S(7)-Co(1)-Co(4)	52.43(4)
Co(2)-Co(1)-Co(4)	60.46(2)	C(4)-Co(2)-S(7)	105.69(17)
C(4)-Co(2)-S(1)	100.39(18)	S(7)-Co(2)-S(1)	102.26(5)
C(4)-Co(2)-S(2)	105.60(17)	S(7)-Co(2)-S(2)	145.04(5)
S(1)-Co(2)-S(2)	87.02(5)	C(4)-Co(2)-Co(3)	146.23(18)
S(7)-Co(2)-Co(3)	102.68(4)	S(1)-Co(2)-Co(3)	55.39(4)
S(2)-Co(2)-Co(3)	55.25(4)	C(4)-Co(2)-Co(1)	100.15(18)
S(7)-Co(2)-Co(1)	54.16(4)	S(1)-Co(2)-Co(1)	152.38(4)
S(2)-Co(2)-Co(1)	104.94(4)	Co(3)-Co(2)-Co(1)	111.25(3)
C(4)-Co(2)-Co(4)	156.27(18)	S(7)-Co(2)-Co(4)	52.58(4)
S(1)-Co(2)-Co(4)	94.41(4)	S(2)-Co(2)-Co(4)	93.53(4)
Co(3)-Co(2)-Co(4)	57.16(2)	Co(1)-Co(2)-Co(4)	60.62(2)
S(3)-Co(3)-S(5)	111.40(5)	S(3)-Co(3)-S(1)	98.32(5)
S(5)-Co(3)-S(1)	84.65(5)	S(3)-Co(3)-S(2)	97.96(5)
S(5)-Co(3)-S(2)	150.29(6)	S(1)-Co(3)-S(2)	86.81(5)
S(3)-Co(3)-S(4)	108.15(5)	S(5)-Co(3)-S(4)	86.67(5)
S(1)-Co(3)-S(4)	153.51(6)	S(2)-Co(3)-S(4)	88.47(5)
S(3)-Co(3)-Co(4)	158.04(5)	S(5)-Co(3)-Co(4)	55.79(4)

S(1)-Co(3)-Co(4)	97.96(4)	S(2)-Co(3)-Co(4)	97.57(4)
S(4)-Co(3)-Co(4)	56.89(4)	S(3)-Co(3)-Co(2)	139.38(4)
S(5)-Co(3)-Co(2)	96.99(4)	S(1)-Co(3)-Co(2)	54.83(4)
S(2)-Co(3)-Co(2)	55.48(4)	S(4)-Co(3)-Co(2)	101.71(4)
Co(4)-Co(3)-Co(2)	62.57(3)	S(7)-Co(4)-S(6)	104.61(5)
S(7)-Co(4)-S(5)	101.14(5)	S(6)-Co(4)-S(5)	96.98(5)
S(7)-Co(4)-S(4)	152.36(5)	S(6)-Co(4)-S(4)	100.46(5)
S(5)-Co(4)-S(4)	87.04(5)	S(7)-Co(4)-Co(3)	106.13(4)
S(6)-Co(4)-Co(3)	142.68(5)	S(5)-Co(4)-Co(3)	56.66(4)
S(4)-Co(4)-Co(3)	56.62(4)	S(7)-Co(4)-Co(2)	53.39(4)
S(6)-Co(4)-Co(2)	156.43(5)	S(5)-Co(4)-Co(2)	95.95(4)
S(4)-Co(4)-Co(2)	99.82(4)	Co(3)-Co(4)-Co(2)	60.27(2)
S(7)-Co(4)-Co(1)	53.61(4)	S(6)-Co(4)-Co(1)	102.62(4)
S(5)-Co(4)-Co(1)	151.18(4)	S(4)-Co(4)-Co(1)	109.60(4)
Co(3)-Co(4)-Co(1)	112.49(3)	Co(2)-Co(4)-Co(1)	58.92(2)
C(7)-S(1)-Co(2)	109.31(17)	C(7)-S(1)-Co(3)	110.30(16)
Co(2)-S(1)-Co(3)	69.78(4)	C(8)-S(2)-Co(3)	108.87(16)
C(8)-S(2)-Co(2)	111.55(16)	Co(3)-S(2)-Co(2)	69.27(4)
C(10)-S(3)-C(9)	100.7(2)	C(10)-S(3)-Co(3)	107.3(2)
C(9)-S(3)-Co(3)	107.23(17)	C(13)-S(4)-Co(3)	111.41(17)
C(13)-S(4)-Co(4)	108.61(16)	Co(3)-S(4)-Co(4)	66.49(4)
C(14)-S(5)-Co(4)	107.82(16)	C(14)-S(5)-Co(3)	116.24(16)
Co(4)-S(5)-Co(3)	67.56(4)	C(16)-S(6)-C(15)	101.4(2)
C(16)-S(6)-Co(4)	106.77(18)	C(15)-S(6)-Co(4)	107.10(17)
Co(4)-S(7)-Co(2)	74.03(4)	Co(4)-S(7)-Co(1)	73.96(4)
Co(2)-S(7)-Co(1)	72.05(4)	O(1)-C(1)-Co(1)	178.1(5)
O(2)-C(2)-Co(1)	178.5(5)	O(3)-C(3)-Co(1)	175.5(4)
O(4)-C(4)-Co(2)	178.0(5)	C(8)-C(6)-C(7)	111.6(4)
C(8)-C(6)-C(9)	113.8(4)	C(7)-C(6)-C(9)	111.4(4)

C(8)-C(6)-C(5)	107.2(4)	C(7)-C(6)-C(5)	107.2(4)
C(9)-C(6)-C(5)	105.2(4)	C(6)-C(7)-S(1)	117.6(3)
C(6)-C(8)-S(2)	118.4(3)	C(6)-C(9)-S(3)	121.6(3)
C(13)-C(12)-C(14)	111.9(4)	C(13)-C(12)-C(11)	107.8(4)
C(14)-C(12)-C(11)	106.3(4)	C(13)-C(12)-C(15)	111.2(4)
C(14)-C(12)-C(15)	113.9(4)	C(11)-C(12)-C(15)	105.2(4)
C(12)-C(13)-S(4)	118.1(3)	C(12)-C(14)-S(5)	119.1(3)
C(12)-C(15)-S(6)	119.8(3)	N(1S)-C(2S)-C(1S)	177.6(10)

-Chapter IX-

References

1. Lippard, S. J. & Berg, J. M. *Principles of Bioinorganic Chemsitry* (University Science Books, Mill Valley (CA), 1994).
2. Kaim, W. & Schwederski, B. *Bioinorganic Chemistry: Inorganic Elements in the Chemistry of Life* (John Wiley & Sons Ltd, 1995).
3. Holm, R. H., Kennepohl, P. & Solomon, E. I. Structural and functional aspects of metal sites in biology. *Chem. Rev.* **96**, 2239-2314 (1996).
4. Hall, D. O., Cammack, R. & Rao, K. K. Role for Ferredoxins in Origin of Life and Biological Evolution. *Nature* **233**, 136-138 (1971).
5. Mansy, S. S. & Cowan, J. A. Iron-sulfur cluster biosynthesis: Toward an understanding of cellular machinery and molecular mechanism. *Accounts Chem. Res.* **37**, 719-725 (2004).
6. Frazzon, J. & Dean, D. R. Formation of iron-sulfur clusters in bacteria: an emerging field in bioinorganic chemistry. *Current Opinion in Chemical Biology* **7**, 166-173 (2003).
7. Burgess, B. K. & Lowe, D. J. Mechanism of molybdenum nitrogenase. *Chem. Rev.* **96**, 2983-3011 (1996).
8. Stephenson, M. & Stickland, L. H. *Biochemical Journal* **25**, 205-214 (1931).
9. Vignais, P. M., Billoud, B. & Meyer, J. Classification and phylogeny of hydrogenases. *Fems Microbiology Reviews* **25**, 455-501 (2001).
10. Frey, M. Hydrogenases: Hydrogen-activating enzymes. *Chembiochem* **3**, 153-160 (2002).
11. Thauer, R. K. Biochemistry of methanogenesis: a tribute to Marjory Stephenson. *Microbiology-(UK)* **144**, 2377-2406 (1998).

12. Zirngibl, C., Hedderich, R. & Thauer, R. K. N5,N10-Methylenetetrahydromethanopterin Dehydrogenase from Methanobacterium-Thermoautotrophicum Has Hydrogenase Activity. *Febs Letters* **261**, 112-116 (1990).

13. Zirngibl, C. et al. H_2-Forming Methylenetetrahydromethanopterin Dehydrogenase, a Novel Type of Hydrogenase without Iron-Sulfur Clusters in Methanogenic Archaea. *Eur. J. Biochem.* **208**, 511-520 (1992).

14. Berkessel, A. & Thauer, R. K. On the Mechanism of Catalysis by a Metal-Free Hydrogenase from Methanogenic Archaea - Enzymatic Transformation of H_2 without a Metal and Its Analogy to the Chemistry of Alkanes in Superacidic Solution. *Angew. Chem.-Int. Edit. Engl.* **34**, 2247-2250 (1995).

15. Berkessel, A. Activation of dihydrogen without transition metals. *Current Opinion in Chemical Biology* **5**, 486-490 (2001).

16. Buurman, G., Shima, S. & Thauer, R. K. The metal-free hydrogenase from methanogenic archaea: evidence for a bound cofactor. *Febs Letters* **485**, 200-204 (2000).

17. Shima, S. et al. The cofactor of the iron-sulfur cluster free hydrogenase Hmd: Structure of the light-inactivation product. *Angew. Chem. Int. Edit.* **43**, 2547-2551 (2004).

18. Lyon, E. J. et al. Carbon monoxide as an intrinsic ligand to iron in the active site of the iron-sulfur-cluster-free hydrogenase H-2-Forming methylenetetrahydromethanopterin dehydrogenase as revealed by infrared spectroscopy. *J. Am. Chem. Soc.* **126**, 14239-14248 (2004).

19. Volbeda, A. et al. Crystal-Structure of the Nickel-Iron Hydrogenase from Desulfovibrio-Gigas. *Nature* **373**, 580-587 (1995).

20. Montet, Y. et al. Gas access to the active site of Ni-Fe hydrogenases probed by X-ray crystallography and molecular dynamics. *Nat. Struct. Biol.* **4**, 523-526 (1997).

21. Armstrong, F. A. Hydrogenases: active site puzzles and progress. *Current Opinion in Chemical Biology* **8**, 133-140 (2004).

22. Huynh, B. H. et al. Desulfovibrio Vulgaris Hydrogenase - a Nonheme Iron Enzyme Lacking Nickel That Exhibits Anomalous EPR and Mössbauer Spectra. *Proceedings of the National Academy of Sciences of the United States of America-Biological Sciences* **81**, 3728-3732 (1984).

23. Nicolet, Y., Lemon, B. J., Fontecilla-Camps, J. C. & Peters, J. W. A novel FeS cluster in Fe-only hydrogenases. *Trends Biochem.Sci.* **25**, 138-143 (2000).

24. Adams, M. W. W. The Structure and Mechanism of Iron-Hydrogenases. *Biochimica Et Biophysica Acta* **1020**, 115-145 (1990).

25. Nicolet, Y., Piras, C., Legrand, P., Hatchikian, C. E. & Fontecilla-Camps, J. C. Desulfovibrio desulfuricans iron hydrogenase: the structure shows unusual coordination to an active site Fe binuclear center. *Struct. Fold. Des.* **7**, 13-23 (1999).

26. Peters, J. W., Lanzilotta, W. N., Lemon, B. J. & Seefeldt, L. C. X-ray crystal structure of the Fe-only hydrogenase (Cpl) from *Clostridium pasteurianum* to 1.8 angstrom resolution. *Science* **282**, 1853-1858 (1998).

27. Pierik, A. J., Hulstein, M., Hagen, W. R. & Albracht, S. P. J. A low-spin iron with CN and CO as intrinsic ligands forms the core of the active site in Fe-hydrogenases. *Eur. J. Biochem.* **258**, 572-578 (1998).

28. Lemon, B. J. & Peters, J. W. Binding of exogenously added carbon monoxide at the active site of the iron-only hydrogenase (CpI) from *Clostridium pasteurianum*. *Biochemistry* **38**, 12969-12973 (1999).

29. De Lacey, A. L., Stadler, C., Cavazza, C., Hatchikian, E. C. & Fernandez, V. M. FTIR characterization of the active site of the Fe-hydrogenase from Desulfovibrio desulfuricans. *J. Am. Chem. Soc.* **122**, 11232-11233 (2000).

30. Popescu, C. V. & Munck, E. Electronic structure of the H-cluster in Fe-hydrogenases. *J. Am. Chem. Soc.* **121**, 7877-7884 (1999).

31. Rao, P. V. & Holm, R. H. Synthetic analogues of the active sites of iron-sulfur proteins. *Chem. Rev.* **104**, 527-559 (2004).

32. Pereira, A. S., Tavares, P., Moura, I., Moura, J. J. G. & Huynh, B. H. Mössbauer characterization of the iron-sulfur clusters in Desulfovibrio vulgaris hydrogenase. *J. Am. Chem. Soc.* **123**, 2771-2782 (2001).

33. Chen, Z. J. et al. Infrared studies of the CO-inhibited form of the Fe-only hydrogenase from *Clostridium pasteurianum I*: Examination of its light sensitivity at cryogenic temperatures. *Biochemistry* **41**, 2036-2043 (2002).

34. Cao, Z. X. & Hall, M. B. Modeling the active sites in metalloenzymes. 3. Density functional calculations on models for Fe -hydrogenase: Structures and vibrational frequencies of the observed redox forms and the reaction mechanism at the diiron active center. *J. Am. Chem. Soc.* **123**, 3734-3742 (2001).

35. Bruschi, M., Fantucci, P. & De Gioia, L. Density functional theory investigation of the active site of Fe -hydrogenases: Effects of redox state and ligand characteristics on structural, electronic, and reactivity properties of complexes related to the 2Fe (H) subcluster. *Inorg. Chem.* **42**, 4773-4781 (2003).

36. Liu, Z. P. & Hu, P. A density functional theory study on the active center of Fe-only hydrogenase: Characterization and electronic structure of the redox states. *J. Am. Chem. Soc.* **124**, 5175-5182 (2002).

37. Posewitz, M. C. et al. Discovery of two novel radical S-adenosylmethionine proteins required for the assembly of an active [Fe]-hydrogenase. *J. Biol. Chem.* **279**, 25711-25720 (2004).

38. Reissmann, S. et al. Taming of a poison: Biosynthesis of the NiFe-hydrogenase cyanide ligands. *Science* **299**, 1067-1070 (2003).

39. Roseboom, W., Blokesch, M., Bock, A. & Albracht, S. P. J. The biosynthetic routes for carbon monoxide and cyanide in the Ni-Fe active site of hydrogenases are different. *Febs Letters* **579**, 469-472 (2005).

40. Herskovitz, T. et al. Structure and Properties of a Synthetic Analog of Bacterial Iron-Sulfur Proteins. *Proc. Natl. Acad. Sci. U. S. A.* **69**, 2437-2441 (1972).

41. Lane, R. W., Ibers, J. A., Frankel, R. B. & Holm, R. H. Synthetic Analogs of Active-Sites of Iron-Sulfur Proteins - Bis(o-Xylyldithiolato)Ferrate(III) Monoanion, a Structurally Unconstrained Model for Rubredoxin Fe-S_4 Unit. *Proc. Natl. Acad. Sci. U. S. A.* **72**, 2868-2872 (1975).

42. Zhou, J. & Holm, R. H. Synthesis and Metal-Ion Incorporation Reactions of the Cuboidal Fe_3S_4 Cluster. *J. Am. Chem. Soc.* **117**, 11353-11354 (1995).

43. Stack, T. D. P. & Holm, R. H. Subsite-Specific Functionalization of the $[4Fe4S]^{2+}$ Analog of Iron Sulfur Protein Clusters. *J. Am. Chem. Soc.* **109**, 2546-2547 (1987).

44. Whitener, M. A., Peng, G. & Holm, R. H. Subsite-Differentiated Analogs of Biological [4Fe-4S] Clusters Effected by Binding of a Macrocyclic Polyether Trithiol. *Inorg. Chem.* **30**, 2411-2417 (1991).

45. Walsdorff, C., Saak, W. & Pohl, S. A new preorganized tridentate ligand bearing three indolethiolate groups. Preparation of 3:1 subsite- differentiated Fe4S4 clusters. *J. Chem. Soc.-Dalton Trans.*, 1857-1861 (1997).

46. Cai, L. S. & Holm, R. H. Synthesis and Electron Delocalization of $[Fe_4S_4]$-S-Fe(III) Bridged Assemblies Related to the Exchange-Coupled Catalytic Site of Sulfite Reductases. *J. Am. Chem. Soc.* **116**, 7177-7188 (1994).

47. Zhou, C. Y., Cai, L. S. & Holm, R. H. Synthesis of a $[Fe_4S_4]$-S-ferriheme bridged assembly containing an isobacteriochlorin component: A further analogue of the active site of sulfite reductase. *Inorg. Chem.* **35**, 2767-2772 (1996).

48. Rao, P. V., Bhaduri, S., Jiang, J. F., Hong, D. & Holm, R. H. On $[Fe_4S_4]^{2+}$-(μ_2-SR)-M^{II} bridge formation in the synthesis of an A-cluster analogue of carbon monoxide dehydrogenase/acetyl coenzyme A synthase. *J. Am. Chem. Soc.* **127**, 1933-1945 (2005).

49. Panda, R. et al. Initial structure modification of tetrahedral to planar Nickel(II) in a nickel-iron-sulfur cluster related to the c- cluster of carbon monoxide dehydrogenase. *J. Am. Chem. Soc.* **126**, 6448-6459 (2004).

50. Lee, S. C. & Holm, R. H. The clusters of nitrogenase: Synthetic methodology in the construction of weak-field clusters. *Chem. Rev.* **104**, 1135-1157 (2004).

51. Einsle, O. et al. Nitrogenase MoFe-protein at 1.16 angstrom resolution: A central ligand in the FeMo-cofactor. *Science* **297**, 1696-1700 (2002).

52. Lee, S. C. & Holm, R. H. Speculative synthetic chemistry and the nitrogenase problem. *Proc. Natl. Acad. Sci. U. S. A.* **100**, 12522-12524 (2003).

53. Reihlen, H., Gruhl, A. & Hessling, G. Uber den photochemischen und oxydativen Abbau von Carbonylen. *Liebigs Ann. Chem.* **472**, 268-287 (1929).

54. Hieber, W. & Gruber, J. Metallcarbonyle. 94. Zur Kenntnis Der Eisencarbonylchalkogenide. *Z. Anorg. Allg. Chem.* **296**, 91-103 (1958).

55. Seyferth, D., Henderson, R. S. & Song, L. C. Chemistry of μ-Dithio-Bis(Tricarbonyliron), a Mimic of Inorganic Disulfides.1. Formation of Di-μ-Thiolato-Bis(Tricarbonyliron) Dianion. *Organometallics* **1**, 125-133 (1982).

56. King, R. B. & Bitterwolf, T. E. Metal carbonyl analogues of iron-sulfur clusters found in metalloenzyme chemistry. *Coord. Chem. Rev.* **206**, 563-579 (2000).

57. Seyferth, D. et al. Novel Anionic Rearrangements in Hexacarbonyldiiron Complexes of Chelating Organosulfur Ligands. *Organometallics* **6**, 283-294 (1987).

58. Le Cloirec, A. et al. A di-iron dithiolate possessing structural elements of the carbonyl/cyanide sub-site of the H-centre of Fe-only hydrogenase. *Chem. Commun.*, 2285-2286 (1999).

59. Lyon, E. J., Georgakaki, I. P., Reibenspies, J. H. & Darensbourg, M. Y. Carbon monoxide and cyanide ligands in a classical organometallic complex model for Fe-only hydrogenase. *Angew. Chem. Int. Edit.* **38**, 3178-3180 (1999).

60. Schmidt, M., Contakes, S. M. & Rauchfuss, T. B. First generation analogues of the binuclear site in the Fe-only hydrogenases: $Fe_2(\mu\text{-}SR)_2(CO)_4(CN)_2^{2-}$. *J. Am. Chem. Soc.* **121**, 9736-9737 (1999).

61. Lawrence, J. D., Li, H. X., Rauchfuss, T. B., Benard, M. & Rohmer, M. M. Diiron azadithiolates as models for the iron-only hydrogenase active site: Synthesis, structure, and stereoelectronics. *Angew. Chem. Int. Edit.* **40**, 1768-1771 (2001).

62. Song, L. C., Yang, Z. Y., Bian, H. Z. & Hu, Q. M. Novel single and double diiron oxadithiolates as models for the active site of Fe-Only hydrogenases. *Organometallics* **23**, 3082-3084 (2004).

63. Razavet, M. et al. All-iron hydrogenase: synthesis, structure and properties of {2Fe3S}-assemblies related to the di-iron sub-site of the H-cluster. *Dalton Trans.*, 586-595 (2003).

64. Razavet, M., Davies, S. C., Hughes, D. L. & Pickett, C. J. {2Fe3S} clusters related to the di-iron sub-site of the H-centre of all-iron hydrogenases. *Chem. Commun.*, 847-848 (2001).

65. George, S. J., Cui, Z., Razavet, M. & Pickett, C. J. The di-iron subsite of all-iron hydrogenase: Mechanism of cyanation of a synthetic {2Fe3S}-Carbonyl assembly. *Chem.-Eur. J.* **8**, 4037-4046 (2002).

66. Zhou, T. J., Mo, Y. R., Liu, A. M., Zhou, Z. H. & Tsai, K. R. Enzymatic mechanism of Fe-only hydrogenase: Density functional study on H-H making/breaking at the diiron cluster with concerted proton and electron transfers. *Inorg. Chem.* **43**, 923-930 (2004).

67. Zhao, X., Georgakaki, I. P., Miller, M. L., Yarbrough, J. C. & Darensbourg, M. Y. H/D exchange reaction in dinuclear iron thiolates as activity assay models of Fe-H_2ase. *J. Am. Chem. Soc.* **123**, 9710-9711 (2001).

68. Gloaguen, F., Lawrence, J. D., Rauchfuss, T. B., Benard, M. & Rohmer, M. M. Bimetallic carbonyl thiolates as functional models for Fe-only hydrogenases. *Inorg. Chem.* **41**, 6573-6582 (2002).

69. Justice, A. K., Linck, R. C., Rauchfuss, T. B. & Wilson, S. R. Dihydrogen activation by a diruthenium analogue of the Fe-only hydrogenase active site. *J. Am. Chem. Soc.* **126**, 13214-13215 (2004).

70. Service, R. F. The hydrogen backlash. *Science* **305**, 958-961 (2004).

71. Holladay, J. D., Wang, Y. & Jones, E. Review of developments in portable hydrogen production using microreactor technology. *Chem. Rev.* **104**, 4767-4789 (2004).

72. in *http://www.dft.gov.uk/stellent/groups/dft_roads/documents/page/dft_roads_024056.hcsp* (U.K. Department for Transport, 2003).

73. Zhao, X. et al. Catalysis of H_2/D_2 scrambling and other H/D exchange processes by [Fe]-hydrogenase model complexes. *Inorg. Chem.* **41**, 3917-3928 (2002).

74. Mejia-Rodriguez, R., Chong, D. S., Reibenspies, J. H., Soriaga, M. P. & Darensbourg, M. Y. The hydrophilic phosphatriazaadamantane ligand in the development of H_2 production electrocatalysts: Iron hydrogenase model complexes. *J. Am. Chem. Soc.* **126**, 12004-12014 (2004).

75. Ott, S., Kritikos, M., Akermark, B., Sun, L. C. & Lomoth, R. A biomimetic pathway for hydrogen evolution from a model of the iron hydrogenase active site. *Angew. Chem. Int. Edit.* **43**, 1006-1009 (2004).

76. Capon, J. F., Gloaguen, F., Schollhammer, P. & Talarmin, J. Electrochemical proton reduction by thiolate-bridged hexacarbonyldiiron clusters. *J. Electroanal. Chem.* **566**, 241-247 (2004).

77. Kolomyjec, C., Whelan, J. & Bosnich, B. Biological Analogs - Synthesis of Vicinal Trimercapto Ligands. *Inorg. Chem.* **22**, 2343-2345 (1983).

78. Maisonnat, A., Devillers, J. & Poilblanc, R. Assembling Potentialities of an Anionic Tripod Ligand - Trirhodium and Triiridium Complexes of 1,1,1-Tris(Sulfidomethyl)Ethane - Molecular-Structure and Crystal Packing of $Ir_3(CH_3C(CH_2S)_3)(CO)_6$. *Inorg. Chem.* **26**, 1502-1507 (1987).

79. Ghilardi, C. A., Midollini, S., Orlandini, A. & Vacca, A. Reactivity of the Tripodal Trithiol 1,1,1-Tris- (Mercaptomethyl)Ethane toward Methyl-Mercury and Ethyl-Mercury Halides. *J. Chem. Soc.-Dalton Trans.*, 3117-3121 (1993).

80. Ghilardi, C. A., Midollini, S., Orlandini, A. & Scapacci, G. Synthesis and crystal structure of the complex $(CH_3C(CH_2PPh_2)_3)Rh(CH_3C(CH_2S)_3)$ center dot 0.5THF. *Inorg. Chim. Acta* **266**, 113-116 (1997).

81. Hu, J. & Mattern, D. L. Ferrocenyl derivatives with one, two, or three sulfur-containing arms for self-assembled monolayer formation. *J. Org. Chem.* **65**, 2277-2281 (2000).

82. Smith, M. B. & March, J. *March's Advanced Organic Chemistry - Reactions, Mechanisms, and Structures* (Wiley, New York, 2001).

83. Furniss, B. S., Hannaford, A. J., Smith, P. W. G. & Tatchel, A. R. *Vogel's Textbook of Practical Organic Chemistry* (Longman, Essex, 1989).

84. Nakamoto, K. *Infrared and Raman Spectra of Inorganic and Coordinatino Compounds* (Wiley, New York, 1997).

85. Cotton, F. A. & Wilkinson, G. *Advanced Inorganic Chemistry* (Wiley, New York, 1988).

86. Winter, A., Zsolnai, L. & Huttner, G. Dinuclear and Trinuclear Carbonylairon Complexes Containing 1,2-Dithiolato and 1,3-Dithiolato Bridging Ligands. *Z.Naturforsch.(B)* **37**, 1430-1436 (1982).

87. Li, H. X. & Rauchfuss, T. B. Iron carbonyl sulfides, formaldehyde, and amines condense to give the proposed azadithiolate cofactor of the Fe-only hydrogenases. *J. Am. Chem. Soc.* **124**, 726-727 (2002).

88. Razavet, M. (Department of Biological Chemistry, John Innes Centre, Norwich, 2002).

89. Zampella, G. et al. Dissecting the intimate mechanism of cyanation of {2Fe3S} complexes related to the active site of all-iron hydrogenases by DFT analysis of energetics, transition states, intermediates and products in the carbonyl substitution pathway. *Chem.-Eur. J.* **11**, 509-520 (2005).

90. Krogh-Jespersen, K. et al. Molecular and Electronic Structures of Pentaammineruthenium(II)-Thioether Complexes. The Nature of Ru(II)-S Back-Bonding Elucidated by Structural, Electronic Spectral, and Molecular Orbital Studies. *J. Am. Chem. Soc.* **114**, 4345-4353 (1992).

91. Jacobsen, H., Kraatz, H. B., Ziegler, T. & Boorman, P. M. A New Look at an Old Ligand: Surprises with Thioethers. A Density Functional-Study. *J. Am. Chem. Soc.* **114**, 7851-7860 (1992).

92. Mullen, G. E. D., Went, M. J., Wocadlo, S., Powell, A. K. & Blower, P. J. Electron transfer induced C-S bond cleavage in rhenium and technetium thioether complexes: Structural and chemical evidence for π back-donation to C-S σ^* orbitals. *Angew. Chem.-Int. Edit. Engl.* **36**, 1205-1207 (1997).

93. Solomon, E. I., Hedman, B., Hodgson, K. O., Dey, A. & Szilagyi, R. K. Ligand K-edge X-ray absorption spectroscopy: covalency of ligand-metal bonds. *Coord. Chem. Rev.* **249**, 97-129 (2005).

94. Talarmin, J., Gloaguen, F. & Schollhammer, P. Catalysis of the electrochemical H_2 evolution by di-iron sub-site models. *Coord. Chem. Rev.* **in press** (2005).

95. Dewar, M. J. S., Hashmall, J. A. & Trinajst.N. Ground States of Conjugated Molecules. XXII. Polarographic Reduction Potentials of Hydrocarbons. *J. Am. Chem. Soc.* **92**, 5555-& (1970).

96. Parker, V. D. Energetics of Electrode Reactions. II. Relationship between Redox Potentials, Ionization Potentials, Electron Affinities, and Solvation Energies of Aromatic Hydrocarbons. *J. Am. Chem. Soc.* **98**, 98-103 (1976).

97. Howell, J. O. et al. Electron Transfer from Aromatic Hydrocarbons and Their π-Complexes with Metals. Comparison of the Standard Oxidation Potentials and Vertical Ionization Potentials. *J. Am. Chem. Soc.* **106**, 3968-3976 (1984).

98. Chatt, J., Kan, C. T., Leigh, G. J., Pickett, C. J. & Stanley, D. R. Transition Metal Binding Sites and Ligand Parameters. *J. Chem. Soc.-Dalton Trans.*, 2032-2038 (1980).

99. Artero, V. & Fontecave, M. Some general principles for designing electrocatalysts with hydrogenase activity. *Coord. Chem. Rev.* **in press** (2005).

100. Bard, A. J. & Faulkner, L. R. *Electrochemical Methods. Fundamental and Applications* (Wiley, New York, 1980).

101. Liu, T. B. et al. Synthesis, structures and electrochemical properties of nitro- and amino-functionalized diiron azadithiolates as active site models of Fe-only hydrogenases. *Chem.-Eur. J.* **10**, 4474-4479 (2004).

102. Steudel, E., Posdorfer, J. & Schindler, R. N. Intermediates and Products in the Electrochemical Reduction of Nitrosobenzene. A Spectroelectrochemical Investigation. *Electrochim. Acta* **40**, 1587-1594 (1995).

103. Best, S. P. Spectroelectrochemistry of hydrogenase enzymes and related compounds. *Coord. Chem. Rev.* **in press** (2005).

104. Nakamoto, K. & Rundle, R. E. Spectroscopic Study of the Monomer and the Dimer in Nitrosobenzene Derivatives. *J. Am. Chem. Soc.* **78**, 1113-1118 (1956).

105. Hacker, N. P. Investigation of the Polymerization of 1,4-Dinitrosobenzene by Low-Temperature Infrared and UV Absorption Spectroscopy. *Macromolecules* **26**, 5937-5942 (1993).

106. Averill, B. A., Herskovitz, T., Holm, R. H. & Ibers, J. A. Synthetic Analogs of Active-Sites of Iron-Sulfur Proteins. 2. Synthesis and Structure of Tetra[Mercapto-μ_3-Sulfido-Iron] Clusters, $[Fe_4S_4(SR)_4]^{2-}$. *J. Am. Chem. Soc.* **95**, 3523-3534 (1973).

107. Wong, G. B., Bobrik, M. A. & Holm, R. H. Inorganic Derivatives of Iron Sulfide Thiolate Dimers and Tetramers - Synthesis and Properties of Halide Series $[Fe_2S_2X_4]^{2-}$ and $[Fe_4S_4X_4]^{2-}$ (X=Cl, Br, I). *Inorg. Chem.* **17**, 578-584 (1978).

108. Wang, X. B. et al. Probing the intrinsic electronic structure of the cubane 4Fe-4S cluster: Nature's favorite cluster for electron transfer and storage. *J. Am. Chem. Soc.* **125**, 14072-14081 (2003).

109. Cai, L. S., Weigel, J. A. & Holm, R. H. Analogs of Bridged Biological Active-Site Assemblies - the [Fe_4S_4]-Sulfide-Heme Unit. *J. Am. Chem. Soc.* **115**, 9289-9290 (1993).

110. Daley, C. J. A. & Holm, R. H. Reactions of site-differentiated $[Fe_4S_4]^{2+,1+}$ clusters with sulfonium cations: reactivity analogues of biotin synthase and other members of the S-adenosylmethionine enzyme family. *J. Inorg. Biochem.* **97**, 287-298 (2003).

111. Yakobson, G. G., Kobrina, L. S. & Vorozhtsov, J., N. N. Aromatic Nucleophilic Substitution. IV. Reaction of pentachloro derivatives of benzene with sodium methoxide. *Zhurnal Obshchei Khimii* **35**, 137-141 (1965).

112. Hardy, A. D. U., Macnicol, D. D. & Wilson, D. R. New Approach for the Design of Inclusion Compounds. *J. Chem. Soc.-Perkin Trans. 2*, 1011-1019 (1979).

113. Stack, T. D. P. & Holm, R. H. Subsite-Differentiated Analogs of Biological $[4Fe4S]^{2+}$ Clusters - Synthesis, Solution and Solid-State Structures, and Subsite-Specific Reactions. *J. Am. Chem. Soc.* **110**, 2484-2494 (1988).

114. Pollak, J. & Schadler, B. Uber homologe Dimerkaptobenzole. VI. Mitteilung uber mehrwertige Merkaptane der Benzolreihe. *Monatshefte fur Chemie* **39**, 129-147 (1918).

115. Stack, T. D. P., Weigel, J. A. & Holm, R. H. The Cavitand Concept in the Synthesis of Subsite-Differentiated Analogs of Biological $[4Fe4S/Se]^{2+}$ Clusters - Cluster Capture Reactions, Ligand Conformational-Analysis, and the Structure of a Trigonal $[4Fe4Se]^{2+}$ Analog. *Inorg. Chem.* **29**, 3745-3760 (1990).

116. Depamphilis, B. H., Averill, B. A., Herskovitz, T., Que, L. & Holm, R. H. Synthetic Analogs of Active-Sites of Iron-Sulfur Proteins. 6. Spectral and Redox Characteristics of Tetranuclear Clusters $[Fe_4S_4(SR)_4]^{2-}$. *J. Am. Chem. Soc.* **96**, 4159-4167 (1974).

117. Holm, R. H., Phillips, W. D., Averill, B. A., Mayerle, J. J. & Herskovitz, T. Synthetic Analogs of Active-Sites of Iron-Sulfur Proteins. 5. Proton-Resonance Properties of Tetranuclear Clusters $[Fe_4S_4(SR)_4]^{2-}$. Evidence for Dominant Contact Interactions. *J. Am. Chem. Soc.* **96**, 2109-2117 (1974).

118. Ciurli, S. et al. Subsite-Differentiated Analogs of Native $[4Fe4S]^{2+}$ Clusters - Preparation of Clusters with 5-Coordinate and 6-Coordinate Subsites and Modulation of Redox Potentials and Charge- Distributions. *J. Am. Chem. Soc.* **112**, 2654-2664 (1990).

119. Perdew, J. P. Density-Functional Approximation for the Correlation-Energy of the Inhomogeneous Electron-Gas. *Phys. Rev. B* **33**, 8822-8824 (1986).

120. Becke, A. D. Density-Functional Exchange-Energy Approximation with Correct Asymptotic-Behavior. *Phys. Rev. A* **38**, 3098-3100 (1988).

121. Schafer, A., Huber, C. & Ahlrichs, R. Fully Optimized Contracted Gaussian-Basis Sets of Triple Zeta Valence Quality for Atoms Li to Kr. *J. Chem. Phys.* **100**, 5829-5835 (1994).

122. Boyke, C. A., Rauchfuss, T. B., Wilson, S. R., Rohmer, M. M. & Benard, M. $Fe_2(SR)_2(\mu\text{-}CO)(CNMe)_6^{2+}$ and analogues: A new class of diiron dithiolates as structural models for the H-ox(Air) air state of the Fe-only hydrogenase. *J. Am. Chem. Soc.* **126**, 15151-15160 (2004).

123. Winter, M. & Brodd, R. J. What are batteries, fuel cells, and supercapacitors? *Chem. Rev.* **104**, 4245-4269 (2004).

124. Vijaikanth, V., Capon, J. F., Gloaguen, F., Schollhammer, P. & Talarmin, J. Chemically modified electrode based on an organometallic model of the [FeFe] hydrogenase active center. *Electrochem. Commun.* **7**, 427-430 (2005).

125. Pickett, C. J. & Ryder, K. S. Bioinorganic Reaction Centers on Electrodes - Modified Electrodes Possessing Amino-Acid, Peptide and Ferredoxin-Type Groups on a Poly(Pyrrole) Backbone. *J. Chem. Soc.-Dalton Trans.*, 2181-2189 (1994).

126. Ibrahim, S. K., Pickett, C. J. & Sudbrake, C. Peptide Derivatized Poly(Pyrrole) Modified Electrodes with Built-in Ion-Exchange Functions. *J. Electroanal. Chem.* **387**, 139-142 (1995).

127. Passos, M. S., Queiros, M. A., LeGall, T., Ibrahim, S. K. & Pickett, C. J. Solid-phase chemistry of electropolymers. *J. Electroanal. Chem.* **435**, 189-203 (1997).

128. Razavet, M. et al. Transient FTIR spectroelectrochemical and stopped-flow detection of a mixed valence {Fe(I)-Fe(II)} bridging carbonyl intermediate with structural elements and spectroscopic characteristics of the di-iron sub-site of all-iron hydrogenase. *Chem. Commun.*, 700-701 (2002).

129. Razavet, M., Artero, V. & Fontecave, M. Proton electroreduction catalyzed by cobaloximes: Functional models for hydrogenases. *Inorg. Chem.* **44**, 4786-4795 (2005).

130. Breslow, D. S. & Heck, R. F. Mechanism of the Hydroformylation of Olefins. *Chem. Ind.*, 467-467 (1960).

131. Szabo, P., Fekete, L., Bor, G., Nagymago.Z & Marko, L. Phosphorus-Containing Cobalt Carbonyls. III. Monosubstituted Derivatives of Dicobalt Octacarbonyl with Phosphines and Phosphites. *J. Organomet. Chem.* **12**, 245-248 (1968).

132. Diana, E. et al. $Co_6(\mu_3\text{-}S)_8(CO)_6.3S_8$ - Structure, Bonding, and Vibrational Analysis of an Exceptionally Electron-Rich Carbonyl Cluster. *Inorg. Chem.* **30**, 294-299 (1991).

133. Natile, G. & Bor, G. Studies of Differences in Ligand Transfer, Stability, and Fragmentation on Electron-Impact of Some Organosulfur Derivatives of Cobalt and Iron Carbonyls. *J. Organomet. Chem.* **35**, 185-193 (1972).

134. Liu, S. T. et al. Substituted boat-shaped Co_6 carbonyl cluster derivatives containing a semi-interstitial P atom and both bridging dithiolate and heterocyclic phosphido ligands. *Polyhedron* **21**, 1073-1080 (2002).

135. Hu, X., Liu, Q. W., Liu, S. T., Zhang, L. P. & Wu, B. S. Boat-Shaped Co_6 Carbonyl Cluster Derivatives Containing a Semi-Interstitial P-Atom and Bridging Thiolate or Heterocyclic Phosphido Ligands. *J. Chem. Soc.-Chem. Commun.*, 139-140 (1994).

136. Riaz, U., Curnow, O. J. & Curtis, M. D. Desulfurization of Organic Sulfur-Compounds Mediated by a Molybdenum/Cobalt/Sulfur Cluster. *J. Am. Chem. Soc.* **116**, 4357-4363 (1994).

137. Angelici, R. J. Heterogeneous Catalysis of the Hydrodesulfurization of Thiophenes in Petroleum: an Organometallic Perspective of the Mechanism. *Accounts Chem. Res.* **21**, 387-394 (1988).

138. Solomon, E. I., Basumallick, L., Chen, P. & Kennepohl, P. Variable energy photoelectron spectroscopy: electronic structure and electronic relaxation. *Coord. Chem. Rev.* **249**, 229-253 (2005).

139. Niu, S. Q. & Hall, M. B. Theoretical studies on reactions of transition-metal complexes. *Chem. Rev.* **100**, 353-405 (2000).

140. Siegbahn, P. E. M. & Blomberg, M. R. A. Transition-metal systems in biochemistry studied by high- accuracy quantum chemical methods. *Chem. Rev.* **100**, 421-437 (2000).

141. Demir, D. & Demir, C.. Differential quantum calculation of the Ripes system. *J. Velv. Undergr.* **113**, 628-639 (2003).

142. El Amraoui M., Spears B., Ferrer S.. Simulation of a dynamic system by the KPMG method. *Fan. De*. **26**, 269-286 (2000).

List of publications

Tard, C., Liu, X. M., Hughes, D. L. & Pickett, C. J.
A novel $\{Fe^{I}\text{-}Fe^{II}\text{-}Fe^{II}\text{-}Fe^{I}\}$ iron thiolate carbonyl assembly which electrocatalyses hydrogen evolution.
Chemical Communications, 133-135 (2005).

Tard, C., Liu, X. M., Ibrahim, S. K., Bruschi, M., De Gioia, L., Davies, S. C., Yang, X., Wang, L. S., Sawers, G., Pickett, C. J.
Synthesis of the H-cluster framework of iron-only hydrogenase.
Nature **433**, 610-613 (2005).

Liu, X. M., Ibrahim, S. K., **Tard, C**. & Pickett, C. J.
Iron-only hydrogenase: Synthetic, structural and reactivity studies of model compounds.
Coordination Chemistry Review, **249**, 1641-1652 (2005).

Conferences

Cédric Tard, X. Liu, S.K. Ibrahim, C.J. Pickett
Synthesis of {2Fe3S} cores related to the sub-site of [Fe]-Hydrogenase: towards total synthesis of the H-Cluster (*poster presentation*).
COST Meeting (7th International Hydrogenases Conference), Reading, UK, August 2004.

Cédric Tard, X. Liu, S.K. Ibrahim, C.J. Pickett
Synthesis of {2Fe3S} cores related to the sub-site of [Fe]-Hydrogenase: towards total synthesis of the H-Cluster (*poster presentation*).
Gordon Conference (Nitrogen Fixation), New London, NH, USA, June 2004.

Cédric Tard, X. Liu, S.K. Ibrahim, S. Davies, D. Hughes and C.J. Pickett
Toward Synthesis of a Free-Standing H-Cluster (*poster presentation*)
COST Meeting (Active Sites of Hydrogenases), Muelheim, Germany, September 2003.

Cédric Tard, X. Liu, S.K. Ibrahim, S. Davies, D. Hughes and C.J. Pickett
The Active-Site of the All-Iron Hydrogenase (*oral communication*)
Seminar of the Department of Inorganic Chemistry, University of East Anglia, UK, September 2004.

Cédric Tard, X. Liu, M. Razavet and C.J. Pickett
{2Fe3S}–Assemblies Related to the Sub-Site of All-Iron Hydrogenase (*poster presentation*)
Dalton Discussion 5, Leiden, The Netherlands, April 2003.